Current Assisted Sintering of Thermoelectric Materials

Francesco Gucci

Submitted in partial fulfilment of the requirements of the Degree of Doctor of Philosophy

School of Engineering and Materials Science,

Queen Mary, University of London

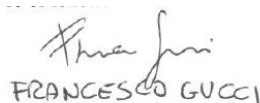**London, United Kingdom**

December 2018

Declaration

I, Francesco Gucci, confirm that the research included within this thesis is my own work or that where it has been carried out in collaboration with, or supported by others, that this is duly acknowledged below, and my contribution indicated. Previously published material is also acknowledged below.

I attest that I have exercised reasonable care to ensure that the work is original and does not to the best of my knowledge break any UK law, infringe any third party's copyright or other Intellectual Property Right, or contain any confidential material.

I accept that the College has the right to use plagiarism detection software to check the electronic version of the thesis.

I confirm that this thesis has not been previously submitted for the award of a degree by this or any other university.

The copyright of this thesis rests with the author and no quotation from it or information derived from it may be published without the prior written consent of the author.

Signature:

Date: 19 December 2018

Abstract

The performance of thermoelectric materials (ZT), their capability of converting a temperature gradient into electricity, is dependent not only on their composition but also how they were processed (pressure-less, hot pressed or Spark Plasma Sintered (SPS) etc).

SPS is a state of art process where current passes mostly through a graphite die, small or none through the sample, causing rapid Joule heating (typically 100 °C/min). A newly developed processing technique, called flash sintering, passes current directly through the sample achieving higher heating rates (100 °C/s or more). Thermoelectric materials could benefit from rapid heating, but they are too electrically conductive for traditional flash and too mechanically weak for Flash-SPS. Multi-physic software was used to develop and optimise a new process hybrid Flash-SPS (hFSPS), which uses a thin walled stainless-steel tube to constrain the powders and redirect the current to reduce Peltier cooling (a source of uneven sintering).

HFSPS was used to sinter a skutterudite, a chalcopyrite and a half-Heusler which were compared to a reference SPSed sample. The rapid heating of hFSPS resulted in better phase purity (93 vs 90 %) when reactively sintering a skutterudite and an increase in ZT (0.81 vs 0.46 at 500 °C). HFSPS produced a Half-Heusler with higher power factor and lower thermal conductivity leading to an improved ZT (0.44 vs 0.35 at 350 °C) with the same density (92.5%). hFSPS reduced the amount of sulphur loss of chalcopyrite during sintering resulting in lower electrical resistivity (100 µohm*m vs 300 µohm*m). Flashed samples also showed improved ZT (0.21 vs 0.07 at 350 °C) and an improved thermal stability.

A brief study was also performed showing a modest improvement on the oxidation resistance of $Mg_{2.1}Si_{0.48}Sn_{0.5}Sb_{0.013}$ protected by a hybrid coating when aged for 120 h at 500 °C, while no success was obtained for Higher Manganese Silicide.

Acknowledgements

Table of Contents

Table of Figures

List of Tables

Chapter 1 Introduction

Thermoelectric technology has gained significant interest in the past decades because of its unique ability of converting a thermal gradient into electricity without moving parts. The need for renewable and pollution free technologies is the driving force for the studies in this field. It is known that most of the energy produced worldwide is still coming from oil, gas and coal with a growing but still small contribution from renewable source. Engines used for energy production, including cars, cannot convert fully the chemical energy into electricity; as example gas-turbine engines have an efficiency slightly above 50% while a four stroke gasoline engine does not reach 30% [1]. The remaining energy is released as heat and dissipated into the system or environment, and only in few cases can be partially reused (co-generative system). A solid-state thermoelectric device could be used to recover that heat and could be used in combination with any other source of heat, such as photovoltaic [2] The efficiency of a thermoelectric device is largely dependent on the dimensionless figure of merit

$$ZT = \frac{\sigma S^2 T}{k} \qquad\qquad 1.1$$

where σ is the electrical conductivity, S is the Seebeck coefficient , T is absolute temperature and k is the total thermal conductivity.[3]. With the introduction of nano-structuring, thermoelectric materials experienced a significant improvement of their properties, and several material have been reported with high figure of merit: $AgPb_{18}SbTe_{20}$ (ZT 2.2 at 800 K [4]), $Bi_{0.52}Sb_{1.48}Te$ (1.47 at 450 K [5]), Bi_2Te_3/Sb_2Te_3 superlattice (2.2 at 300 K [6]), $(Mm, Sm)_yCo_4Sb_{12}$ (1.6 at 800 K, Mm is mischmetal [7]). A more recent approach is the so-called "panoscopic approach" where scattering defects, such as grain boundaries, in mesoscale region are introduced to further reduce the thermal conductivity [8]. This approach has been used for (PbTe-PbS 2.2 at 900 K [9, 10]), but it has been obtained also with porosity ($CoSb_{2.75}Si_{0.075}Te_{0.175}$ ZT 1.6 at 725 K [11], $CoSb_{2.875}Te_{0.125}$ ZT 1.1 at 820 K [12]) using post-sintering annealing or Plasma-Activated Sintering (PAS).

Processing has a significant influence on the properties, in particular thermal conductivity, as microstructure and defects can widely influence phonon scattering [8,

13, 14]. The very same material can have different properties if sintered using different techniques [12] and therefore the identification of new sintering techniques can be helpful in the research for better thermoelectric materials. Spark Plasma Sintering (SPS) is a field assisted technique that has become a state of the art method for sintering ceramics [15]. It produces materials with good properties thanks to its fast heating and the ability to produce microstructures different from those obtained using conventional methods, such as hot pressing. Several thermoelectric materials have been produced using SPS and reactive sintering has also been investigated with good results. More recently, a new field assisted technique has been developed, called flash sintering, mostly because of the impressive sintering rates, which occur in seconds when the optimum conditions are used. There are several setups used, but most of them require a pre-sintered sample of low density and a furnace to heat up the sample until it becomes sufficiently conductive. When the conductivity is increased the application of a voltage will cause a sudden shrinkage and often untypical microstructure. The first material to be flash sintered was nano-grain zirconia [16], but more oxides and high temperature materials, such as $KNbO_3$ [17],TiO_2 [18], SiC [19] and many others have now been flash sintered [20]. The application of a power pulse during SPS has been shown to induce a similar behaviour in high temperature ceramic under the application of a relatively low voltage (<10 V) and SPS itself can be used to pre-heat the sample so that its conductivity was in a suitable range (Fig 4.22) to enable flash sintering and produce sudden shrinkage. Material like ZrB_2 [21], SiC [22] or Ti_4O_7 can be flashed, but also relatively low sintering temperature thermoelectric materials, such as $Mg_{2.1}Si_{0.48}Sn_{0.5}Sb_{0.013}$ [23]; the effect of the massive Joule heating significantly influenced their microstructure. This method is usually called Flash-SPS. The purpose of this thesis was to develop a new processing technique for thermoelectric material, combining the versatility of SPS with the massive heating rate of flash, to produce new microstructures and improve the properties

1.1 Objectives

- Understand the behaviour of the SPS furnace, controlling parameters and reliability of output data.
- Develop a model to understand the critical issues of FSPS, considering each single effect at a time and develop a more suitable derivative.

- Understand the critical issues of the new sintering methodology, as example the variation of temperature distribution and power dissipation due to vertical contacts.

- Apply the new sintering method to material of different classes and observe the effect of fast heating on their properties and microstructures when compared to SPS.
    o Reactive sintering of skutterudite.
    o Sintering of material with high temperature susceptibility.
    o Sintering of high temperature thermoelectric.

Chapter 2 Review of Thermoelectric materials and Processing

2.1 Thermoelectric effects

Thermoelectricity incorporates all the phenomena involving the conversion of heat into electricity and vice versa. It shows up in many materials, but the effect is usually so small that it can be ignored in most materials. This behaviour can be used to develop energy generator or coolers, with several advantages if compared to other methods. In order to obtain efficient devices a good understanding of the phenomena and the related material structure and properties relationships is required. There are three mains reversible effects involved in thermoelectric devices (there is a substantial difference with Joule heating which also involves heat and electrical current but only happens as a dissipative process): Seebeck effect, Peltier effect and Thomson effect.

2.1.1 Seebeck effect

The Seebeck effect was discovered in 1821 by Thomas Seebeck, who noticed the presence of a voltage difference at the junctions of a two-cycle loop conductor under an applied thermal gradient. A simple way to express S is the ratio between the voltage difference ΔV and the temperature difference ΔT at the two opposite junctions (Fig 2.1) [3].

$$S=-\Delta V/\Delta T \qquad\qquad 2.1$$
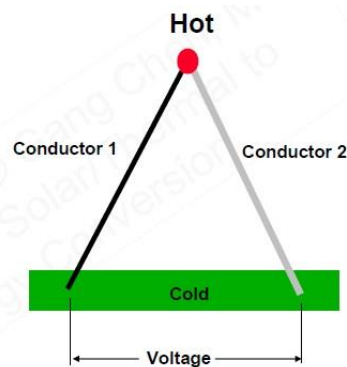
Figure 2.1 Schematic picture of Seebeck effect [24]

4

The sign of the coefficient is the same as that of the main charge carriers. The origin of the Seebeck effect can be understood from a physical point of view, by considering the behaviour of charge carriers under the application of a thermal gradient (Fig 2.2).

Figure 2.2 Seebeck effect in a single material [25]

At the initial time, the average concentration of charge carriers of any energy is the same in the whole volume. When heat is applied at one extremity, the charge carriers acquire additional energy and their mean value increases. In order to restore equilibrium, the high-energy carriers of the hot side tend to move towards the cold side, where the mean energy is lower. In this way, they accumulate at one end, producing a difference of electric potential that exists as long as the thermal gradient is maintained. It must be said that this interpretation does not belongs to Seebeck, but is related to the Thomson effect. A more accurate description requires an understanding of electronic transport theory and energy level consideration, the Mott formula for degenerate semiconductors and metals can be useful [25]:

$$S = \frac{8\pi^2 k}{3eh^2} m^* T \left(\frac{\pi}{3n}\right)^{\frac{2}{3}}$$
2.2

where k_B is the Boltzmann constant, h Is the Planck constant, e is the charge unit, T is the absolute temperature, m^* is the effective mass of charge carrier and n is their concentration. Effective mass depends on electronic band structure and for a more comprehensive explanation, as well as a more complete description of the Seebeck effect, it is recommended to read [3, 26]

2.1.2 Peltier effect

Discovered in 1834 by French physicist Jean Charles Attanhase Peltier, it represents the reverse of Seebeck effect. He noticed that, if at the same junction a current flows (instead of a thermal gradient), one of the junctions will absorb heat and the other will produce it, the sign of the heat exchange depends on the current

direction. The ratio between the heat flow and the applied current defines the Peltier coefficient [3, 25].

$$\Pi = Q/I \qquad\qquad 2.3$$

where Π is the Peltier coefficient, Q is the heat flow and I is the current.
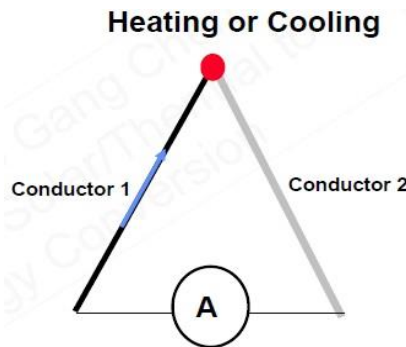
Figure 2.3 *Schematic picture of Peltier effect [24]*

2.1.3 Thomson effect

The Thomson effect is a combination of Peltier and Seebeck effect, described by Lord Kelvin in 1843.It describes the behaviour of a conductor subjected to a current and a thermal gradient, heat is produced if current and heat flow have the same direction, otherwise it is absorbed [25] :

$$\frac{dQ}{dx} = \ \tau I \frac{dT}{dx} \qquad\qquad 2.4$$

where τ is the Thomson coefficient, I is the applied current, $\frac{dQ}{dx}$ is the heat flow per unit length and $\frac{dT}{dx}$ is the temperature gradient. Lord Kelvin found also a relationship between Peltier and Seebeck coefficient [26].

$$\Pi = ST \qquad\qquad 2.5$$

where Π is the Peltier coefficient, S is the Seebeck coefficient ant T is the absolute temperature.

2.2 Thermoelectric devices

The basic structure of both cooler and generators is based on several units of p and n type legs, thermally in parallel and electrically in series. In order to modify the output parameter (Voltage, current, heat flow), legs length, legs number or total surface can be adjusted [27].
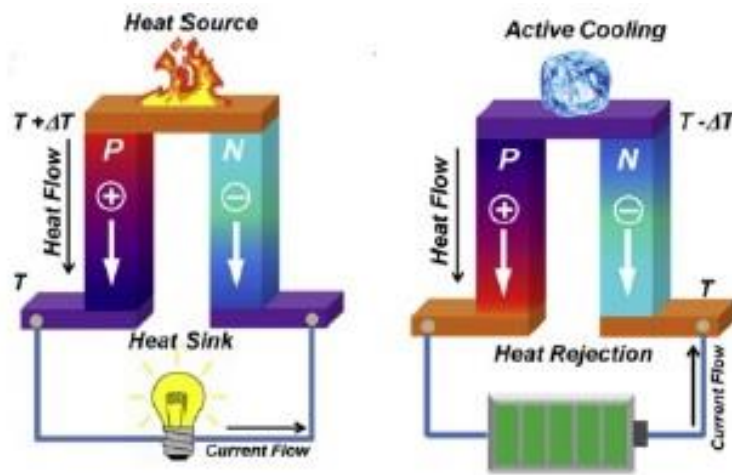
Figure 2.4 *Thermoelectric generator (left) and cooler (right) scheme [28]*

The actual efficiency of a thermoelectric device is expressed by Atkinson`s equations and has as the upper limit the efficiency of a Carnot cycle with the same hot (*TH*) and cold (*TC*) temperature [29]:

$$\eta_G = \frac{TH - TC}{TC} \frac{\sqrt{1 + ZT} - 1}{\sqrt{1 + ZT} + \frac{TC}{TH}} \qquad 2.6$$

$$\eta_C = \frac{TC}{TH - TC} \frac{\sqrt{1 + ZT} - \frac{TH}{TC}}{\sqrt{1 + ZT} + 1} \qquad 2.7$$

Where η_G is the efficiency of a generating system and η_C is the efficiency of a cooling system. The ZT or figure of merit, is a dimensionless parameter influenced by physical transport properties that can be expressed as: [3]

$$ZT = \frac{\sigma S^2 T}{k} \qquad 1.1$$

where σ is the electrical conductivity, S is the Seebeck coefficient and k is the total thermal conductivity obtained as the sum of k_e (electronic contribution) and k_{lat} (lattice contribution), the product σS^2 is usually defined as power factor.

Thermoelectric devices will be competitive with other methods to produce energy when it will be possible to use inexpensive materials with ZT >=4.
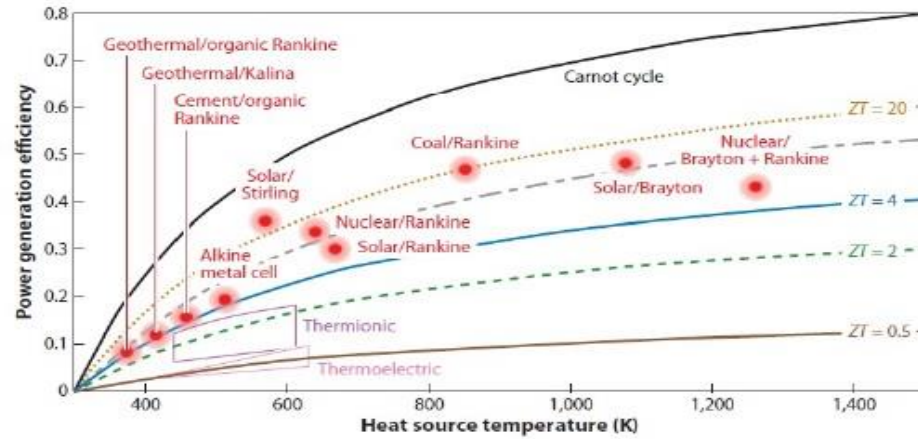
Figure 2.5 *Power generation efficiency of conventional method, low temperature 300 K [26]*

2.3 Improving the Figure of merit

The ideal material for a high figure of merit would be a Phonon Glass Electron Crystal (PGEC), as proposed by Slack [30]. It would have the thermal conductivity of a glass and the electrical properties of a crystal. Such a material has not been discovered yet, but these properties can be tuned in suitable materials to improve their overall performance. It is simple to see that it is necessary to increase the power factor or decrease the k, but this is complex because parameters are interconnected in an unfavourable way, as it they are related through the following equations [31]:

$$S = \frac{8\pi^2 k}{3eh^2} m^* T \left(\frac{\pi}{3n}\right)^{\frac{2}{3}}$$
$$\hspace{10cm} 2.2$$

$$\sigma = ne\mu \hspace{8cm} 2.8$$

$$k = k_{lat} + k_e = k_{lat} + L\sigma T \hspace{6cm} 2.9$$

Here e is the electron charge value, h is Planck constant, k_B Is Boltzmann constant, n is the carrier concentration, m^* is the effective mass of the carrier, T is the absolute temperature and L is the Lorentz number. The equation are approximations from complex models but they show the challenge for thermoelectric material, S and σ are inversely proportional for increasing n, σS^2 (power factor) have a maximum at around 10^{20} cm^{-3}, at the same time k_e is directly proportional to σ and therefore to n.
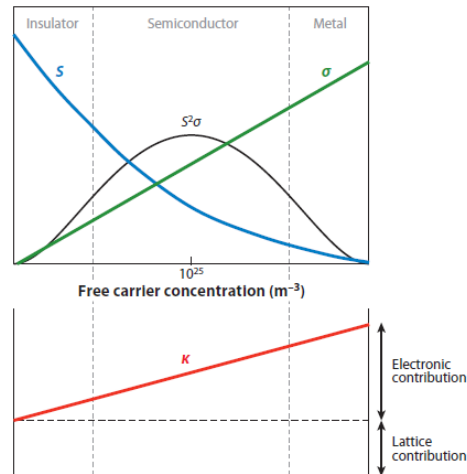
Figure 2.6 *Graphical plot of the correlation between thermoelectric parameter and carrier concentration, here expressed as m^{-3} [32]*

On the other hand, the lattice contribution to the thermal conductivity is independent from the other parameters and can be influenced in several ways. As shown in Fig 2.6, there is a maximum in the power factor at a specific carrier concentration, which can be obtained by doping [33]. Special cases have been reported where one or both properties were increased: introduction of resonant states in the band structure increased Seebeck coefficient in Tl doping of PbTe [26, 34]; multicomponent oxides based on In$_2$O$_3$ have shown significant improvement in power factor, as well as carrier energy filtering, in Pb-Sb$_2$Te$_3$ nanocomposite [35]; band convergence in Na-PbTeSe increased both electrical conductivity and Seebeck coefficient (doping induced the convergence of different conduction bands associated with different direction, thus increasing both properties) [36]. These strategies are complex to apply and require a deep understanding of the mechanisms, but they show a significant potential to further improve the figure of merit.

A more viable approach is to reduce the lattice thermal conductivity without effecting too much the electrical properties. The classical kinetic theory defines the lattice thermal conductivity as:

$$K_{lat} = \frac{1}{3} C_v v_s l \qquad\qquad 2.10$$

where C_v is the specific heat at constant volume, v_s is the average velocity of sound, l is the mean free phonon path [37]. At temperatures higher than the Debye temperature the value of C_v approaches the constant value of *3R*, which means the main contribution comes from the mean free phonon path, therefore its reduction will produce a reduction in thermal conductivity. More complex equations can be used to describe it, like Keyes equation [37], but the classical theory is useful. Phonons can be defined as lattice vibrations with different wavelengths, able to transport energy through the material. In order to reduce their mean free path or increase the scattering, several strategies have been proposed and experimentally tested [8, 26, 31, 32]:

- Introduction of isostructural compounds, such as BiSb in Bi_2Te_3, this method cannot reduce the thermal conductivity below an "alloy limit" [3, 31].
- Introduction of phonon scattering centres:
  - crystal defects
  - quantum dots
  - nanoparticles
  - grain boundaries
  - super lattice structure

The high variability of phonon wavelength requires structures with comparable dimension in order to achieve effective scattering. Lattice defects, alloying element and quantum-dots are not big enough to scatter mid and long wavelength phonons, this is possible only with larger structures such as nanoparticles or grain boundaries; therefore, the panoscopic approach has been developed. Introducing defects on different size scale (nano to micro), it is possible to increase the scattering of a broader spectrum of phonons and therefore further reduce k if compared with pure nano-structuring. [8-10, 12] An example of this approach is the Na-doped SrTe-PbTe system, atomic scale modification produces a ZT of 1.1, nano-structuring increases it to 1.7, while the addition of a mesoscale structuring brings it to an impressive 2.2 at

900 K with a significant reduction in lattice thermal conductivity [10]. Similar effects has been shown with mesoscale porosity in Te-doped $CoSb_3$ [12]
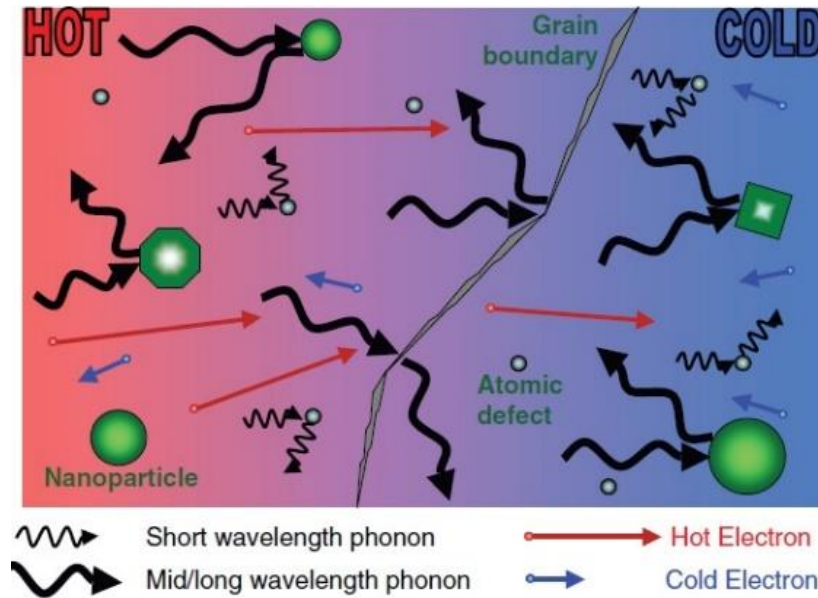
Figure 2.7 *Scheme of scattering mechanism with the effect of different sized structures [32]*

2.4 Main classes of thermoelectric materials

Thermoelectric materials are a quite wide class of materials that have received a lot of interest in the last decades. They can be classified according to the temperature range at which they can be used as low (< 200 °C), medium (200-600 °C), and high temperature (> 600 °C). Here we present a short review on materials of interests.

2.4.1 Bismuth Telluride

Bismuth telluride is the most important thermoelectric material in the low temperature range and the one with the largest amount of literature. It is a

semiconductor that crystallizes with the rhombohedral R$\overline{3}$m space group where plates of five atomic layer (Te1-Bi-Te2-Bi-Te1) are stacked along the c-axis of the unit cell thanks to Van der Walls interactions (Fig 2.8) [37].

Undoped Bi_2Te_3 is a p-type conductor that can be produced as single crystal by zone melting. It has a thermal conductivity of about 1.5 W/m*K at room temperature [38], and electrical conductivity and Seebeck of about 7 µohm*m and 160 µV/K respectively [39]. The introduction of solid solution is effective at improving the properties, as it can reduce k and modify the sign of the Seebeck coefficient. Commonly Sb is used to replace Bi with x<= 0.5 in p-type and Se to replace Te for n-type thermoelectric.
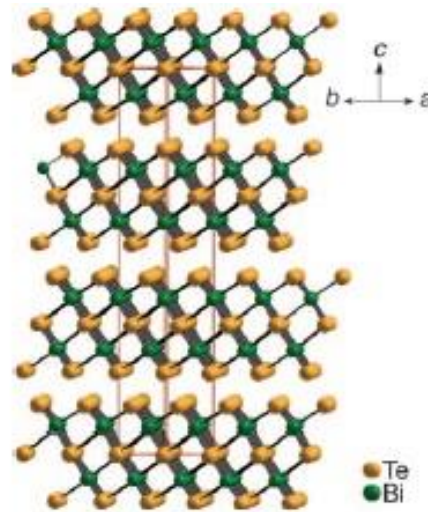
Figure 2.8 *Structure of rhombohedral Bi_2Te_3 [37]*

This layered structure shows anisotropic properties, electrical and thermal conductivities are different on the ab plane than on the c plane [40]. In a one-carrier regime, the Seebeck does not depends on orientation, and since the hole mobility anisotropy is similar to lattice conductivity anisotropy, a polycrystalline p-type materials is virtually isotropic (single crystal and randomly-oriented will still have different value of thermal and electrical conductivities) [41]. The same is not true for electrons mobility and therefore non-aligned polycrystalline n-type is not virtually isotropic. Practically different level of orientation may still show significant variation

[42, 43] as the isotropy is true only in single carrier conduction and minor carrier are not always negligible [41].

It is also worth bearing in mind that ZT can be overestimated in both types, when combining properties measured along different direction in partially oriented samples [44]. Since the preparation of samples large enough to measure both direction can be challenging, a correlation between the ratio of k_c and k_{ab} as a function of the orientation factor has been proposed by Shen et al.[44].

Commercial alloys are usually prepared by zone melting and unidirectional solidification which allows the synthesis of oriented and highly pure crystals [45]. Non-commercial single crystal obtained with this method can show a peak ZT of about 1 at 350 K for $Bi_{0.4}Sb_{1.6}Te_3$ derived from a resistivity of about 9 µohm*m, a Seebeck of about 180 µV/K and a k of about 1.8 W/m*K [46]. A polycrystalline sample, prepared with same technique by Jiang et al. [47], showed a peak ZT at 350 K of about 1.15 due to low thermal conductivity, 1.5 W/m*K , and good electrical properties, 225 µV/K and 10 µohm*m in a sample prepared so as not to be an oriented crystal.

As mentioned, preferred orientation is a relevant mechanism to improve TE properties. Moreover the variation between properties in different directions can be relevant, as shown by Fan et al [48], a p-type $Bi_{0.4}Sb_{1.6}Te_3$ ball milled and then extruded shows a variation of ZT when its properties are measured parallel or perpendicular to the extrusion direction (0.8 vs 0.95 at about 350 K) as all properties varied between 50 and 10 %.

Zhu et al. [49] used zone melted rod cut perpendicularly to the growth direction and then hot deformed at 80 MPa and 723 K (ZT of 1.3 at 300 K for $Bi_{0.5}Sb_{1.5}Te_3$). While Luo et al.[50] used a classical metallurgical method to prepare the powders and then melted them under various magnetic fields at 1023 K for 30 min before cooling. The high ZT value obtained in the direction parallel to magnetic field was related to the high level of alignment and the unpredicted formation of nano-rods (ZT of 1.71 at 323 K for $Bi_{0.5}Sb_{1.5}Te_3$ melt under 2T). Xie et al. [51] used commercial melt spun ingots as starting material. They melt spun the ingots and hand ground the ribbons. Finally, they used SPS at 773 K for 5 min and 30 MPa. The melt spun-SPS sample shows a lower thermal conductivity than the zone melted-SPS samples without showing substantial changes in the electronic properties. It might be related to the

peculiar microstructure where, beside the presence of amorphous phase, a relatively coherent interface between nano-crystalline phases still existed (ZT of 1.56 at 300 K for $Bi_{0.56}Sb_{1.44}Te_3$)

The best result has been obtained by Kim et al. [52] who produced an ingot by melt spinning and subsequently sintered them with SPS at 480 °C (above melting point) and 70 MPa. The sample containing excess Te under the transient liquid sintering produced a sample with dislocation arrays at the grain boundaries. This feature was not present in the stoichiometric sample and it was thought to be the reason for the reduction of thermal conductivity (0.65 vs 0.9 W/m*K at 330 K) which, combined with unaffected electrical properties, produced an increase in ZT of about 50% (1.86 vs 1.26 at 330 K for a $Bi_{0.5}Sb_{1.5}Te_3$).

2.4.2 Skutterudites

Skutterudites are thermoelectric materials suitable for application in the medium-high temperature range. They have a complex structure based on $CoAs_3$, symmetry is cubic with space group $Im\overline{3}$ and contains 32 atoms. A transition metal (Co, Rh, Ir, Ni or Fe) forms eight cubes, six of these are filled with a pnicogen (Sb, As, Te or P) forming square planar rectangles. The original thermoelectric skutterudites was $CoSb_3$ (Fig 2.9) which is a p-type conductor with good electrical properties (200 µV/K and 24 µohm*m at 600 K) but also a high thermal conductivity (5 W/m*k with peak ZT of 0.18 at 600 K) [53, 54]. It is possible to fill the voids with several element, often rare earth such as Yb or In, to obtain improved properties [55].

Skutterudites can be produced by several techniques: melting [56], ball milling [57], polyol [58], melt spinning [59] , arc melting [60] and others [61, 62]. If the sample obtained is a powder, common sintering technique are hot pressing [57, 63], SPS [64, 65], high pressure [60] and others [61]. Single step synthesis through SPS has been attempted for Fe and Ni-doped [66, 67] and for Te-doped [12] materials, with the production of nearly single phase samples.

Good results have been obtain with unfilled Te-doped skutterudite, Liang et al [12] obtained a ZT of 1.1 for a hierarchically structured $CoSb_{2.875}Te_{0.125}$ using a one-step Plasma Activated Sintering (PAS) process at about 100 K/min, the highest for a single doped compound. Khan et al [11] produced a co-doped $CoSb_{2.75}Si_{0.075}Te_{0.175}$, synthesized in quartz tube (cycled at three different temperature with total holding

time of 22 h), ground, pressed and re-heated in quartz tube before being sintered in SPS. The material showed a dramatic increase of its ZT after being further annealing for 15 h to induce nano-porosity (ZT 0.8 at 500 °C for SPS, ZT of 1.6 after post sintering annealing). This new microstructure produced a drop of k from 5 W/m*K to about 1.5 W/m*K at 500°C with a limited reduction of power factor from about 4000 $\mu W/m*K^2$ to about 3000 $\mu W/m*K^2$.
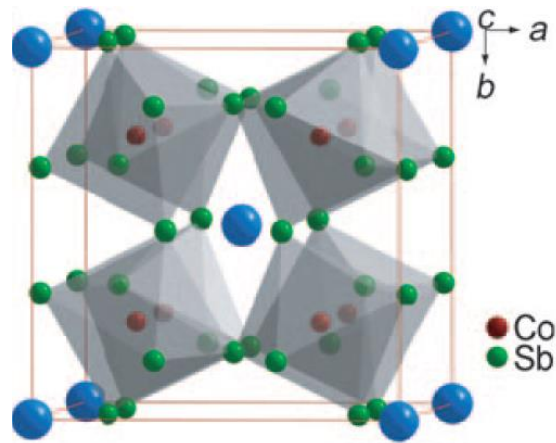
Figure 2.9 *Unit cell of CoSb3 Blue sphere are voids, the transition metal Co is at the centre of octahedral sites formed by pnicogen Sb [37]*

Another typical doping element is Ni, which can substitute for Co in lattice and, as shown in the phase diagram (Fig 5.7). They still form the skutterudite phase in the Co-rich site but can also easily form the second phase of (Co,Ni)Sb, in which Co and Ni have perfect solubility with each other [68]. Some author reports the presence of a (Co,Ni)Sb$_2$ second phases. The presence of Ni reverses the sign of Seebeck coefficient from positive to negative and can lower the thermal conductivity [57, 69, 70], also in combination with a filling element like Sn [71].

Zhang et al [67] used in situ SPS synthesis method to produce Ni$_x$Co$_{4-x}$Sb$_{12}$. They mixed the elemental powder in stoichiometric amount by milling in absolute alcohol, and then they heated it up in SPS at a heating rate of 150 K/min to 900 K at 30 MPa. As expected the samples were n-type conductor and Seebeck and electrical conductivity increases with Ni content, thermal conductivity decreases as well and have its minimum for Ni=0.2. Best ZT obtained was 0.6 at 800 K (-200 μV/K, about 3.5 W/m*K and 10 μohm*m) for Ni$_{0.2}$Co$_{3.8}$Sb$_{12}$.

He et al [57] produced a $Co_{1-x}Ni_xSb_3$ by ball milling the stoichiometric amount of powders into an alumina jar for 25-50 h (rpm are not specified), followed by hot pressing at 550–780 °C for 1-6 min at 60-160 MPa. The maximum Ni doping tested was 0.09 as sample with higher content broke after sintering. Again, higher Ni content increased the conductivity and reduced the Seebeck but also made it less temperature dependant and shifted its peak at higher temperature. Higher ZT obtained was 0.7 at 500 °C (14 µohm*m, 2.9 W/m*K and -190 µV/K).

The highest ZT obtained on this type of material is related to multiple-filled skutterudite, both p and n-type, where the void are filled with different elements to optimize the electrical properties and vibration frequencies for phonon scattering [72]. A very high ZT of about 1.8 has been obtained for n-type (Sr**,** Ba, Yb)$_y Co_4 Sb_{12}$ [73] while 1.45 has been obtained for p-type $DD_{0.59}Fe_{2.7}Co_{1.3}Sb_{11.8}Sn_{0.2}$ [74]; both material were synthesized using quartz tube method, ball milled and subjected to High Pressure Torsion and the full process lasted for more than a week.

2.4.3 Half-Heusler Intermetallic compound

Half-Heusler materials are a class of intermetallic compounds with potential high-temperature application, with the general formula XYZ, where X and Y are transition metals and Z is a main group element. The structure is based on MgAgAs crystal lattice, with three filled interpenetrating fcc sublattices with an additional vacant sublattice (Fig 2.10). They are usually stable, melt between 1100 and 1300 ° C, and can be considered to have zero sublimation up to 1000 °C [37]. Chemical substitutions can be obtained at all sites. Substitution on X and Y sites is efficient at reducing thermal conductivity, Z substitution can provide carrier tuning and increased electrical properties [75]. The most studied composition are the n-type MCoSb and the p-type MSnTi (M=Ti, Zr, Hf, Nb or V). Generally, they possess high power factor but relatively high thermal conductivity. A variety of composition have been studied, but still ZT has not reached extremely high values.

The best result has been obtained by Sakurada et al.[76] with a ZT of 1.5 at 700 K with a $Zr_{0.5}Hf_{0.5}NiSn$ doped with Ti and Sb. The reduction of thermal conductivity (2.8 vs 3.2 W/m*K at 700 K) combined with a reduction of resistivity (1.5 vs 2 mohm*cm at 700 K) and an increased Seebeck (-300 vs -240 µV/K at 700 K) produced an increase of more than 100 % in ZT.

Rogl et al [77] produced the same nominal composition using a longer process. Pure powders were arc melted, then further remelted three times in a high frequencies induction furnace and subsequently annealed in a sealed quartz ampoule for 48 h. After that, the compound was ground and ball milled with a densification aid for 4.5 h before hot pressing at 1100 °C for 1 h. The resistivity of the sample was 1 mohm*cm at 823 K, while the Seebeck coefficient was -210 µV/K with a peak of -230 µV/K, while the thermal conductivity remained almost constant and about 2.2 W/m*K. In the end the ZT obtained was again 1.5 but at 823 K.   Replacing Hf with Nb and V, less expensive elements, produced compound with lower resistivity (0.48 mohm*cm Nb and 0.6 mohm*cm V at 823 K) but lower Seebeck (-150 µV/K Nb and -170 µV/K V at 823 K) and higher thermal conductivity (3.9 W/m*K Nb and 3.5 W/m*K V at 823 K) which lead to a lower ZT (1.2 for V and 1.1 for Nb at 823 K). The results were explained by DFT calculations.

Downie et al [78] investigated the effect of adding extra Cu, Co and Ni on TiNiSn. They produced samples by mixing and pressing the elemental powder into pellets, which were wrapped in Ta foil and then sealed in quartz tube. The tube was heated up to 900 K for a day, then the pellet was reground, and the process was repeated at the same temperature but for 2 weeks. The obtained phases were a mixture of half-Heuslers with small stoichiometric deviations with the presence of small amount of full-Heusler phase. The Ni and Co were found to reduce the electrical properties and did not represent a potential Hf substitute, while Cu did show better effect. Resistivity dropped from 5 mohm*cm (non-degenerate semiconductor behaviour) at 723 K to about 1 for all Cu sample (degenerate semiconductor behaviour). Seebeck was therefore reduced from -260 µV/K for the undoped sample to -180 µV/K for 0.025 Cu doping. The final power factor was increased for the best sample from 1500 mW/mK^2 to 2000 for 0.025 Cu at 723 K, but no data for thermal conductivity were provided.

Barczak et al [79] used the same process to add Cu in TiNiSn and then sintered the pellet in hot press for 20 min at 875 °C. They found out that Cu was mostly present as interstitial, and compositional variations were present leading to the formation of a low fraction of full-Heusler grains. Extrusion of excess Cu appeared to form Cu-rich layer between grains acting as sintering aid. As observed in Downie`s work, the addition of Cu induced a degenerate semiconductor behaviour and the resistivity was

reduced with increasing amount of Cu as well as the Seebeck coefficient. The Cu doping gradually suppressed the minority carrier thermal conductivity since the undoped sample had a minimum at 550 K (5 W/m*K) which was shifted and then disappeared for higher doping. The thermal conductivity value was reduced for doping of 0.05 and below (minimum of 4.6 W/m*K at 623 K for 0.025 Cu, 4.4 W/m*K at 700 K for 0.05,), but increased again for higher amount of Cu (5 W/m*K at 773 K for 0.075 and 5.6 W/m*K at 773 K for 0.1). The enhanced electrical properties and reduced thermal conductivity lead to a ZT of 0.6 at 773 K for 0.05 Cu while the pure TiNiSn reached only 0.35.

Interesting results on the p-type were obtained by Ran et al. [80] with a ZT of 1.2 at 973K for NbFeSb doped with Ti. The compound was prepared by several subsequent arc-melting steps, followed by ball milling for 3 h and then consolidated by hot pressing at 1373 K for 2 min at 80 MPa and a heating rate of 100 °C/min. The introduction of Ti produced a significant reduction in k (0.4 vs 0.8 W/m*K at 973 K) and modified the trend of Seebeck coefficient (-200 vs -20 µV/K at 973 K) and the reduction of an order of magnitude of the resistivity. Their calculation at room temperature on the different components of lattice thermal conductivity suggested this material is quite insensitive to grain boundaries, but probably grains smaller than 100 nm may be effective, and point defects and electron phonons interactions seems to be effective as well.

Grain boundary scattering was suggested to be effective in the previously mentioned size range for n-type (Hf, Zr, Ti) NiSn as suggested by Schrade et al. [81]. Moreover the presence of defects, vacancies and second phases can be positive for a variety of compounds as shown for example by Kim et al. [82], Lei et al. [83] and Kirievsky et al. [84]. It is also worth considering the complexity of the phase diagram of these systems, p-type as example can coexist with skutterudite phase as pointed out by Romaka et al. [85] for the V-Co-Sb system.
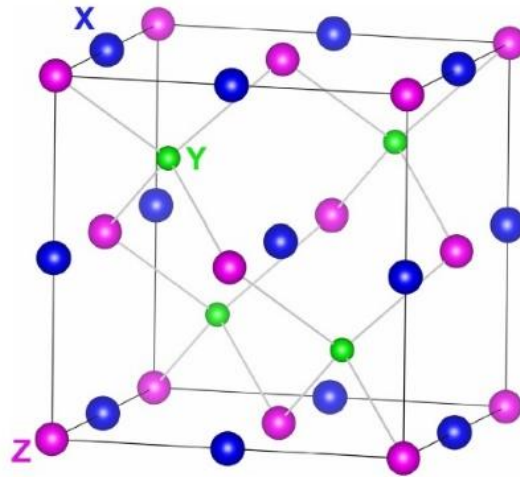
Figure 2.10 *Crystal structure of an half-Heusler material, blue, green and pink spheres are X,Y and Z atoms forming fcc sublattices, the fourth is made by voids [86]*

2.4.4 Sulphides

Sulphides are a wide class of thermoelectric materials, since sulphur is an extremely common element on earth and they are relatively cheap and have low toxicity. Significant amount of studies were initially done on binary sulphides which are currently studied in many other energy application, such as photovoltaics [2, 87] or lithium batteries [88]. Thermoelectrics binary sulphides has been studied for low, medium and high temperature application (400 K to 1000 K) such as Bi_2S_3, TiS_2, PbS, SnS, but particularly interesting is the CuS_2 system.

Table 2.1 *Non-comprehensive summary of thermoelectric binary sulphides*

Composition	ZT
Bi_2S_3	0.72 at 773 K (CuBr2 doping) [89]
	0.25 at 573 K (Ag-doping) [90]
	0.13 at 573 K (Bi-doping) [91]
TiS_2	0.45 at 800 K (Cu intercalation) [92]
	0.34 at 663 K ($Ti_{1.008}S_2$) [93]
	0.48 at 700 K ($Ti_{1.025}S_2$) [94]
PbS	at 923 K ($PbCl_2$ doping and dispersed Bi_2S_3) [95]
	at 923 K (Na-doping and s dispersed CdS) [96]
	0.8 at 900 K (PbTe addition) [97]
SnS	0.65 at 800 K (Na-doping) [98]
	0.6 at 873 K (Ag-doping) [99]
Cu_2S	1.4 at 1000 K (Cu1.98S) [100]
	1.75 at 1000 K (Cu1.97S) [100]
	0.7 at 1000 K [100]

In Cu_2S, the copper-ions have a liquid-like behaviour, which intrinsically lead to a low thermal conductivity. It possess three main phases, α-Chalcocite phase below 370 K, a β-Chalcocite phase between 370 K and 700 K, and a cubic Digenite phase above 700 K, respectively [101]. The liquid-like behaviour is typical of the cubic phase and is analogous to the Cu_2Se system, were the Se forms a rigid lattice and the Cu are highly disordered and exhibit a superionic behaviour [102]. The compositional stability of cubic phases allows the production of sub and over-stoichiometric phases $Cu_{2-x}S$ (-0.02<x<0.268), allowing the tuning of carrier concentration. Remarkable results have been obtained for $Cu_{1.98}S$ (ZT of 1.4 at 1000 K [100]) and $Cu_{1.97}S$ (ZT of 1.7 at 1000 K [100]). Dennler et al. [103] pointed out tough that binary copper sulphides have been known for 30 years and were not exploited as they suffer for thermal instability.

Among the Copper-based sulphides it is possible to find more complex compounds which have been studied as potential thermoelectric materials, most known is tetrahedrite ($Cu_{12}Sb_4S_{13}$), thanks to an intrinsically low thermal conductivity due to a complex crystal structure and the presence of lone-pair electrons [104, 105], Heo et al. [106] reported the highest ZT of 1.13 at 575 K for Mn doping.

More recently another ternary sulphide (Chalcopyrite $CuFeS_2$) has attracted interest because it has thermoelectric properties in the mineral form [107] and possess magnetic properties which are supposed to influence the thermoelectric behaviour [107, 108].

Chalcopyrite has a tetragonal crystal structure based on zinc-blende with a doubled c-axis. space group $I\bar{4}2d$ (Fig 2.11). Similar structure is shared by other compounds with semiconductor behaviour [109], commonly used for photovoltaic and solar cell applications [87]. Previous studies showed the complexity of the phase diagram and phase decomposition/transformation of the Cu-Fe-S systems with unknown areas and un-synthesized phases [110].
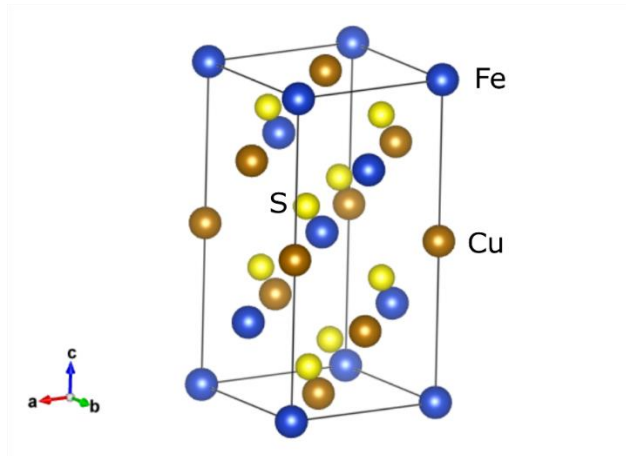
Figure 2.11 *Crystal structure of chalcopyrite generated through VESTA [111] Yellow spheres are sulphur, blue spheres are iron and brown spheres are copper.*

Engin et al. [112] observed the XRD and resistivity changes with temperature for a synthetic chalcopyrite. They used a synthetic material to reduce the impurity and inhomogeneity as many authors obtained different results. A stoichiometric amount of elements was sealed in a silica tube and heated up to 723 K for 7 days, naturally cooled and then reground and fired up to 1123 K for 2 days before being cooled at 25 K/h. They observed the coexistence of a tetragonal and cubic phase between 773 K and 798 K followed by a significant drop of resistivity (0.07 Ohm*cm to 0.01 Ohm*cm or less), when it becomes a cubic single phase. They also observed that the loss of sulphur at high temperature could cause irreversibility in the structural, magnetic and electronic phase transitions

Li et al [113] studied the effect of sulphur deficiency for synthetic chalcopyrite. Initially they measured the properties of stoichiometric phase by testing different ball milling time of stoichiometric amount of elements and sintering temperature, they identified the best condition as ball milling for 13 h at 450 rpm and sintering in SPS at 923 K for 5 min at 50 MPa. The resistivity of such sample was quite stable, compared to other samples (about 500 μohm*m at 293 K increasing to about 650 μohm*m at 573 K) and similarly for the Seebeck (-450 μV/K at 293 K decreasing to -400 at 573 K). Thermal conductivity followed a typical trend (5 W/m*K at 293 K decreasing to 2.4 W/m*K at 573 K) leading to a peak ZT of 0.07 at 573 K. After that, they test the effect of sulphur deficiency by using the identified condition on powder

containing less sulphur ($CuFeS_{2-x}$). Less sulphur causes the formation of a cubic phase, ($Cu_{1.10}Fe_{1.10}S_2$) which appear to be the main phase for a sulphur loss of 0.25.

The properties of the pure chalcopyrite were different in this second batch of test, resistivity decreases with temperature (1800 µohm*m at RT to 1200 µohm*m at 573 K) and Seebeck still have a decreasing trend (-550 µV/K at RT to –400 µV/K at 573 K). The properties trends appear to change with sulphur deficiency, resistivity decreased and get an almost constant value with a slope change for sulphur loss of 0.2 and 0.25 at 500 K. Seebeck had a constant value that decreased for lower sulphur content and thermal conductivity decreased as well with sulphur, gaining a smaller temperature dependence. The best figure of merit was obtained for $CuFeS_{1.8}$ (ZT 0.21 at 573 K with a resistivity of about 70 µohm*m, Seebeck of about -220 µV/K and a thermal conductivity of about 1.9 W/m*K). XRF measurement suggested also a variation in the Cu-Fe ratio.

Xie et al. [114] studied the effect of extra sulphur in the starting powder to counterbalance the loss due to processing ($CuFeS_{2+2x}$). Each sample was synthesized by mixing a stoichiometric amount of elements, which were grinded and pressed at 10 MPa before being sealed into a quartz tube. The quartz tube was then placed into an oven, already at the synthesis temperature (1173 K -1373 K) and held there for 20-90 s (rapid thermal explosion). The highest purity was obtained at 1273 K and 40 s, as lower temperature did not allow the reaction, while higher produced unwanted reaction products. Sample with different sulphur content were synthesized at the optimal condition and then sintered with PAS (Plasma Activated Sintering) at 873 K for 5 min with 40 MPa. The sulphur content influenced the crystal structure and two main phases were identified: chalcopyrite (apparently pure at x=0.15) and a cubic phase (probably talnakhite $Cu_{1.1}Fe_{1.1}S_2$ apparently for x=0). These two phases were mixed for 0<x<0.15 and this resulted in a peculiar behaviour of electrical resistivity (two slope changes typical of phase transformation at about 475 K and 525 K). Thermal conductivity and Seebeck increased with initial sulphur content while electrical conductivity decreased. The best results were obtained for $CuFeS_{2.05}$ with a ZT of 0.23 at 625 K but all the samples, except the $CuFeS_{2.15}$ (pure chalcopyrite, ZT 0.1 at 623 K), were quite similar.

Li et al. [115] showed the effect of Fe enrichment ($Cu_{1-x}Fe_{1+x}S_2$) on the thermoelectric properties of un-doped chalcopyrite produced by synthesis-annealing-sintering process. Stoichiometric amount of high purity elements was sealed in a quartz tube and slowly heated to 1400 K and kept there for 36 h, cooled naturally and reground. The new powder was pressed in a pellet, resealed and heated up to 800-900 K for 7 days, cooled down and ground again, then sintered in SPS at 820 K and 60 MPa. A higher content of Fe decreases resistivity (210, Seebeck coefficient and thermal conductivity, optimal Fe doping of x=0.03 and x=0.05 can lead to a ZT of 0.32 at 700 K while pure one has about 0.21.

Tsuji et al. [108] firstly showed the potential effect of Zn doping on chalcopyrite ($Cu_{0.95}Zn_{0.05}FeS_2$). First the Cu and Fe powder were purified by heating under Ar/H_2 stream at 750 K for 36 h, then all the metal powder were sealed in quartz tube and heated up to 973 K for a day, then cooled and maintained at 650 K for another day. Finally, the sample was cooled down to room temperature for a day. Process was repeated and then the sample was sintered in SPS at 773 K for 5 min at 40 MPa. After sintering, the samples were annealed at 650 K for a day with a small amount of sulphur. The sample had a small amount of ZnS (2%) and therefore the composition was shifted from the original one. Compared to Fe-rich samples ($Cu_{0.95}Fe_{1.05}S_2$ and $Cu_{0.97}Fe_{1.03}S_2$), the resistivity but also the Seebeck were increased with a significant raise of power factor (1.1 mW/m*K^2 for Zn-doped, 0.95 mW/m*K^2 for $Cu_{0.97}Fe_{1.03}S_2$ and 0.19 mW/m*K^2 for reference $CuFeS_2$ at 400 K). Thermal conductivity was reduced (9.7 W/m*K for $CuFeS_2$ to 5-6 W/m*K for doped samples at 400 K) leading to an increased ZT (0.008 for $CuFeS_2$, 0.07 for Zn-doped and 0.065 for $Cu_{0.97}Fe_{1.03}S_2$ at 400 K)

Tsuji et al. [116] also observed a higher thermal stability of chalcopyrite with higher density. Sample were synthesized using the method described before (here more than 97% density after annealing) which appeared to be stable up to 700 K and have no transformation up to 820 K (in line with literature), while the sample produced only with solid state reaction (SSR with 80 % density) seemed to lose S at 590 K. The power factor of the sample decreased after a maximum at 400 K (1.1 mW/m*K^2) to a lower value at 600 K (0.75 mW/m*K^2), extrapolating the thermal conductivity data from the previous paper they predict a peak ZT of 0.12 at 700 K.

Xie et al. carried out a detailed study of the effect of Zn doping [117]. They synthesized the compound by mixing stoichiometric amount of elements, sealing them

in quartz tube and heating up to 1373 K for 24 h. The ingots were then ground and sintered with PAS at 873 K for 5 min at 40 MPa. They produced $Zn_xCu_{1-x}FeS_2$ (0<x<0.1) and found the solubility limit of Zn as 0.03 since with higher content it started to precipitate as ZnS. The addition of Zn (and the ZnS) reduced the resistivity (about 205 µohm*m for x=0 vs about 80 µohm*m for x=0.08 at 623 K), the Seebeck (-375 µV/K for x=0 vs -250 µV/K for x=0.08 at 623 K) and more limitedly the thermal conductivity (2.5 W/m*K for x=0 vs 2.05 W/m*K for x=0.08 at 623 K). This resulted in an increased ZT of 0.26 for x=0.08 at 623 K, almost twice the value obtained for x=0 (0.135).

Most of this works does present good results, but the true stability over time and temperature was rarely assessed since data are provided usually on a single heating cycle. The discussion over the phase stability suggests the various composition might be susceptible of transformation induced by high temperature exposure. Moreover, techniques such as TGA may not be able to spot a very small amount of sulphur loss, which could instead induce significant properties changes.[117]. Many papers, especially in the mineralogy field, evidence the high complexity of the phase diagram and several uncertainty in the interpretation [110, 118], also because of the similarity of crystal structures of closely related phases [119]. Transformation due to sulphur loss, formation of composite phases and low stability of different stoichiometry was indeed observed for chalcopyrite and its metal-rich counterparts [120, 121].

2.5 Synthesis of thermoelectric materials

An important factor influencing the final properties of a thermoelectric bulk material are synthesis and processing. Different methods will produce different purity, grain size, microstructure and density, and the development of more sophisticated techniques may lead to some further improvement. It is also important to consider the time needed for each technique and its complexity, as it could reduce its potential application in industry.

2.5.1 Melting

Melting is a well-established technique for producing bismuth telluride based thermoelectric materials. It requires heating above the melting point of all the elements

or the desired compound, if higher, for enough time to allow the reaction to occur and then subsequent cooling to room temperature with or without an intermediate stage. The technology has used a variety of setups, but the processes are quite similar, they require a heating stage, a holding stage at high temperature to reach thermodynamic stability and a cooling stage that can or cannot be with an intermediate holding stage. The cooling stage is also quite important as different cooling rates can modify the microstructure and could be used to induce or prevent the precipitation of second phases.

Typical melt processing equipment consists of a simple furnace where powders are placed into a container, usually alumina boat, and then placed in a furnace usually filled with flowing gas (tubular or cylindrical), slowly heated up and held at high temperature for several hours before being cooled down. Similar setups used a sealed tube. In this case, the powders are placed into a quartz or silica tube, which is then sealed in vacuum. To prevent contamination, a crucible or a surface treatment on the glass can be used. Both methods require several hours of processing and a further pulverization before sintering as they will contain large grains due to the long processing time, on the other hand single phase of complex material can be obtained [74].

Induction heating provides heat through the production of eddy currents due to an alternating magnetic field. Since the heat is produced inside the sample by Joule heating, it can allow high heating rates, but it is susceptible to the amount of material as the magnetic field may not penetrate homogenously. For synthesis purpose, it requires a container (often Cu) which may cause contamination and limit the cooling rate. This type of heating is used for Czochralski growth, where a solid seed of the required material is immersed in a melt as a nucleation centre to produce single crystal with a homogeneous composition. Using this method good thermoelectric properties have been achieved $((Bi_2Te_3)_{1-x-y}(Sb_2Te_3)_x(Sb_2Se_3)_y$ p and n with ZT of 1 and 1.1 at 350 K [122].This technique has also been used to synthesize complex compounds such as clathrates, but the obtained rods can have a slight variation of composition at different distance from the seed. The $Ba_8Ga_{16}Ge_{30}$ produced by Saramat et al [123] had a peak ZT of 1.35 at 900 K for a sample cut at the highest distance from the seed, but composition have minimal variation along the rod length (Fig 2.12).
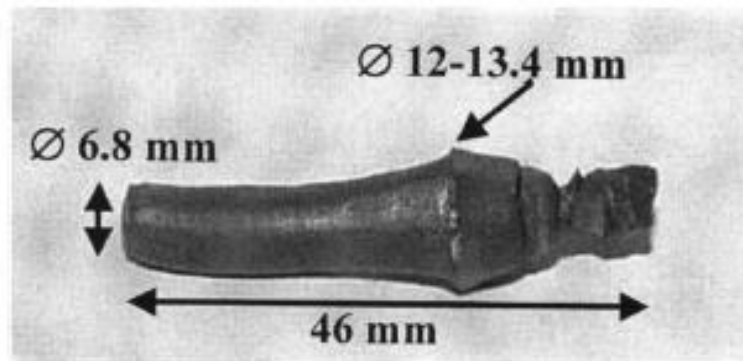
Figure 2.12 *Image of clathrate crystal grown by Czochralski method*

A more expensive variation is the levitation melting where an additional coil is coupled with the primary induction heater to produce a magnetic field. The technique does not require a container for the melted material, thus avoiding reactions and contamination.

Arc melting can produce high temperatures for melting refractory metal. It uses an electrode to produce and arc that heats the powder, thanks to radiative heat and current, up to 3000 °C. The powder is placed on a water cooled base (usually Cu) but the bottom part may not melt, which often requires more heating to ensure homogenization and/or further annealing [124]. Serrano Sanchez et al. [125] used arc melting to produce $Bi_{0.35}Sb_{1.65}Te_3$ without further reprocessing. They found a peculiar layered nano-structuring where nano-sheets of materials stacked one onto each other (Fig 2.13). It results in a high Seebeck at 395 K exceeding 350 µV/K and figure of merit of 1.1.
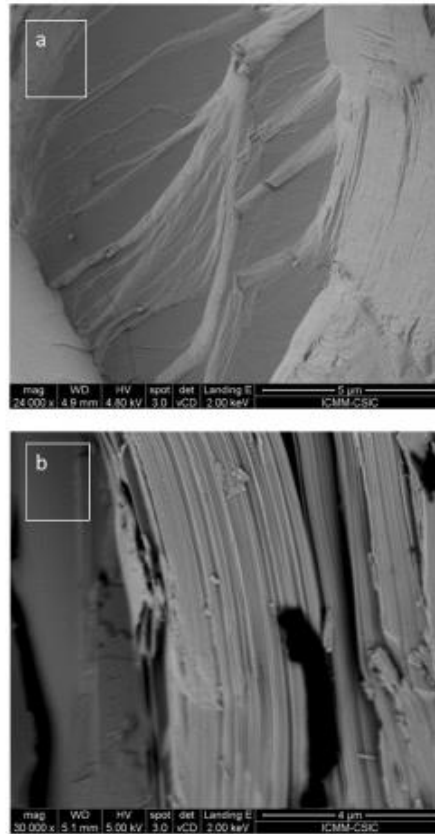
Figure 2.13 Microstructure of as arc-melted pellets of Bismuth telluride [125]

2.5.2 Ball milling

Ball milling (BM) is a very popular method for producing powders of thermoelectric materials. It can be split into mechanical grinding (BM) and mechanical alloying (MA). In addition to the grinding effect, the MA process can lead to the synthesis of compounds from elemental powders by the mechano-chemical effect. Despite the variety of existing machines, such as planetary, rotating or mixing, the working principle is pretty much the same. A vial is filled with balls made from a hard material (stainless steel, alumina, zirconia or carbides) and put into motion (rotation, shaking). The inertia of the grinding balls produces high-energy impacts on the particles, which produces cold welding, fracturing and re-welding, leading to further pulverization. Ball milling is a quite versatile technique and many parameters can be modified including ball size, ball to powder ratio, speed and time. Moreover, it can be done in a wet or dry environment where additional agents, such as stearic acid, can be added to prevent sticking of powders to the vial or balls.

Ball milling usually produces quite homogeneous compounds and fine or even nano-powders. Moreover, it will introduce defects and strain or stresses in the material, which can act as scattering centres for phonons or photons [126, 127]. A drawback is the time needed for some materials to be produced, which can exceed 90 h of processing time [128], and the welding issue, which, when anti-welding agents are not effective, requires to re-crush the powders in the vial and therefore a periodic stop of the process.

A variety of materials have been produced by ball milling and compacted with different methods, and a non-exhaustive list can be found in Tab 2.2.

Table 2.2 *Non-exhaustive list of some BM material, consolidation techniques used and ZT peak.[129]. BM (Ball-Milling), MA (Mechanical alloying), HP (Hot Press), SPS (Spark Plasma Sintering)*

Material class	Material	Method	Peak ZT and temperature	Reference
Bi2Te3 based alloy	BiSbTe	Ingots BM+HP	1.4 at 373 K	[130]
	BiSbTe with dispersed SiC	MA+SPS	1.33 at 373 K	[131]
	BiSbTe	Melt BM+HP	1.3 at 300 K	[132]
Skutterudite	$CoSb_{3-x}Te_x$	MA+SPS	0.93 at 820 K	[133]
	$CoSb_3$	BM	N/A	[134]
	$CoSb_{3-x}Te_x$	MA+SPS	1.1 at 823 K	[135]
Sulfides	$CuFeS_2$	MA+SPS	0.2 at 573 K	[113]
	$Cu_{1.96}S$	MA+SPS	0.5 at 673 K	[136]
	SnS	MA+SPS	0.16 at 823 K	[137]
Half-Hesuler	(ZrHf)Co(SbSn)	Ingot BM+HP	0.8 973 K	[138]
	FeVSb	MA+SPS	0.31 573 K	[139]
	TiNiSn	MA+SPS	0.32 785 K	[140]

2.5.3 Melt Spinning

Melt spinning (MS) is an efficient method for the rapid cooling of molten liquids (Fig 2.14). A flow of liquid is injected onto a rotating wheel that is internally cooled. The sample solidifies into a ribbon-like structure and its microstructure can be modified by changing the rotation speed of the wheel (and then the cooling rate), which can reach up to 10^7 K/min. Such an extreme cooling rate can freeze atoms into glassy phases, like metal-glass [141], producing amorphous phases that can be retained after sintering [51] or metastable compounds such as Al_6Ge_5 [142].
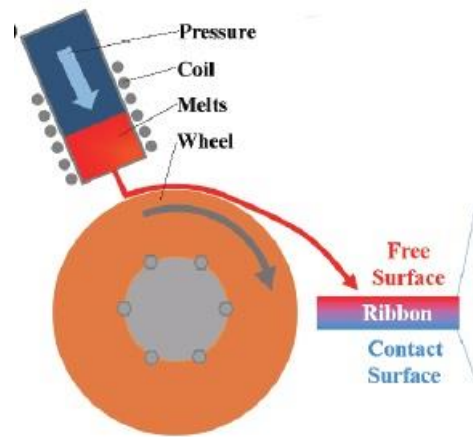
Figure 2.14 *The setup of a melt-spinning device [129]*

2.5.4 Soft chemical

Soft chemistry is usually a more complex approach for the synthesis of material, but can lead to the production of fine powders at low temperature with complex shape, such as rods or tubes. The most common techniques are hydrothermal synthesis, solvothermal synthesis and sol-gel.

Hydrothermal synthesis is used to control the size and shape of nanoparticles. It requires the dissolution of a stoichiometric precursor into water (a substrate can also be used) and then load it, seal it and heat it in an autoclave for a specific amount of time at a fixed temperature. Parameter such as pH, concentration of additives and pressure are strictly controlled, different structures can be obtained with different temperature, time and stirring/sonication. Importantly, this method allows the careful control of doping and grain orientation [129, 143]. Liu et al. [144] produced a $Bi_{2-x}Sb_xTe_3$ powders using a hydrothermal process followed by encapsulated sintering and obtained a sample with density lower than 90%. The final properties (x=1.55) showed a low thermal conductivity (less than 0.44 W/m*K when 160 K<T <300 K), influenced by the nano-grains and nano-porosity, combined with good power factor (above 20 µW/cm*K^2 when 160 K<T<300 K) leading to a high ZT peak of 1.75 at 270 K.

The solvothermal process is quite similar, but uses organics solvents or additives with both hydrophilic and hydrophobic groups. While the hydrophobic part can form the core of aggregates, the hydrophilic groups will affect the growth of target material and allows to achieve a controlled morphology.

Both these methods can be microwave assisted, which is more efficient than conventional heating, but it can influence the activation of physical reaction. Despite some advantages, it also presents some problem, as pointed out by Nüchter et al. [145], which makes difficult to compare different work, as example penetration depth is unknown for organic solvent, there are discrepancy for different temperature measurement method (shielded thermocouples, IR-sensor, fibre optics), and there is no standardized protocol for the experiments.

Sol gel processing is another easy and scalable technique commonly used for the synthesis of nanoparticles. It requires the use of precursor dispersed in a solvent and/or water, which will start to react under specific conditions, such as a specific pH. It is possible to modify the process as most parameters can be controlled; precursor, surfactants, stirring temperature and time, water/precursor/solvent ratio and washing-drying conditions [146]. It is also possible to produce nanocomposite such as core-shell particles [147].

Table 2.3 *Non-exhaustive list of thermoelectric material produced by solvothermal (ST) or hydrothermal (HT) method and peak ZT. [129]*

Material class	Material	Method	Peak ZT and temperature	Reference
BiTe based	$Bi_{0.5}Sb_{1.5}Te_3$	HT	1.15 at 300 K	[148]
	$Bi_{2-x}Sb_xTe_3$	HT	1.75 at 270 K	[144]
	Bi_2Te_3	ST	0.6 at 600 K	[149]
Sulphides	SnS	ST	0.25 at 773 K	[150]
	Ag doped-PbS	ST	1.7 at 850 K	[151]
	$Cu_{12}Sb_4S1_3$	ST	0.85 at 720 K	[152]
Skutterudite	n-type $CoSb_3$	ST	0.5 at 600 K	[153]
	$CoSb_3$	ST	0.11 at 650 K	[154]

2.6 Sintering techniques

Some of the synthesis method described can produce solid samples that can be directly tested or used in a device. More commonly, the synthesized material is in the form of a powder or subsequently crushed into fine grained or nano-sized powders and then compacted. The method used can further influence the final properties and improve its final performance. The most commonly used techniques for the

compaction of thermoelectric materials are hot pressing and Spark Plasma Sintering (SPS).

2.6.1 Spark Plasma Sintering

Spark plasma sintering is a field-assisted technique based on low voltage, direct current and pressure assisted, allowing sintering and sometimes synthesis. The device is based on a mechanical loading system acting as a high-power electrical circuit in controlled atmosphere (Fig 2.15). The tools are good electrical conductors, allowing the passage of high current (1 to 10 kA) at low voltage (below 10 V). The heat is efficiently transferred, even in the case of non-conductive materials, and can reach 1000 °C /min with a cooling rate of about 150 °C/min. The heating process can be carried out with the application of a force up to 250 kN. The temperature can be monitored with thermocouples or with pyrometers and the process can be controlled using several limiting parameters, including temperature, piston displacement or power. The punches are generally made of graphite and the maximum temperature reachable is around 2400 °C. The graphite is usually heated through the Joule effect and it transfers heat to the sample, unless the sample is more electrically conductive, in which case the sample is heated directly. The maximum pressure usable is limited by the mechanical and creep resistance (if high temperatures are used) of the tooling material. It can be used to delay or reduce grain growth but the high heating rate is also beneficial to prevent grain growth; the dominant densification mechanism, such as grain boundary diffusion, have higher activation energy than coarsening mechanism such as surface diffusion, and therefore quickly reaching the sintering temperature can increase the densification rate and reduce coarsening [15]. A shorter holding time will also reduce the coarsening. This effect depends also on the initial particle size, for agglomerated nanoparticles the final grain size can be larger than for coarser particles [155].

Concerning the presence of current, some further effects can be produced in some materials [15]. As mentioned above, if the powder is more conductive than the tooling, a significant current will flow through the sample. Since the green body is not homogeneous, a percolative conductive network will form a preferential path for electrons. Joule heating through this network may produce hot spots and temperature higher than the recorded one, potentially inducing even melting. The tooling/powder

combination will also produce a Peltier effect at the junction, which is proportional to the Seebeck coefficient. This means that, especially for thermoelectric materials, there is the significant chance of producing an inhomogeneous distribution of heat within the sample [15, 129]. Finally electrochemical interactions with the tooling could be induced by the current and potentially can be used to produce new compounds, a useful example is the synthesis of thermoelectric clathrate $K_{4.2}Na_{3.8}Si_{46}$ starting from NaSi [156].

SPS has been used to sinter several thermoelectric material showing high ZT [157, 158]. It can also induce phase separation, nano-precipitates and can potentially be used to produce in situ synthesis with good results [66, 67, 84, 117, 159, 160].
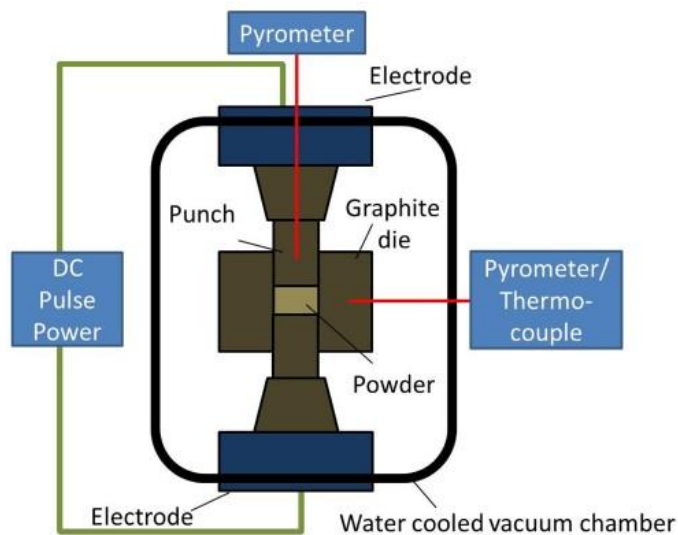
Figure 2.15 *Simple scheme of SPS setup [15]*

2.6.2 Hot pressing

Hot pressing is based on a graphite or stainless-steel mould and punch system which is heated up using an induction coil placed around the mould or a set of resistance heaters (Fig 2.16). It can be used to sinter a wide variety of ceramic as the graphite can be used up to 2400 °C in an inert environment and the maximum pressure will depend on the dimension and material of the mould itself. Homogeneous heating can be challenging when induction heating is used as the die should be placed exactly in the centre.

The induction heat will not be produced through all the thickness of the mould and therefore its thermal properties are important, as the heat has to be transferred to the sample. Moreover, high heating rates are not recommended as they can crack the mould because of differences in thermal expansion between inner and outer surface. When heating elements are used, it is easier to get homogeneous temperature when a long dwell time is used, but this can allow grain growth [157] and requires a lot energy.

It is possible to obtain very high density when the time and temperature are optimised. In some case it is possible to observe better properties in SPS samples than hot-press sample, as it can give lower thermal conductivity and smaller grain size [157, 158].
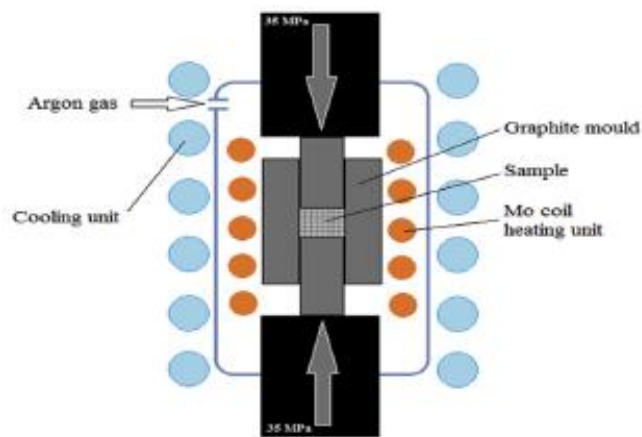
Figure 2.16 *Scheme of hot pressing with Mo heating elements [161]*

A few variation of this technique are available, such as microwave-assisted hot pressing [162], rapid hot press [163] or hot isostatic press (pressure is applied also on the side all).

2.7 Post-sintering

Sometimes further processing is required in order to tailor the microstructure and further increase the properties of thermoelectric materials. In some cases post-sintering processes just involve a simple annealing, which can be used to increase homogeneity and phase purity, reduce stresses and/or to induce the precipitation of second phases [164]. It has also been used to produce multi-scale porosity by evaporation of Te in $CoSb_{2.75}Si_{0.075}Te_{0.175}$, inducing a limited reduction in electrical properties coupled with a drastic decrease in lattice thermal conductivity and a consequent increase of ZT of a 100% [11].

Anisotropic materials, such as Bi_2Te_3-based or SnSe, can be post-processed to induce preferred grain orientation, as the properties vary significantly in different crystal lattice directions and the production of oriented material can increase the overall performance [44, 165]. The main techniques used for thermoelectric materials are hot forging and SPS-forging, which are based on a similar principle (Fig 2.17). A bulk sample with a specific diameter is placed into a die having larger size and then pressed at high temperature. The combination of plastic deformation and grain growth produce a re-orientation of grains along the pressing direction. This new textured material will commonly have enhanced electrically properties which can potentially increase also the electronic contribution to thermal conductivity.

Moreover, since phonon transport is intrinsically higher in plane than out-of-plane, preferred orientation may increase thermal conductivity. Different effects can occur in the same material under different forging condition. Shen et al. [166] investigated hot forging of Bismuth Telluride and induced the formation of nano-precipitates and an high density of defects, which lowered the thermal conductivity and increased the power factor when compared to simple hot pressing, but the degree of preferred orientation was not high. Jiang et al. [43] used SPS to hot forge a similar composition and obtained oriented samples with a significant amount of defects, increasing resistivity, but unexpectedly producing a higher Seebeck and lower thermal conductivity. Pan et al. [167] obtained an increase in the properties of n-type BiTe using a two stage SPS-forging where the first step induced an increase in thermal conductivity and the second produced nanoscale defects and nanostructures that decreased it while maintaining the electrical properties of non-aligned material.
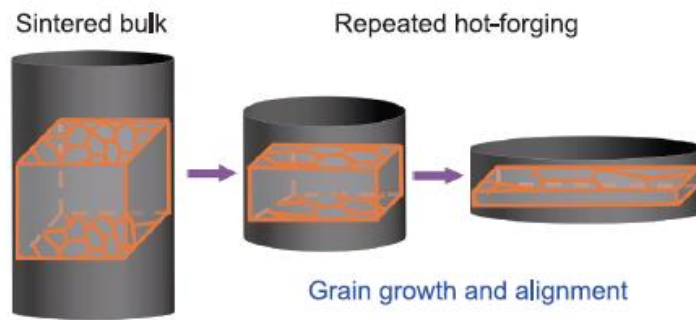
Figure 2.17 Simple schematic of forging principle [129]

Forging can be used to manipulate the microstructure of thermoelectric materials and potentially lead to a significant improvement on final properties.

2.8 Flash sintering

Recently a new technique called flash sintering has gained a significant interest. First introduced by Cologna et al. who sintered nano-grain size zirconia at a temperature of 850 °C, much lower than for conventional sintering at 1600 °C, in a few second [16]. The process was then defined by Raji et al [168] as "*A method of sintering a material comprising simultaneously exposing the material to an electric field and to heat, such that the material is sintered, wherein the electrical field is between 7.5 V/cm and 1000 V/cm, wherein the onset of sintering is accompanied by a power dissipation between 10 to 1000 mWmm^{-3}, wherein the onset of sintering is accompanied by a non-linear increase in the conductivity of the material, and wherein the time between the onset of sintering and the completion of sintering is less than one minute*". A presintered sample (dog-bone, bar or cylinder shape) is heated up to T_{onset} and then is sintered in several seconds under the application of a critical voltage. Setup used can be pressure-less or pressure-assisted in which case it is possible to use an SPS device (Flash-SPS or FSPS).
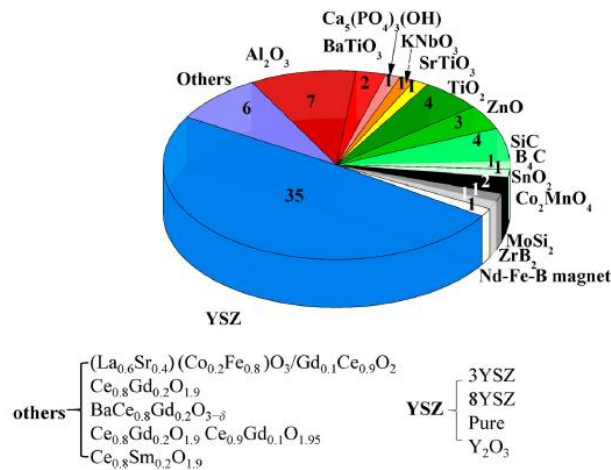
Figure 2.18 Pie chart of material consolidated by flash up to 2017. The conductivity mechanism (at T_{onset}) is colour coded: oxygen ion conductors (blue), insulating oxides (red), semiconductors (green), metals (grey). Some materials might show a mixed conductivity mode depending on the temperature. Some of the materials have been consolidated as composites [20].

This technique has been applied to several material (Fig 2.18) with very different mechanisms of electrical conductivity and properties, often achieving high densities [20]. There are several proposed mechanisms [20] for the densification but they are still under debate.

The process can influence the microstructure of different types of materials in a variety of ways:

- reducing the grain growth compared to SPS, not fully suppressed as it can depends on the sintering variables [169], sometimes with narrower distribution [170] or anisotropy [171].

- Presence of second phases [172] phase separation [23] or new phases [170].

- Forging-like effect (Flash-SPS) [173].

Focusing on the Flash-SPS technique, interaction with graphite should be taken into account as well as the potential effect of Peltier cooling (stronger than in conventional SPS as current passes completely through the punch-sample junction).

Up to now there are only few papers related to the thermoelectric properties of flash-sintered material.

Yu et al. [174] compared the effect of SPS and FSPS on the properties and structure of Ti_nO_{2n-1}. A presintered sample with 50% density, obtained using SPS, was flashed using two different configurations, one with a graphite felt between punch and sample and one without. The fast sintering (5s) observed maintained almost unchanged the original composition and grain size of starting powder, while producing a bulk sample with high density. In addition, the most conductive phase Ti_4O_7 did not disappear as in the SPS sample. The peak figure of merit was 0.085 at 1073 K for the FSPSed sample, despite no data are provided for the SPSsed sample, its higher resistivity suggested a lower value. The use of a felt, in series with the sample, improved the homogeneity of the final pellet.

Du et al. compared the effect of FSPS and conventional SPS on the properties and microstructure of magnesium silicide-stannide SPS (synthesis method is not disclosed). Flash sintering of the green pellet (1000 °C/min) resulted in a very different microstructure in which the oxide contamination layer on the powders was broken and dispersed into a Sn-rich phase that formed at the grain boundaries, probably because of intense joule heating at the interface causing melting. The phase segregation was weaker in the SPS sample and the oxide layer was continuous. The electrical conductivity of the FSPS sample was 4 times lower at 400 °C (200 µohm*m vs 50 µohm*m), while the Seebeck coefficient (-320 µV/K vs -280 µV/K) and thermal conductivity (1.4 W/m*K vs 1.6 W/m*K) were not significantly modified, therefore the peak ZT was increased almost three-fold at the same temperature.

Srinivasan et al. [175] compared the effect of different processing routes: Solid State reaction (SS), Melt Quenching (MQ), conventional SPS (SPS) and hybrid Flash-SPS (hFSPS) on the properties and microstructure of $CuPb_{18}SbTe_{20}$. First synthesis step was the same for all samples, stoichiometric amount of elements was placed into a quartz tube which was sealed and heated up to 1223 K in 12 h and held at that temperature for 15 h. The SS sample was obtained by cooling the melt to room temperature in 18 h, while the MQ sample was obtained by rapidly quenching the tube in water and then annealing it at 873 K for 8 h. SPS and hFSPS sample were produced from powder of MQ. SPS was sintered at 673 K (80 K/min) for 5 min at 85 MPa while hFSPS was sintered at 800 K (10000 K/min) and 80 MPa

It was observed that hybrid Flash-SPS produced a *"multiscale hierarchical architecture"* with large grain surrounded by small grain and submicron-porosity, which induced a low thermal conductivity at 700 K (1 W/m*K for SS and hFSPS, 1.2

W/m*K for MQ and SPS), while still retaining a high power factor (almost 1.2 mW/m*K^2 hFSPS, 0.78 mW/m*K^2 for MQ, about 1.1 mW/m*K^2 for SS and SPS). The final ZT reached 0.8 at 700 K while SS, SPS and MQ samples had a lower value, respectively 0.7, 0.6 and 0.45.

The same authors [176], compared the properties of an SPS sample and an hFSPS with composition $Ge_{0.90}Ga_{0.02}Sb_{0.08}Te$. The powders were synthesized by mixing the elemental powders into a quartz tube, which was then sealed and heated up to 1223 K in 12 h and held there for 12 h before being cooled naturally. SPS samples were sintered at 723 K (80 K/min) for 5 min at 80 MPa while hFSPS was sintered at 873 K (10000 K/min) and 55 MPa.

It was observed a positive effect of the fast heating, which reduced the total thermal conductivity producing a similar hierarchical structure (about 0.5 W/m*K smaller between 473 K and 723 K). The lower carrier density reduced the electrical conductivity (about 50%) and enhanced the Seebeck coefficient (about 20 %), leading to a reduced power factor (about 3 mW/m*K^2 vs 3.8 mW/m*K^2 in the temperature range of 600 K to 773 K). The significant reduction in thermal conductivity, allowed the hFSPS to reach a high and stable value of ZT (1.95 peak at 723 K, ZT>1.75 in the range of temperature 600 K-773 K) while SPS reach a lower peak and a larger variation with the temperature (1.75 at 723 K, 1.25 at 600 K).

Mikami et al. [177] used a zirconia mould and graphite punches to Flash-SPS Sb_2Te_3, with AC current (to control the Peltier cooling) and compared the thermoelectric properties with an SPS sample.). Three different currents were ideally applied for 1 s (0.7 kA, 1 kA and 1.2 kA) with three different density obtained (84%, 95% and 97%), heating rate was higher than 10000 °C/min. They observed a slightly lower degree of orientation for the FSPS sample (0.25 vs 0.3). All sample resulted in similar Seebeck coefficient but different electrical conductivity (0.75*10^5 S/m at 500 K for the 84% dense FSPS, about 1.1 *10^5 S/m for the 95% and 97% FSPS samples and 1.4*10^5 S/m for SPS). The thermal conductivity was influenced as well, but microstructural differences are not described in detail (0.8 W/m*K for the 84% dense FSPS, about 1.1 for the 95% dense FSPS, about 1.2 for the 97% dense FSPS and 1.3 for SPS at 500 K). Because of the anisotropy of the material the authors did not provide the ZT because the electrical and thermal properties were measured perpendicularly to each other.

Other potential thermoelectric materials have been processed with pressure-less flash (SrTiO [170]) and pressure assisted flash (ZnO [171]) but no properties comparison are available, as the evaluation of functional properties was not the focus of the authors. It is clear that flash sintering might have a beneficial effect on the properties of thermoelectric materials, but it is difficult to predict what properties the fast heating might effect. This especially because different materials showed different behaviour and most of work reported to date has been performed on oxide compounds or ceramics requiring high sintering temperatures and functional properties are not reported.

2.9 Conclusion

Microstructure can significantly influence the properties of thermoelectric materials. It has been shown that defects, nanostructures, hierarchical structure (grains or porosity), defects and dislocation can reduce thermal conductivity and/or modify the electrical properties (usually electrical conductivity is reduced). Being able to optimise a microstructure with useful features is therefore of great interest for engineering high performance thermoelectric materials. Synthesis and sintering techniques are important in order to produce and retain a specific crystal structure or feature (such as amorphous phase for melt-spun material), but also to modify microstructure (reduced grain growth in SPS, defects in hot forging, porosity in post-sintering annealing). The effect of high heating rates (>1000 °C/min) has been explored for ceramics requiring high sintering temperatures, mostly in terms of microstructure and rarely in terms of properties. The unique features observed are expected to be beneficial for some thermoelectric and the versatility of SPS device can allow a variety of processing conditions and setups (such as forging) that could lead to better properties.

Chapter 3 Experimental Details

3.1 Samples Description

3.1.1 Commercial powder and received powders

Skutterudite sample are made from commercial powder produced by MATRES s.c.r., Higher Manganese Silicide $MnSi_{1.74}$ (HMS) samples are made using powder provided by PowerDriver UK (Limited) and $Mg_{2.1}Si_{0.48}Sn_{0.5}Sb_{0.013}$ (Mg-Silicide) are made using powder provided by European Thermodynamics Ltd (ETL), and therefore synthesis condition cannot be described as they are confidential.

Half-Heusler powder ($Cu_{0.05}TiNiSn$) were produced by solid state reaction by Prof. Bos group (Heriot-Watt Institute, Edinburgh) following the recipe described by Barczak et al. [79] where: "elemental powder (Alfa Aesar; Ti, 325 mesh; Ni,120 mesh; Cu, 625 mesh; and Sn, 100 mesh; all ≥99.8% purity) were mixed together using a mortar and pestle and cold-pressed into 13 mm diameter pellets. The samples were wrapped in 0.025 mm thick Ta foil (Sigma-Aldrich) and annealed in evacuated quartz tubes at 900 °C for 24 h. The mixture was then reground to improve homogeneity, cold-pressed, wrapped in Ta foil and annealed for a further 2 weeks at 900 °C. In the first step the heating rate was 10 °C/min and the cooling rate was 20 °C/min. In the second step, the samples were inserted directly into the furnace at 900 °C and air quenched from 900 °C".

Chalcopyrite powders ($Zn_{0.03}Cu_{0.97}FeS_2$) were provided by Prof. Mori (National Institute of Materials Science Tokyo) and prepared by solid-state reaction following the recipe described by Tsuji et al. [108, 116, 178] "samples were synthesized by the direct reaction of Cu (4N), Fe (3N), and Zn (4N) powders with S (6N)". Before the reaction, Cu and Fe powders were purified by heating under Ar/H_2 stream at 750 K for 36 h, while Zn (3N) powder was used with no further purification. Metal powders and sulphur were sealed in evacuated silica tubes and were heated at 973 K for 1 day, cooled and maintained at 650 K for 1 day. Then the tubes were cooled to room temperature for 1 day". The measurements were performed on a single sample, reproducibility is suggested by the high control of the process, the relatively closed sintering condition and the stability obtained for chalcopyrite sample but a complete study about this could not be performed.3.1.3 Spark Plasma Sintering and derivatives

Spark Plasma Sintering is a field assisted sintering technique (FAST) based on low voltage (<10 V) and pulsed direct current (DC), which can be used with uniaxial pressure, in vacuum or inert atmosphere. Furnace used is an FCT HPD 25; FCT Systeme GmbH, Rauenstein, Germany.
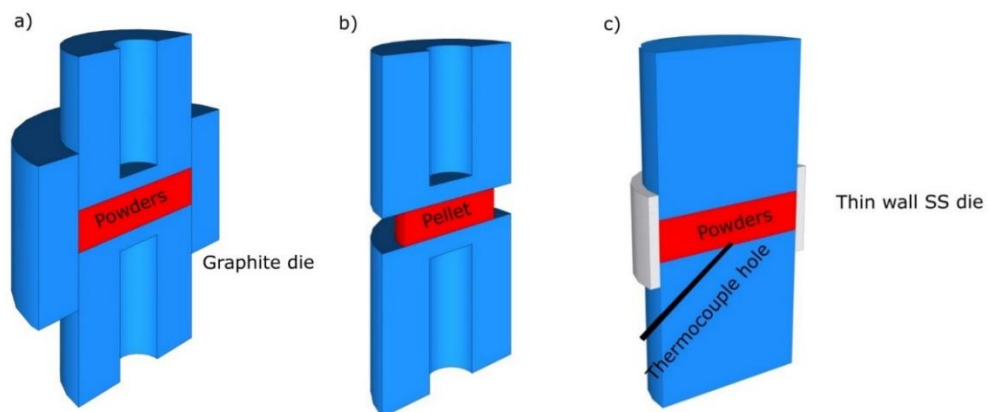
Figure 3.1 *Schematic of different setups: a) SPS, graphite punches and die; b) Flash-SPS graphite punches, dieless c) hybrid-FSPS, graphite punches and thin wall stainless steel die.*

In conventional SPS processing the powders were placed into a graphite die; graphite foil was used to cover the internal surface and the contact between the punch

and sample (it prevents sticking of the sample and helps to remove it). Uniaxial pressure was applied through the punches. Current was then passed through the system to heat it up through Joule heating. The samples obtained using this approach have been used as reference materials and labelled as SPS

Flash-SPS was done using a dieless approach. Samples of $Ni_{0.15}Co_{0.85}Sb_3$ were cold pressed to 70 % theoretical density as 20 mm discs, 4 mm thick, and then placed between 30 mm punches. In this configuration, the current passed through the sample, and heat was produced within it and in graphite. This setup is referred to as Flash-SPS as it has the dieless configuration and sintering with high heating rates (>7000 °C /min) were achieved.

The combination of high temperature and pressure acting on the powder compacts always produced large plastic flow that made it impossible to obtain dense samples, which could not be characterised. The main reason is the high gradient (100°C or more) induced by the setup itself, which is detrimental for material with high Seebeck coefficient, and weak mechanical properties, a more detailed discussion of temperature distribution will be given in Chapter 4.

Hybrid Flash-SPS was developed to solve the above problem. The powders were constrained with a stainless-steel die with an internal diameter of 20 mm or 15 mm and thickness of 2 mm. Such a small wall thickness reduced the thermal mass of the system while still allowing a high heating rates and relatively fast cooling. Stainless steel is suitable for relatively low temperature as its softening point is about 750 °C and therefore can be used for most thermoelectric materials. The high sintering temperature of the half-Heusler powder required the checking of the size of the diameter after each sintering run in order to monitor any deformation and substitute the die if needed, no deformation was observed as the stainless-steel die is at a lower temperature compared to graphite as discussed in Chapter 3.

Table 3.1 *Summary of samples sintered and used in this thesis work.*

Sample	Processing	Sintering Temperature (°C)	Heating Rate (°C/min)	Pressure (MPa)	Pre-heating (°C)	High temperature dwelling (min)
$Ni_{0.15}Co_{0.85}Sb_3$	SPS	750	100	15	No	5
$Ni_{0.15}Co_{0.85}Sb_3$	SPS	750	100	50	No	5
$Ni_{0.15}Co_{0.85}Sb_3$	hFSPS	750	9000	15	300	0

$Ni_{0.15}Co_{0.85}Sb_3$	hFSPS	750	9000	15	300	5
$Ni_{0.15}Co_{0.85}Sb_3$	hFSPS	750	9000	50	300	0
$Ni_{0.15}Co_{0.85}Sb_3$	hFSPS	750	9000	50	300	5
$Cu_{0.05}$ TiNiSn	SPS	850	100	80	No	0
$Cu_{0.05}$ TiNiSn	hFSPS	980	6000	80	400	0
$Cu_{0.05}$ TiNiSn	hFSPS	1040	6500	80	400	0
$Zn_{0.03}Cu_{0.97}FeS_2$	SPS	500	50	40	No	5
$Zn_{0.03}Cu_{0.97}FeS_2$	hFSPS	600	8700	40	No	0
$Zn_{0.03}Cu_{0.97}FeS_2$	hFSPS (twice)	600	8700	40	No	0
HMS	SPS	1050	100	60	No	5
Mg-Silicide	SPS	750	100	50	No	5

The SPS record several parameters, which can be analysed. To describe the process the data used will be temperature, power dissipated, force and piston travel.

Piston travel represents how much the upper piston is moving, the movement is related to the shrinkage of the material, but other variable influence its value (such as elastic compression and thermal expansion), it is useful for comparison but not as absolute value.

3.1.4 Coating and oxidation test

Coating tests were performed on samples of HMS and Mg-Silicide samples cut into bars of 10 mm height and 2 mm square base. The coating material were two resins produced by Aremco: Corr-Paint CP4040 (water based) and CP4040-S1 (solvent based).

The bars were hand-painted with resin, which was afterwards cured in a tubular furnace (Carbolite Gero STF/180, Germany) under Argon atmosphere. Curing was performed in a muffle oven under free air flow (Manfredi OVMAT 2009, Italy), following the procedure recommended by the producer; heating rate 1.7 °C/min and dwell time of 40 min at 250 °C. The coating was completed in two steps as the first was required to cover 5 faces and the second to cover the last one. A second procedure was followed subsequently to improve the coating quality. Resins were applied using a foam brush and the curing was performed in two stages, a first heating up to 90 °C and holding time of 30 min, then heated up to 230 °C and hold for 45 min. Oxidation test were performed in a box furnace under air atmosphere. Samples were slowly heated up to 500 °C and 550 °C and held for 120 h. Each test was done on three identical samples per type (coated CP4040, coated CP4040-S1 and uncoated).

3.2 Characterization

3.2.1 Density measurement

Density was measured using the Archimedean method. The sample had mostly closed porosity therefore it was possible to evaluate the density as:

$$\rho_S = \frac{m_1 \rho_L}{m_1 - m_2} \qquad 3.1$$

Where ρ_S is the density of the sample, ρ_L is the density of a liquid, m_1 is the dry weight and m_2 is the weight measured when the sample is immersed in the liquid. Water is commonly used as liquid, but if a material is reactive, then ethanol or other organic liquids can be used. As common practice, to obtain a more precise value, the measurement was repeated three times and averaged.

3.2.2 X-Ray Diffraction

X-ray diffraction is a powerful technique based on Bragg`s law (Fig 3.2). Combined with calculation it can be used to provide information such as: crystal structure, composition, phase composition or lattice distortion.

It uses an x-ray source with a wavelength in the range of the atomic spacing. The scattered beam constructively interferes only if the extra path they travel into the sample before they are scattered by an atom is an integer multiple of its wavelength. This condition, known as Bragg`s law can be expressed as:

$$2d \sin \theta = n\lambda \qquad 3.2$$
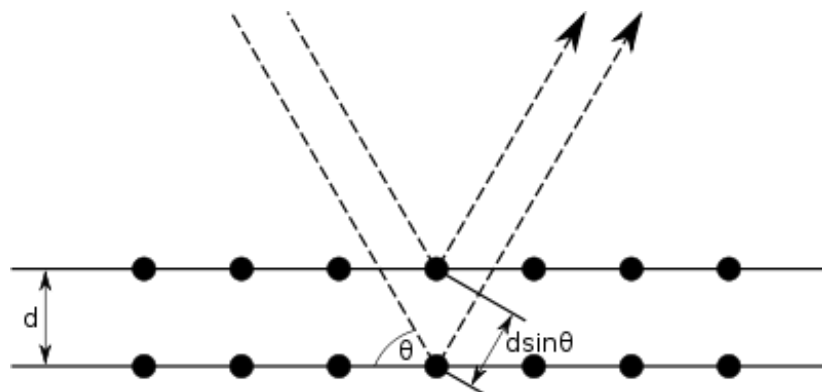
Figure 3.2 Schematic Brag's Law

where d is the atomic spacing, θ is the angle between the x-ray and the atomic plane, λ is the wavelength and n is any integer number. The intensity of the scattered signal is then detected for different ranges of θ producing the sample XRD pattern that can be compared with database or used for calculations that are more complex.

In this work, the XRD data used for phase identification were collected on an X-ray diffractometer (Siemens D5000), using Cu Kα over a 2θ range of 10° to 80°. Phase identification was done comparing the obtained data with standard XRD database.

Rietvald refinement was performed on GSAS (General Structure Analysis System).

3.2.3 Scanning electron microscopy

Scanning electron microscopy uses a focused electron beam, which interacts with atoms at various depths producing several types of interaction that can be detected and used to produce an image showing different information.

The typical microstructures of the samples were analysed by examining their fracture surfaces, using secondary electron detector on a SEM, FEI Inspect TM-F. Polished cross sections (final polishing 1 µm of diamond suspension) were also used for microstructure and elemental mapping using Energy Dispersive X-Ray Spectroscopy (EDS). Coated samples were resin mounted, cut and polished to observe the resin adhesion and the effect of oxidation testing.

To remove some atomic layer of skutterudite sample and observe the undamaged surface of the material, a Focused Ion Beam (FIB) of Ga atoms was used on a FIB/SEM (FEI Quanta 3D FEG)

3.2.4 Electrical characterization

Electrical resistivity and Seebeck coefficient were measured simultaneously on a LSR-3 (Linseis Thermal analysis), from room temperature to the peak temperature of interest for the analysed material. Some data was collected also on the cooling stage to evaluate the stability of the material, as a significant variation would possibly indicate some type of transformation or degradation.

The sample was placed between two platinum electrodes and two thermocouples were placed in contact with the sample (Fig 3.3). For the sintering studies disc shaped

sample of 15 or 20 mm diameter was used, while for oxidation test the bar shaped samples were used. Any coating and oxide layer were removed by polishing in order to achieve good electrical contact.
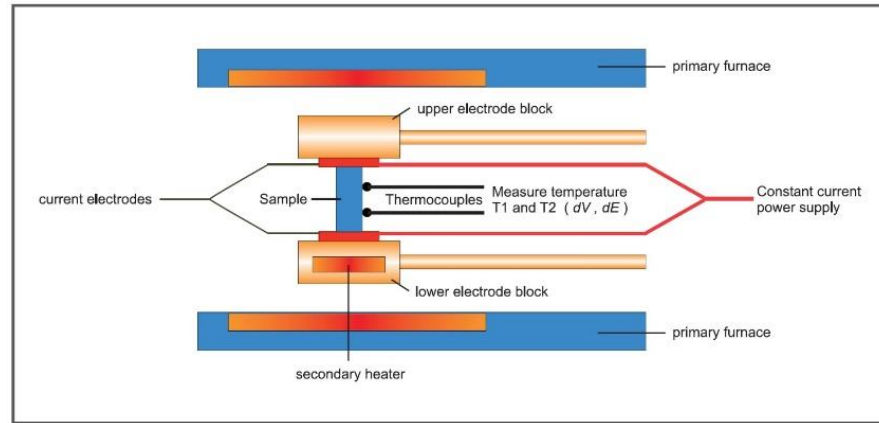
Figure 3.3 *Scheme of Linseis LSR3 [179].*

The Seebeck coefficient was obtained as the ratio between the temperature difference measured by the probes and the measured potential difference V, induced at the same wires (2.1).

Electrical resistance was measured using the DC four terminal method, in which a constant current I is applied to both ends of the sample to measure and determine the voltage drop dV between the same wires of the thermocouple after subtracting the thermo-electromotive force between leads (Fig 3.4). The voltage and current are then used to calculate the resistance through Ohm`s law (3.3) which is then converted into resistivity by knowing the sample dimension and probe distance (3.4):

$$V = RI \ or \ R = \frac{V}{I} \qquad\qquad 3.3$$

$$\rho = \frac{S}{L} R \qquad\qquad 3.4$$

where *V* and *I* are the voltage and current measured, *R* is the resistance, S is the cross-sectional contact area of the sample, L is the probe distance and ρ is the resistivity.
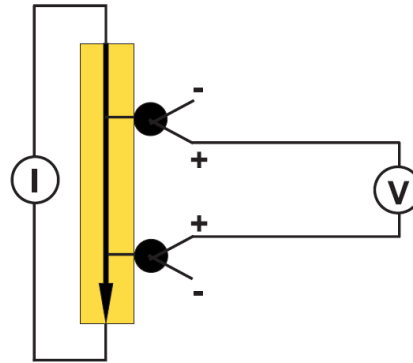
Figure 3.4 *A simple description of 4 terminal method, probes are the thermocouple measuring also T1 and T2 [179]*

3.2.5 Thermal diffusivity

Thermal diffusivity of the samples was measured using a Micro'Flash Apparatus LFA-457 (NETZSCH). Disc shaped samples having diameter of 15 or 20 mm and uniform thickness below 4 mm were used. The sample was held into a furnace in Argon atmosphere and the measurement was done when the set temperature was stable. The sample was homogeneously heated on the lower face with an unfocused laser pulse (Fig 3.5), on the other side the temperature variation as a function of time was measured by an IR detector (InSb cooled by liquid N_2). Both surfaces were coated with Graphite 33 spray (Kontakt-Chemie) to ensure high laser absorption.
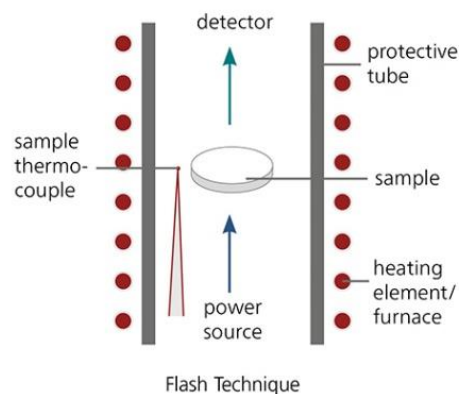
Figure 3.5 *Simple model of the measuring principle [180].*

The basic model to calculate the diffusivity under adiabatic condition is:

$$D = 0.1388 \frac{d^2}{t_{1/2}} \qquad\qquad 3.5$$

where D is the thermal diffusivity in cm^2/s, d is the thickness of the sample in cm and $t_{1/2}$ is the time in s at which the temperature increases at the rear of the sample reach 50% of the maximum value (Fig 3.6).
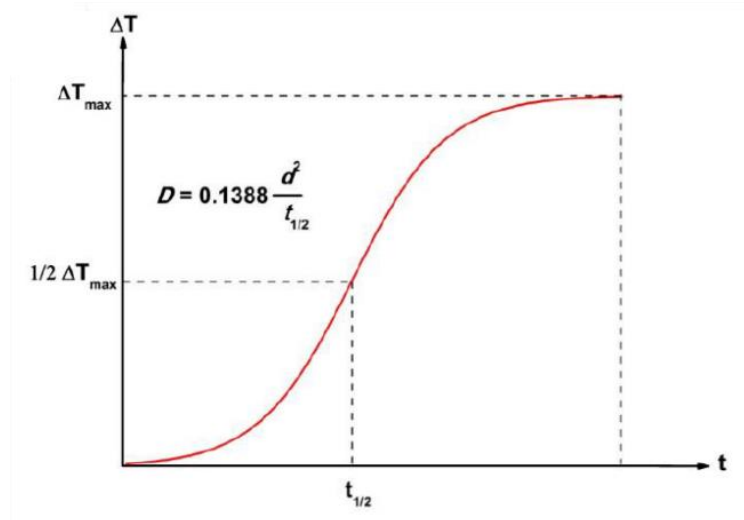
Figure 3.6 *Typical plot of ΔT vs t (modified from [180])*

Thermal conductivity k was then calculated using the equation

$$k = \rho C_p D \qquad\qquad 3.6$$

where ρ is the density of the sample, C_p is the specific heat of the material and D is the measured thermal diffusivity. Density was measured using the previously described method; specific heat was calculated using Petit-Dulong law. This relationship is based on the observation that the molar specific heat of many element was almost a constant at room temperature, later described as:

$$C_p = 3R \qquad\qquad 3.7$$

where C_p is the molar heat capacity at constant pressure (J/mol*K) and R is the gas Boltzmann constant (J/mol*K). Such relationship was found to be a reasonable approximation for several material at mid-temperature range and it is commonly used for the material of interest, $CoSb_3$ (8% error at 850 K, 0% at room temperature) [181], $CuFeS_2$ (error unknown, authors did not provide it) [182], TiNiSn (<8% error from room temperature to 500 K, <1% error between 500 K and 773 K) [183]. 3.2.6 Measurement error

All measurements are subject to some degree of error, knowing the sources is helpful to prevent wrong estimation of the final properties. The electrical resistivity value has an accuracy of 7% while on Seebeck coefficient is 8%, which could affect the power factor as much as 25%. The measurement of different samples with the same condition will provide almost the same relative error (reproducibility is 3%) while the absolute value might be over or under-estimated [184]. The thermal diffusivity error is less than 3% [185] and the calculated thermal conductivity is therefore highly accurate and mostly depends on the specific heat. The absolute value obtained for the figure of merit of all the samples may therefore be not accurate, even though it is difficult to say if over or under-estimated, while the relative relationship for each material is more reliable as all sample of each material were measured with high reproducibility, this confirm the increase of properties due to hFSPS processing.

Chapter 4 Modelling of FSPS and hybrid Flash-SPS

4.1 Introduction

For the reasons discussed in chapter 2, Flash-SPS is a promising processing technique for thermoelectric materials [23, 173, 174, 177]. However, FSPS has not been extensively applied to this class of materials and there are some known and likely unknown complications when processing thermoelectrics. Most worrying is the potential for large temperature gradients to form due to the Peltier effect under DC current (pulsed or continuous), which could lead to uneven densification [186]. However, initial attempts to FSPS typical thermoelectric materials (Skutterudite, Bismuth telluride) failed because of a more basic problem; thermoelectric materials typically have poor thermomechanical properties and the consequently excessive plastic flow of the material under FSPS lead to unusable samples. With these two issues highlighted, it was clear that the FSPS process would have to be significantly modified to successfully sinter thermoelectrics. Instead of trying to optimize the FSPS process through trial and error, modelling software (COMSOL) was used to model the process and observe the temperature gradients, as wells as other important properties, while adjusting various parameters and the system configuration.

To model, including the Peltier effect, the right level of complexity is needed (avoid too much computation time, and avoid poor representation of reality). The conventional-SPS process has been already modelled mostly for two reason: verify the effect of processing parameters and produce prediction or to use the results to explain an experimental observation. The commercially available software has embed packages to simulate the main phenomena occurring, such as heat transfer and radiation, current dissipation and thermoelectric effect. It is possible also to model mechanical behaviour, such as creep, but the production of a fully coupled electro-thermo-mechanical model would require considerable effort. Thermal-electrical models have been used to confirm the presence of thermal gradients [187]. It has been

used to prove the influence of contact resistance, both thermal and electrical [188-190] and more recently to prove the effect of Peltier cooling on thermoelectric materials [186]. Usually these works have been performed on bulk or highly densified pellets in order to reduce the effects due to shrinkage and the intrinsic variation of the sample properties during sintering. Nonetheless, the use of modelling can provide useful information for the design of experiments and the interpretation of results. While absolute accuracy, where the model matches reality, is very difficult to achieve, models are still useful to see the effect of changing certain parameters/configurations. We used a simple thermal-electrical model to compare the main characteristics of FSPS and hFSPS to explain the difference between them and the reasons for using hFSPS to process thermoelectrics.

4.2 Setup

To standardize this work one model was used as a base and modified as required for each new configuration. The base model (Fig 4.1) was cut off at the rams, as at the surface of them have a fixed temperature and applied voltage could be set. The geometry was composed of several domains, each part (including the sample) is modelled as a solid and coupled to its neighbouring parts using electric/thermal contact. This allowed each part and their interfaces to have different material properties. The model assumed fixed temperature on the cooling contact.
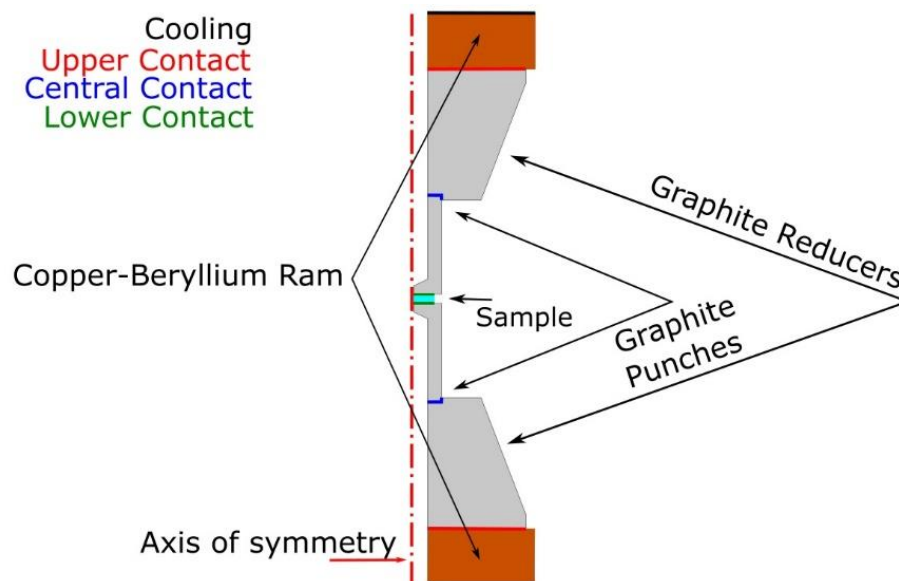
Figure 4.1 *Scheme of the basic setup, contacts are underlined*

The tooling was drawn as an axisymmetric system to reduce the computational cost, and a 3D image can be obtained by simply rotating the 2D results by 360 degree around its axis of symmetry. For different models only the sample setup was modified while reducers, rams and punches are always the same.

4.2.1 The Materials

The punches were made of durograph 20 from Erodex, the reducers were made of a different grade of graphite with a higher thermal conductivity (durograph 17 from Erodex), the sample material chosen was skutterudite as it was well characterised in earlier work [191] and the rams were made of Cu-Be (grade unknown but modelled as grade C).

4.2.2 The interfaces

The temperature at the surface of the cooling rams was fixed at 18 °C to simulate the cooling water. However, there was appreciable thermal resistance at the interface between the internal cooling channels and the water. The height of rams was chosen to approximate the real ones. The interface between the rams, the reducers and upper contact, experienced relatively low pressure (<10 MPa) due to their relatively large area, due to their proximity to the cooling rams it stayed relatively cool. All these contacts have been extensively studied, and the equation used to describe them is shown in 4.8-4.9. Current was considered to be flowing from the lower cooling contact

while the ground was set as the upper cooling contact. The SPS was modelled as a constant voltage power supply, as will be described in the next sections.

4.3 Constitutive relationships

The software package used in this work (COMSOL) had all the required equations for electrical heating and heat transfer built in. However, for reference the equations used for these calculations are shown below.

The time dependant heat transfer is described by the equation:

$$\rho C_p \frac{\partial T}{\partial t} = \nabla * (k\nabla T) + Q \qquad 4.1$$

where ρ is the density of the material, C_p is the specific heat, T is the temperature, k is thermal conductivity and Q is a value describing internal heat generation.

The Joule heating module applied the following equation, considering the charge conservative law under quasi-static potential field

$$\nabla J = 0 \qquad 4.2$$

where J, current density, can be expressed as:

$$J = -\sigma(\nabla V + S\nabla T) \qquad 4.3$$

here σ is the electrical conductivity, V is the electrical potential, S is the Seebeck coefficient and T is the temperature.

The current flow induced two heat generation terms:

$$Q_j = JE \qquad 4.4$$

$$Q_p = -\Pi J \qquad 4.5$$

Where E is the electrical field, Q_j is the heat produce by pure joule heating and Q_p is the heat produced by Peltier effect and Π is the Peltier coefficient.

According to this, the full equation for energy conservation was:

$$\rho C_p \frac{\partial T}{\partial t} = \nabla * (k\nabla T - \Pi J) + JE \qquad 4.6$$

Some boundary condition had to be applied; one term of heat generation is the radiative loss due to black body radiation. This condition was applied on the lateral surfaces of the die and punches and is described by the Stefan-Boltzmann law:

$$Q = B\varepsilon(T_e{}^4 - T_{amb}{}^4) \qquad\qquad 4.7$$

Where T_e is the temperature of the emitting material, T_{amb} is ambient temperature, B is Stefan-Boltzamnn constant and ε is the emissivity of the material.

The thermal contacts were considered as a thin resistive layer with the following equation:

$$-\overrightarrow{n_d}(-k_d\nabla T_d) = -\frac{(T_u - T_d)}{R_s} \qquad\qquad 4.8$$

$$-\overrightarrow{n_u}(-k_u\nabla T_u) = -\frac{(T_d - T_u)}{R_s} \qquad\qquad 4.9$$

Where k_d is the thermal conductivity of the material considered, u and d indicate the source and destination contact surfaces respectively, $\vec{n}$ is the normal surface and R_s is the resistance of the layer expressed in K*m^2/W.

The electrical contact at the interfaces were considered to be impedances and described by the following equation:

$$\vec{n}J_1 = \frac{1}{\rho_s}(V1 - V2) \qquad\qquad 4.10$$

$$\vec{n}J_2 = \frac{1}{\rho_s}(V2 - V1) \qquad\qquad 4.11$$

where $\vec{n}$ is the normal vector, ρ_s is the surface resistance in ohm*m^2 and ΔV is the voltage drop across the interface. The value of ρ_s at each interface will be discussed more in detail.

4.4 Properties of materials Introduction

The temperature dependence of all material properties is important for the solution of the constitutive equation and needs to be available at all of the temperatures calculated by the model. This was why, whenever practical, all the materials used in

the model were characterized using a Linseis LSR-3 and laser flash (Netzch LFA 453) to obtain electrical resistivity, thermal conductivity and Seebeck coefficient vs temperature plots. This equipment allowed characterization up to 1000 °C, but this was not always possible in practice, for example the skutterudite could be measured up to 550 °C. As a last resort, the high temperature properties for a material could be extrapolated from existing data. However, the temperature dependence of most material properties is typically non-linear and therefore an extrapolation quickly becomes inaccurate as the temperature increases. The modelling software was set up to interpolate the data measured from the LSR and laser flash, instead of trying to fit to a calculated equation. The value of emissivity is not influencing the results as the temperature involved in this model are relatively low. The value of all properties was not obtained under pressure as this is was not possible in the measuring equipment used.

4.4.1 Punch Graphite

The graphite of punches is made of Durograph 20 (Erodex) and has the following properties. The data provided by the company are only at room temperature, so a temperature dependent measurement was required. The properties of graphite may slightly vary from batch to batch since they are obtained from large blocks and may not be perfectly homogeneous. The value of Seebeck coefficient is negative as other graphite in literature [192]. The value is influenced by the grade and isotropy as it happen for resistivity [193]. This makes important to measure its properties as the variability is extremely high.

Table 4.1 *Properties of graphite*

Electrical conductivity	See Fig 4.2
Heat capacity at constant pressure	See Fig 4.3
Surface emissivity	0.8
Density	1950 kg/m^3
Thermal conductivity	See Fig 4.4
Seebeck coefficient	See Fig 4.5
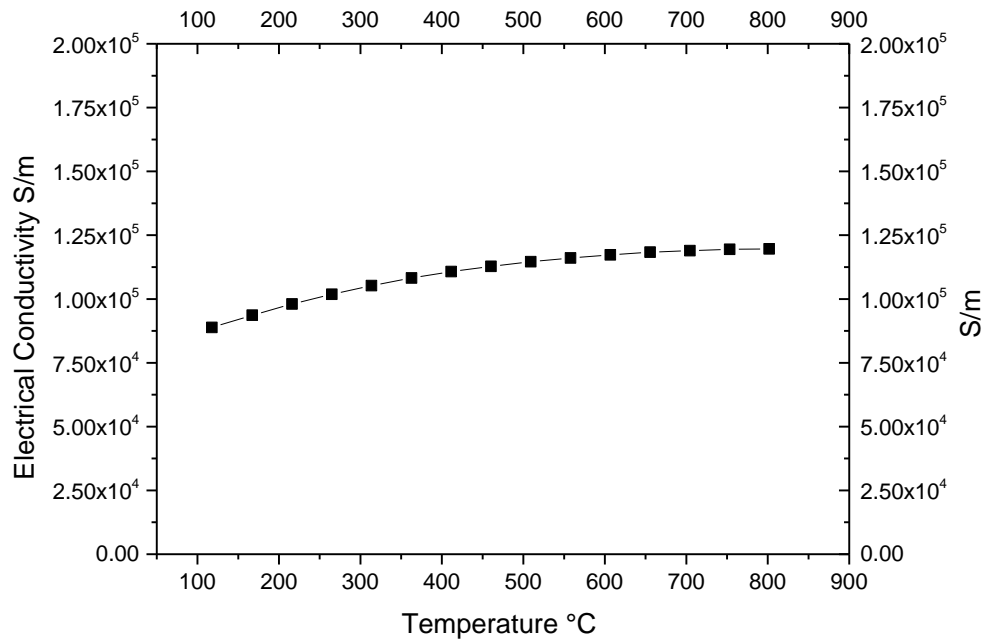
Figure 4.2 Conductivity of Graphite
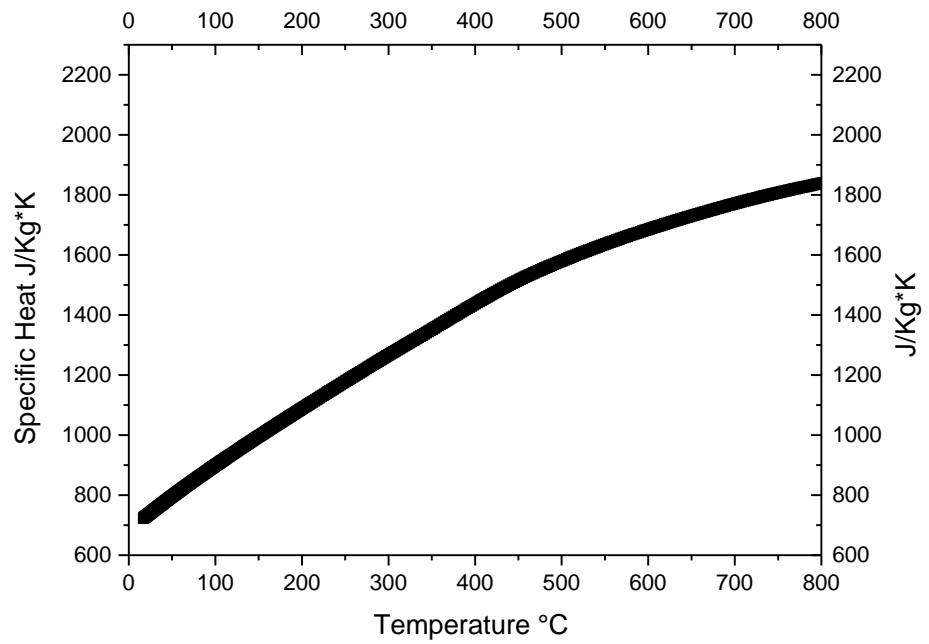
Figure 4.3 Heat capacity of graphite, data extracted from [194]
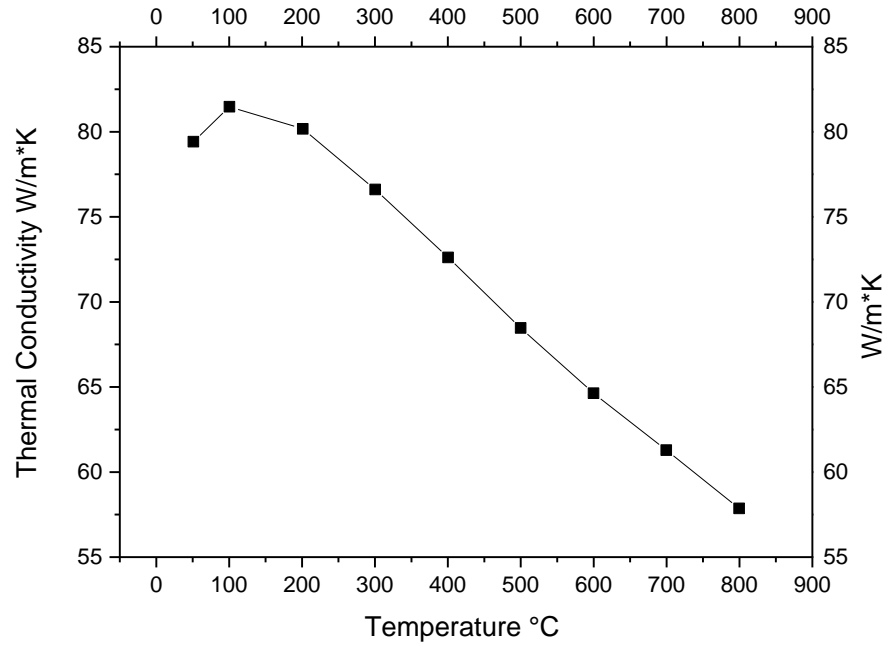
Figure 4.4 *Thermal conductivity of graphite (punch grade)*
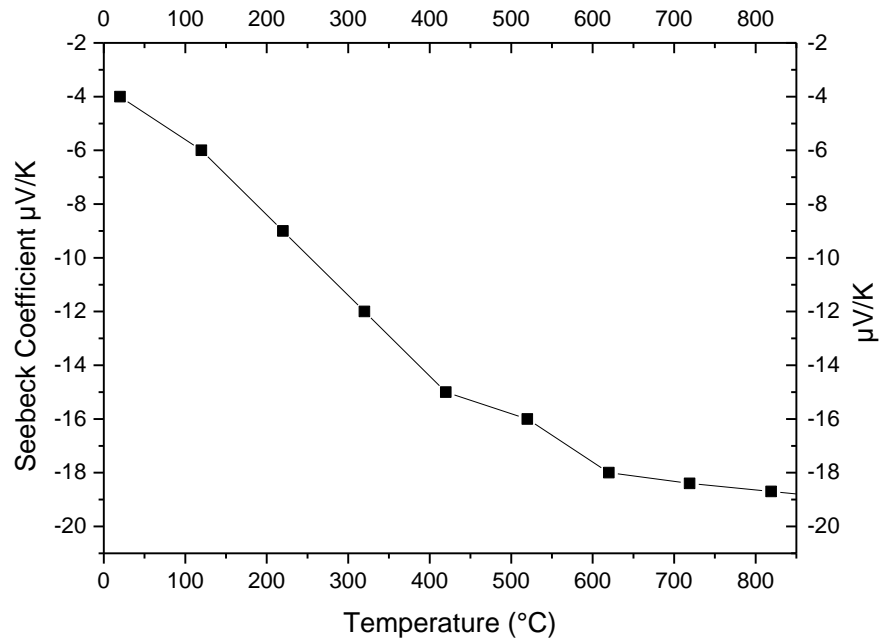
Figure 4.5 *Seebeck coefficient of graphite*

4.4.2 Reducer Graphite

The thermal conductivity of the graphite used for the reducer (Durograph 17) was slightly different from the graphite used for the punches (Durograph 20) (Fig 3.6), while other properties were considered the same as for the punches. The reducers are subjected to a lower pressure compared to punches therefore a lower grade can be used, the higher conductivity is also useful to increase the cooling rate
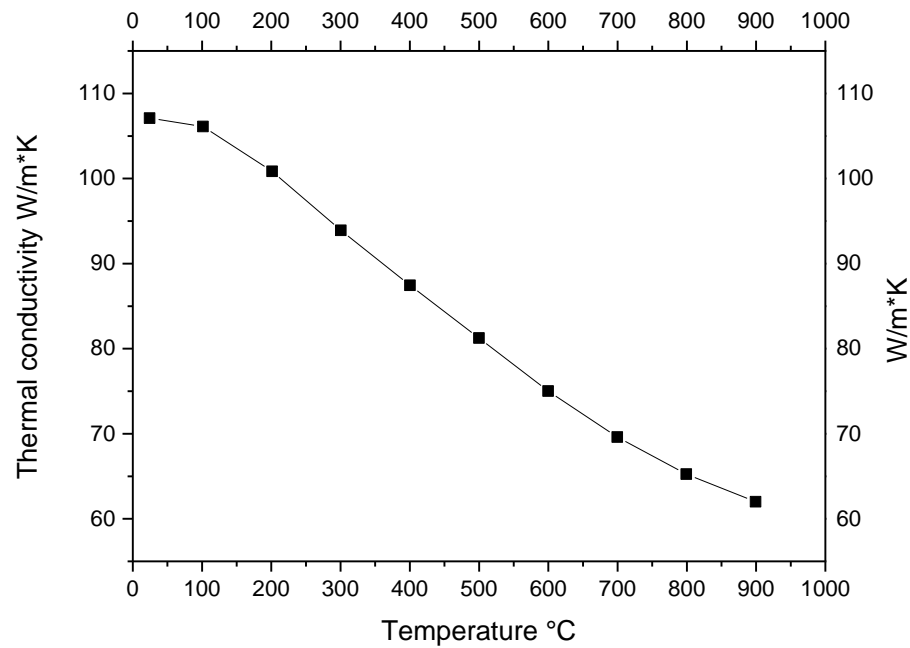
Figure 4.6 Thermal conductivity of graphite (reducer grade)

4.4.3 Beryllium-Copper

Table 4.2 Properties of Beryllium-Copper. Values are for room temperature.

Electrical conductivity	$1.16*10^6$ S/m
Heat capacity at constant pressure	420 J/Kg*K
Surface emissivity	0.8
Density	8250 kg/m^3
Thermal conductivity	118 W/m*K
Seebeck coefficient	Negligible

As the material for the rams could not be measured, the properties were taken from the materials library built-in to COMSOL. High temperature data was not needed as the rams were water-cooled.4.4.3 Stainless Steel AISI 304

Table 4.3 *Properties of Stainless Steel at room temperature*

Electrical conductivity	See Fig 4.7
Heat capacity at constant pressure	500 J/Kg*K
Surface emissivity	0.8
Density	7880 kg/m^3
Thermal conductivity	See Fig 4.8
Seebeck coefficient	Negligible

Stainless-steel grade 304 has been used and data for temperature dependence properties has been taken from online dataset [195].
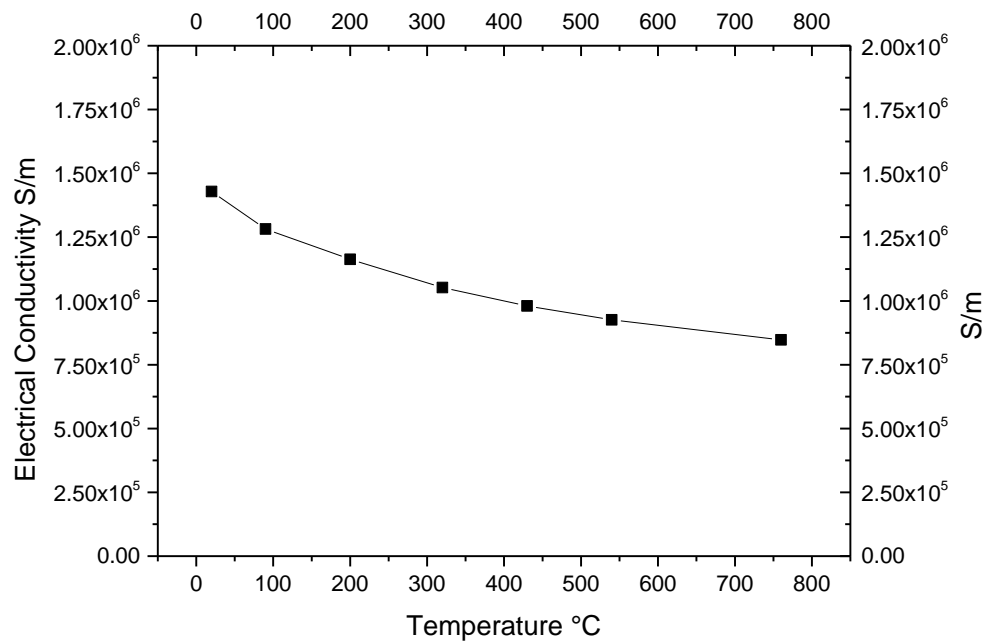
Figure 4.7 *Conductivity of Stainless Steel AISI 304*
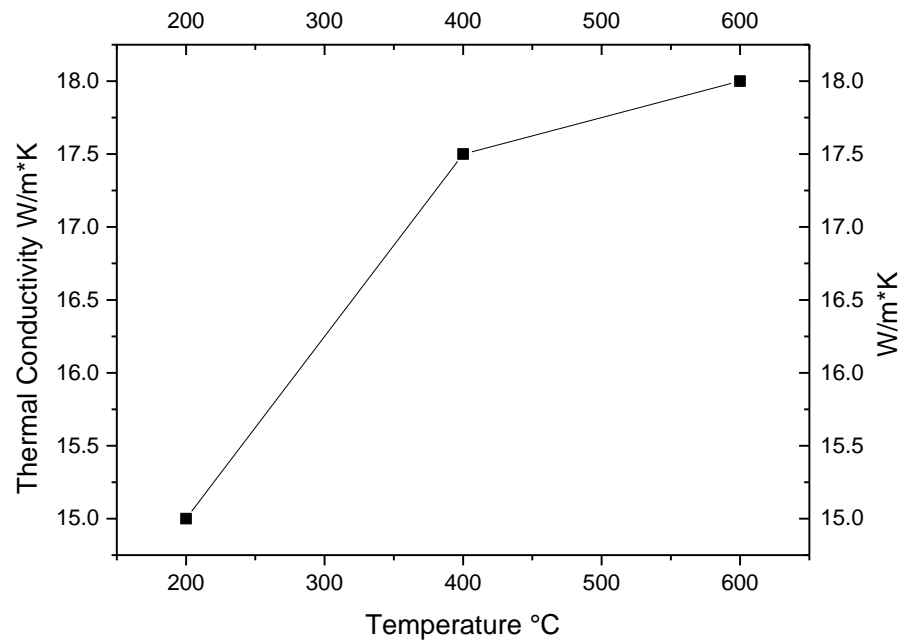
Figure 4.8 *Thermal conductivity of Stainless Steel AISI 304*

4.4.4 Ni$_{0.15}$Co$_{0.85}$Sb$_3$ Skutterudite

For this model a sample of Skutterudite was used to be representative of a typical thermoelectric material. Its properties could only be measured up to 550 °C, as it was unstable if heated any further. While this meant that the model lacked data above 550 °C, this was not a problem as the processing condition were chosen so as not to exceed this value. This was also representative of reality, where overheating samples should be avoided.

Table 4.4 *Properties of Skutterudite*

Electrical conductivity	See Fig 4.9
Heat capacity at constant pressure	261 J/kg*K
Surface emissivity	0.8
Density	7335 kg/m^3
Thermal conductivity	See Fig 4.10
Seebeck coefficient	See Fig 4.11
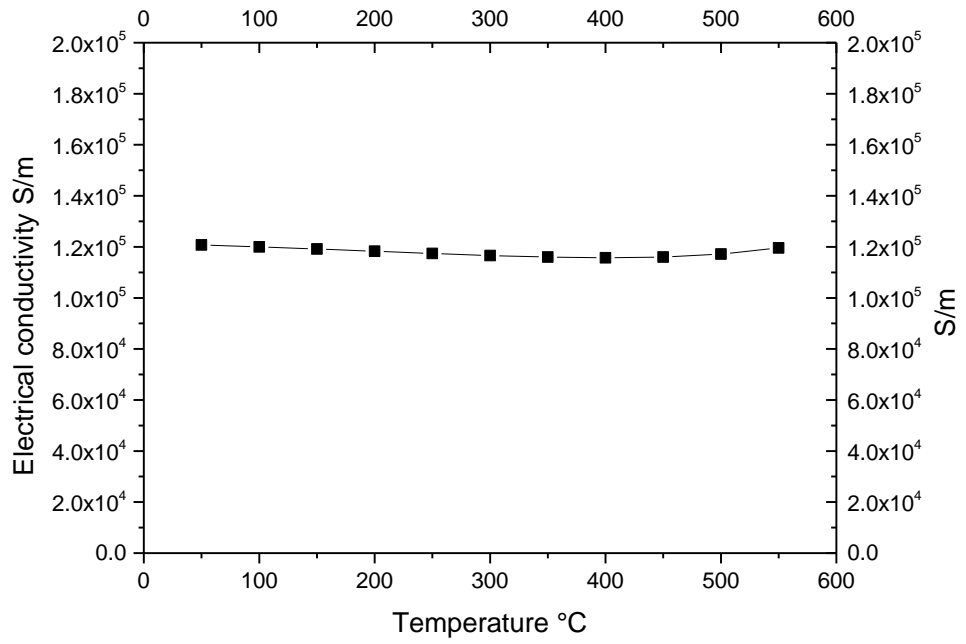
Figure 4.9 *Conductivity of skutterudite*
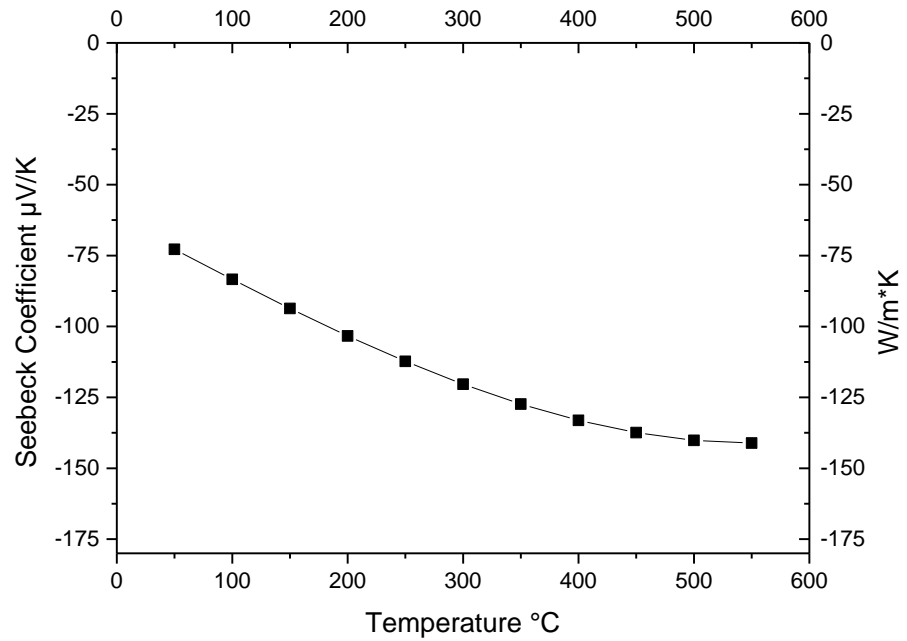
Figure 4.10 *Seebeck coefficient of skutterudite*
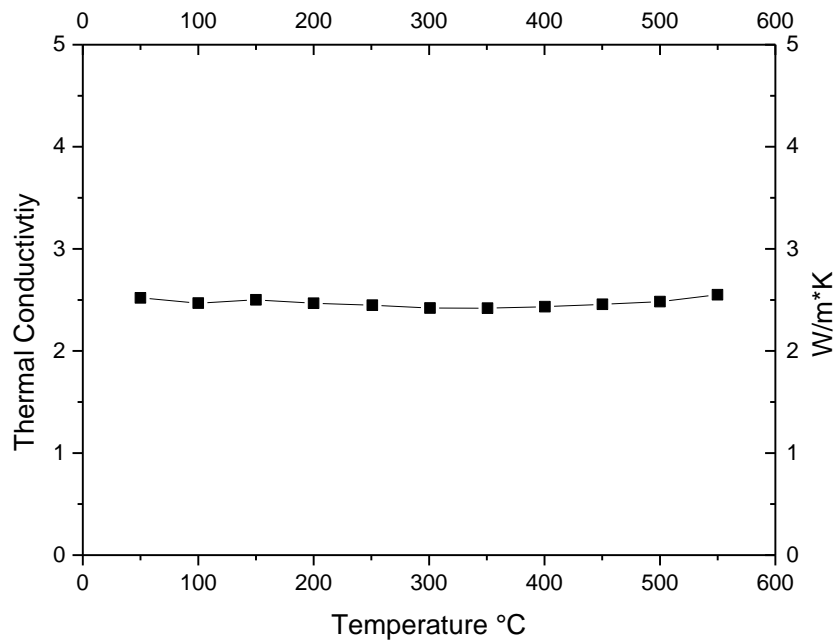
Figure 4.11 Thermal conductivity of skutterudite

4.4.5 Graphite foil

Graphite foil is a common material used for sealing and gaskets. In SPS it is commonly used to provide electrical contact between the SPS punches and die. It also serves to prevent the sample from sticking to them. The foil used was Sigraflex grade E and the properties were taken from producer's datasheet [196].

Table 4.1 Properties of Sigraflex

Electrical conductivity	$12*10^5$ S/m in plane 1600 S/m through plane (25 °C)
Heat capacity at constant pressure	1000 J/kg*K
Surface emissivity	0.8
Density	1000 kg/m^3
Thermal conductivity	200 W/m*K in plane, 5 W/m*K through plane (25 °C)
Seebeck coefficient	As Graphite

While this data sheet did not include any temperature or pressure dependence these relationships could be obtained from other sources. The datasheet of Grafoil (GrafTech) [197], which is very similar to sigraflex E, states the properties, in

particular the through plane thermal and electrical resistivity, are dependent on the applied pressure/density [197].

Despite how thin the foil was, its properties could have a large effect on the overall system, this is mostly due to the high electrical resistivity of the foil at least over 10 times the resistivity of any of the other material in the model.

Therefore, to improve the model accuracy some experiments were performed to obtain a value for the resistivity of the sigraflex under typical SPS pressures. The details of this experiment will be discussed later. While the resistivity varied with time, temperature and pressure, under the limited set of conditions used in the model, most of this behaviour could be ignored. A fixed resistivity value of about 250 µohm*m under 50 MPa was a very reasonable approximation. The temperature dependence of thermal conductivity could not be easily measured under same conditions and have been taken as constant, as at lower temperature the value is not supposed to change significantly [198].

4.4.6 Constantan

Constantan (Good Fellows) was used to measure the current applied by SPS. For this purpose, only the electrical resistivity was needed. Its resistivity is $5.2*10^{-7}$ Ohm*m with a temperature coefficient of +/- 0.00002 K^{-1}

4.5 Contacts

Now that the material properties of all the parts in the model has been described, the contact between the parts must also be considered. Contact resistances can have a significant effect on temperature gradients; they cause discontinuity in temperature between parts, as well as increased Joule heating at interfaces. For this reason electrical and thermal contact at interfaces has been studied by several authors focusing in SPS modelling. Wei et al. [188] calculated the electrical resistance at a graphite-graphite interface under various pressures. Their conclusion was that electrical contact resistance played a small but noticeable part in determining temperature distributions, but thermal contact resistance could be safely ignored in most cases.

The relationship proposed by Wei et al. [188] was used to model the interfaces

$$R(T,P) = (-0.24 lnT + 1.94) * (27.61 * P^{-1.09}) \hspace{2cm} 4.12$$

where T is temperature in Celsius and P is the pressure in MPa, here R is mohm*cm^2. Values were calculated at each interface according to the applied pressure, considering a force of 16 kN.

Thermal contact was considered as 0.00004 m^2*K/W. The thermal contact is mostly controlled by the presence of a graphite foil (Sigraflex), which is used to enhance the electrical contact between reducer and rams, properties provided by manufacturer were used to estimate the value. [196, 199]

4.6 Experimental measurements

Now that the required model geometry and material properties have been described, the model should heat up and reach similar temperatures to the real SPS equipment under the same applied power. However, there is some uncertainty with the applied power in the SPS and any errors can cause large deviations in the calculated temperature. The material properties of sigraflex also needs to be measured under representative conditions.

4.6.1. Measuring V and I

The value of V and I are vital for the simulation of an electrically heated process and should be as precise as possible. As shown in equation 4.3, current is responsible for the Joule heating and Peltier cooling which are the main heat sources of the system. A variation of 5% in current would become a 10% error on the power dissipation and such an error would then integrate over the total heating time. The SPS has a built-in sensor for current which is based on the Hall effect, unfortunately this sensor was designed to operate over a wide range of currents (up to 20 kA), and, as a result, at low currents its accuracy is limited. This could cause significant error in measuring current in typical SPS current ranges (0 to 3 kA). A set of experiments was performed to better understand the true behaviour of the SPS equipment, including alternative ways of measuring the current. Voltage was measured through an external datalogger (National Instruments USB-6221) at a frequency of 20 kHz, data were averaged using the RMS method. Temperature measurements (current calibration) were also

performed using K-type thermocouples using isolated wires (to remove common ground noise) and connected to an external USB multimeter (MTTR01 Mercury USB True-RMS Multimeter, 6000 Counts).

When controlling the SPS to produce rapid heating for FSPS the system was not controlled using temperature measurement and feedback, instead a power limit was set. However, from the manufacturer documentation it was not clear what this actually controlled, (power, voltage or current). To understand what this power limit setting was controlling, a simple experiment was designed.

In this experiment a typical FSPS setup with 20 mm punches (Fig 4.15-a) was used but with no sample or graphite foils (6.7 mOhm). The machine was programmed in power control to apply 10% power for 3s then the sample was allowed to cool for 5 mins, the same was repeated increasing the power in steps of 10% until the full power was applied (Fig 4.15 b). The application time was short to prevent the temperature to reach the thermocouple limit (900 ˚C) at high power level. The same was repeated with a 30 mm punch set, which had lower resistance due to its greater diameter (3 mOhm), and compared with the previous data to see what the controlled variable was.
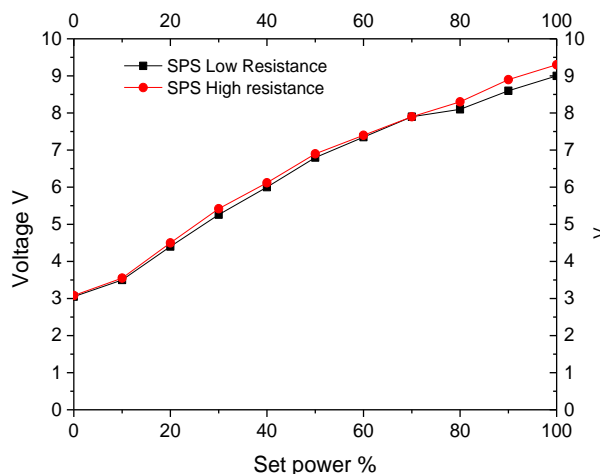
Figure 4.12 *SPS voltage value for low and high resistance*
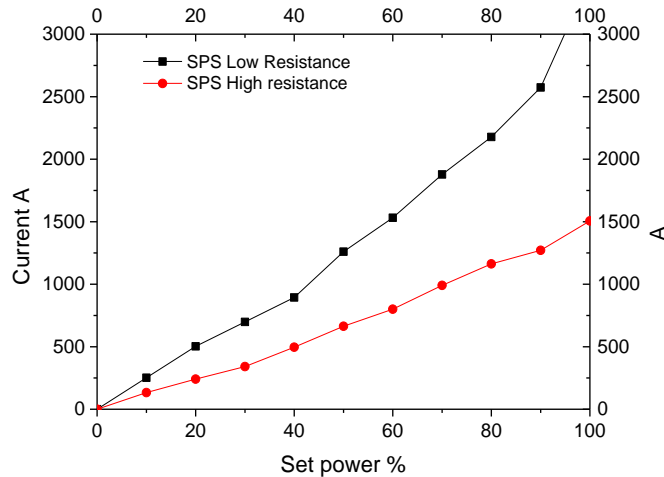
Figure 4.13 *SPS current value for low and high resistance*

From this experiment it was clear that the power limit was controlling voltage, as both high and low resistance configuration had very similar voltage curves (Fig 4.12), while the current has a different behaviour (Fig 4.13).

However, the voltage was not directly proportional to the set power and there were clues that the SPS data for voltage was suspect (Fig 4.12). At 10 % over 3 V was supposedly being applied, but increasing to 20 % the voltage only increased to under 4.5 V, while the current almost doubled.

This lead to the next experiment to verify the actual voltage applied. This setup was the same as the first, but probes were placed in the reducers to measure the voltage and only the 20 mm punches were used. This would not give the voltage at the hypothetical top surface of the rams, which was where the voltage was applied in the model, but it would be close. This was because the voltage drop due to the rams and lower half of the reducer could be considered negligible since they are good conductors. The rams were 80 mm diameter cylinders of copper beryllium and the reduces were truncated 60 mm cones of graphite, due to their relatively large cross-sectional area the voltage drop was minimal even at kA currents.
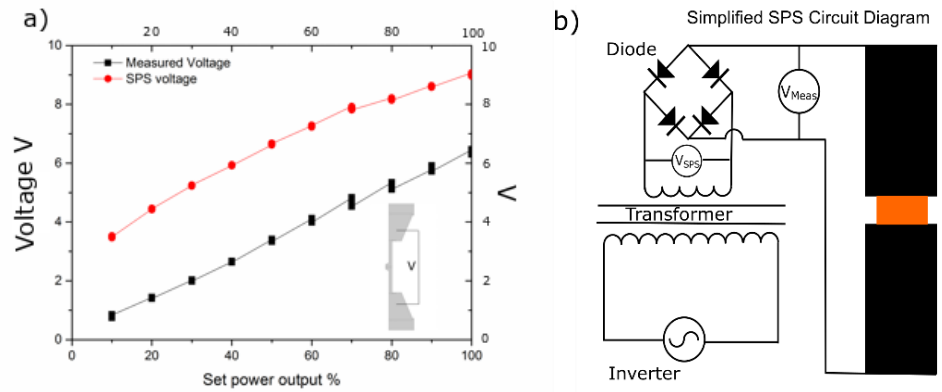
Figure 4.14 Measured voltage vs SPS voltage

The difference between the external measured values and the stated values from the SPS was quite large (Fig 4.14) and the difference could not be explained by the voltage drop due to tooling. The large relatively constant voltage drop could be caused by a rectifying diode after the SPS transformer, if the voltage was measured before the diode

In general, SPS devices provide a pulsed DC current [200], even when operating in non-pulsed (usually inserted as DC according to the manufacturer specifications) mode (Fig 4.15 c-d). The output voltage data provided is given every second, while the transformer provides an oscillating voltage at kHz frequency (Fig 4.15 d). The SPS output is the average of the applied voltage, which has a non-square shape. This behaviour is the results of the current manipulation by the electrical component in series (Fig 4.14-b). The current is initially converted into a tri-phase AC current by the inverter and then to a single-phase AC by the transformer. The inverter does produce a 1 kHz square pulse with dead time, while the transformer cannot produce a perfect square pulse or a clean DC waveform. At high current, the transformer may saturate which will increase the difference between the initial and final voltage peak of the pulse. Finally, the diode converts the AC current into a DC current of the same shape effectively doubling the frequency. The example shown in Fig 4.15-d was sampled at a rate of 10 kHz but at higher rate the curve would come with higher definition.
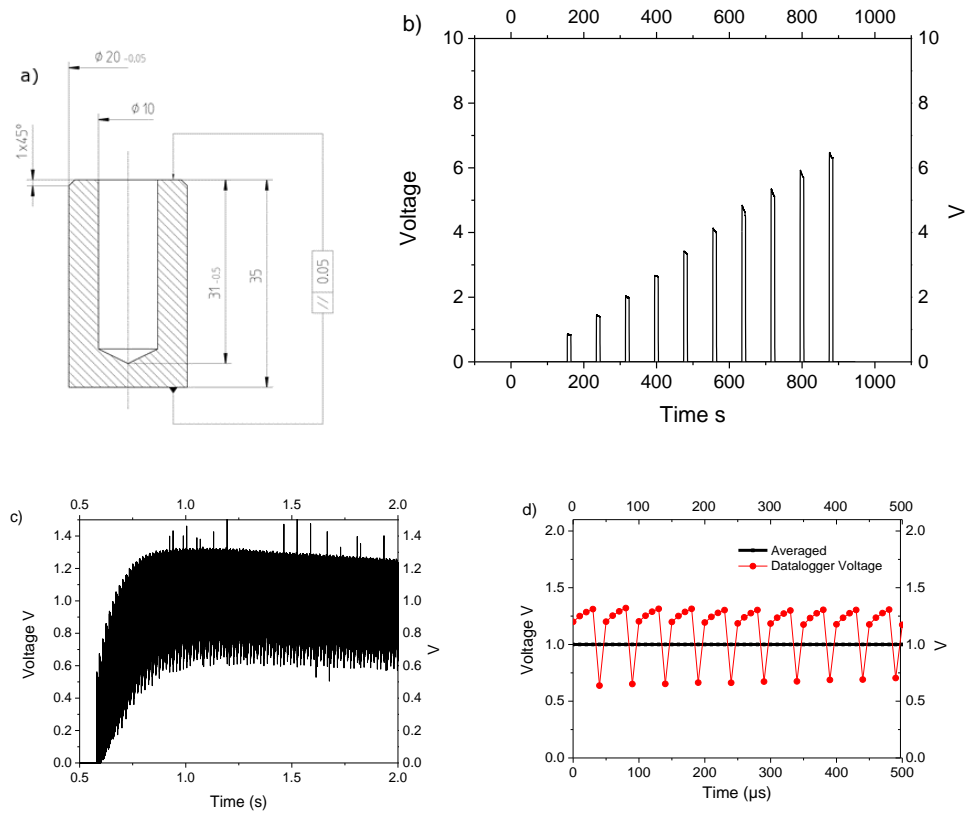
Figure 4.15 *a) Drawings of 20 mm diameter punch used in SPS experiments.*
b) Measured voltages (drop across the rams) plotted at different timescales, c) 3 s
DC pulse and d) refers to 50 % of power.

4.6.2 Current calibration

To measure more accurately the voltage and current passing through a sample we used an FSPS setup (Fig 4.16) without any graphite paper to reduce the number of heating sources. The sample was 20 mm thick with a diameter of 20 mm and we placed thermocouples 5 mm from the top and outer surface (Fig 4.16). The chosen material was constantan because of its stable electrical properties. The thermocouples were connected to a data-logger, which recorded the temperature and the voltage drop every ms, as already described.
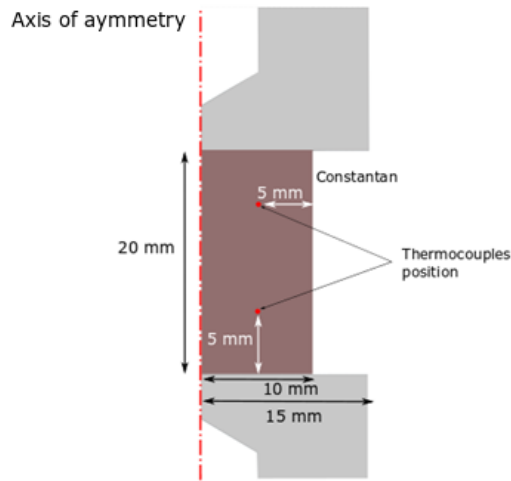
Figure 4.16 *COMSOL Drawing of the setup used for the experiment, thermocouples position is evidenced and symmetric.*

The machine was programmed to apply 10 % power for 3 s then the sample was allowed to cool for 5 min, then 20 % power was applied for 3 s, and so on until 100% power. The pulse time was short in order to ensure the temperature did not rise above the thermocouple limit (900 ˚C). Once the voltage was measured, the current could be calculated simply through Ohm`s law (3.3).
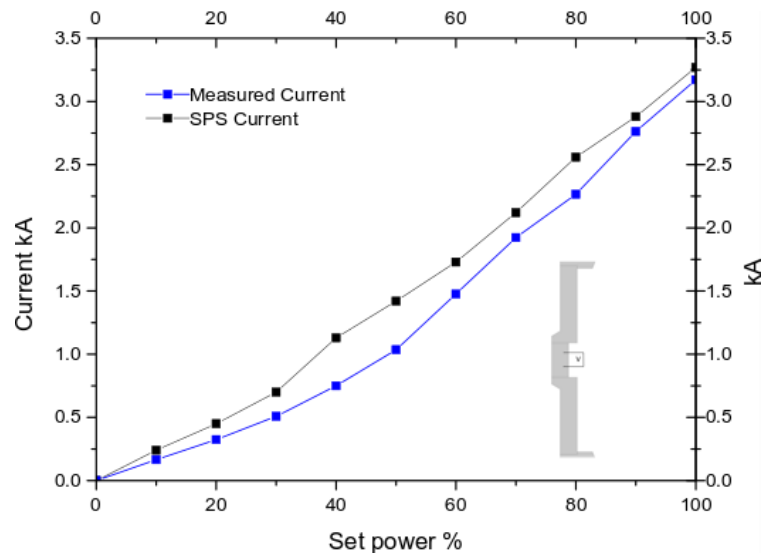
Figure 4.17 *Current measured within constantan sample and output data from SPS, inset is to remind the voltage probe placement within the constantan*

The difference between the measured value and the value given by the SPS sensor (Fig 4.17) was between 0.1 and 0.4 kA. More significantly, the percent variation (the potential error) was higher when the current was below 1.5 kA, as the current was increased the variation dropped to 5 % (Fig 4.18).
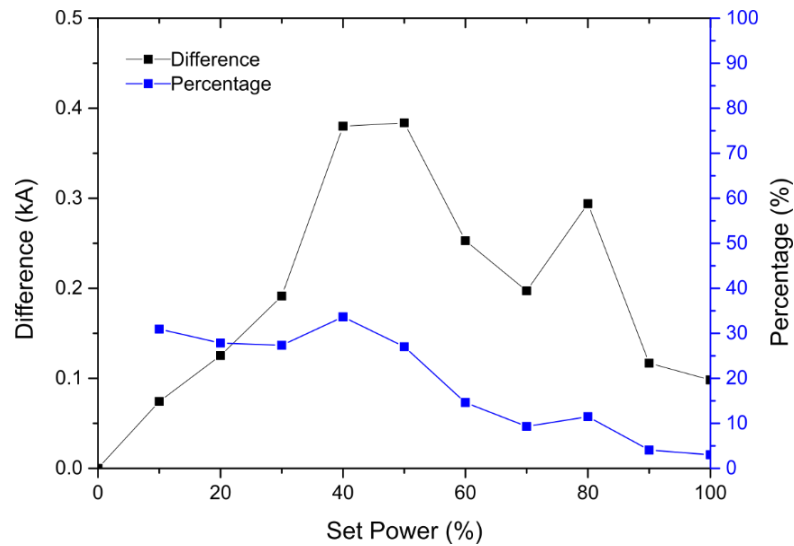
Figure 4.18 *Value of difference between SPS and measured value and relative percent variation*

Even this small variation in current value could produce an overestimation of the dissipated power by 10% since the relationship between I and P is quadratic. The error in power dissipation in the low current regime was higher.

4.6.3 Graphite foil calculation

Using a similar setup (Fig 4.19) the resistivity of the graphite foil was estimated.
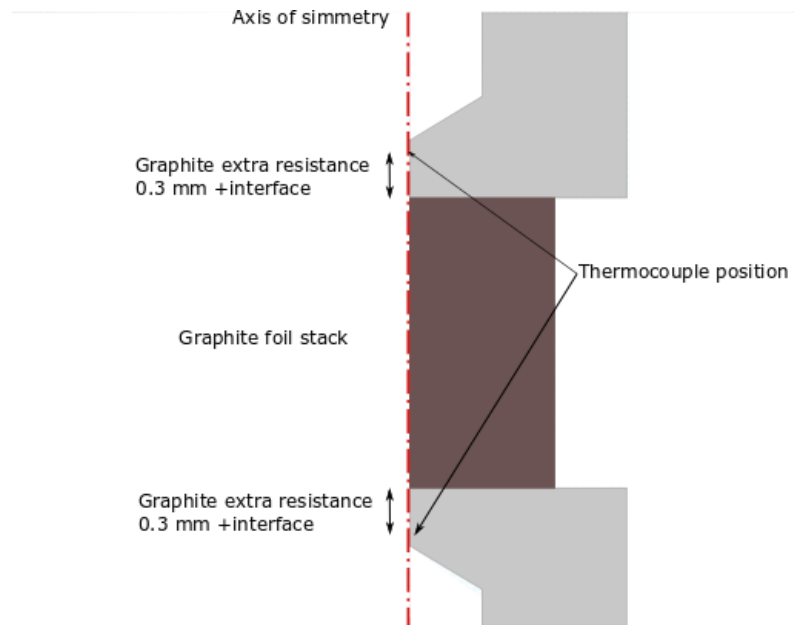
Figure 4.19 *COMSOL drawing of the setup used to calculate the graphite paper electrical resistance. Thermocouple position and distances are specified.*

A stack of 20 graphite foils was used as a sample and the voltage was measured across the punch at a fixed distance. However, the measurements would also take into account any graphite between the two probes, as they were in series with the graphite paper stack. To remove this error, a test was first performed without any stack (Table 4.6) and the resistance calculated through Ohm`s law *R=V/I (3.4)*. Each time the power was applied for 2 s and the system was allowed to cool down before next pulse.

Table 4.6 *Data obtained for graphite stack*

Power applied	Current A	Voltage V	Resistance Ohm
10	300	0.97	0.00323
20	540	1.54	0.00285
30	830	2.18	0.00263
40	1120	2.78	0.00248
50	1380	3.36	0.00243
60	1700	3.99	0.00235
70	1980	4.56	0.0023
80	2310	5.15	0.00223

| 90 | 2600 | 5.76 | 0.00222 |
| 100 | 3100 | 6.3 | 0.00203 |

To calculate the conductivity of graphite foil a few calculation steps were required (Tab 4.7).

1. First the resistance of the full system was calculated through Ohm`s law.
2. The stack resistance was obtained as the difference between the actual system and the previous measurement.
3. Normalized resistivity is the specific value of a single foil, it was obtained using the definition of specific resistance (3.4) $\rho_r=(R/20)*S/L$ where *R/20* is the resistance of a single foil, *S* is the surface area of the foil ($3.14*10^{-4}$ m^2) and *L* is the thickness of a single foil ($2*10^{-4}$ m). For this calculation, the thickness of the graphite foil was presumed constant. However, the thickness was actually variable, as the material shrunk and sintered during the processing, but under pressure the thickness decreased less than 10 %.
4. Normalized conductivity is the inverse of normalized resistivity since $\rho_r=1/\sigma$.

Table 4.7 Table of calculated data

Power %	Current A	Voltage V	Resistance ohm	Stack resistance ohm	Normalized resistivity µohm *m	Normalized conductivity S/m
10	130	2.2	0.01692	0.01369	6.84487E-4	1460.94774
20	250	3.05	0.0122	0.00935	4.67407E-4	2139.46117
30	390	3.74	0.00959	0.00696	3.48162E-4	2872.22715
40	550	4.43	0.00805	0.00557	2.7862E-4	3589.11612
50	710	5	0.00704	0.00461	2.30374E-4	4340.77618
60	990	5.4	0.00545	0.00311	1.55374E-4	6436.06952
70	870	6	0.0069	0.00459	2.29676E-4	4353.95814
80	1230	6.4	0.0052	0.00297	1.48691E-4	6725.36836
90	1200	6.95	0.00579	0.00358	1.78814E-4	5592.40007
100	1640	7.5	0.00457	0.00254	1.27046E-4	7871.18749

For the model, the behaviour of the graphite paper had to be simplified, because the model was predominantly used in high voltage conditions (over 60%), the nonlinear low temperature/voltage behaviour could be ignored. Accordingly for the model the sigraflex was modelled as a fixed conductivity of 4000 S/m (250 µohm*m). The test was only for the properties in one orientation, through plane, but from the

data sheet the properties are highly anisotropic. However, there was no reason to expect the in-plane properties to change. This was because the foil is composed of aligned graphite flakes, pressed together, resulting in lamella-like pores between the flakes. During sintering these pores will close, lowering the through plane conductivity, but this should not affect the in-plane conductivity.

4.7 Final consideration and purpose of modelling

As discussed in the previous section it is clear that modelling is a powerful tool, but one that requires great effort to achieve accuracy. A few parameters remained difficult to evaluate and reduced this model's utility as a predictive tool

- Temperature and pressure dependence of contacts and materials
- Properties of graphite foil over time, temperature and pressure
- Materials properties are available at temperatures lower than sintering
- Mechanical and chemical behaviour (reaction) would require another set of parameters, which are complex to estimate.
- Model does not cover densification and the change in sample properties vs density.

With these limitations in mind, the model has poor absolute accuracy, but can still be used to understand the differences between various FSPS setups. The model was particularly useful to investigate the effect of die configuration on temperature gradients, as these are otherwise hard to investigate, requiring either excessive instrumentation, e.g. 8+ thermocouples, or microstructure analysis, which does not provide second by second data.

The sample setup for all the other configurations were built using a 20 mm punch and sample (Fig 4.20) having 2 mm thickness. A voltage corresponding to 100 % set power (6.5 V) was applied for 2 s (starting from second 1) and then model calculate the evolution of temperature for other 18 s.

.
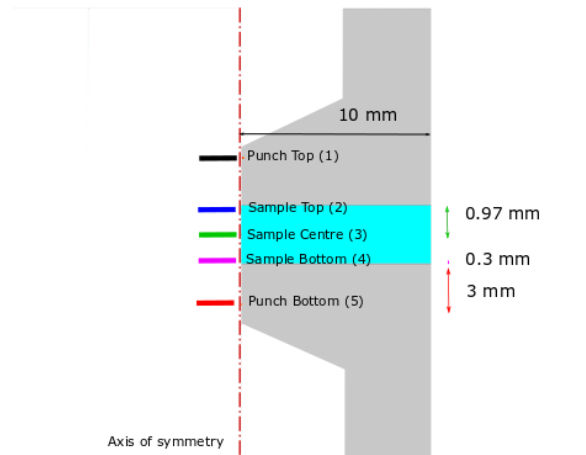
Figure 4.20 *COMSOL drawing of the sample setup used for the simulations. Virtual thermocouples were placed on the axis of symmetry and their relative position is described.*

Two virtual thermocouples (1-5) were placed on the axis of symmetry on the top and bottom punch at 3 mm from the sample and close to the end of the hole were pyrometer measure the temperature, so should give similar temperature to what the SPS pyrometer would produce. A further two virtual thermocouples (2-4) were placed at the top and bottom surface of the sample, 0.3 mm inside it, a last virtual thermocouple (3) was placed in the centre of the sample at 1 mm from the surface.
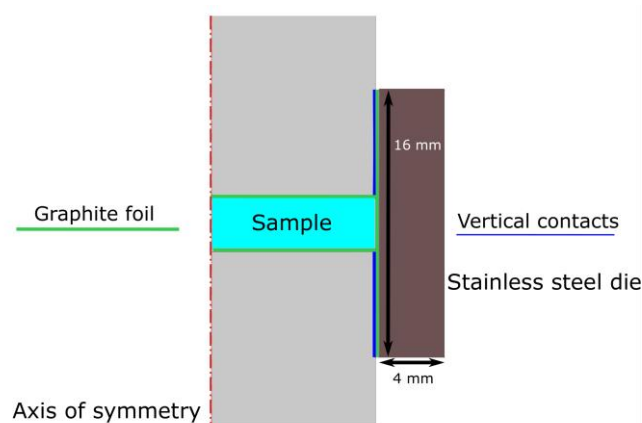
Figure 4.21 *COMSOL drawing of the modified sample setup with stainless steel die (4 mm thickness x 16 mm height). The graphite foil and vertical contact position used are evidenced.*

The setup used for hFSPS (Fig 4.21) used a die, which was 4 mm thick, and 16 mm tall, the position of the vertical contacts is highlighted in blue, while the graphite foil is evidenced in green. Thermocouples were placed in the same positions within the sample and on the graphite punches as described before (Fig 4.20)

The mesh chosen for the sample and graphite foil (when used) was extremely fine free triangular elements with a maximum element size of 0.204 cm, a maximum growth rate of 1.1, a curvature factor of 0.1 and resolution of narrow region of 2. The remaining parts of the model had a free triangular extra fine mesh with maximum element size of 0.408, maximum element growth rate of 1.2, curvature factor of 0.25 and resolution of narrow regions of 1.

4.8 Considerations with Flash-SPS

Flash-SPS has been widely used to sinter high temperature ceramics [21, 22], and this often required the samples to be preheated until they reached an electrical conductivity sufficient to experience appreciable Joule heating from the voltage applied by the SPS. Samples with high resistivity ($> 1000 \, \mu ohm \, *m$) require a higher voltage than the SPS can provide. At the maximum voltage (6.5 V) that can be applied to the sample very little current flows, and consequently little power can be dissipated. Samples that are too conductive ($< 10 \, \mu ohm \, *m$) would also not experience significant Joule heating compared to the tooling. Even with the SPS is at 100 % power the current is limited to 3.5 kA by the resistance of the punches, and at these current the sample does not drop much voltage, and so again does not dissipate much power (but it will be heated by contact with the hot graphite punches. Since the tooling is made of graphite, to evaluate the main heat source, the relative ratio between the resistance of the sample and graphite punches should be considered.

To obtain a more complete picture of how the sample resistance affects the power dissipation in the sample and the punches, a simple graph was produced; 20 mm punches and reducers were considered, with a 20 mm diameter sample of thickness 4 mm. At room temperature the punch/reducer can be considered to have a resistance of 1.5 mohm each (top and bottom), while the ram and circuitry can be

ignored being large diameter conductive metal and cabling (as example a 10 cm height section of copper-beryllium would have a resistance of 0.017 mohm). Considering the Rs of the sample as unknown and a sample having 20 mm diameter and 4 mm height:

$$Rs=\rho s*L/S \qquad\qquad 3.4$$

$$I=V/(Rs+Rg) \qquad\qquad 4.12$$

$$P= I^2*R=I^2Rg+I^2*Rs=Pg+Ps \qquad\qquad 4.13$$

$$Ps=P-Pg \qquad\qquad 4.14$$

where R is the resistance in ohm, ρ is the specific resistance in ohm*m, S is the surface of the samples in m^2, L is the height of the sample in m, V is the voltage applied in Volts, I is the current flowing in the system in Ampere, P is the power dissipated in W, s is referred to sample and g to graphite. Here we consider the Voltage as 6.5 V corresponding to the maximum that can be applied by the SPS equipment, and the power dissipation within the sample Ps can be therefore calculated as a function of Rs or ρs.
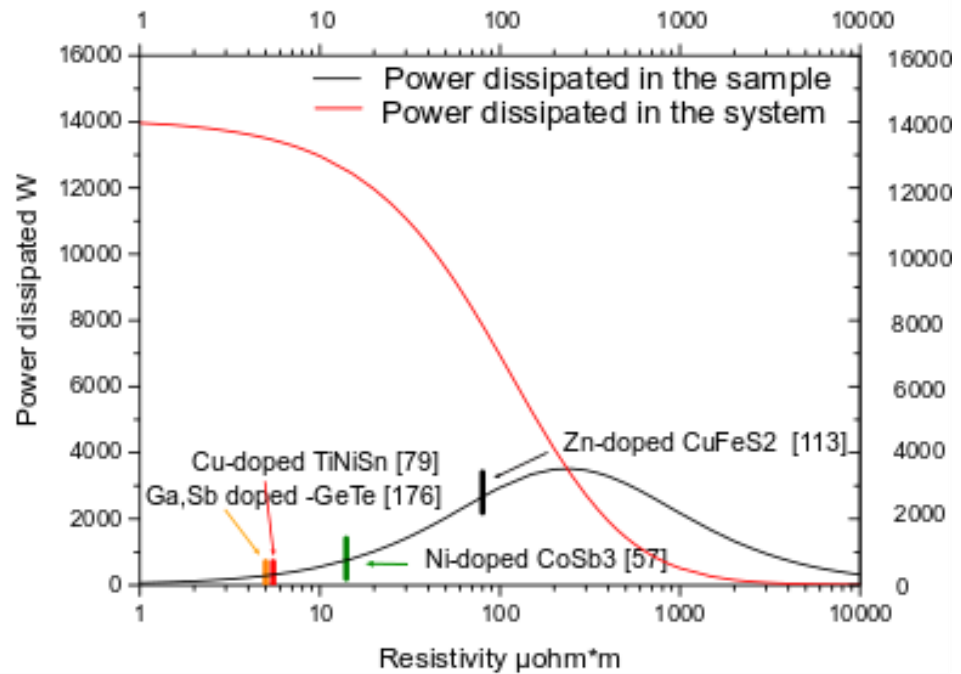
Figure 4.22 Power dissipation plot of power dissipation within sample and punches as a function of resistance

- For the sample size used, materials less resistive than graphite, below 10 µohm*m would have limited or no joule heating

- Materials comparable to graphite or slightly less conductive (100 to 1000 µohm*m) would experience Joule heating and limited power would be dissipated within the graphite

- Materials more resistive than graphite, (1000 to 10000 µohm *m Joule heating would mostly happen in the sample likely leading to extreme temperature gradients with limited total amount of power due to the high resistance.

- Material with resistivity above 10^{-2} ohm*m (more than 10000 µohm *m) are so resistive that basically no current would pass through the system, so there would be no heating in the punches or graphite

This graph presumed the resistance of the material did not change, while most real materials would change their resistance as they heated up and densified. The resistance of the punches also changes with temperature, but the graph still provides a useful way to predict the behaviour of materials in FSPS.

The graphite foil had a higher specific resistance than graphite, about a factor of 20, but is extremely thin (0.2 mm), the total resistance will be therefore very small compared to the total system and will not produce a high voltage drop. Including the graphite foil in the graphite section, the added resistance would be 0.16 mohm per foil, the curve would therefore be slightly shifted to the right.

Good thermoelectric materials usually have resistivity below 100 µohm*m and therefore would be suitable of being processed with FSPS without preheating, and from the above graph one would expect most of the heat to come from the graphite punches. For a more detailed understanding, the full model is required.

4.8.1 Main model

To evaluate the temperature distribution in FSPS we will compare different situations where the voltage applied is constant at 6.5 V and is applied for only 2 s (from second 1 to 3). We will show each property under the same scale. All the tooling dimensions and materials properties are unchanged unless specified, the sample has the properties of hFSPS-cool skutterudite (chapter 5).

- Effect of oversized punch in FSPS

- Effect of Peltier cooling

- Effect of graphite paper

- Comparison between dieless (FSPS) and stainless-steel die (hFSPS) configuration

- Effect of vertical contact in hFSPS

Each couple of results will be compared in terms of power dissipation, temperature field at second 3, temperature measured at the five virtual thermocouples (Fig 19) and the temperature difference between three couples of thermocouples (1-5, 2-4, 2-3). For the temperature field 3D model (expressed in °C), the lines represent point at the same temperature (iso-temperature lines) and are drawn every 20 °C to maintain a good readability of the plots. The power dissipation is expressed in W/m^3 and the scale for the peak value obtained is similar to typical power dissipation in flash sintering (estimated at 10^8-10^9 W/m^3 or higher [20]), being calculated and not measured though, the value can be overestimated when the model see it as very concentrated and might be influenced by mesh size.

4.8.2 Effect of oversized punch

A common practice in FSPS is to use oversized punches so that when the sample softens, it can increase in diameter, while still maintain contact with the punches. However, there are several issues with this setup; most important is the poor homogeneity in the sample. Therefore, a model was created to see if the inhomogeneity could be explained by current concentration due to the reduced sample size. First configuration was 20 mm sample between 20 mm punches, the second was 13.6 sample between 20 mm punches (the ratio is the same as the typical configuration of a 20 mm sample between 30 mm punches). The effect of Peltier cooling was not calculated and no graphite foil was used to show only the effect of the sample size.
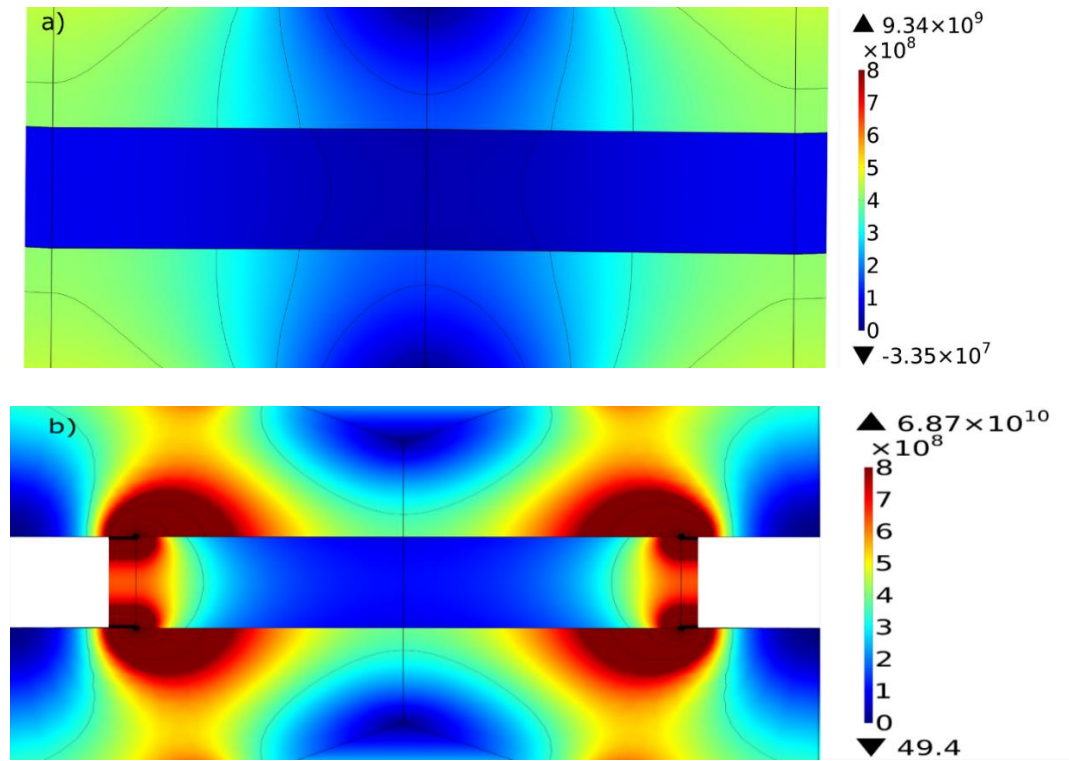
Figure 4.23 *Total power dissipation for a) regular punch b) oversized punch*

The reduction in diameter concentrated the current on the outer surface of the sample, which caused higher local power dissipation (Fig 4.23-b), this induce a strong inhomogeneity in temperature distribution due to the significant localized heat production (Fig 4.24-b).
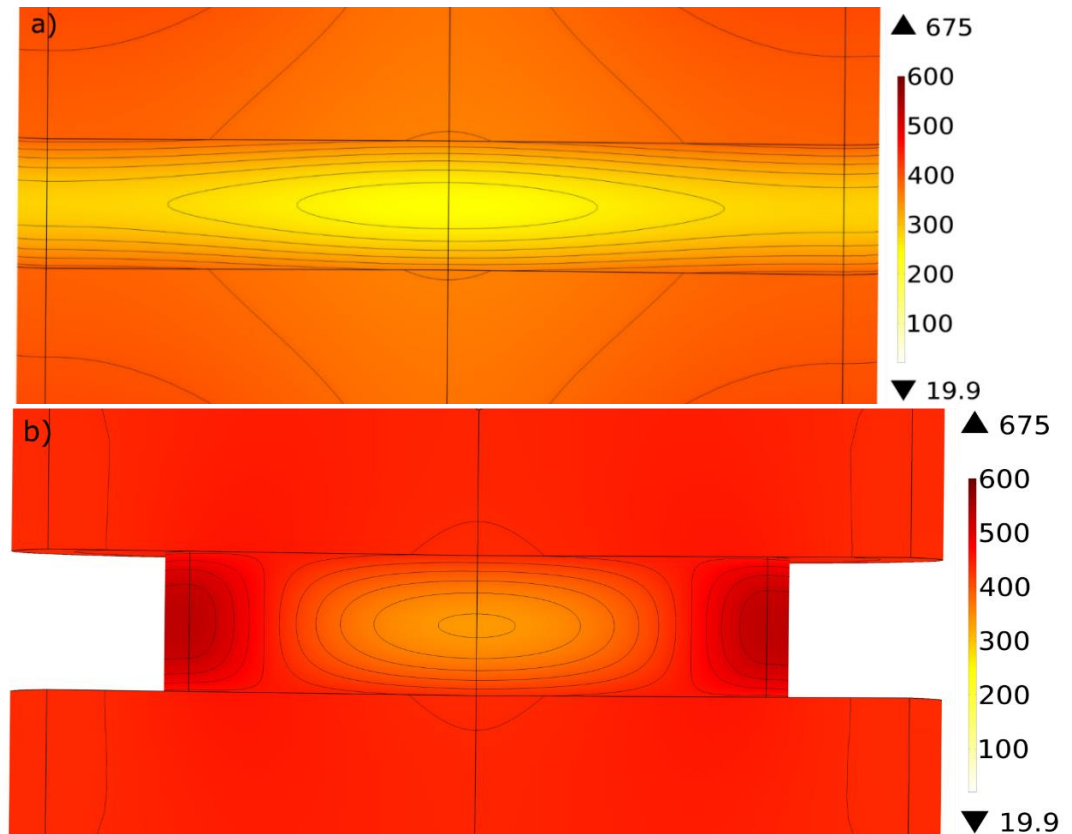
Figure 4.24 *Temperature field for a) regular and b) oversized punches after 3 s, iso-temperature lines are drawn every 20 °C.*

The outer temperature was therefore increased and the inhomogeneity of the sample was enhanced (higher density of iso-temperature lines). The temperature on the outer surface overcome 600 °C, as the colour is dark red, while the centre of the sample is at around 400 °C. Such a large gradient (Fig 4.24-b) would be risky for thermoelectric as they are often brittle and possess complex phase diagrams; high gradient and higher peak temperature than measured could induce unexpected phase separation or transformation. Since the virtual thermocouples are placed on the symmetry axis, this gradient does not appear, but the curves are still different (Fig 4.25).
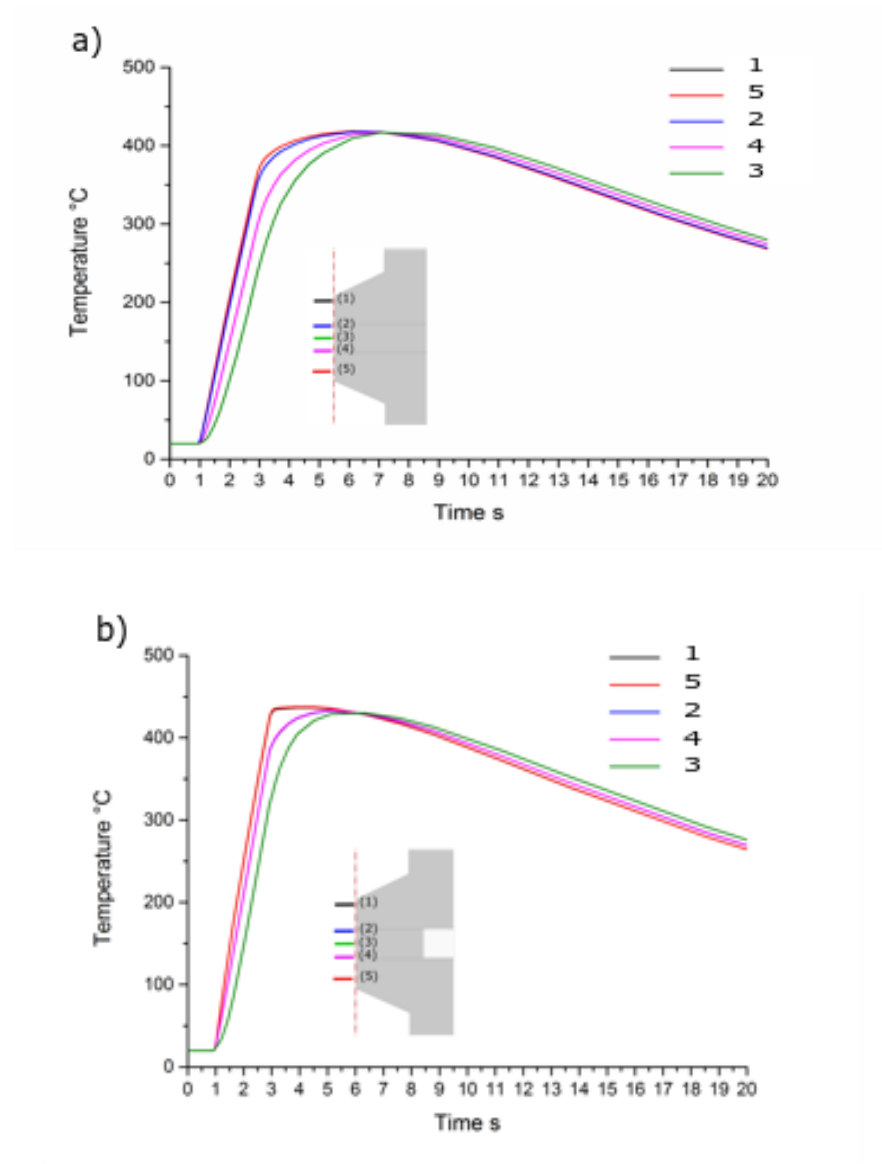
Figure 4.25 *Temperature evolution at the virtual probes for a) regular and b) oversized punches, power is applied after 1 s*

Punch and sample reach a higher temperature for oversized punches (450 °C vs 400 °C) but the temperature appear to get homogeneous quicker as there is an internal heat source, the cooling is similar and all probes calculate a similar temperature, Observing the temperature differences (Fig 4.26), this appears clearer.
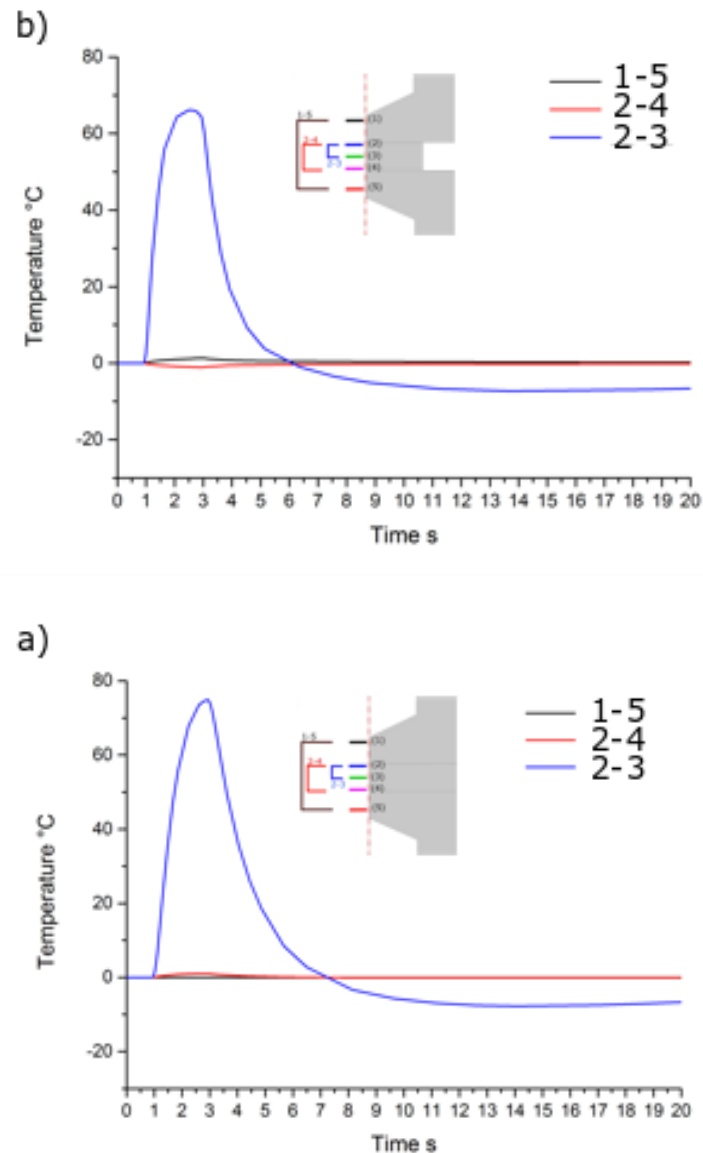
Figure 4.26 *Temperature difference among virtual thermocouples for a) regular and oversized punches*

The temperature difference is slightly smaller in oversized punch (Fig 4.26-b) because some heat is generated in the sample and a minimum heating, despite the low thermal conductivity is given by the internal source. The difference between the 2-3 probes becomes slightly negative (<10 °C) because the centre reaches the peak temperature slightly later and need a longer time to cool down because of the low thermal conductivity.

4.8.3 Thermoelectric gradient in Flash-SPS

Few papers have considered the possibility that a temperature gradient can form due to the Peltier effect when sintering thermoelectric materials by SPS [15, 186]. During FSPS it is expected that this effect would be even greater because of the higher current densities. To evaluate how significant these temperature gradients might be a comparative model was made. For this model the two setups were identical (diameter of samples and punch is 20 mm) except for one the equation for Peltier cooling was solved.
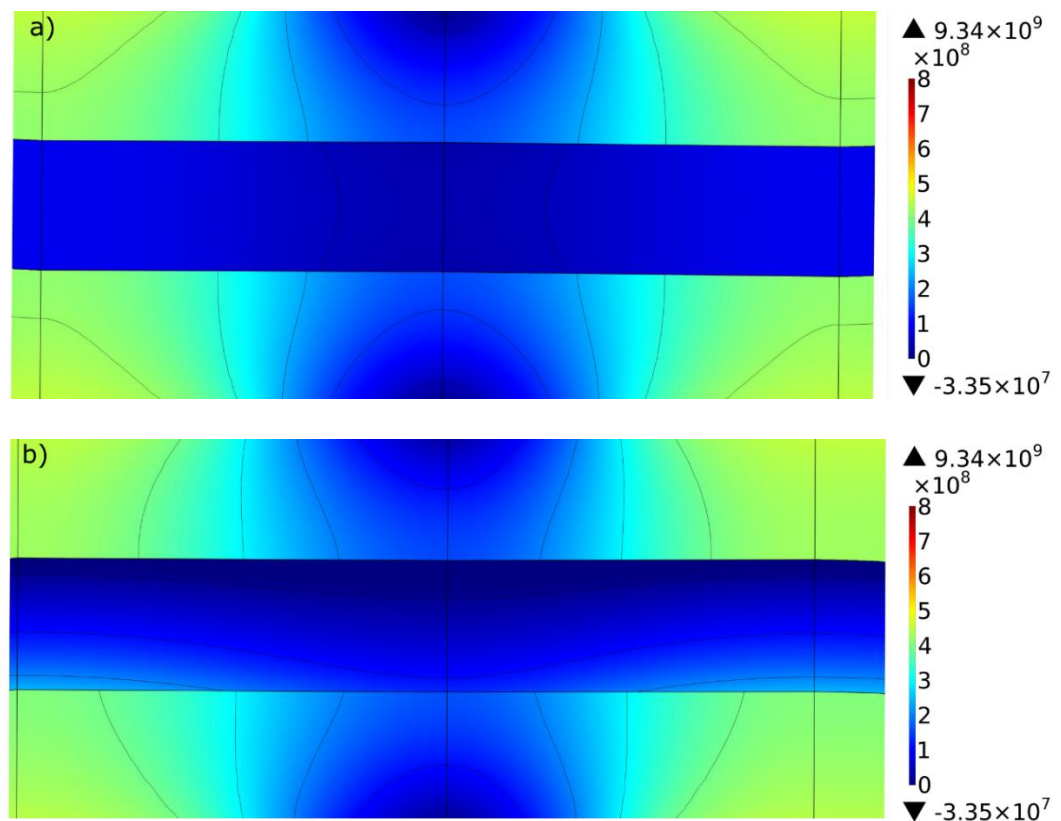
Figure 4.27 *Power dissipation a) without and b) with the Peltier cooling taken into account. When the Peltier cooling was considered the sample showed power dissipation at the lower surface (lighter blue) and power absorption at top surface (dark blue).*

A significant amount of heat was dissipated by the graphite punches and the sample experienced homogeneous Joule heating (Fig 4.27-a). The lack of power dissipation close to the punches was due to the low resistivity of the samples. As

83

expected, there was no top bottom asymmetry. If the Peltier cooling is taken into account (Fig 4.27-b), an asymmetry is visible and the lower section appear to have a higher dissipation of heat. This variation is not perfectly homogeneous because the punch has a hole, which reduces the current passing through the central axis.
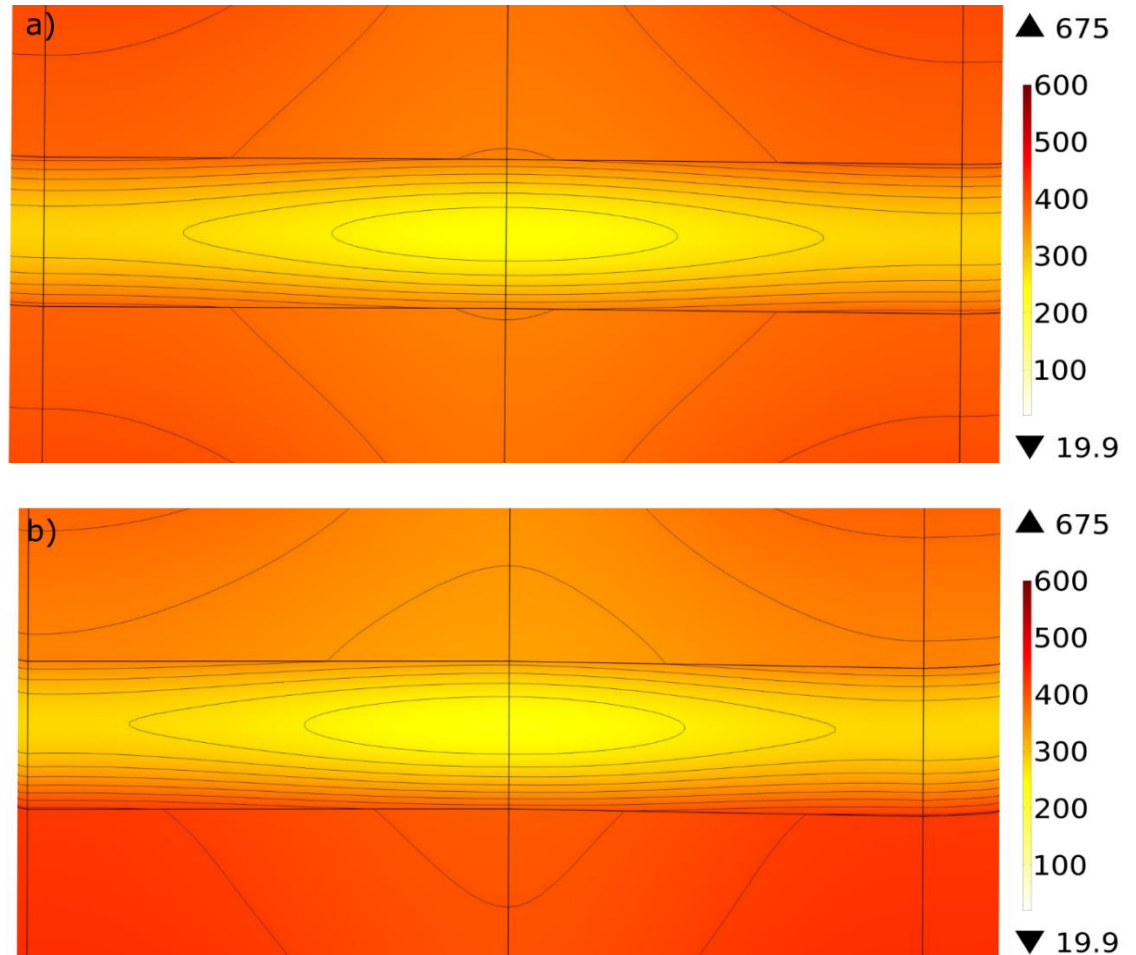
Figure 4.28 Temperature Field a) without and b) with Peltier equation solved after 3 s. Iso-temperature lines are drawn every 20 °C.

Therefore, the Peltier cooling induce an asymmetry in the temperature field (Fig 4.28-b), since the lowest temperature is not on the centre anymore (Fig 4.28-a) and there are more iso-temperature lines on the bottom of the sample.
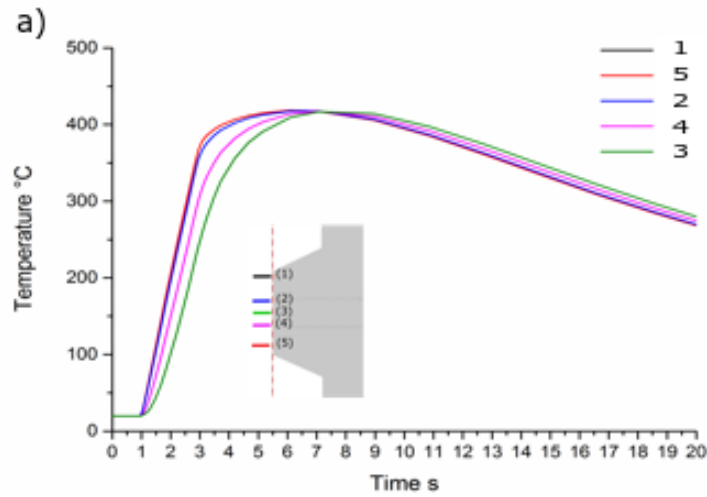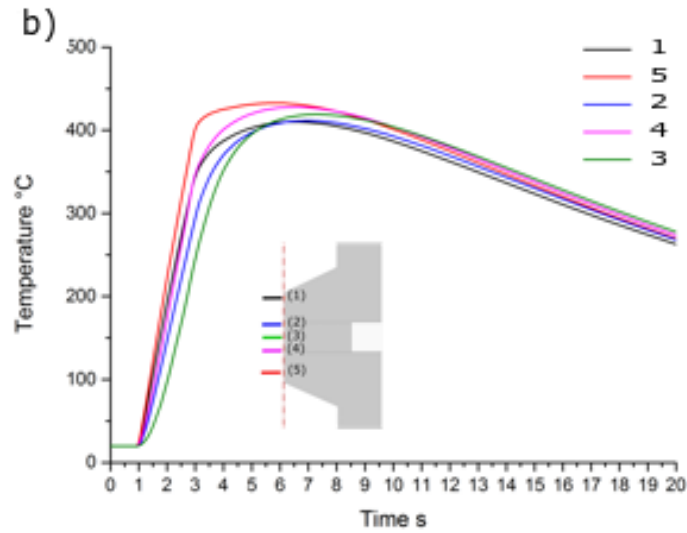
Figure 4.29 *Temperature evolution at the virtual probes a) without and b) with Peltier cooling, power is applied after 1 s.*

In terms of temperature there is not a significant difference between the peak values (Fig 4.29) but the asymmetry between top and bottom is evident, when the Peltier cooling is considered (Fig 4.29-b).
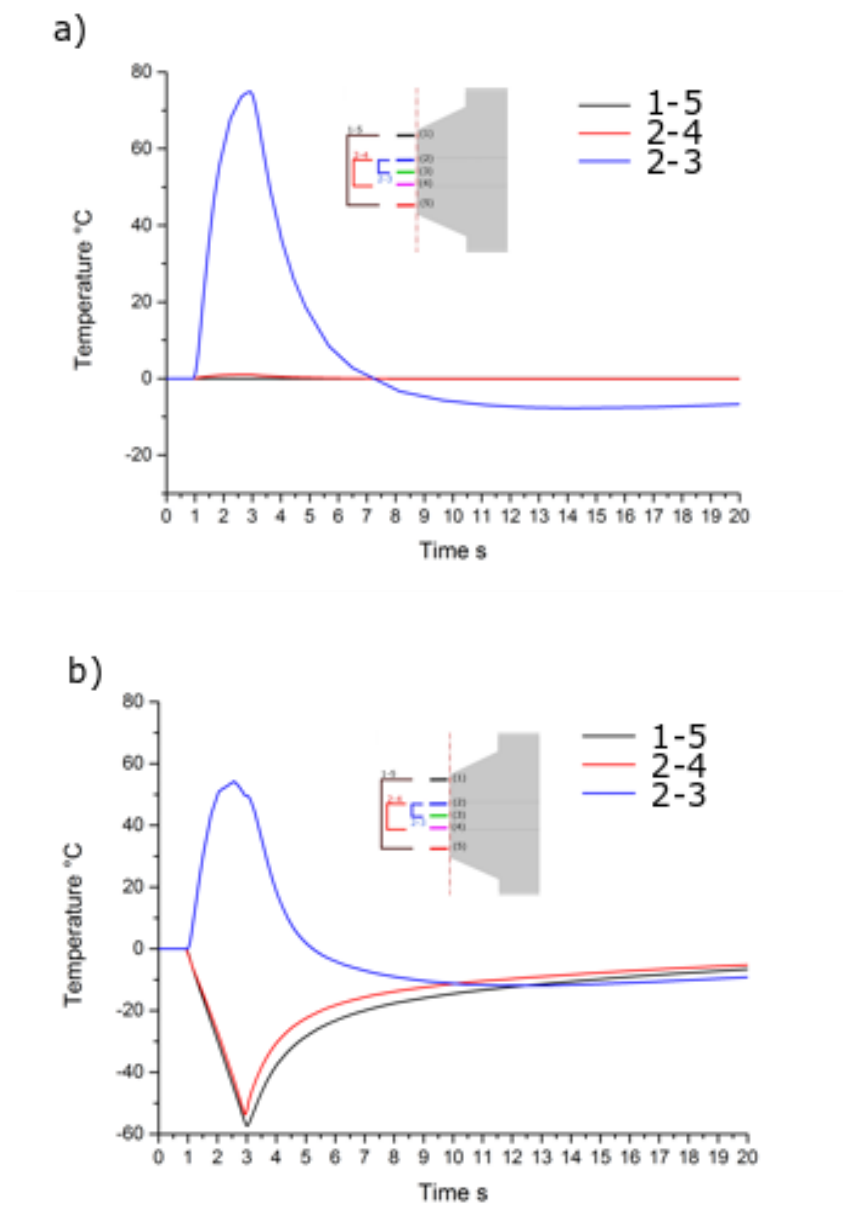
Figure 4.30 *Temperature differences among virtual thermocouples a)*
without and b) with Peltier cooling.

The temperature difference between 2-3 is about 75 °C (Fig 4.30-a) and seems to decrease when we consider the Peltier cooling as only 55 °C are calculated (Fig 4.30-b). The reason is the position of thermocouple 3 (Fig 19), which is perfectly centred in the sample and is not at the lowest temperature when the Peltier cooling is considered. A significant gradient (about 50 °C) is visible between 1-5 and 2-4 (Fig 4.30-b) which would be not present without the Peltier effect (Fig 4.30-a). The negative value is due to the higher temperature of the bottom side.

86

The Seebeck coefficient of sintered skutterudite was not particularly high but still induced a gradient so other materials could show an even larger effect. As well as causing issues with uneven densification, this thermal gradient could contribute to thermal stress induced cracking.

4.8.4 Effect of graphite paper

Graphite foil is commonly used in SPS as a sacrificial layer to stop the sample sticking to the punches. The sample can react and stick to it, but due to the weak bonding between the layers, it is easy to peel the remaining paper from the reacted material. It is also used to provide radial contact between the sliding graphite punches and die. As previously discussed graphite foil has a relatively low conductivity (4000 S/m) and low thermal conductivity through plane (5 W/m*K). In FSPS, it was placed as a 0.2 mm thickness layer on the top and bottom of the samples, so it was electrical and thermally in series with the sample.
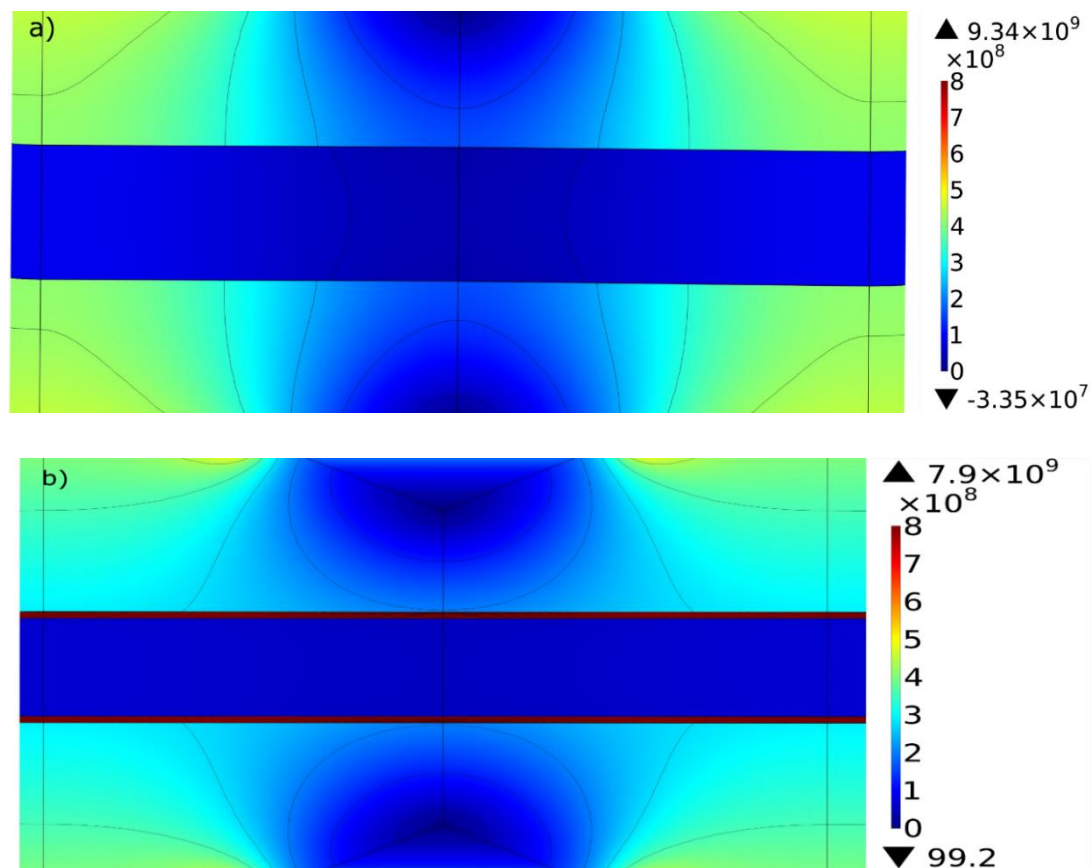
Figure 4.31 *Total power dissipation density a) without and b) with graphite paper*

The presence of graphite foil generates a new heat source at the graphite-sample interface (Fig 4.31), which alone would be expected to increase the temperature closer to the interfaces and slightly reduce the cooling because of low thermal conductivity.
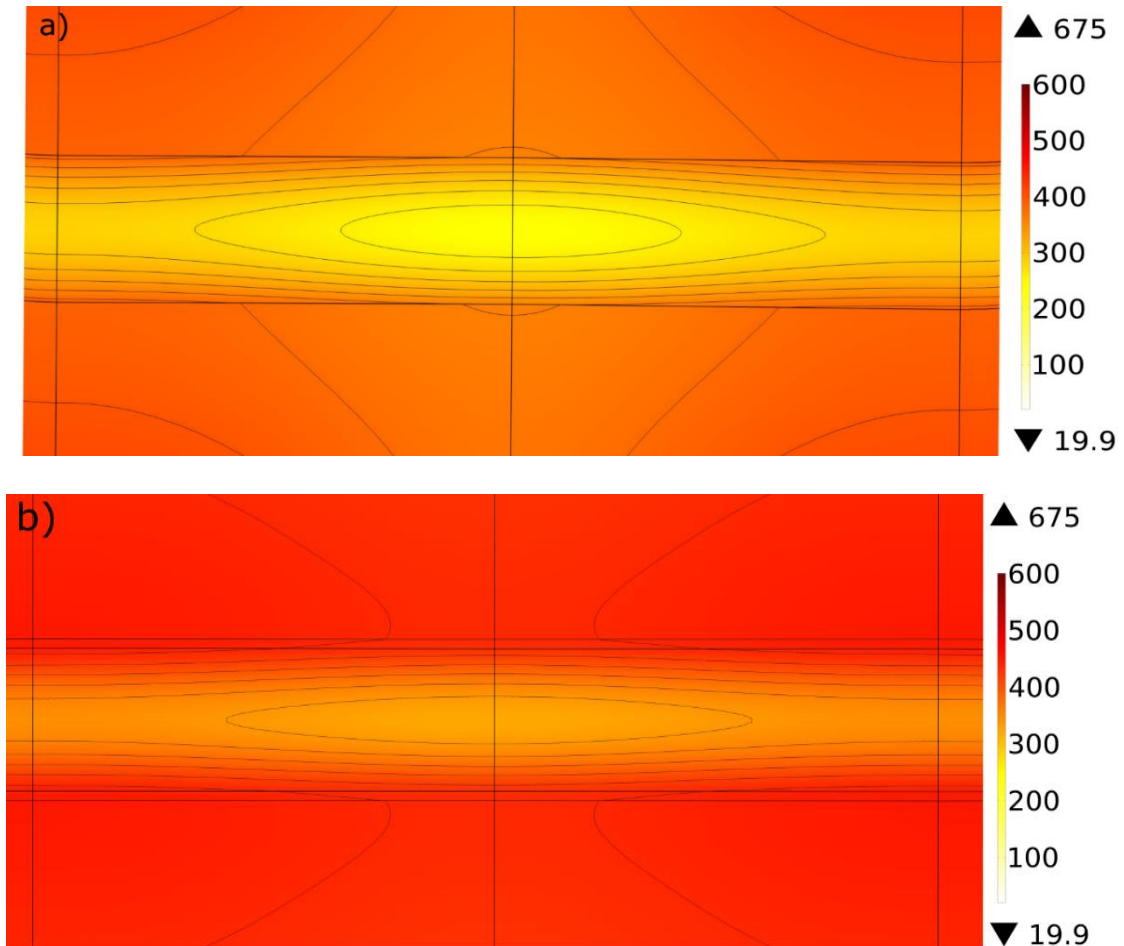
Figure 4.32 *Temperature field after 3 s a) without and b) with graphite paper. The iso-temperature lines are drawn every 20 °C.*

The setup with graphite foil has strong surface to centre gradient formed during heating but shows a symmetric field (Fig 4.32). The gradient did equilibrate after the power was cut but the cooling was slightly slower and, more importantly, there was a noticeable difference of about 30 °C between the sample temperature and the punch temperature induced by the additional heat source at the interface (Fig 4.33). This

condition would cause an overestimation of the temperature in the sample since a direct measure is not possible.
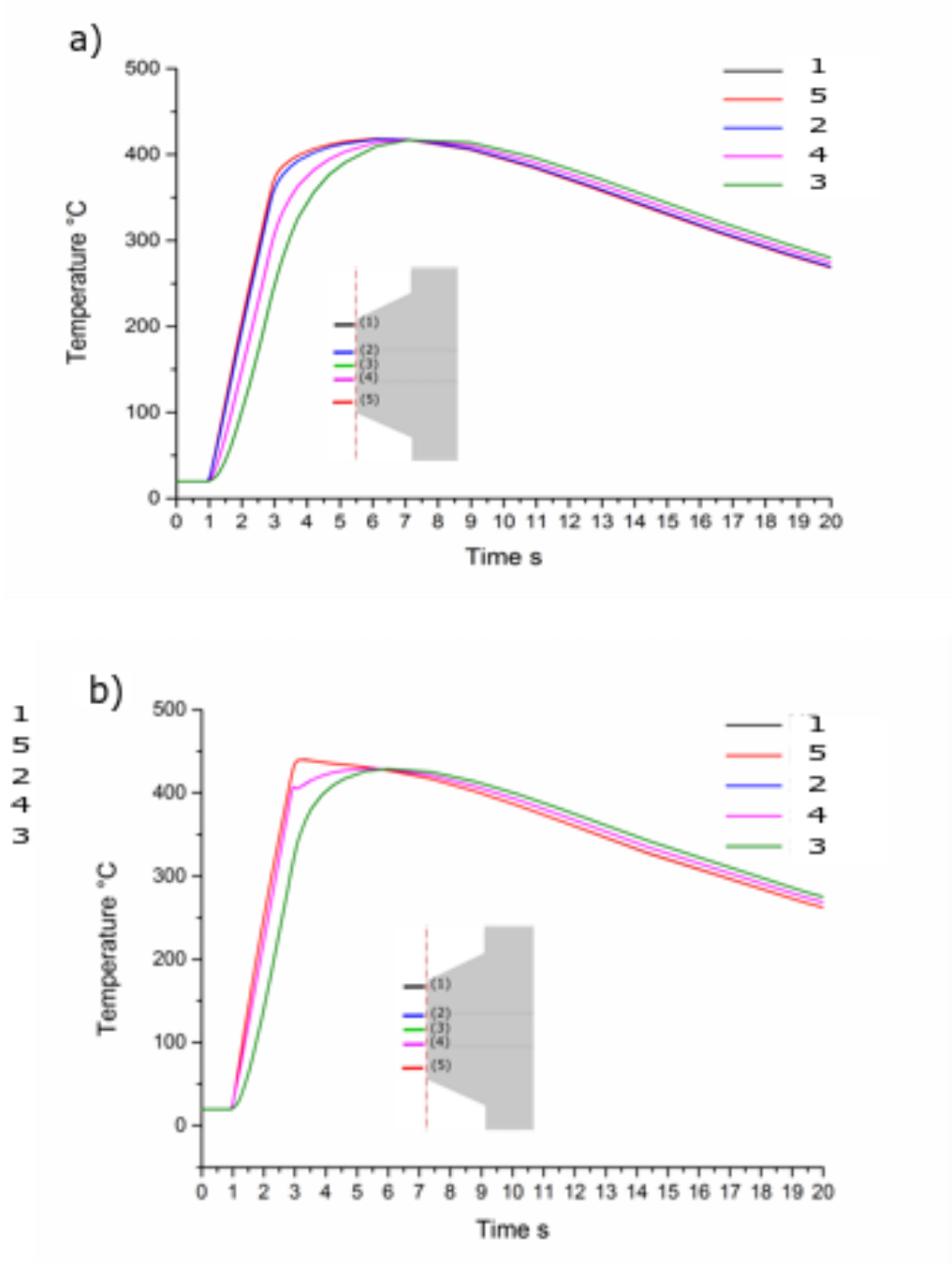
Figure 4.33 *Temperature evolution at the virtual probes a) without and b) with graphite paper, power is applied after 1 s.*

The temperature difference calculation suggests that the use of paper may increase the temperature gradient happening between the centre and the interfaces (Fig 4.34)
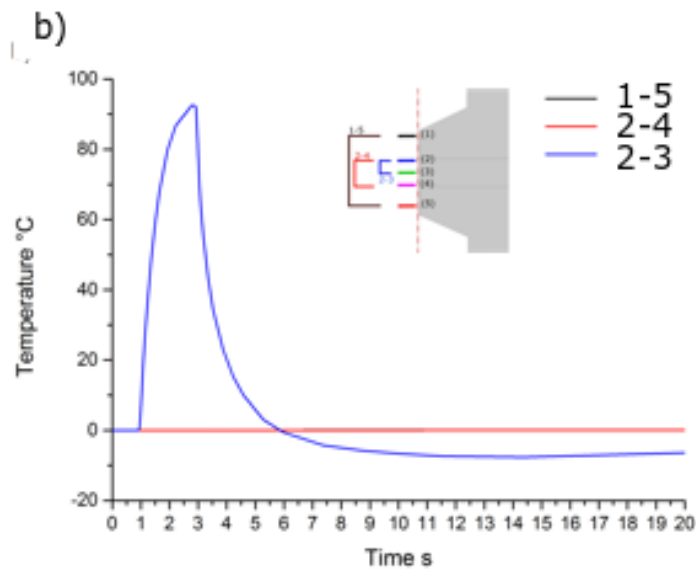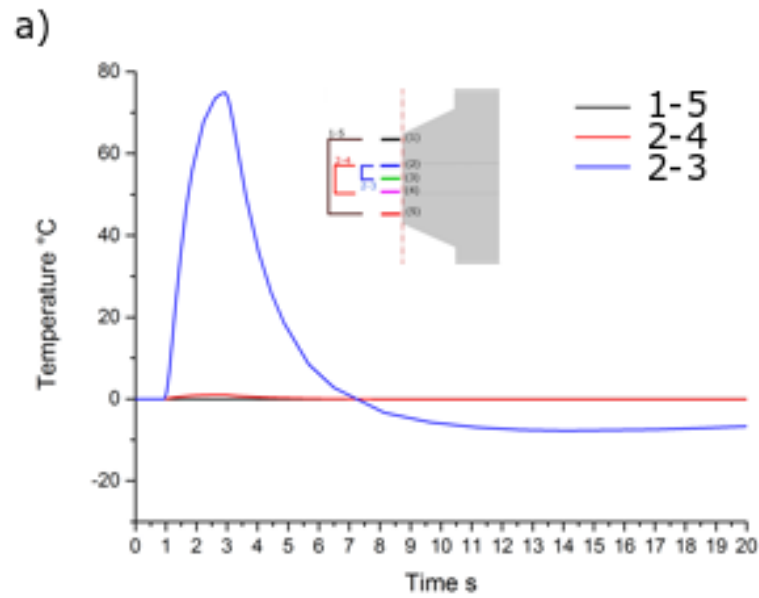
Figure 4.34 *Temperature differences among virtual thermocouples a) without and b) with graphite paper.*

The gradient should be strongly dependant on sample thickness as it is caused by surface heating, thinner samples should experience less gradient as the heat sources would be closer to the centre. For this reason, it should be seen as unavoidable, if the samples do not stick to graphite then it should be omitted. Graphite paper could also be used to intentionally produce local heating for low resistance samples.

4.8.5 Temperature Gradient Flash-SPS vs hybrid Flash-SPS

As seen from the models above there are some issues with using FSPS to produce internal Joule heating. Joule heating tended to produce centre to outside temperature gradients, large errors in measuring temperature and Peltier cooling causes further gradients. It is possible to flash sinter without having significant Joule heating [21], this occurs for samples on the conductive left side of the power dissipation curve (Fig 4.22) where the sample was heated by the graphite punches, but this heating mode comes with its own downsides. In an attempt to solve the problems with Joule heating mentioned above, as well as the issues with using oversized punches, a new type of FSPS was developed using a thin stainless-steel die.

The use of a stainless-steel die also served a practical purpose to constrain the sample during sintering. Thermoelectric materials are softer than previously studied Flash-SPS materials (SiC, B_4C, ZrB_2), so would deform excessively (over 100% increase in diameter) in a typical FSPS setup. The thickness of the die wall was minimized to reduce the thermal mass of the system and allow fast cooling and heating. Other materials could have been used but any die must have reasonable high temperature strength to survive. One interesting variable with this setup was how much current flowed through the die; this could be altered using an insulating die or an insulated layer on the internal wall. An insulated die would be closer to the die less configuration as all the current would be forced to pass through the sample. The electrical conductivity of bare stainless steel reduced the peak temperature reached for a given voltage and the die acted as a heat sink, cooling the side of the sample.

To see how effective this hybrid FSPS setup might be it was compared to a FSPS setup. All the before mentioned effects were considered (oversized punch, Peltier cooling and graphite paper).
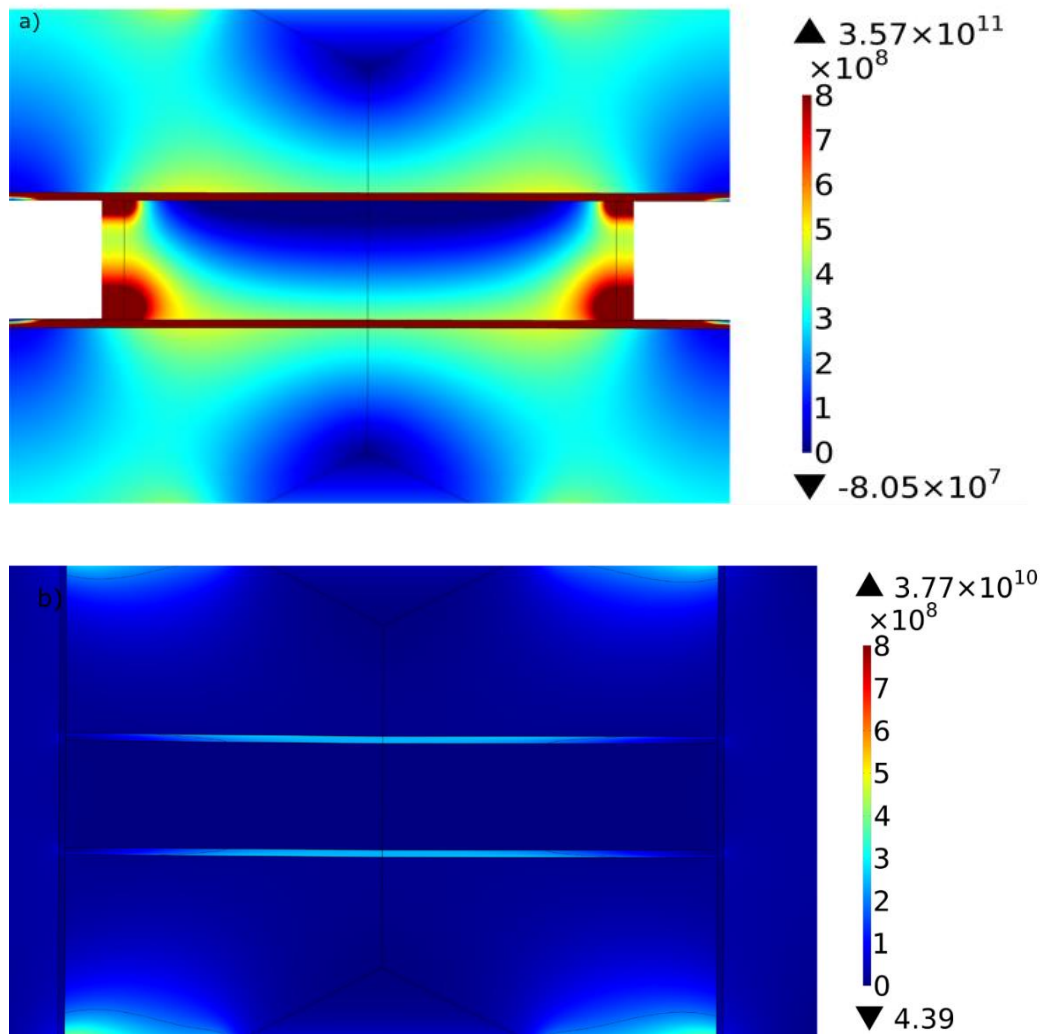
Figure 4.35 *Total power dissipation density for a) FSPS and b) hybrid-FSPS*

Power dissipation is very inhomogeneous in the dieless configuration and this is enhanced by the Peltier effect (Fig 4.35-a). On the other hand, the hybrid setup had most of the heat produced within the graphite punches, above the contact with stainless steel, and little within the sample. The stainless steel, while carrying most of the current, did not dissipate much heat due to its relatively low resistivity (Fig 4.35-b).
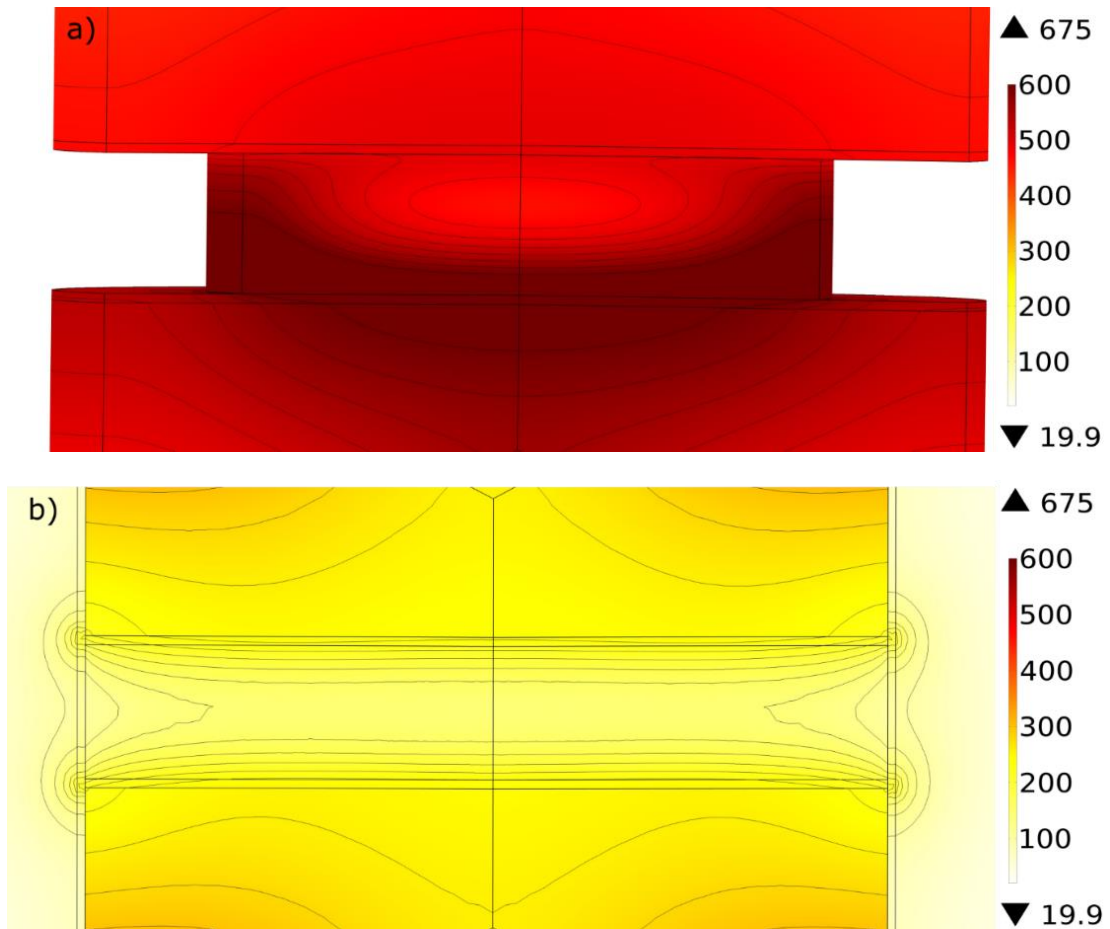
Figure 4.36 *Temperature field for the FSPS and hybrid FSPS after 3 s. Iso-temperature lines are drawn every 20 °C.*

The uneven power dissipation resulted in a strong temperature asymmetry, the outer and lower surface of the sample reached a higher temperature than the surrounding regions (Fig 4.36-a), overcoming 600 °C. This could cause a variety of problems in a real sample; from cracking, phase separation and even melting if the material was sintered close to its melting point. The stainless-steel die did have several down sides; it reduced the overall temperature significantly and caused some temperature gradients, due to effect of the sides (Fig 4.36-b).
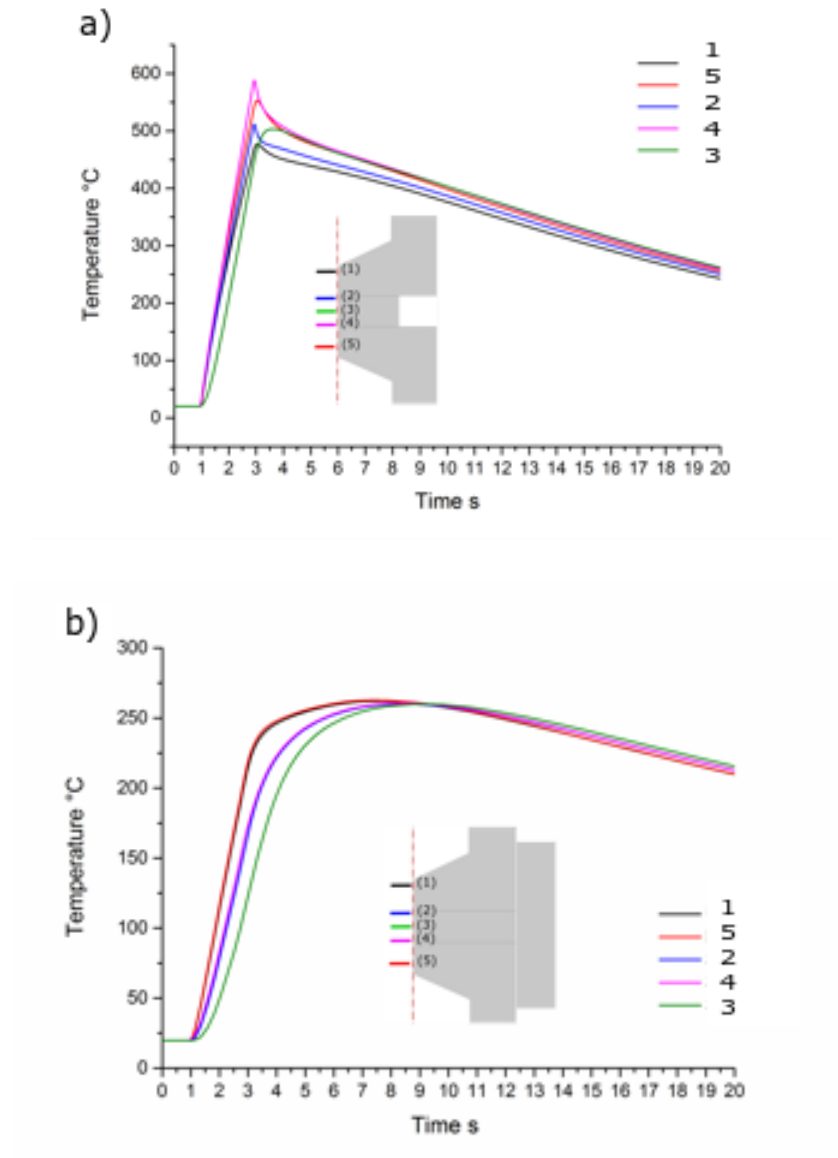
Figure 4.37 *Temperature evolution at the virtual probes a) without and b) with die, power is applied after 1 s.*

The dieless configuration produces a sharp increase in temperature at the virtual thermocouples (Fig 4.37-a), characterized by significant variation between them, the centre reaches its peak temperature later because of low thermal conductivity, should be notice that this is not the point at the lowest temperature (Fig 4.36-a).

The stainless die caused a delay to the heating of the sample (Fig 4.37-b); the centre of the sample reached its peak temperature 5 seconds after the power was removed. This was due to the time it takes to the heat to move from the graphite

punches (region not covered by stainless steel) and the presence of the pyrometer hole which reduces the overall heat carrying section. The overall gradient on the central axis where the virtual thermocouples are placed is anyway reduced (45 °C vs 90 °C, Fig 4.38-b).
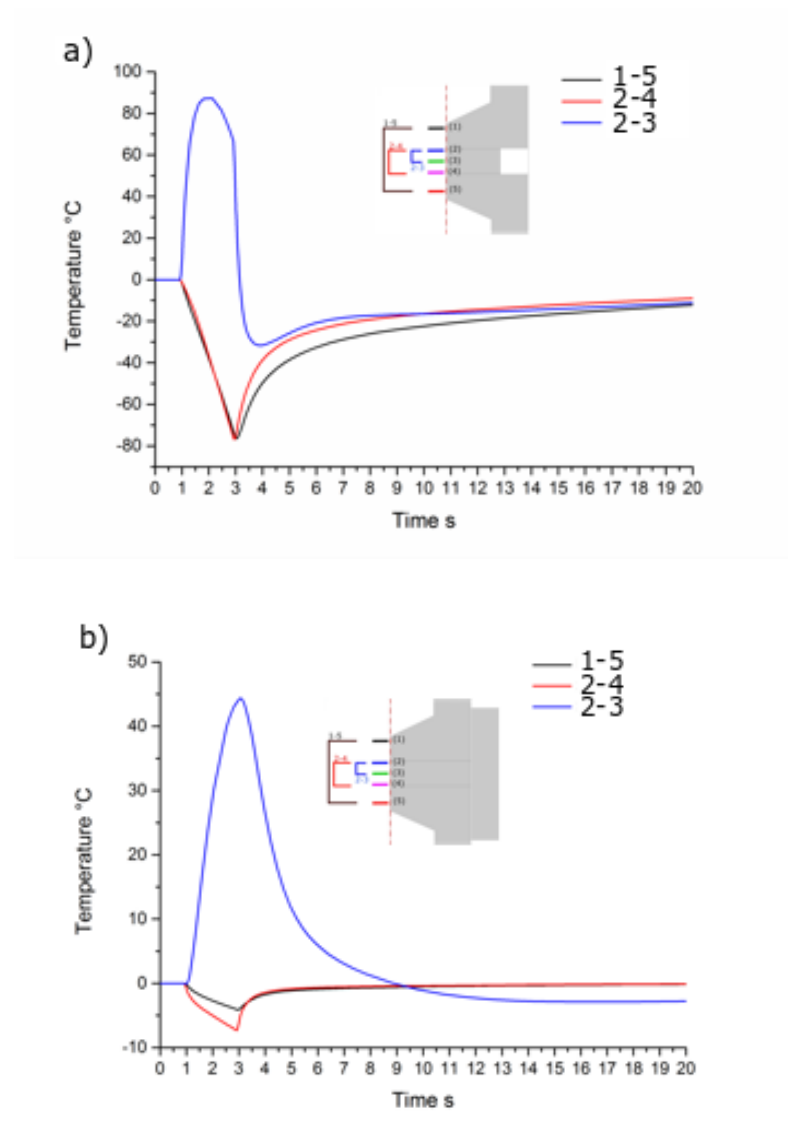
Figure 4.38 *Temperature differences at the virtual probes a) without and b) with die, power is applied after 1 s.*

It is worth noting that the hybrid configuration had a centre-side temperature gradient but smaller than the dieless configuration (Fig 4.36), this was because the stainless steel acted as a heatsink. Moreover the dieless configuration has a swap in

95

the sign of the gradient due to the delayed heating of the core through conduction which becomes hotter than the surrounding, considering the position of the virtual thermocouple 3, such gradient will be stronger were the temperature is at its minimum.

For hFSPS in real conditions the sample shrinkage would reduce the effect of heating gradient, the heat sink effect of the die would prevent the sample reaching higher temperature. The effect of shrinkage will influence the FSPS configuration too, the reduction of thickness during heating can lower the gradient but cannot remove the Peltier effect, and even if the diameter would increase, it could not prevent the initial overheating at the edges. The inhomogeneity of FSPS sample would therefore be quite significant and would be detrimental for thermoelectrics.

4.8.6 Effect of vertical contacts

While the previous model was an attempt to reasonably approximate the difference between real FSPS and hybrid configurations, one factor was ignored. The vertical contact resistance between the graphite paper and stainless die could have a massive effect on the temperature distribution in the hybrid configuration. These contacts are important and their value is not as negligible as the horizontal contact at the sample-punch interface. Under real conditions, as the setup heats up, the sample softens, it densifies, but it also experiences plastic flow. This results in a compressive pressure applied by the punches, converted into a radial force on the region of the die in contact with the sample. This causes the die to bend slightly. With the thin wall stainless used in the hybrid setup this bending could cause a loss in contact pressure in the regions not in contact with the sample. This would therefore increase the electrical and thermal resistance of the punch die interface. To visualize how significant this effect might be, a comparative model that split the die contact into 3 regions was made. The upper and lower region in contact with the punches and the middle region in contact with the sample. The contact values at the stainless-graphite paper-graphite interfaces (Fig 4.21) were chosen among the highest values found in literature (Tab 4.1) to simulate a very negative condition. The electrical contact resistance was set at 10^{-6} Ohm*m^2 and the thermal resistance at 10^{-3} K*m^2/W. It is worth considering that the variability of the literature value comes from the method used to calculate them, it can be experimentally measured or it can be a refined value that allows the model to fit experimental data. If the value is refined, error may come from the modelling mesh used, as it may have discontinuity even for extra fine values,

influencing the behaviour calculated, or the type of approach used for modelling (thin layer, 2D domain). Moreover, the parameter (such as *V* or *I*) used to calculate such value may influence the results (measured value or SPS output value).

Table 4.14 Literature value of electrical and thermal contacts

Author	Electrical contact resistance (Ohm*m²)	Thermal contact resistance (K*m²/W)
Maizza et al [201] Giuntini et al [202]	$1.33*10^{-7}$	$7.58*10^{-4}$
Matsugi et al [203]	$5*10^{-5}$	$6.62*10^{-6}$
Zavaliangos et al [204]	$8*10^{-8}$	$4.17*10^{-4}$
Vanmeensel et al [189]	$2.76*10^{-6}$	/
Wei et al [188]	$1.08*10^{-6}$	/
Munoz et al [205]	$1.2*10^{-7}$	$4*10^{-4}$
Maniere et al [190]	$8*10^{-8}$	$5*10^{-3}$

The values tabulated above were taken at 1000 °C, but, as determined by Maniere et al [190], the order of magnitude of resistance does not change with different temperature.
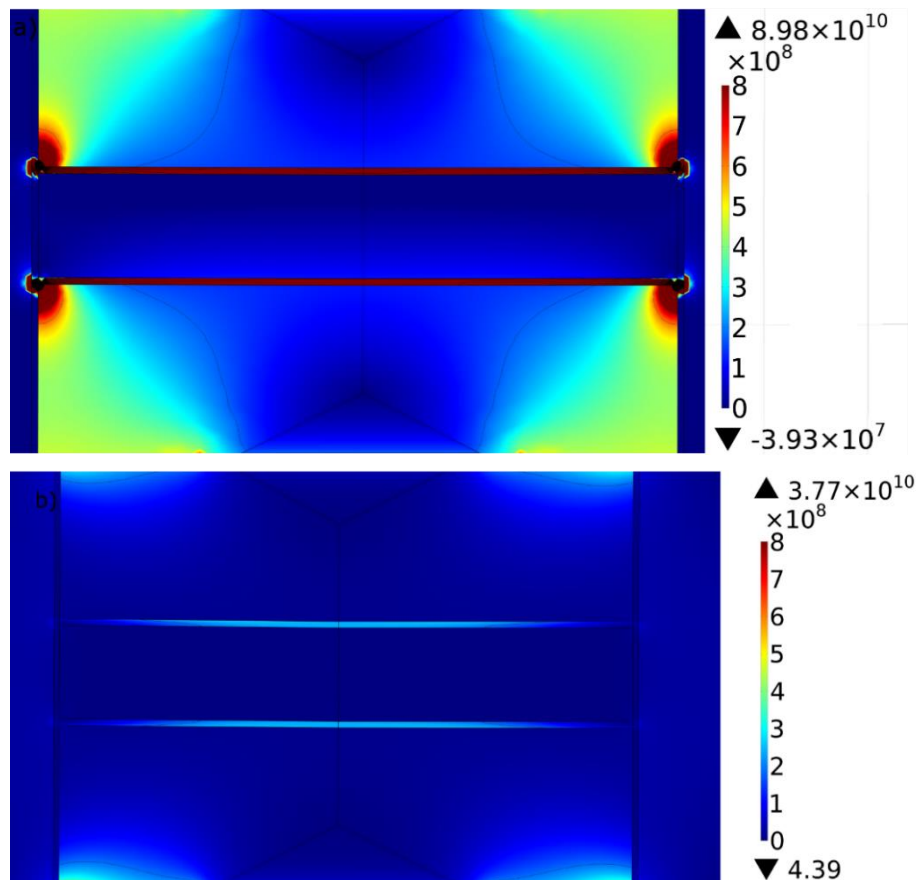
Figure 4.39 Total power dissipation a) with and b) without vertical contacts

Comparing a perfect contact with a poor contact (Fig 4.39) shows that under poor contact the radial graphite foil would produce a higher power. The high contact value chosen meant that the current did not all travel through the die in contact with the punch and significant current only started flowing through the die near the sample, where the contact was lower. This means the current flowed through the graphite for longer, so the heating region was closer to the sample. It also means that a higher current is passed through the sample and induce a limited Peltier cooling, as evidenced by the lighter colour at the bottom surface of the sample. With poor contact, the average temperature was higher because more heat was produced closer to the sample (Fig 4.40). The temperature symmetry is not changed and the outer surface, in contact with the die, are still at a lower temperature.
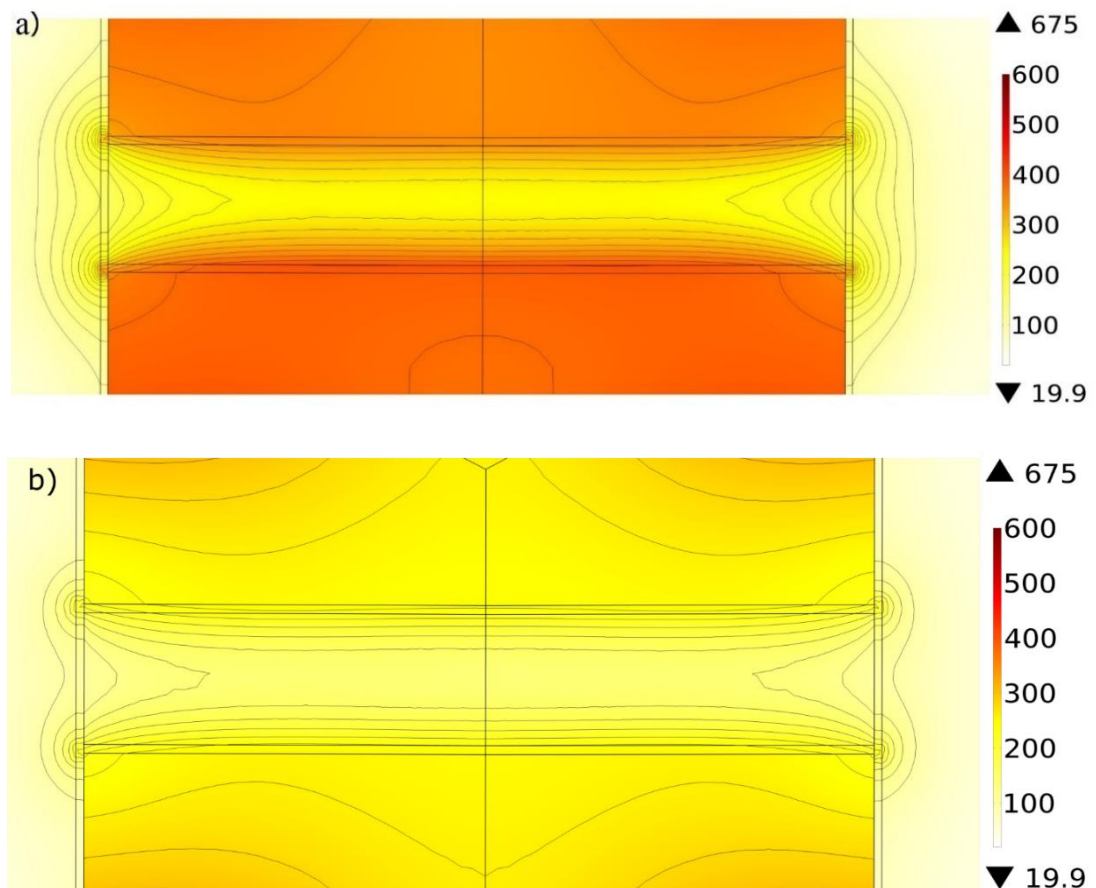
Figure 4.40 *Temperature field a) with and b) without vertical contact after 3 s, iso-temperatures lines are every 20 °C.*

This also affected how the temperature changed with time, and poor contact resulted in a sharper temperature response (Fig 4.41-a) and a higher temperature at the punches with a faster cooling. The heat rate calculated is roughly 160-170 °C/s (9600-10200 °C/min), which is close to heating rate obtained experimentally, and a cooling rate of about 500 °C/min, similar to what obtained experimentally.
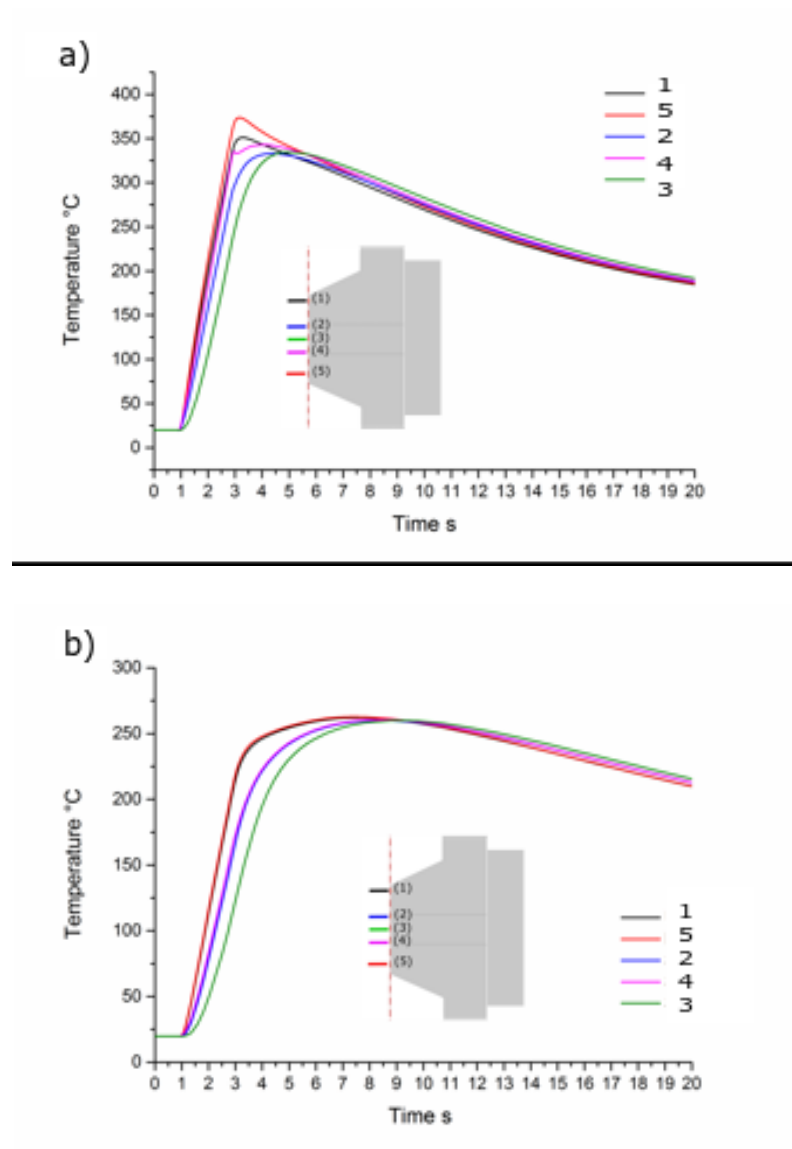
Figure 4.41 *Temperature evolution at the virtual probes a) with and b) without vertical contacts, power is applied after 1 s.*

The temperature gradient with poor contact was slightly greater than with good contact (Fig 41), being about 60 °C instead of 45 °C but still better than the 90 °C of the die less configuration (Fig 4.42).
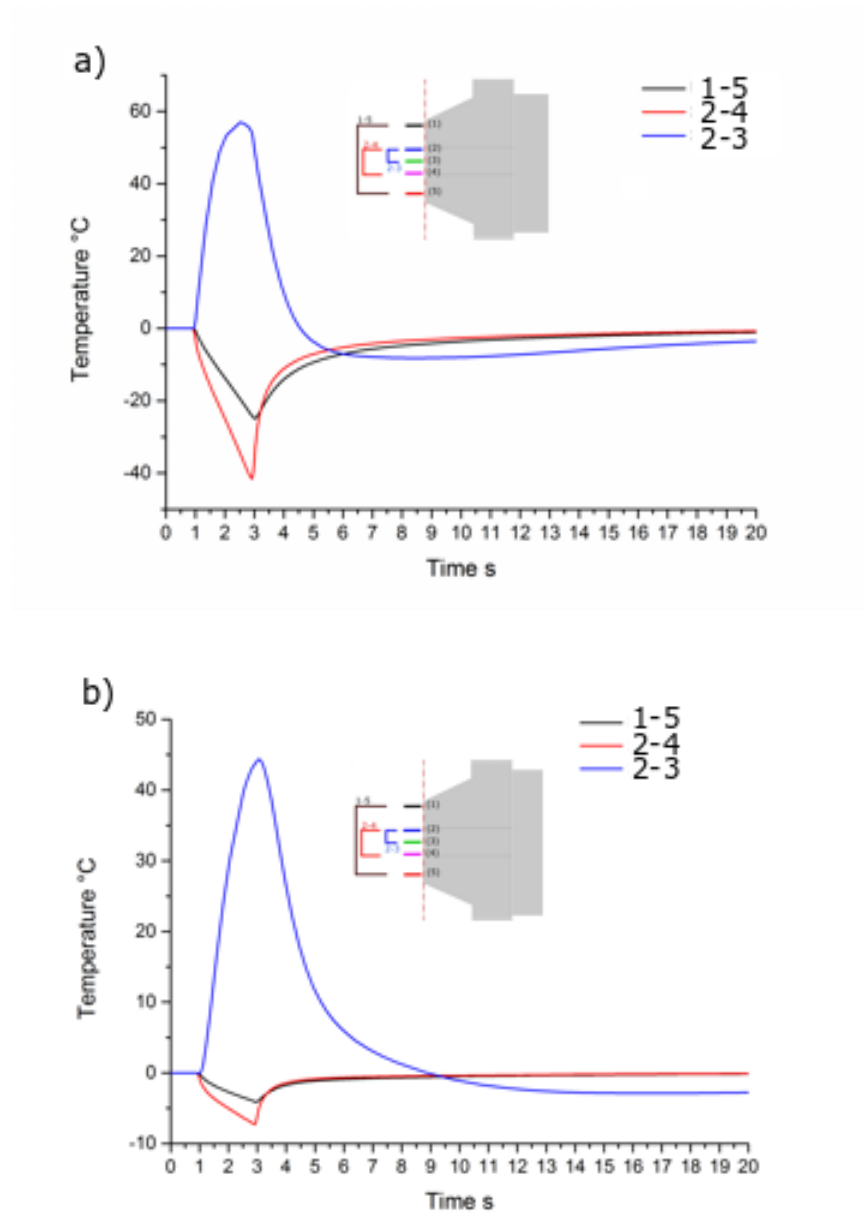
Figure 4.42 *Temperature difference at the virtual probes with and without vertical contacts, power is applied after 1 s.*

The contact resistances chosen are quite high but produced results close to what was seen experimentally, the contact value chosen are temperature-independent while, in reality, they would be influenced by temperature and pressure evolution during the sample sintering.

4.9 Conclusion

The analysis performed showed the difference between the hybrid and die less configuration for the same material. A material with good thermoelectric properties should be processed in a way that minimizes the Peltier heating and the hybrid setup achieved this by reducing the current flowing thought the sample, without significantly reducing the heating rate. The excessive heating produced by the size reduction and Peltier effect was removed, reducing the risk of overheating. On the other hand, the die acted as a heat sink so the average temperature was lower. It was also clear how significant the effect of contact pressure was on the graphite paper. The setup preparation should be careful, as damaging the vertical paper could have negative effect, since it may increase the contact resistance or modify the current path. Since the Peltier effect may not be fully removed, the high-power pulse should not be applied for very long time, as the high current may still induce a gradient within the sample. Because of the introduction of a highly conductive die, the resistivity of the material is less important. Very resistive materials would still be heated up at high heating rates because of the die. The use of mechanically strong materials, such as stainless steel, allows the application of high pressure, moreover, since the temperature of the die is consistently lower than graphite and sample, it would not reach the softening point (750 °C) until higher temperatures are reached. This was confirmed by experiments on half-Heusler which were sintered at 980 °C and 1040 °C without any change in the die shape.

Chapter 5 Hybrid-Flash SPS of Ni-doped Skutterudite

5.1 Introduction

As discussed in the thermoelectric review section, skutterudite is a promising thermoelectric material and several compositions, dopants and filler atoms have been investigated. It was of interest to exploit the potential of high heating rates on reactive sintering of Ni-doped $CoSb_3$ as limited work has been done on this type of processing and its effect on the reactions is unknown. Some preliminary experiments done with Flash-SPS were not successful. We therefore used hybrid Flash-SPS (hFSPS). Thermoelectric properties were evaluated for samples produced at a low pressure (L) 16 MPa, (hFSPS-cool-L) and high pressure (no label) 50 MPa (hFSPS-cool) using a preheating stage before the pulse and subsequent cooling. A set of samples were held at the sintering temperature to separate the effect of heating rate and holding time and ideally complete the reaction (hFSPS-hold-L and hFSPS-hold).

5.2 Experimental Setups

Polycrystalline samples of nominal composition $Ni_{0.15}Co_{0.85}Sb_3$ were prepared from commercial powder and sintered using an SPS furnace. Sample were processed using SPS, Flash-SPS and hFSPS. Pre-compacted pellet for FSPS were obtained by loading powder into a 20 mm stainless steel die and pressing at 150 MPa. Each time about 4.5 g of material were used.

The SPS processing temperature and time was guided by preliminary experiments; a heating rate of 100 °C/min and a dwell time of 5 min at the sintering temperature of 750 °C, pressures of 16 MPa (minimum) and 50 MPa (optimised) were applied at the holding temperature

Hybrid flash-SPS samples were produced with a preheating of the samples at 300 °C, to homogenise the powder without starting the reaction (see XRD Fig 5.3). Samples at low and high pressure (hFSPS-cool-L and hFSPS-cool) were prepared. Pressure was applied during the low temperature holding. Another series of samples were produced by holding the samples at the sintering temperature for 5 minutes (hFSPS-hold-L and hFSPS-hold). This allowed the separation of the effect of rapid heating rate (9000 °C /min) from the high temperature dwell in order to enhance the conversion rate. Temperature was controlled using a thermocouple placed in the punch about 3 mm from the sample.

Flash-SPS samples using pre-sintered or pre-compacted pellets resulted in significant plastic flow induced by temperature gradient, and the samples were extremely thin (<1 mm). This is probably due to the higher temperature induced by current concentration on the outer surface as discussed in Chapter 4.

5.3 Result and discussion

The force, piston travel, temperature and power dissipation data can be useful to understand the sintering process (SPS Fig 5.1, hFSPS-cool Fig 5.2, hFSPS-hold Fig 5.3). It should be noticed that the data recording ends before the sample reached room temperature when the minimum pressure was applied.
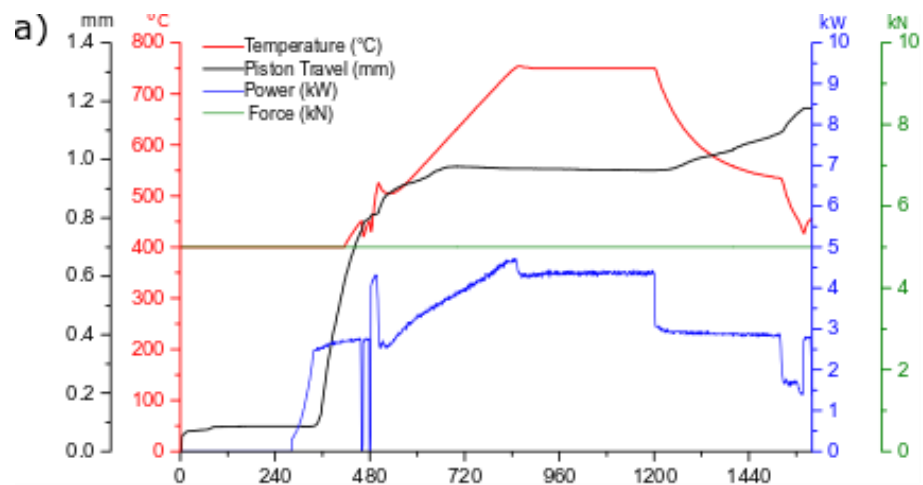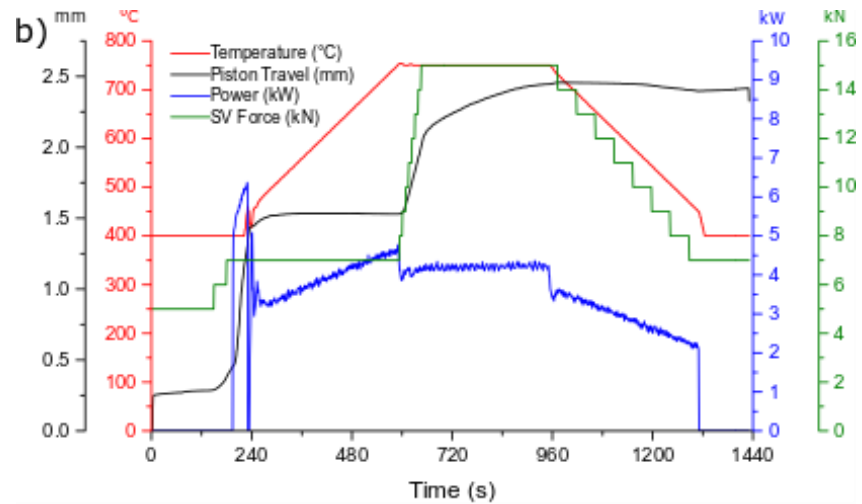
Figure 5.1 *Processing plot for a) SPS-L and b) SPS*

The floating power seen in SPS-L (Fig 5.1-a) is a common feature observed when predicted temperature value and measured value from pyrometer are quite different. More importantly, the piston travel, after some variation due to power spikes, reached an almost stable value at 750 °C and started to increase during cooling. The reaction was happening during the high temperature holding but it may have begun at lower temperatures. A similar situation occurred for the SPS sample (Fig 5.2-b), piston travel almost stabilized at 750 °C and then a further shrinkage was induced when the pressure was applied which indicated a subsequent densification of the sample. Although the piston seemed to keep traveling (Fig 5.1-a) at the end of dwell period, this was probably an artefact due to creeping of material caused by a small flow of the material on the side of the walls. The total processing time for both samples was more than 20 minutes, with an average power dissipation of 3.27 KW for 1393 s (1.27 kWh) in SPS-L and 3.7 kW for 1125 s (1.15 kWh) in SPS.
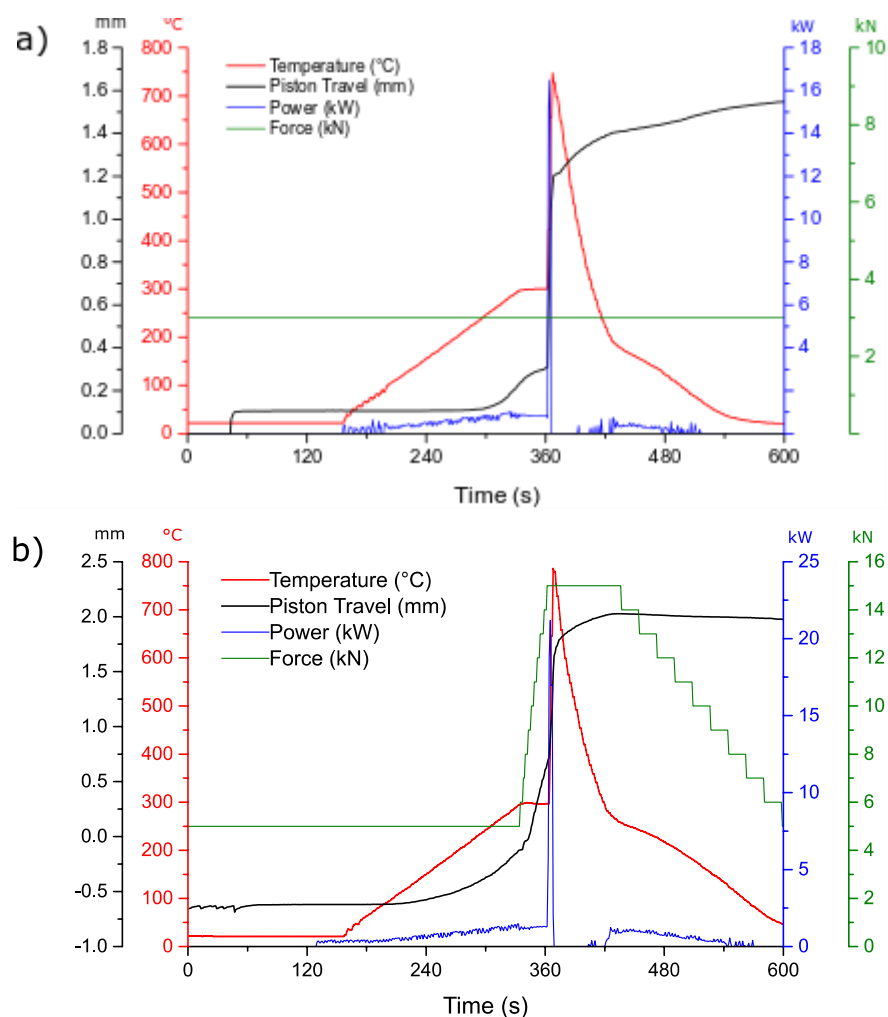
Figure 5.2 *Processing plot for a) hFSPS-cool-L and b) hFSPS-cool*

For the hFSPS-cool-L sample (Fig 5.2-a) there was a power spike at the beginning that quickly raised the temperature up to 300 °C and then the sample cooled down to follow the set heating ramp. There was no reaction during this stage, as determined from the XRD data (Fig 5.4). The sample piston travel reach a value stable up to the end of the low temperature dwell period. HFSPS-cool sample (Fig 5.2-b) did not reach a stable value as no power spike occurred during the first heating stage and the further increase in piston travel during the low temperature dwell was due to the application of increased pressure. A 3 s power pulse of higher power was then applied (about 17 kW for hFSPS-cool-L and about 21 kW for hFSPS-cool), which produced a heating rate of about 9000 °C /min. During this pulse the piston displacement suddenly increased evidencing the occurrence of a flash event. The cooling rate after the flash event was about 500 °C /min and slightly decreased when the average temperature

105

reached 200 °C. This suggest the cooling rate is mostly related to the tooling materials, rather than other parameters. The total processing time was less than 10 min with an average power dissipation of about 0.93 kW for 271 s (0.07 kWh) for hFSPS-cool-L and 1 kW for 339 s (0.09 kWh) for hFSPS-cool, less than a tenth of what used for the SPSed samples.
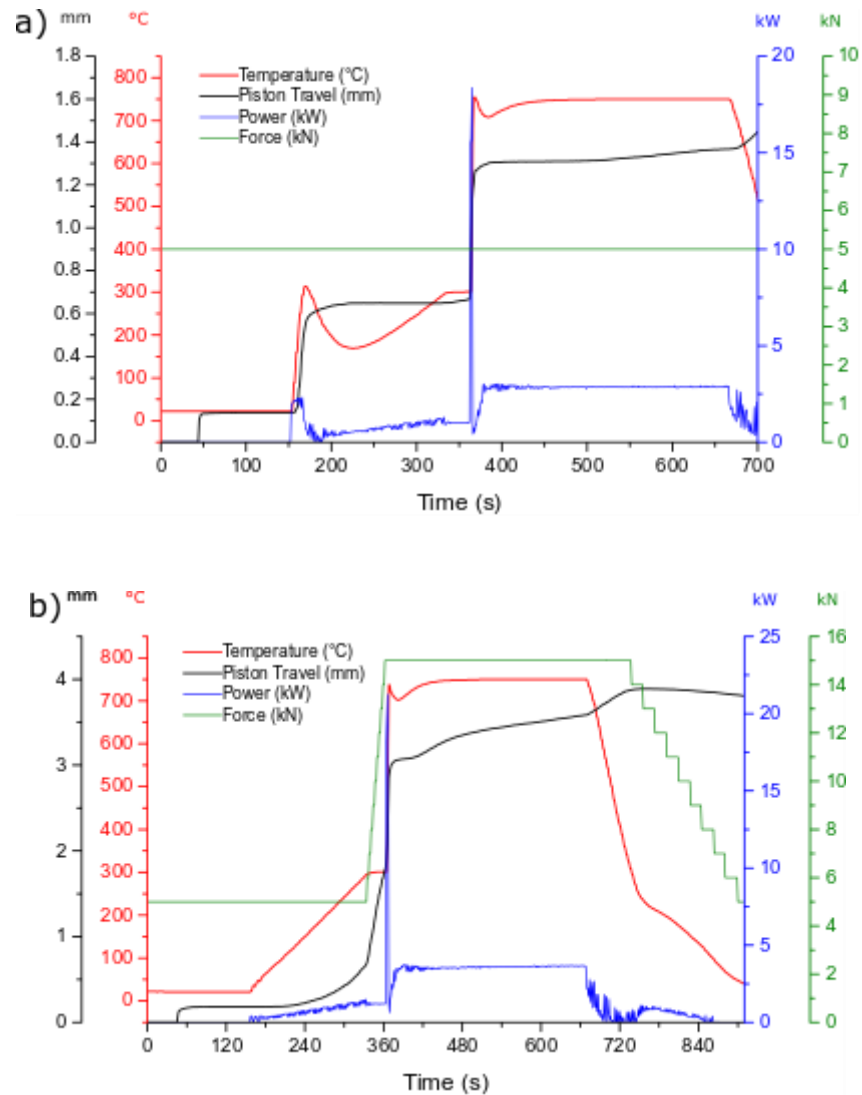
Figure 5.3 *Processing plot for a) hFSPS-hold-L and b) hFSPS-hold*

When the high temperature dwelling was used, as it would be expected, the behaviour is similar to the hFSPS-cool counterparts until the high temperature dwelling was applied. The initial drop after the pulsed power/heating, happening both in hFSPS-hold-L (Fig 5.3-a) and hFSPS-hold (Fig 5.3-b) was due to the difference

between cooling rate and power supply response leading to a quick cooling before the equipment could restore the temperature. The hFSPS-hold sample showed a different piston travel behaviour, during the dwell period the sample displacement kept increasing, this was probably due to material flowing into the gap between graphite foil and die. The total processing time was still shorter than SPS with an average power dissipation of about 2.17 kW for 558 s (0.34 kWh) in hFSPS-hold-L and 2.08 kW for 683 s (0.4 kWh) in hFSPS-hold (hFSPS-hold-L did not record the full set so the data are slightly underestimated).

XRD analysis (Fig 5.4) showed that the reaction occurred in both processing techniques with similar conversion rate (Tab 5.1) and it did not start at 300 °C where the peaks are practically unchanged from the original powders, which are composed by Sb and Co/Ni (overlapping peaks).
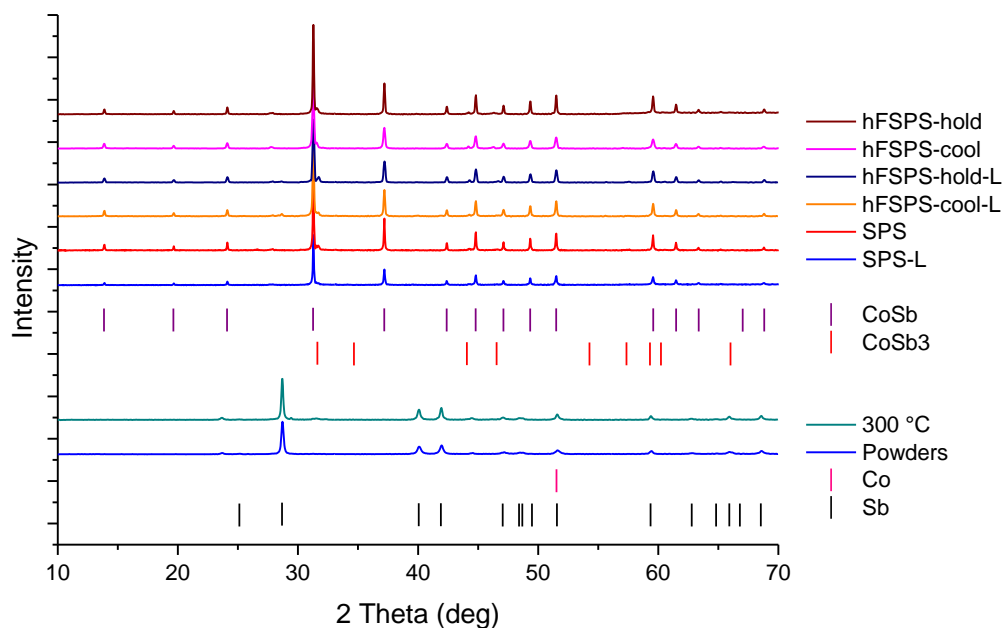
Figure 5.4 *XRD pattern of obtained samples and peak position for reference phases*

The main phase in the sintered samples was identified as Skutterudite (PDF card 47-1769),while the second phase was identified as a CoSb/NiSb, which have almost

corresponding peaks [206] (PDF card 03-065-1899 and 03-065-0835) and complete solubility . The presence of a second phase can be related to phase diagram (Fig 5.5-a-b) where the CoSb₃ is the η phase [68]. The small window at which there exists as single phase is highlighted by a blue square. Minimal variation of composition within the sample can shift the equilibrium to produce precipitation of the Υ phase, a solid solution of NiSb and CoSb. This has been observed for example by Katsuyama et al [54], while other authors such as Kim et al [62] showed the precipitation of ζ (Co,Ni)Sb₂.
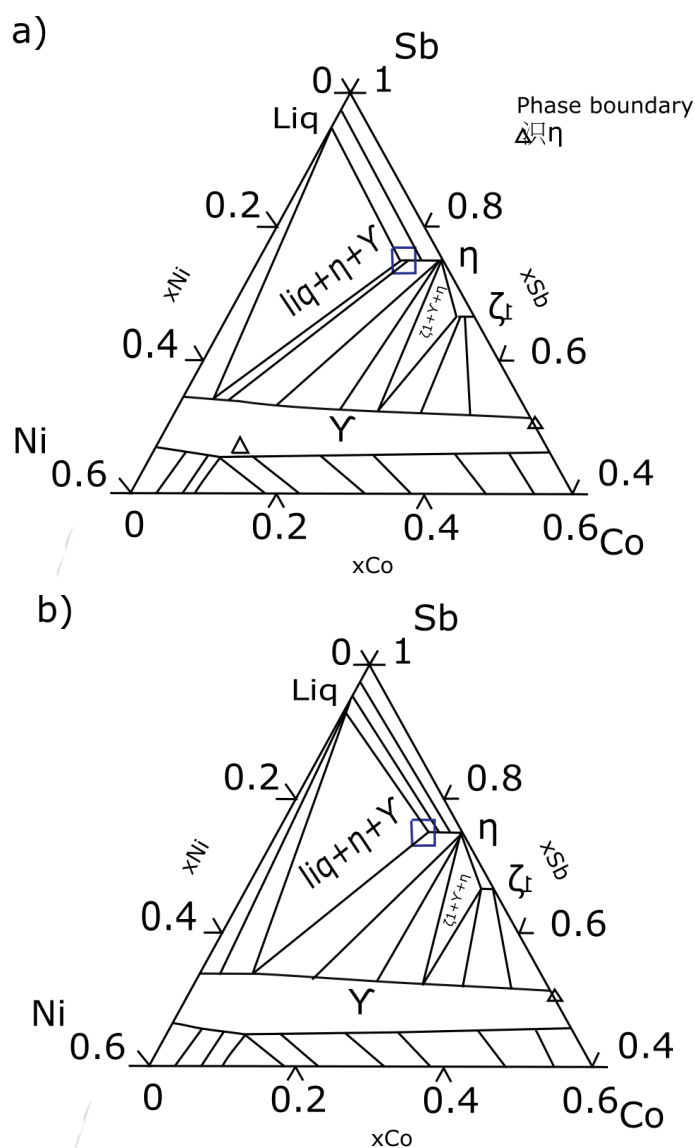
Figure 5.5 *Phase diagram of Co-Ni-Sb, adapted from [68] a) 650 °C b) 750 °C Blue square evidence the η phase (Ni-CoSb₃)*

Measured and relative densities are shown in Tab 5.1, as expected higher pressure produced denser samples, but all the sample have extremely close values. Samples sintered at low pressure showed a lower density, but both the samples flashed at the same pressure had a similar value. Phase refinement was performed on the samples sintered at high pressure (Tab 5.1)

Table 5.11 *Densities and composition of studied samples. Theoretical density is taken from [207]*

Sample name	Density g/cm3	Relative Density	Main phase %	Second phase %
SPS-L	6.95	91.2	/	/
SPS	7.35	96.4	91	9
hFSPS-cool-L	6.7	87.9	/	/
hFSPS-cool	7.335	96.2	93	7
hFSPS-hold-L	6.8	89.2	/	/
hFSPS-hold	7.377	96.7	86	14

The thermoelectric properties for all the samples were measured up to 550 °C, except for the hFSPS-hold samples, which was damaged after reaching that temperature and further measurements were done up to 450 °C.
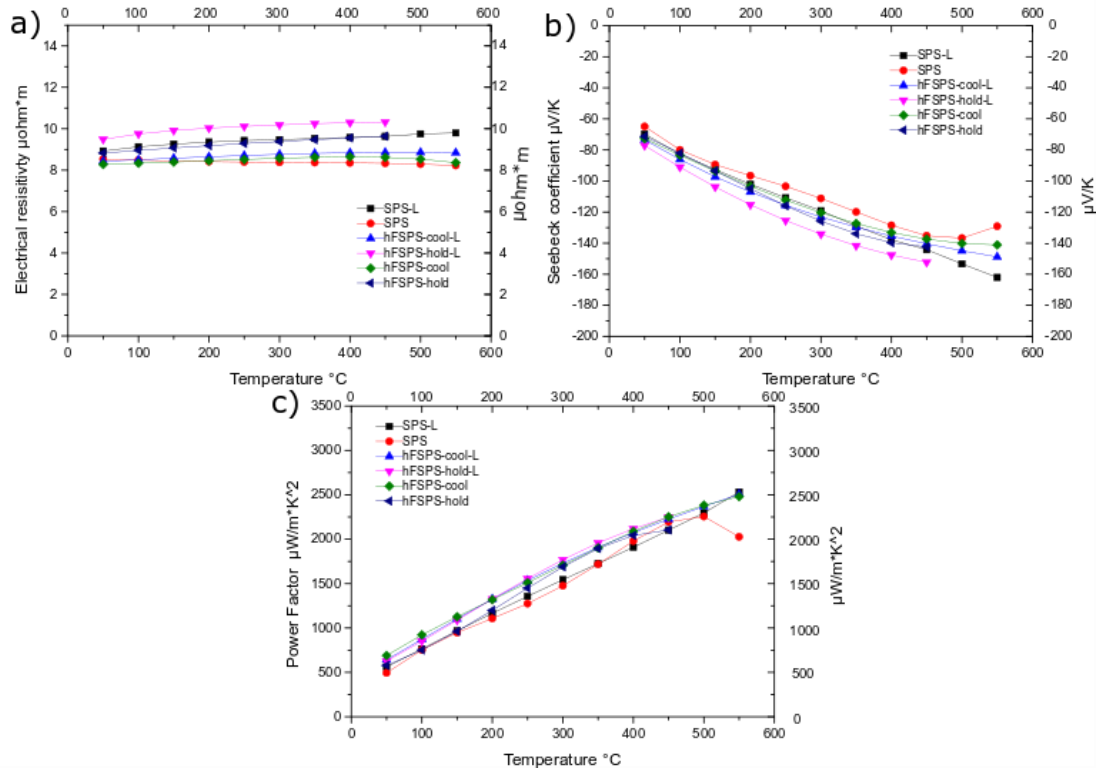
Figure 5.6 *Temperature dependence of a) Resistivity b) Seebeck coefficient*

c) Power factor

Undoped $CoSb_3$ is a p-type semiconductor (Fig 5.6 a) and the Seebeck coefficient of all the samples were negative (Fig 5.6-b), which indicates the effective introduction of Ni into the lattice [54]. The curves had similar trends and approached a maximum at higher temperature. The SPS sample was an exception as its value dropped at 550 °C, while the SPS-L sample kept increasing in the measured range. The highest Seebeck coefficient was shown by the hFSPS-hold-L sample (-80 to -150 µV/K) while the hFSPS-hold sample had a slightly lower values at all temperature (-71 to -141 µV/K). A similar variation was seen between the hFSPS-cool-L (-73 to 149 µV/K) and hFSPS-cool samples (-70 to 143 µV/K) evidencing a minor effect of pressure during processing. A different behaviour was shown by the SPS and SPS-L samples, which showed a similar trend up to 450 °C (-64 to 135 µV/K vs -69 to -139 µV/K), which was the peak for SPS while SPS-L kept increasing. The average values were consistent with the literature [54, 56]. Resistivity values (Fig 5.6 a) showed a similar trend, the SPS sample had a nearly constant value, with no drop at 550 °C, and showed the lowest resistivity (about 8.4 µohm*m). While both the hFSPS-cool and

hFSPS-cool-L samples, despite their lower density, had slightly higher and similar resistivity respectively (8.2 to 8.6 µohm*m and 8.4 to 8.85 µohm*m). Similarly to the Seebeck values, the hFSPS-hold sample showed a higher resistivity (8.8 to 9.6 µohm*m at 450 °C), comparable to the low density SPS-L (8.8 to 9.8 µohm*m) and lower than the hFSPS-hold-L sample (9.4 to 10.3 µohm*m at 450 °C). The variation of electrical properties did not influence significantly the corresponding power factor (Fig 5.6 c), all peak at about 550 °C at close to 2500 µW/m*K^2 with a variation of less than 50 µW/m*K^2, except for the SPS sample which showed a significant drop due to its lower Seebeck coefficient. The processing conditions did not have a strong impact on the electrical properties, but it was more significant on the thermal conductivity.
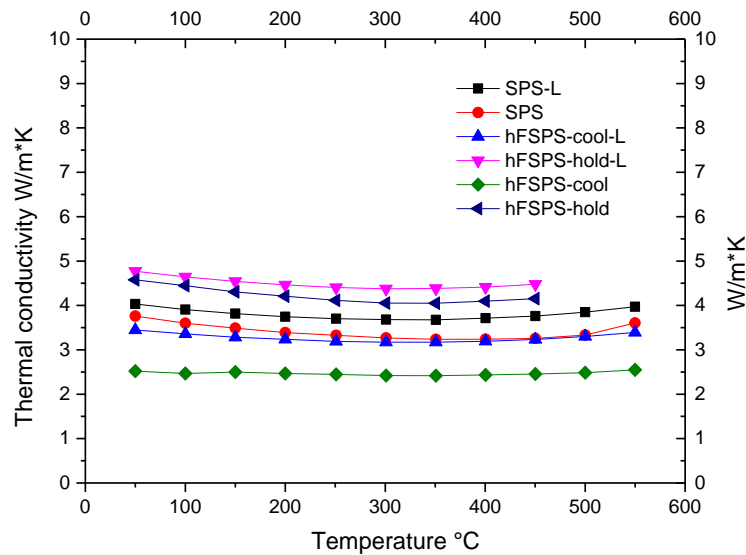
Figure 5.7 *Total thermal conductivity*

It is known that Ni can reduce the thermal conductivity of CoSb$_3$ even though with different degree of success [54, 62, 67, 69] from a high value of 10 W/m*K [207].

The thermal conductivity (Fig 5.7) of the hFSPS-cool sample reached an almost temperature-independent value of 2.5 W/m*K, much lower than that of the hFSPS-hold (>4 W/m*K) and SPS (>3.2 W/m*K) samples having the same density. A similar relationship exists between the low-pressure samples, the hFSPS-cool-L sample had a conductivity lower than that of the SPS-L sample, the hFSPS-hold-L sample showed the highest thermal conductivity. Interestingly the value measured is close to that of the SPS sample.

It is useful to separate the different contributions to the thermal conductivity as it can help to understand the origin of any changes in the thermal conductivity. The lattice contribution can be calculated by subtracting the electronic contribution from the total thermal conductivity. The electronic contribution can be calculated from electrical conductivity through the relationship:

$$k_e = \quad L\sigma T \qquad\qquad 5.1$$

Where L is the Lorentz factor, σ is the electrical conductivity and T is the absolute temperature. The Lorentz number is often considered as a constant value of $2.44 \times 10^{-8} W\Omega K^{-2}$. This value is true for most of metals and degenerate semiconductor, but in other cases it will produce an underestimation of k_{lat} and in some case even an impossible negative value [208].

The Lorentz factor was therefore calculated as suggested by Kim et al.[209], using the relationship:

$$L = 1.5 + \exp\left(\frac{|S|}{116}\right) \qquad\qquad 5.2$$

Where L is in $10^{-8} W\Omega K^{-2}$ and S in $\mu V/K$. This approximation is rather good when acoustic phonon scattering is the main mechanism and in the absence of a parabolic band. The deviation for such complex system can be as high as 25% for $ZrNiSn_{0.99}Sb_{0.01}$ as calculated by the authors, but much smaller than using the value for the degenerate limit.

The Lorentz number calculated using eq. 5.2 was used to evaluate k_e using eq. 5.1 (Fig 5.8-a), the lattice thermal conductivity was therefore calculated as the difference between k and k_e and is shown in Fig 5.8-b.
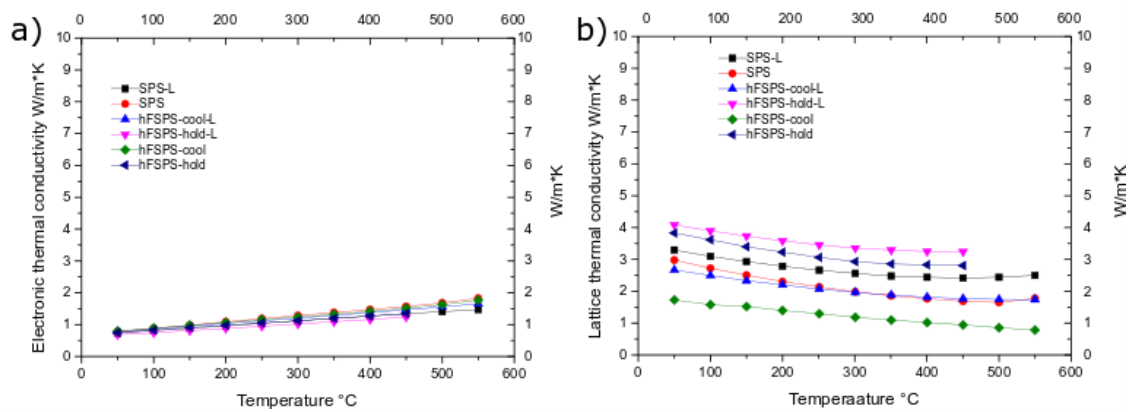
Figure 5.8 a) Electronic thermal conductivity b) Lattice thermal conductivity

As would be expected from the measured resistivity, there is not a significant difference between the electronic conductivities and they all increase with temperature, therefore the variation of total thermal conductivity has to be related mostly to lattice conductivity.

The hFSPS-cool sample showed the lowest lattice conductivity, which went from 1.75 to 0.75 W/m*K at high temperature, while the hFSPS-cool-L and SPS samples had similar lattice contributions (2.7 to 1.75 W/m*K and 3 to 1.7 W/m*K). It is clear that the processng condition (fast heating and cooling) had a significant influence, as both hFSPS-cool samples, showed better properties than their SPS counterpart. On the other hand, it is also evident the detrimental effect of the high temperature dwell period, as both of the hFSPS-hold samples had significantly higher *k* and *klat*.
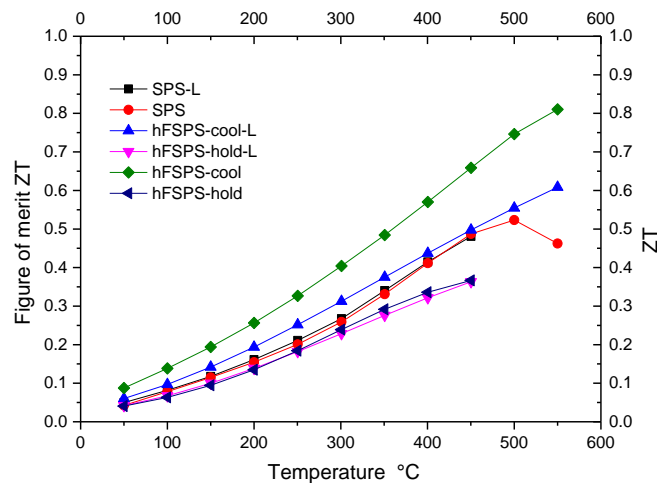
Figure 5.9 Figure of merit

The effect of hFSPS on thermal conductivity had a positive effect on the figure of merit (Fig 5.9), in particular the hFSPS-cool sample showed the highest ZT (0.81 at 550 °C), followed by the hFSPS-cool-L and SPS samples, which had rather similar values except at 550 °C (0.6 vs 0.46). The SPS-L had a slighly lower ZT of 0.54. Both of hFSPS-hold samples had almost the same ZT through all of the temperature range and reached 0.34 at 450 °C.

Microstructural analysis was conducted on the high pressure samples (hFSPS-cool, hFSPS-hold and SPS).This was because they all had similar densities and

therefore the difference in k_{lat} could be related to some microstructural differences as the porosity would have had a similar effect(Tab 5.1).

The starting powders were a mixture of particles of different sizes, Ni/Co large partices of about 10-20 µm and finer particles below 5 µm (Fig 5.9–a). Low magnification images of the hFSPS-cool sample (Fig 5.10-d) showed unusual regions, where high aspect ratio grain are twisted to form a spiral (see arrows), while other grains are below 1 µm in size. These grain had smoother corners, which might imply the presence of nanoporosity at the triple points. The origin of these spiral was probably due to the large Ni/Co particles; during the reactive sintering the Sb can diffuse or dissolve into them.The diffusion can induce the growth of columnar grains towards the center. The large grains areas (arrowed region Fig 5.10 b-e), which look to have originated from the spiral grains, probably grew during the high temeperature dwell periods during the processing. The average grains size was also increased in both samples (1-2 µm in SPS Fig 5.10- c), while the grains shape of the SPS samples presents sharper corner and defined faces. It was not possible to identify the position of the second phase. It was probably too smal to be identified at the SEM magnification and the beam volume interaction makes the use of EDS not reliable for sub-micron and nanoscale inclusion.
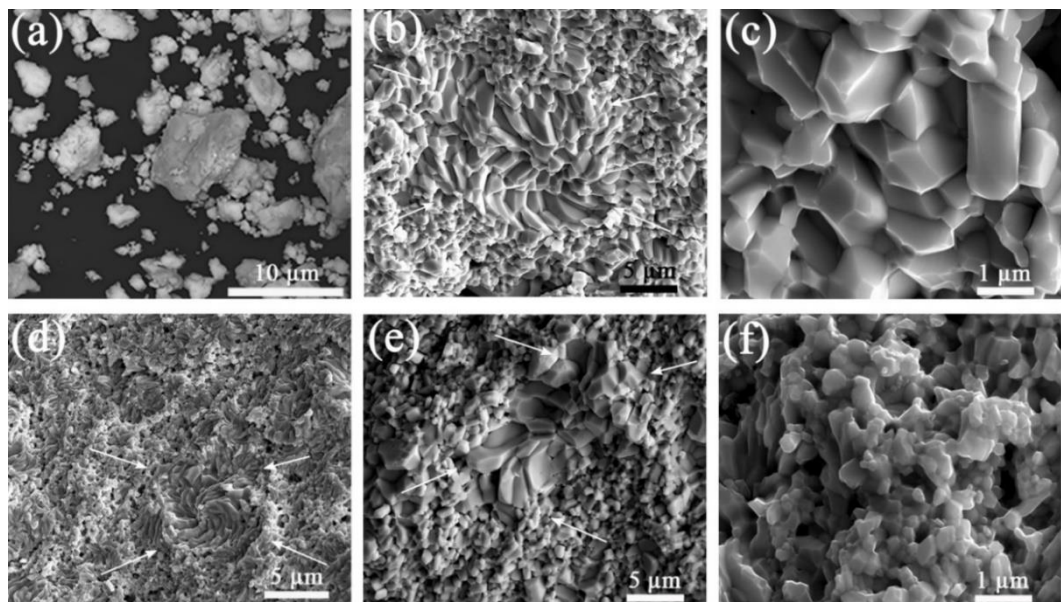
Figure 5.10 *SEM images of a) elemental powders b) and c) low and high magnification of SPS fracture surface, d) and f) low and high magnification of hFSPS-cool e) low magnification of hFSPS-hold. Arrows indicate spiral and large grains areas.*

To further investigate the microstructures, polished cross-sections where prepared, here grains boundaries results weakaned and SEM images showed a high degree of porosity on the surfaces (Fig 5.11-a-b-c) which actually made it more difficult to interpret the microstructure as the observed density was much lower than the measured one.
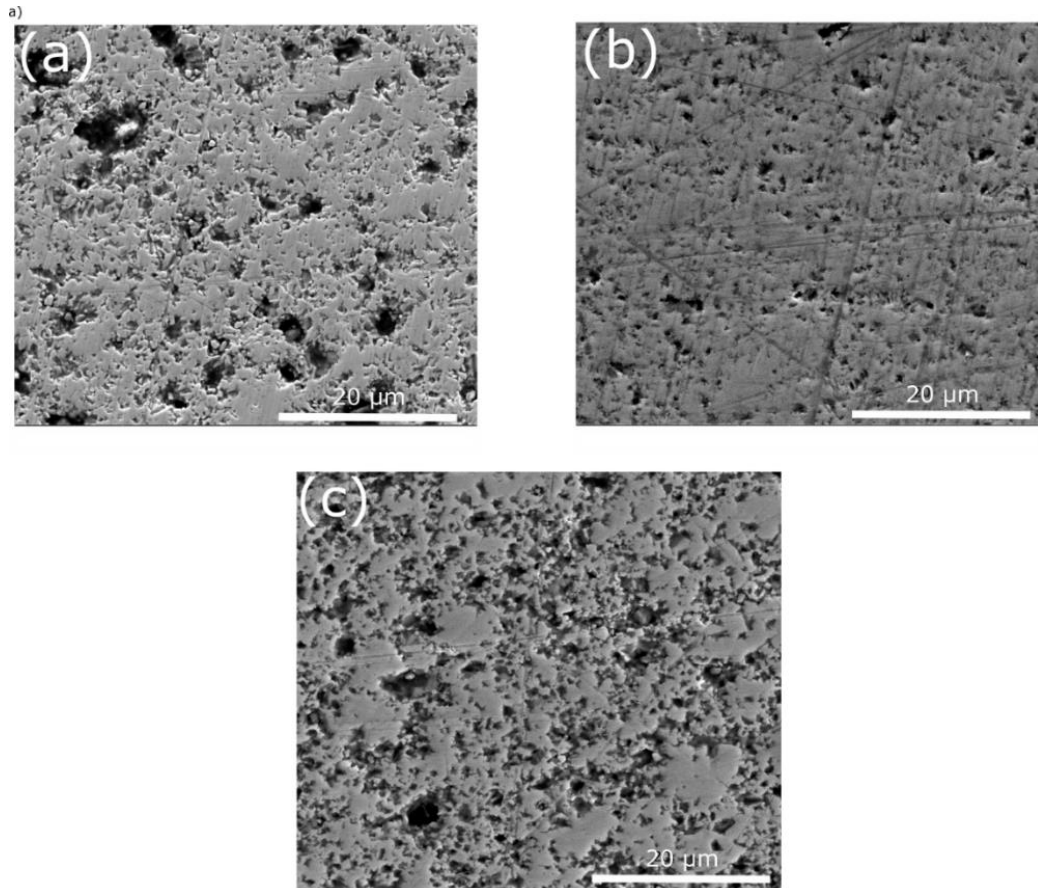
Figure 5.11 SEM cross section images of a) SPS b) hFSPS-cool c) hFSPS-hold

The origin of this fake porosity was unclear, but probably related to weaker grain boundaries, which caused the removal of grains during the mechanical polishing. To confirm that this effect was present only on the surface and the porosity seen was not real, we prepared a Focused Ion Beam section to remove a few microns of surface and observe a deeper section. The surface after milling did not show the same level of porosity and looks closer to the measured density (Fig 5.12).
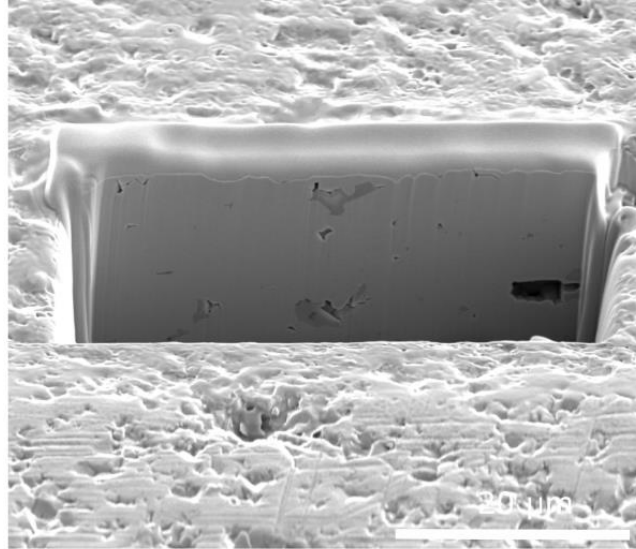
Figure 5.12 FIB section of SPS

Second phases, grain size and porosity can influence the grain cohesion. The three samples showed different amounts of damage, the hFSPS -cool sample had smaller "pores", while the other samples showed more and larger "porosity". The hFSPS-hold sample was also mechanically poor as cracks were visible along the surface, as seen during electrical measurements since the sample did not survive the full range of temperature. This could be due to the microstructural differences observed previosuly on the fracture surfaces, the hFSPS-cool sample had smaller grains with smooth corner, smaller spiral regions and smaller amounts of second phase.

5.4 Conclusion

Polycristallyne samples of $Ni_{0.15}Co_{0.85}Sb_3$ were sintered using hybrid Flash-SPS and SPS at different pressures. The SPS-processing data were analyzed. The densities of all of the samples were measured and similar value were obtained for the samples prepared with high pressure processing. All of the samples presented a main skutteruite phase, and calculations performed on high pressure samples showed an higher conversion rate in the hFSPS-cool samples. The thermoelectric properties were analyzed and minor variations were observed in resistivity and Seebeck, but with no substantial changes in the overall power factors. A significant reduction in thermal conductivity was observed in the hFSPS-cool and hFSPS-cool-L samples, which was dramatically lost for sample prepared with dwell at high temperature. Such reduction has to be mainly related to the suppression of lattice contribution since the electronic part appear almost unchanged. It is not possible to strictly relate the lattice thermal conductivity with some specific feature of the samples, but microstructural differences were observed between the hFSPS-cool, hFSPS-hold and SPS samples, which probably had a sinergic effect. The highest figure of merit was obtained for hFSPS-cool (0.81 at 550 °C).

Chapter 6 Hybrid Flash-SPS of Chalcopyrite

6.1 Introduction

Chalcopyrite is an interesting material for thermoelectric applications, in particular because of its inexpensive components and the natural occurrence as a mineral. It also exhibits magnetic properties, which are of particular interest from a theoretical point of view. However, limited work has been done on this particular composition for thermoelectric applications, particularly the Zn-doped composition. However, the Cu-Fe-S system represents a challenge because compounds in the system can have a wide variation in stoichiometry on all sites and have the potential for sulphur loss during processing.

Fast heating and cooling was used in this work in an attempt to reduce the amount of sulphur loss during the sintering process, as it should have reduced the high temperature exposure that is linked to the decomposition.

Samples of composition $Zn_{0.05}Cu_{0.95}FeS_2$ were sintered in collaboration with Tsuji et al [108] using a novel processing technique called hybrid-Flash SPS (details in chapter 3). Samples were not subjected to a post-sintering annealing in an attempt to reduce the processing time typically required for these materials.

6.2 Experimental setup

In this work, Chalcopyrite powders were processed using different techniques/conditions, due to its complicated phase diagram and the effect of stoichiometry these different techniques produced samples with very different properties. All of the samples in this work were made from powder supplied by Prof.Takao Mori group and prepared using a solid state reaction process [108, 116, 178].

All of the samples were sintered using an SPS furnace. The baseline sample was sintered by conventional SPS at a temperature of 500 °C (773 K) and a pressure of 40 MPa (this sample was labelled SPS) [108]. Two further samples were made by hybrid Flash-SPS, one was sintered from fresh powder at 600 °C (label hFSPS-1), a second one was sintered twice (sintered-crushed-resintered) at the same temperature (label hFSPS-2). Sample were produced with 15 mm diameter.

The processing conditions used were found by trial and error, with the flash time (and resulting temperature) progressively increased until a high density was reached. For the hFSPS samples, the temperature was recorded at both the upper and lower punches in order to better control the homogeneity of the samples and further confirm the reliability of the modelling performed in chapter 4. For the SPS samples, the temperature was controlled using a single thermocouple placed in the wall of the die. Thermocouples have the advantage of recording temperature from room temperature unlike the pyrometers that are only accurate above 450 °C.

6.3 Results and discussion

Plot presenting data on applied force, temperature, piston travel and power dissipated were useful to understand the densification behaviour. No evidence of Sulphur loss was evident from any sample but due to the small amount of powder (1.5 g), this was not surprising. Only a 1% loss of sulphur could substantial change the stoichiometry, yet would correspond only 0.005 g.
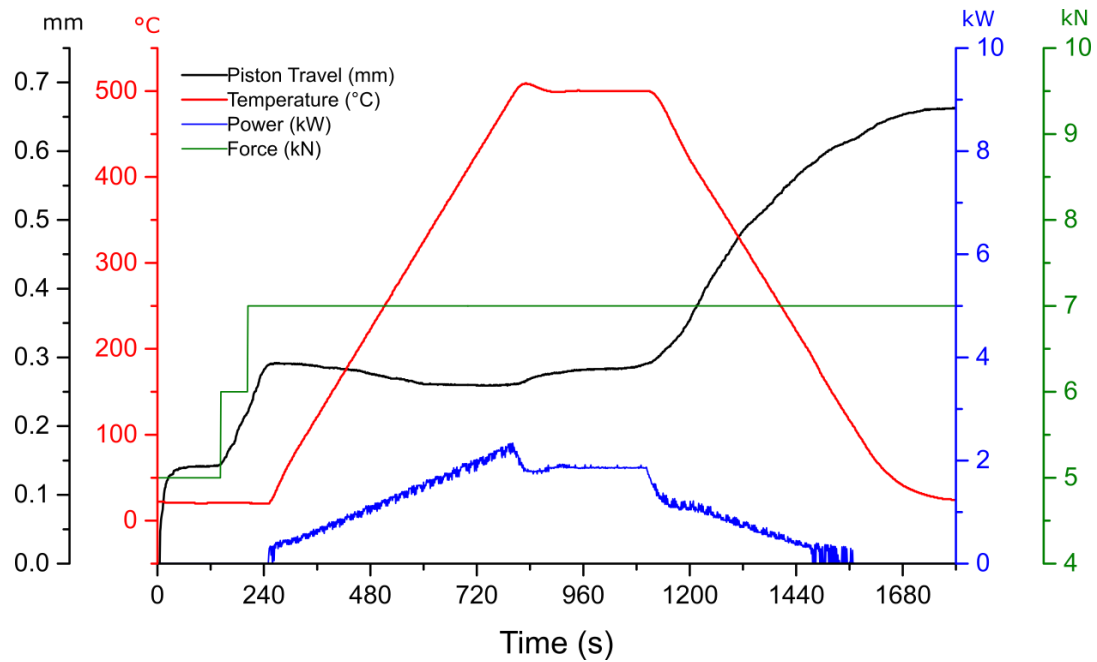
Figure 6.1 *Processing data for SPS*

SPS (Fig 6.1) had a smooth heating and cooling rate with a small overshoot at the transition to the dwell stage. This overshoot was because the PID was tuned for 20 mm and larger dies and not the 15 mm die used here.

The piston travel increased when the pressure was applied and was stable for several minute until it started to increase at the end of the dwelling process, at which point sintering occurred. The piston travel increased during cooling due to thermal contraction of the graphite tooling and sample,

The total processing time was almost 30 min with an average power dissipation of 1.23 kW for 1280 s (0.56 kWh total energy consumption).

The sintering profile of the hFSPS made from fresh powder (hFSPS-1) (Fig 6.2) was quite typical, the piston started to travel after 50 s, when the pressing stage started, and the displacement stabilized when the set pressure was constant, implying minimal densification. After the flash pulse, the sintering temperature was reached in 4 s (8700 °C /min), after which it cooled to below 200 °C (473 K) in less than 60 sec. The shrinkage appeared to be slightly delayed, which could be due to the time it took for the bulk of the sample to be heated to the softening point. The temperatures measured

at the top and bottom thermocouples were practically overlapping which implied a symmetrical temperature distribution within the sample.
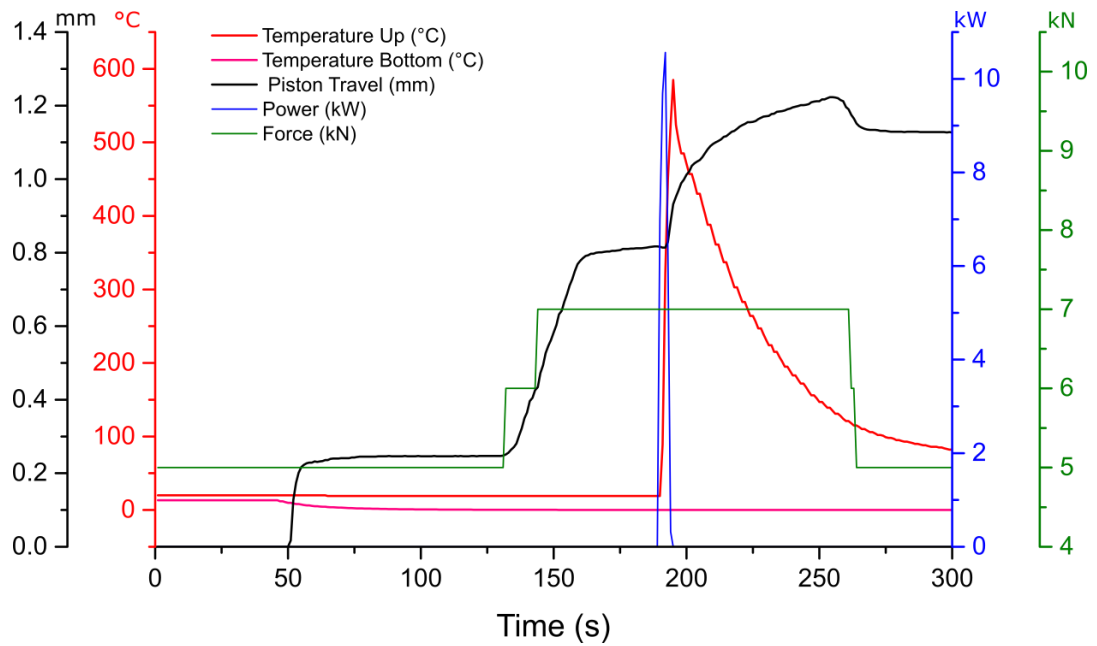
Figure 6.2 *Processing data for hFSPS-1*

The total processing time was 5 min, with average power dissipation of 8.4 kW for 4 s (0.0375 kWh total energy consumed)

Similar behaviour was observed when ground powders were processed (hFSPS-2) (Fig 6.3).
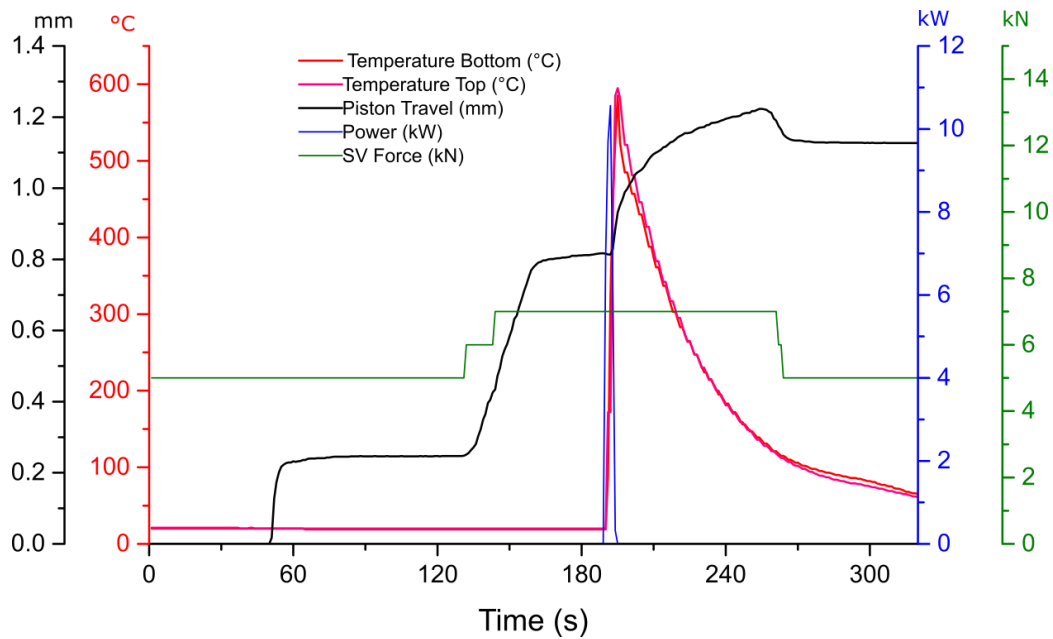
Figure 6.*3 Processing data for hFSPS-2*

For the FPSP with fresh powder and reground powder the piston travel and temperature profiles were extremely similar, the only difference was a slightly lower peak power, averaging 9.1 kW over the 4 s pulse (0.04 kWh total energy consumed).

The SPS sample had the highest density with nearly fully dense (theoretical density of CHP phase is 4.1 g/cm^3), followed by the hFSPS-2 and then hFSPS-1 samples (Tab 6.1). This was reasonable, as achieving the final pore closing step during sintering might not have had time to occur during FSPS. However, high density is normally associated with good thermoelectric performance (porosity is detrimental for electrical conductivity) but, as will be shown, this was not the case for these samples,

Table 6.1 *Table of densities*

Sample	Density	Temperature	Heating rate °C/min
SPS	99%	500 °C (773 K)	100
hFSPS-1	93 %	600 °C (773 K)	8700
hFSPS-2	97 %	600 °C (773 K)	8700

The samples were supposed to contain a single phase chalcopyrite ($CuFeS_2$) with ZnS either going into the lattice or as nano-precipitates [117]. However, there are several other related compound (talnakhite, haycockite or mooihoekite

) that have a very similar composition to chalcopyrite and even have a similar main peak in XRD [119]. The phase diagram of Cu-Fe-S contains a variety of compounds closely related that can transform between each other due to changes in pressure [118], cooling rate [210, 211] and small changes in stoichiometry. These compounds and their composition is tabulated in Tab 6.2 and the simulated XRD patterns for these compounds was plotted in (Fig 6.4) [110]. From these plots, it was clear that XRD was only of limited use in characterizing the samples produced.

Table 6.2 *Non-exhaustive list of sulphide closely related to chalcopyrite*

Name of the phase	Composition	PDF card
Chalcopyrite	$CuFeS_2$	03-065-1573
Haycockite	$Cu_4Fe_5S_8$ ($CuFe_{1.25}S_2$)	01-071-0367
Mooihoekite	$Cu_9Fe_9S_{16}$ ($Cu_{1.25}Fe_{1.25}S_2$)	01-071-0527
Talnakhite	$Cu_9Fe_8S_{16}$ ($Cu_{1.25}FeS_2$)	01-071-0527
Isocubanite	$CuFe_2S_3$ ($Cu_{0.66}F_{1.33}eS_2$)	00-027-0166
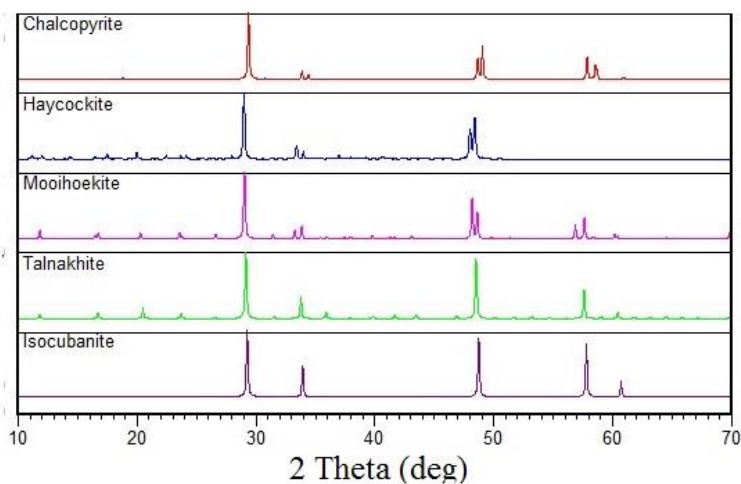
Figure 6.4 *Simulated patterns of the sulphides described in Tab 6.2*

XRD analysis could still give some information to understand the sample behaviour (Fig 6.5). Unfortunately, all of the samples had a large percenatge of iron in their lattice and iron atoms will interact with the Cu-radiation source used in the XRD equipment. This has been known to cause issues with relative peak intensites,

even hiding some peaks [212]. Different phases would be very hard to separate, as not only it was possible to have a mix of these very similar phases, but also each phase has its own stoichiometry range, which would slightly distort the peak positions (Fig 6.4).
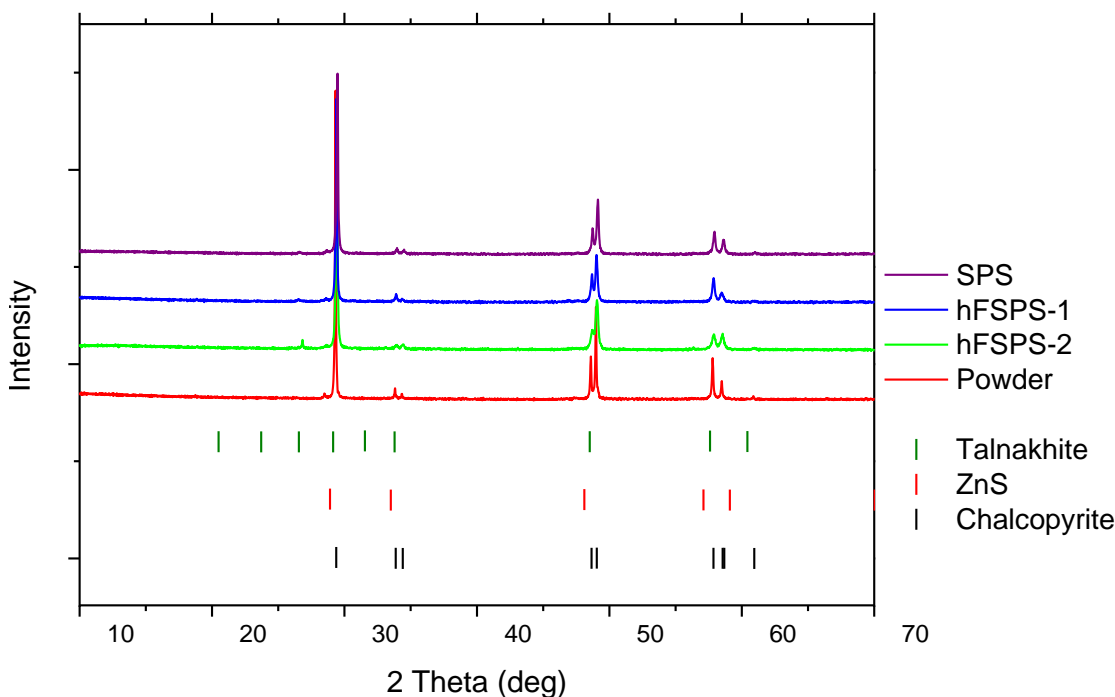
Figure 6.5 *XRD pattern of SPS and hFSPS samples, main peaks of the identified phases are evidenced*

Despite the limitations mentioned, it was clear that all of the samples produced in this work were not pure chalcopyrite (Fig 6.5). Samples likely contained talnakhite or another metal-rich compound, but it was not possible to clearly establish the relative proportions. The main peak positions of talnakhite and chalcopyrite are close; the main difference is related to the high angle peaks (around 47 and 58 degree), where chalcopyrite has a split peak due to its supercell structure. Looking at the simulated patterns for the pure phases (Fig 6.4), the peaks at 47 and 58 degree always had different heights; however, the hFSPS-2 sample did have both peaks with similar

height implying it cannot be a single phase. Traces of ZnS (PDF 65-1691) appear to be present in all samples.

The starting powder had relatively large particles with a wide distribution of sizes, which was reasonable considering the powder was obtained by solid state reaction and were not ball-milled. Some of the large particles appeared to be agglomerates of smaller grains formed during the synthesis that the grinding could not break up. (Fig 6.6-a).
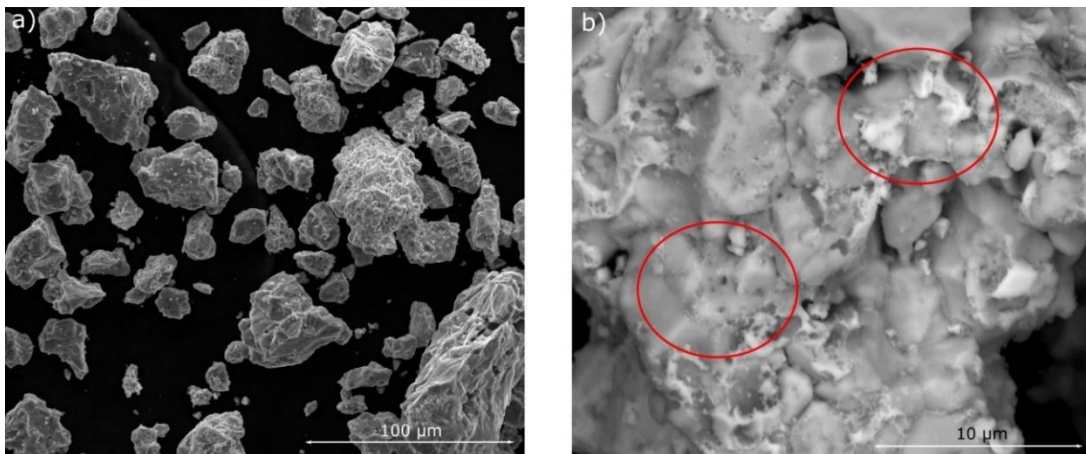
Figure 6.6 a) Secondary electron image of the starting powder b) backscattered electron image of the starting powder, brightness variation are evidenced by circles.

Backscatter imaging suggested the agglomerates might contain a small amount of second phase (Fig 6.6-b), but the contrast could have been caused by topographic changes, as even backscatter imaging is not immune to edge charging. Unfortunately, EDS could not be used be used to confirm the presence of second phases as the interaction volume was significantly larger than the region of interest.

Once sintered, the samples microstructure depended on the processing conditions, but all of the samples shared a common feature, which was a high degree of fake porosity due to grain pull-out. This was caused by the softness of the material (especially the weak intra-grain bonding) which made it difficult to obtain a representative polished cross section.

The SPS sample showed the highest level of fake porosity in SEM (Fig 6.7), but the Archimedean method showed that they were nearly fully dense. This implied the

SPS sample had the weakest inter grain bonding, which might explain why this sample had the highest electrical resistivity (Fig 6.9), as a higher degree of disorder at grain boundaries can represents an additional resistance for electrons.
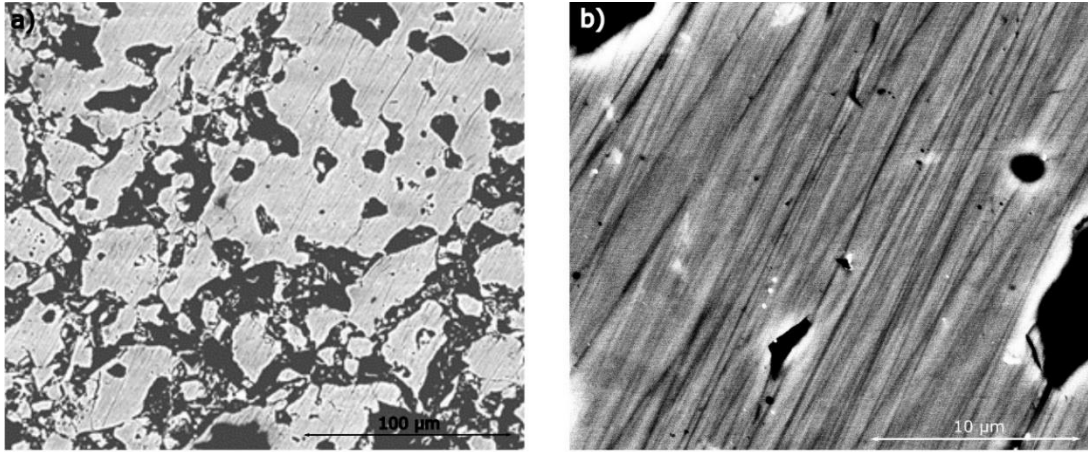
Figure 6.7 Backscattered electron image of SPS sample a) low magnification b) high magnification. Low focus is due to the high level of surface damage

It was difficult to identify any second phase in the backscattered electron images (Fig 6.7-b), also because of the damage received during polishing (see the scratches in fig b), the white particles visible in the matrix might be related to ZnS [117]

The hFSPS-1 sample was more porous (93%) than the SPS sample and still showed grain boundary weakness, as the apparent porosity was significant (Fig 6.8-a), but to a lesser extent. Backscatter imaging of the hFSPS-1 sample (Fig 6.8-c) showed several regions of secondary phase, as indicated by regions of lower contrast. This second phase was distributed homogeneously throughout the material. The second phase was only visible by a careful choice of accelerating voltage and contrast setting. This implied the two phases were very similar in composition, most likely chalcopyrite and talnakhite. In literature a similar two phase structure has been observed by Xie et al. [114] and Kitakaze et al. [118] who used different synthesis and sintering techniques.

The hFSPS-2 sample had significanlty less apparent porosity, and a slighlty higher archimedean density. The reduced fake porosity indicated a stronger grain boundary or a different distribution of second phases or stress (Fig 6.8 a-c). It was

probably related to the second sintering processing, which increased the density and mechanical strenght. The same type of two phase structure was visible in hFSPS-2
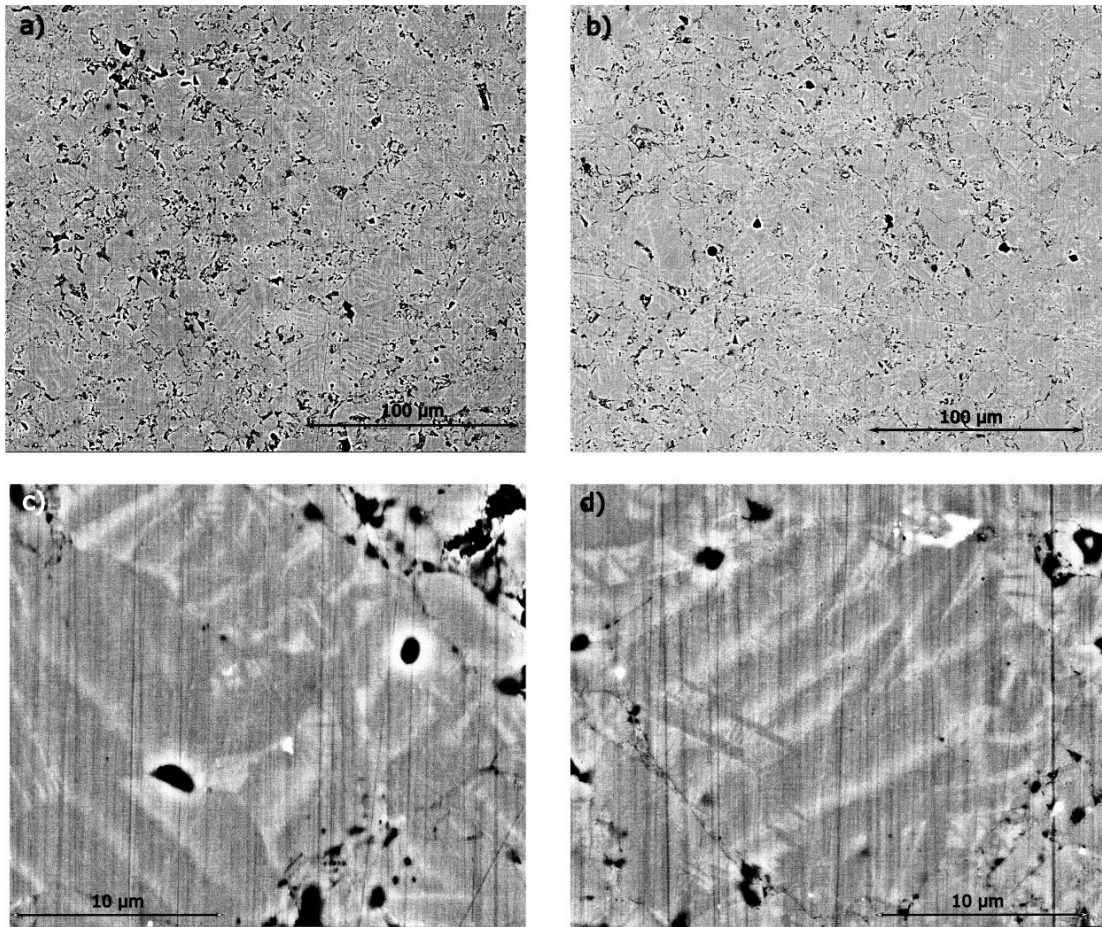
(Fig 6.8 b-d).

Figure 6.8 *Backscattered electrons images of: a) hFSPS-1 low magnification; b) hFSPS-2 low magnification; c) hFSPS-1 high magnification; and d) hFSPS-2 high magnification*

With the clear diffence in microsturcture of the different samples, it was anticipated that the samples would have very different thermoelectric performance. The SPS sample suffered an irreversible change upon heating above 523 K, while the hFSPS-1 sample was not even stable up to 475 K, only the hFSPS-2 sample was stable up to 623 K , the maximum temperature used for testing. The irreversible change in properties could have been casued by oxidation or a phase change. While the equipment was operated in helium, its atmosphere was not perfect and surface

oxidation was visible on all the samples tested as well as other samples tested by our group. While oxidation can cause irreversible changes in propertes, when the surface was reground, the properties should have recovered as the oxide layer was removed, but this did not occur in any of the chalcopyrite sample, therefore it must have been due to some phase change.

The SPS sample was measured up to 623 K and data was collected during heating and cooling (Fig 6.9-a). Because of the unexpected stability issues with the SPS sample, (Tsuji et al. [116] and Xie et al. [117] found similar compositions to be stable beyond 623 K), the hFSPS-1 and hFSPS-2 samples were first measure at a lower temperature (473 K) in an attempt to avoid instability (Fig 6.9 b-c).
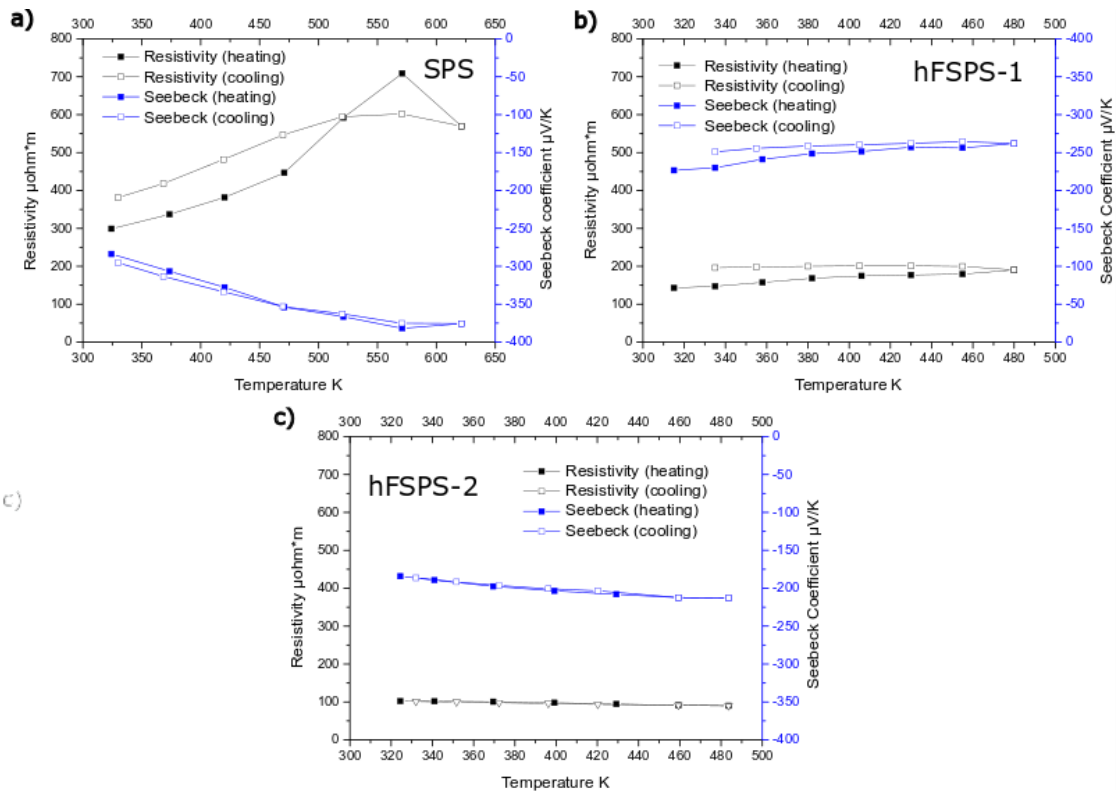
Figure 6.9 *Electrical properties of a) SPS up to 623 K b) hFSPS-1 up to 473 K c) hFSPS-2 up to 473 K*

For the SPS sample the Seebeck values during heating and cooling were very similar, which was in strong contrast to the electrical resistivity. During heating the resistivity experienced a large change in slope at 473 K, implying a sudden change in

properties. The cooling curve was shifted up, compared to the heating curve, but without the sudden change at 475 K, implying the change was irreversible.

For the hFSPS-1 sample (Fig 9-b) during heating, the Seebeck coefficient started at -225 µV/K and increased to about -260 µV/K, but during the cooling the Seebeck remained much more stable, reaching -250 µV/K at 333 K. The resistivity also showed instability, with the initial resistivity of 140 µohm*m increasing to 180 µohm*m during heating, before returning to 200 µohm*m during cooling. The cooling curve was also much flatter, implying the material was now more stable, having experienced an irreversible change upon heating, its nature is difficult to predict, but could be a chalcopyrite to talnakhite transition [110, 112, 210]. The improved inter granular bonding of the hFSPS-1 might explain the higher electrical conductivity compared to SPS (Fig 6.9-b).

The exact point of instability was not clear, but could have been 353 K. The measurement was therefore not repeated up to 623 K.

For the hFSPS-2 (Fig 6.9-c) sample the heating and cooling curves completely overlapped for both the Seebeck and resistivity, implying the sample was completely stable up to the testing temperature of 490 K. The electrical resistivity showed a small decrease with temperature (100 µohm*m to 90 µohm*m), followed by a small increase in the absolute value of Seebeck coefficient (-180 to -215 µV/K). The temperature dependence of Seebeck and resistivity were relatively flat, which tells us something about the nature of the material. The behaviour seen was very similar to that reported in literature for chalcopyrite with a mild sulphur deficiency [114], implying the hFSPS-2 sample was also deficient in sulphur. As the hFSPS-2 sample showed no degradation at 473 K, the properties were measured again but this time up to 623 K (Fig 6.10).
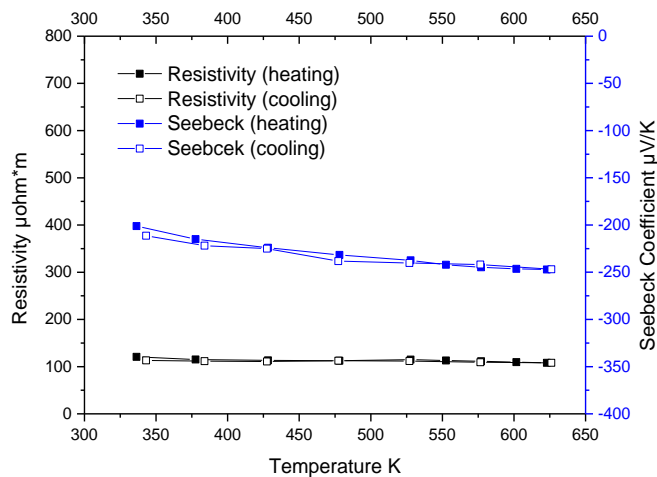
Figure 6.10 *Electrical properties of hFSPS-2 up to 623 K*

The electrical properties looked very similar to the measurements taken at 473 K (Fig 6.9-c), with only minor deviation between the heating and cooling curves near room temperature (≈5 %). This implied the hFSPS sample was functionally stable to 623 K, and by reprocessing the material the distribution of phases was changed such that the material was not only more stable, but also had lower resistivity.

The resistivity of the SPS sample (Fig 6.9-a) was much higher than the other samples. The significant weakness at grain boundaries, seen in SEM (Fig 6.7) was probably the origin of the high resistivity. It was also possible that during the long sintering time sulphur was lost from the lattice, this has been shown to be an issues with samples in literature, where post-sintering annealing steps are used to improve the properties of SPSed samples [108]. The lack of an annealing stage might also have influenced the Zn-doping level and reduced its influence on conductivity [117]. Zn doping can influence the anti-site Cu/Fe defects [117] and Li et al [115] obtained similar values for an un-doped sample produced in similar condition using only different Cu/Fe ratio.

On the other hand chalcopyrite produced by different authors showed very different thermoelectric properties, the values for room temperature resistivity shows a range of values ~300 µohm*m [114], 200 µohm*m [117], ~100 µohm*m [116, 178], ~400 µohm*m [115], 1800 ohm*m [213]. Some of these differences could be caused by processing conditions or method. However, as few authors included the data

measured during cooling it is probably that some of these differences are due to the chalcopyrite samples actually being an unstable mixture of phases.

The heating behaviour of the hFSPS-1 sample (Fig 6.9-b) was similar to doped samples in literature for both resistivity and Seebeck despite having lower absolute values [108, 117]. The difference between the hFSPS-1 and literature could have been related to loss of Zn or sulphur from the lattice [182], both of which have been shown to influence the temperature behaviour of the resistivity and Seebeck coefficient. The higher electrical conductivity of the hFSPS-1 sample was likely influenced by the lower degree of porosity and inter-granular weakness observed in SEM (Fig 6.8-a) compared to the SPS samples.
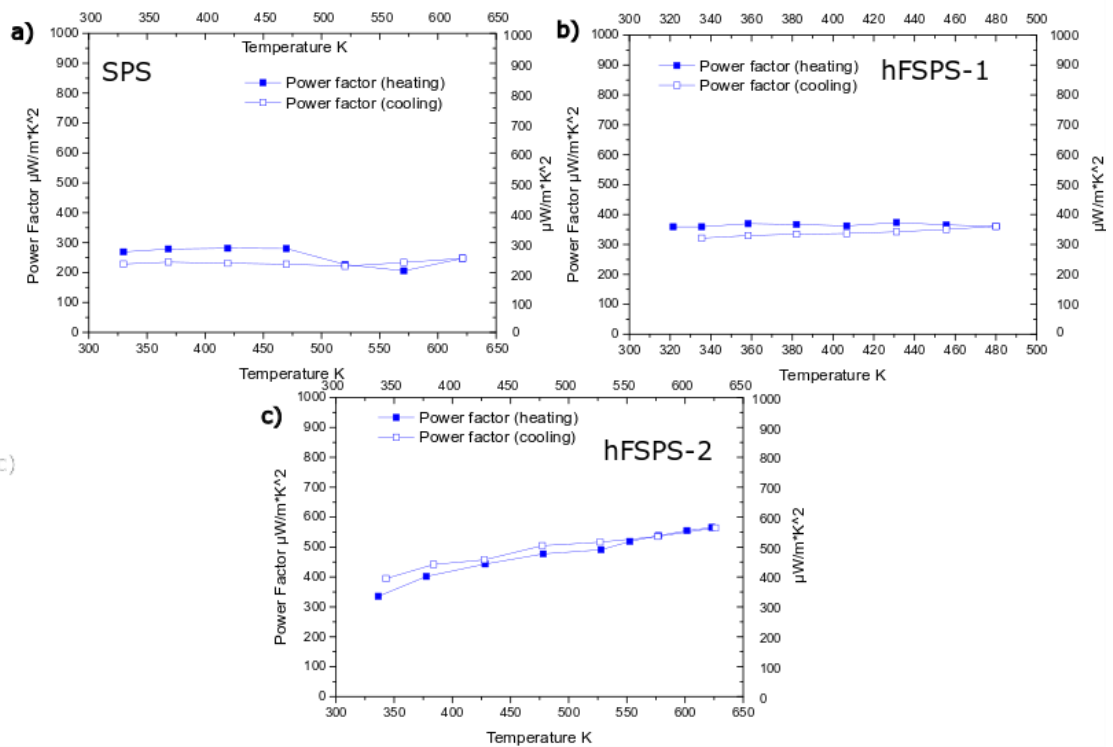
Figure 6.11 *Power factor of a) SPS b) hFSPS-1 c) hFSPS-2. Power factor of hFSPS-2 is calculated up to 623 K because the measurement was not repeated at higher temperature*

The power factor for all the sample was calculated using the heating and cooling data. Despite the instability of the electrical properties of the SPS and hFSPS-1 samples (Fig 6.9), the power factor obtained for all of the samples (Fig 6.11) showed minimal differences between heating and cooling. The SPS and hFSPS-1 samples had

similar values for room temperature Seebeck, 300 µV/K for SPS, 225 µV/K for hFSPS-1 (both from heating curve), while the hFSPS-1 increased to roughly 250 µV/K after cooling.

The power factor for hFSPS-2 has a different behaviour, with a much higher value (Fig 6.11-c), which increased with temperature, reaching a peak at 623 K of about 560 µW/m*K^2. This value was lower than that some reports in the literature [116, 117], with higher power factors at low temperature and negative slopes with increasing temperature. The samples produced in this work were more comparable to composites of talnakhite and chalcopyrite [114, 182, 213]. The most interesting result from this work was the improved stability of the rapidly processed samples, as shown by the electrical properties (Fig 6.9-c).

To calculate ZT, the thermal conductivity needs to be measured, with appreciable differences expected between samples as hFSPS has been shown to lower thermal conductivity in certain materials [175, 176, 191]. Particularly interesting was the lattice conductivity, for thermoelectric performance it is the lattice thermal conductivity that must be minimized, as electronic conductivity is unavoidable to achieve good electrical conductivity.

The thermal conductivity was measured for all of the samples up 623 K, this was to observe if the instability was intrinsic in SPS and hFSPS-1 or somehow related to the equipment. Electronic thermal conductivity was calculated using the same method introduced in Chapter 5,

$$k_e = \quad L\sigma T \qquad\qquad 5.1$$

Where L is the Lorentz factor, σ is the electrical conductivity and T is the absolute temperature. The Lorentz factor was therefore calculated as suggested by Kim et al.[209] using the relationship

$$L = 1.5 + \exp\left(-\frac{|S|}{116}\right) \qquad\qquad 5.2$$

Where L is in 10^{-8}WΩK^{-2} and S in µV/K.

In order to calculate the electronic contribution, the electrical data was used from the cooling curves (Fig 6.9), to provide a reasonable comparison between the samples. Because of the low value of the electrical contribution ($k\ el$), the lattice contribution was not shown as was practically the only contribution (Fig 6.12).
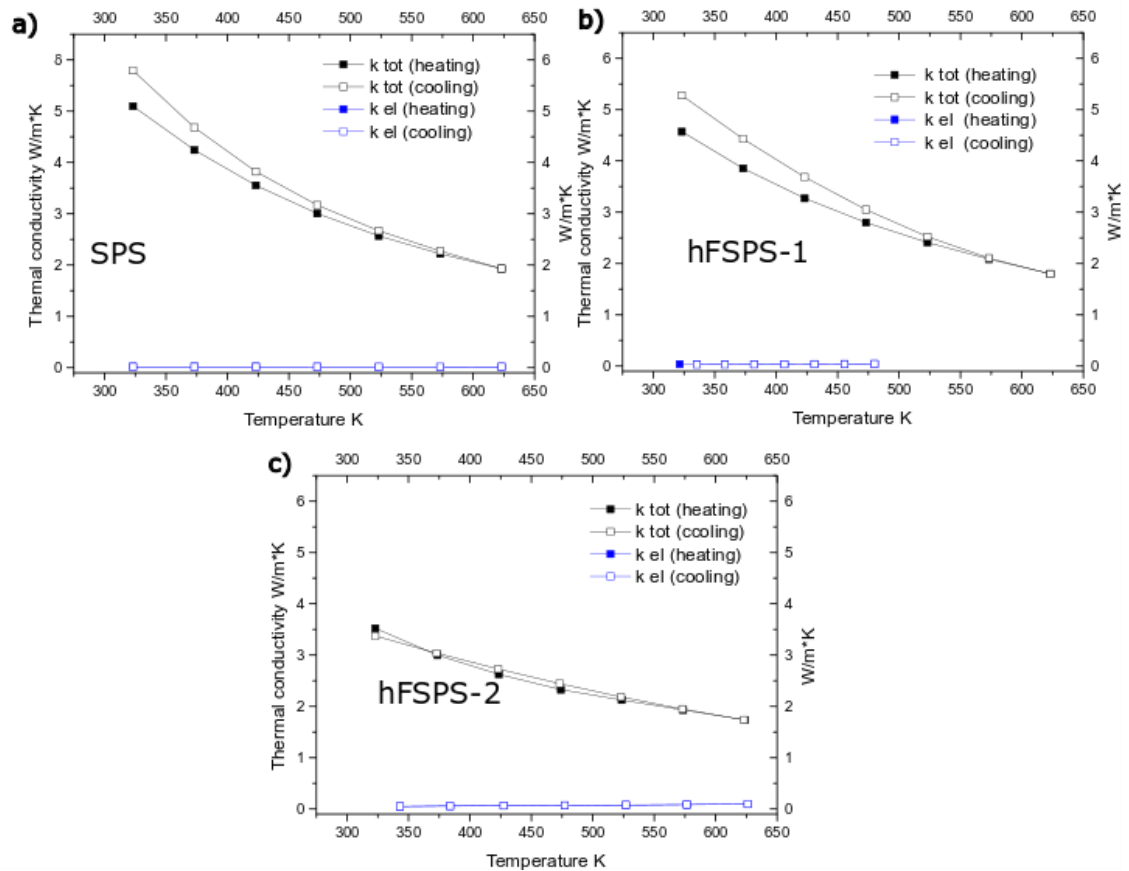
Figure 6.12 *Total thermal conductivity k (black) and electronic thermal conductivity k el (blue) for a) SPS b) hFSPS-1 c) hFSPS-2. The k el (heating) values are almost perfectly overlapped by k el (cooling) values and only a small portion of the square is visible.*

For consistency both the heating and cooling values were shown (Fig 6.12) and again only the hFSPS-2 (Fig 6.12-c) sample was stable, with no significant variation while both the SPS (Fig 6.12-a) and hFSPS-1 (Fig 6.12-b) samples showed increasing thermal conductivity during cooling.

Combining the thermal conductivity data with the electric properties, the ZT could be calculated. Again as a comparison, the power factor from the cooling curve was used and combined with both heating and cooling data for thermal conductivity.

The SPS sample had a very low ZT (Fig 6.13), with a peak of 0.08 at 623 K and was not stable above 473 K as shown in (Fig 6.9-a) and (Fig 6.12-a). The hFSPS-1

sample was only measured to 473 K due to instability but its peak ZT over the range measured was 0.056 at 453 K. The change in thermal conductivity after heating meant that the ZT was lower after cooling, (Fig 6.12-b). The best sample was the hFPS-2 (Fig 6.13) with a peak ZT of 0.202 at 623 K with a small variation in the middle range of temperature due to a minor shift in properties during heating (Fig 6.10-c and Fig 6.12-c).
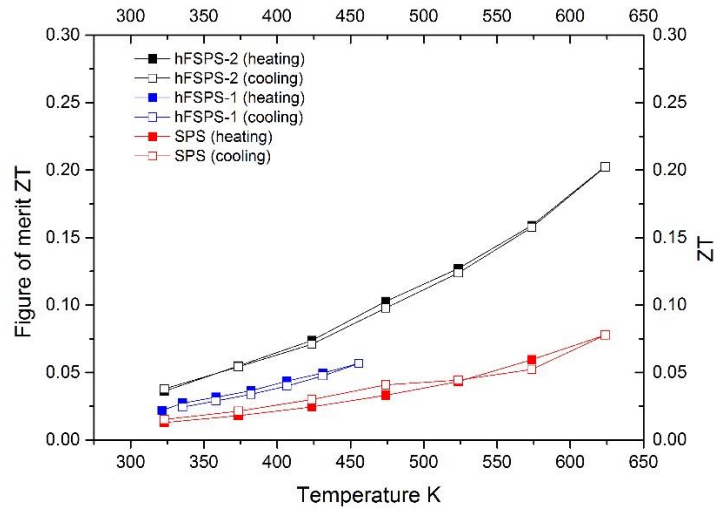
Figure 6.13 *Figure of merit of SPS,) hFSPS-1 and hFSPS-2*

6.4 Conclusion

The Cu-Fe-S system is complex and contains a variety of related compounds having similar XRD [119] patterns, and the peaks of each of these compounds can shift due to slight changes in composition [110, 118]. This does not make it easy to fully characterise the phases present and their distribution, which can be influenced by pressure [118] or cooling speed [210], and some of the proposed phases in the system have never even been synthesized [110]. From the literature, it is clear that processing had a significant effect on microstructure and composition, resulting in very different thermoelectric properties despite the same starting composition. Using rapid heating, we produced a sulphide composite hFSPS-1 (Fig 6.8 c-d). By reprocessing the material (hFSPS-2) using the same rapid heating process the density was increased, as well as the thermal stability and thermoelectric properties. The hFSPS-2 sample also had a very different power factor curve from that measured by Tsuji et al. [108, 116, 178], having a higher ZT than expected from extrapolating low temperature thermal conductivity data. With predicted values of 0.12 at 700 K [116, 178], and experimental values of 0.202 at 623 K for the same initial powders. The ZT of hFSPS-2 was also comparable to other work with pure or doped chalcopyrite [114, 115, 117, 182], in particular the results were similar to the work by Xie et al. [114], in which fast heating rate was used at the synthesis stage, not at the sintering stage. This is strong evidence that rapid heating (beyond SPS) is a powerful tool to improve the properties of thermoelectric materials.

Chapter 7 Hybrid Flash-SPS of half-Heusler

7.1 Introduction

Half-Heusler alloys have been recently discovered as interesting thermoelectric materials. Unfortunately there are several things limiting their application, and typically the best thermoelectric properties are only achieved by alloys containing expensive elements like hafnium (ZT of 1.5 at 423 °C for $Zr_{0.5}Hf_{0.5}NiSn$ [76]). In general half-Heusler alloys have a high power factor, but this does not translate to a high ZT due to their relatively high thermal conductivity.

Significant work has been done to produce half-Heuslers with inexpensive dopants, and promising results were obtained with Sb [214] (ZT 0.5 at 600 °C), Cu (ZT of 0.6 at 600 °C) [78, 79] and Nb [215] (ZT of 0.6 at 900 K), with even better results for co-doped samples such as V and Nb in $Ti_xZr_{1-x}NiSn_{0.98}Sb_{0.02}$ [77] (ZT close to 1.2 at 600 °C).

However, doping did not significantly reduce the thermal conductivity of the material, which was still 4 W/m*K or above), there is a challenge to lower the thermal conductivity by processing. It has been shown that hFSPS can lower the lattice thermal conductivity of thermoelectrics [175, 191, 216]. In the current work, we investigated the hFSPS of half-Heusler. Cu-doped TiNiSn (0.05) was chosen as reference material, having good properties for a single element doped system and it has not been extensively studied before.

7.2 Experimental setup

Powders of TiNiSn- $Cu_{0.05}$ were provided by Prof. Jan Wilhelm Bos, (Heriot Watt University), and were produced using solid state synthesis [79], followed by grinding in a mortar and pestle. Samples were processed using Conventional SPS and hybrid Flash-SPS with 15 mm dies, each samples used about 1.5 g of powder.

The sample sintered using conventional SPS temperature was sintered using similar conditions as Downie et al. [217] but the temperature was chosen based on the hot pressing of the same composition [79]. The temperature was controlled with a thermocouple placed in the die, 5 mm from the sample.

Hybrid Flash-SPS samples were produced using the same setup as in chapter 4, but the preheating stage was 400 °C before a 5 s high power pulse further flash-heated the sample. A pre-heating stage was necessary as a high-power pulse tended to produce unwanted temperature gradient, by preheating, the length of the pulse could be shortened, lessening the gradient. Temperature was controlled by a thermocouple placed in the bottom punch 3 mm from the sample. A second thermocouple was placed in the top punch again 3 mm from the sample which allowed the temperature gradient in the setup to be measured. A pressure of 80 MPa was used when sintering the hFSPS samples and 75 MPa for the SPS samples, because the graphite tended to crack during the slow heating of SPS when 80 MPa was used.

7.3 Results and discussion

The data used to describe the processing will be power dissipation, applied force, piston travel and the measured temperature at the thermocouple.

During the SPS processing (Fig 7.1) the temperature increased smoothly up to the set temperature with a small overshoot typical of the equipment and configuration. The piston travel was stable until the pressure was applied (760 s), at which point there was a rapid rise displacement (likely not densification just compression in the system during the pressure increase). At full pressure the displacement continued to increase (likely densification) until the pressure is removed. This behaviour suggested the powder was sintering mainly due to the effect of pressure, since during heating and

initial dwelling at 28 MPa (before the pressure increase) there was no displacement. In addition, as the displacement did not level off before the end of the holding stage, it was likely the sample was not fully densified. The total processing time was close to 30 min with the dissipation of an average power of 2 kW for 1376 s of heating (0.765 kWh total energy consumption).
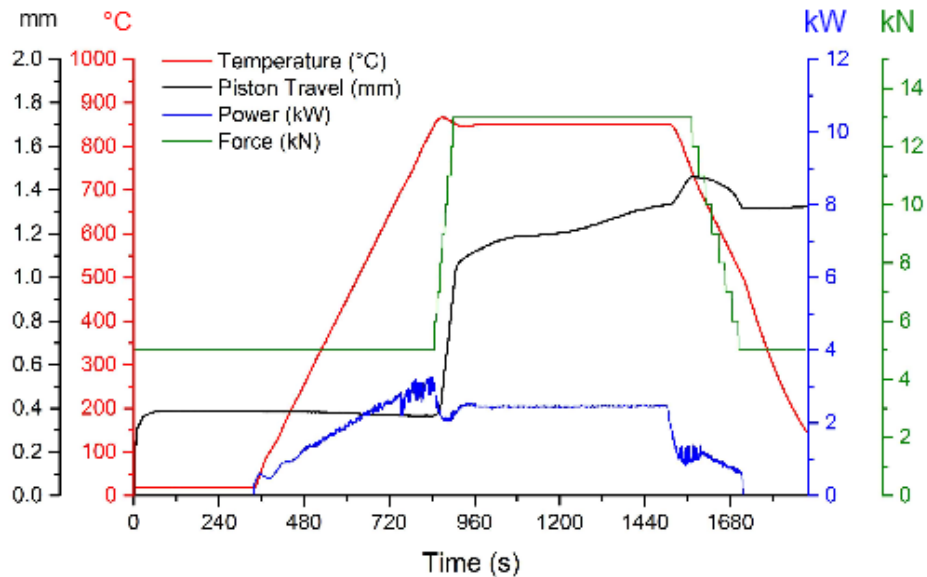
Figure 7.1 Processing plot for SPS

The hFSPS-980 sample (Fig 7.2) had an initial shrinkage during the application of pressure, which was stable during the heating and pre-holding stages. The difference between the temperature measured at the top and bottom thermocouple was due to the internal cooling asymmetry and did not depend on the sample or setup. The power pulse was applied for 5 s and was composed of a 4 s pulse at 13 kW power followed by 1s at 9 kW, this was done as the control software could not produce a 4.5 s pulse, which would have been preferable. This pulsing resulted in a heating rate of 7000 °C /min. During the pulse, the sample started to shrink, but the absence of a sharp peak in piston travel was evidence that the sintering mechanism was due to plastic flow and not just diffusion. The total processing time was about 10 min, with the dissipation of an average power of 0.66 kW for 316 s of heating (0.06 kWh total energy consumption)

138

.
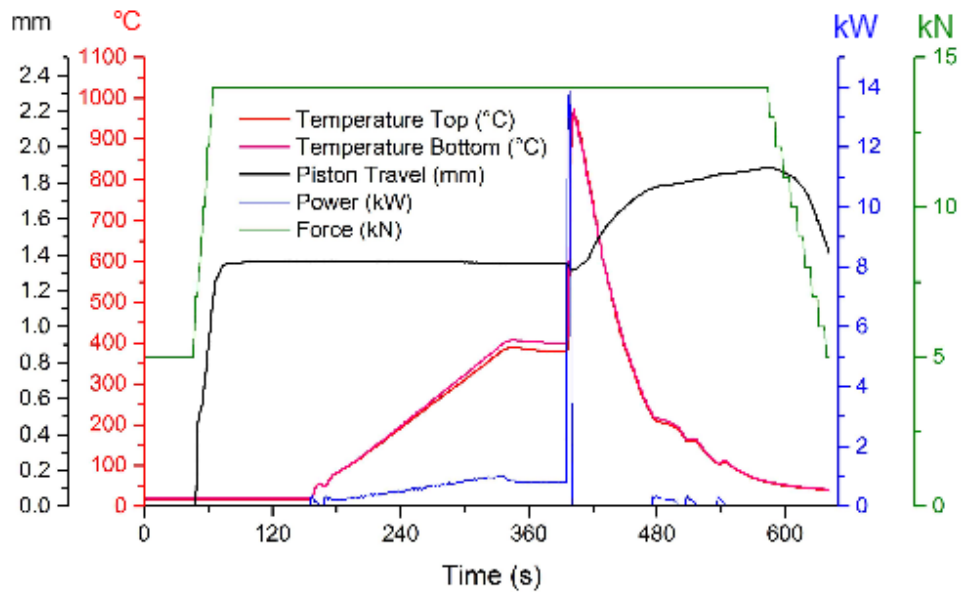
Figure 7.2 *Processing plot for hFSPS-980*

Similar behaviour was shown by the hFSPS-1040 when the power pulse was composed of 5 s at about 13 kW (Fig 7.3). The temperature reached 1040 °C at a heating rate of 7700 °C /min. The limited increase in temperature despite the power increase is due to the high temperature at which the system is slightly more resistive (less Joule heating) and starts to radiate. The total processing time was about 10 min, with the dissipation of an average power of 0.67 kW for 316 s of heating (0.061 kWh total energy consumption).
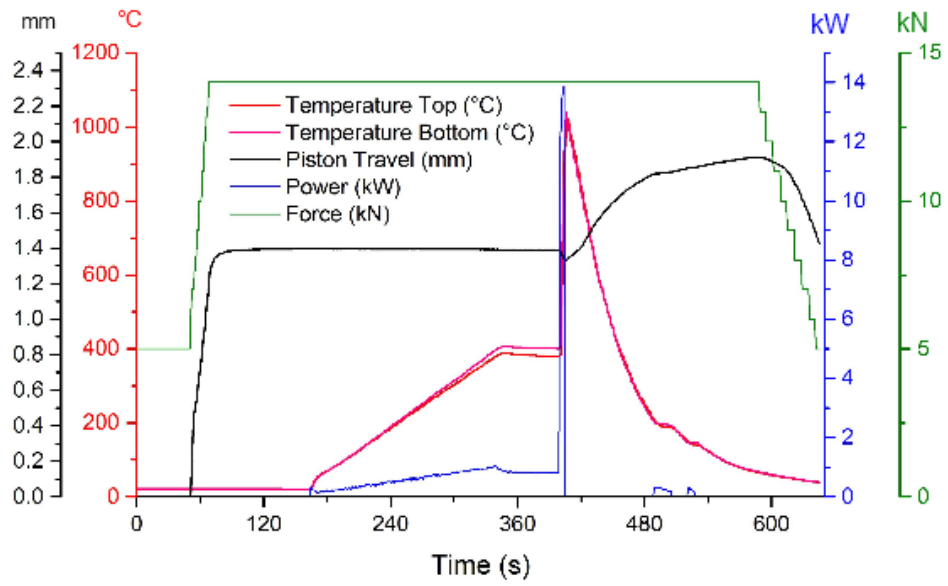
Figure 7.3 *Processing plot for hFSPS-1040*

A summary of density and processing temperature is shown in Tab 7.1.

Table 7.1 *Summary of density and composition*

Sample	Density	Temperature °C	Composition
SPS	92.5%	850	HH+FH+Sn (traces)
hFSPS-980	90.5%	980	HH+Sn (traces)
hFSPS-1040	92.5%	1040	HH+Sn (traces)

It was surprising to see samples produced via different methods and temperatures resulted in very similar densities. The use of a higher temperature with the hFPS-1040 sample produced a slightly higher density. While in hFSPS, a high temperature can be used as it is only maintained for seconds, in SPS a long dwelling time could lead to the formation of second phases [218].

XRD analysis provided (Fig 7.4) evidence that all the samples were majority single phase (TiNiSn), with only small traces of pure Sn in the SPS sample. The longer time spent at high temperature by the SPS processed sample allowed the tin time to better dissolve into the half-Heusler lattice.
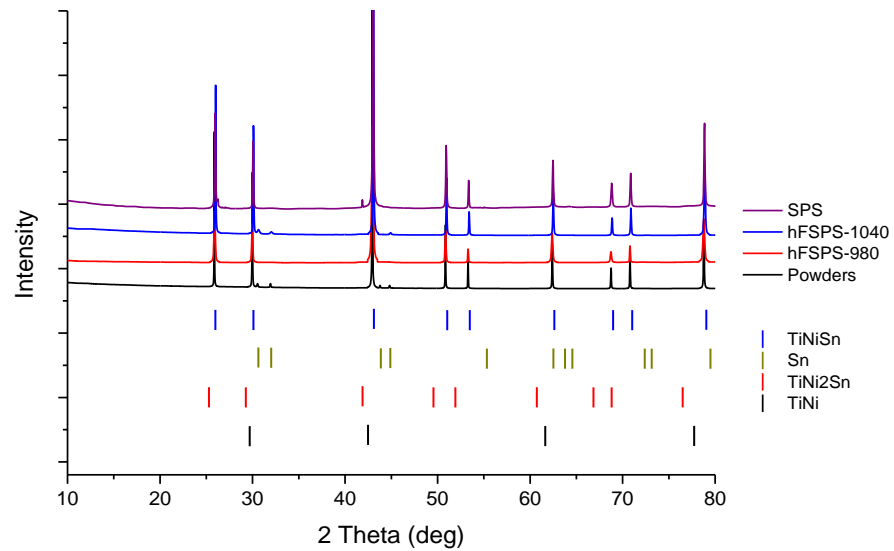
Figure 7.4 *XRD patterns of samples with relevant PDF cards included.*

The incorporation of Cu into the lattice can be detected by XRD as shown by Barczak et al. [79] who noted the shift of the peak at 79 deg, which shifted towards a lower angle when Cu was incorporated as it stretched the unit cell. In this work, both the powder and hFSPS-980 sample had the same peak position (78.8 deg) while the hFSPS-1040 and SPS sampled had a slightly higher angle (about 78.85 deg, in Fig 7.5). This implied there was a lower degree of Cu in the lattice, but the shift could also be explained by other effects such as micro-strain from thermal stress, or finely dispersed second phases [219].
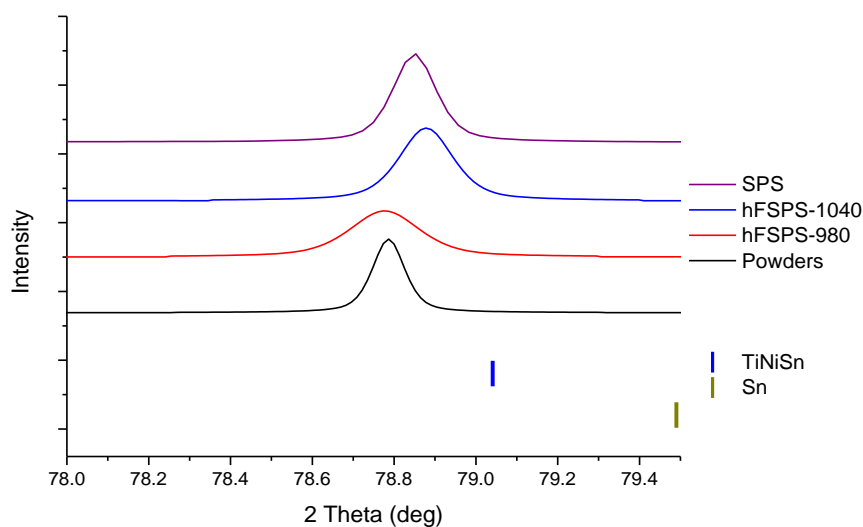
Figure 7.5 *Magnification at 78-79.5 deg [79]*

The peak at 42 deg in the SPS sample could be related to the formation of small amounts of full-Heusler second phase within the half-Heusler matrix (usually Ni-deficient $TiNi_2Sn$ [78, 84, 220, 221]). The full Heusler was not clearly visible in any of the microscopy done, but due to the small amount that was not surprising, moreover its size and the similar contrast expected does make it more difficult to spot. Where the full-Heusler precipitates also complicates the search in SEM, with different papers finding it as nano-inclusions [84], as part of a compositional gradient among different grains [79], or nano-segregated phase, together with Cu-doped phase [78], usually as a decomposition product of Ni-rich TiNiSn. Full-Heusler precipitates can have different shapes (disc-like, platelet-like, nanoparticles) and can have a positive influence on the thermoelectric properties [222], which might explain some of the properties variation in the sample produced here (Seebeck, resistivity). The material can have a wide stoichiometry stable range, such as $Ti_{1-x}Ni_{1+x}Sn$ [223] or $TiNiSn_{0.95}$ [224], producing only a small shift in the XRD peaks. This could explain why EDS could show compositional variation with no significant change in XRD.

The starting powder had a grain size below 200 µm but was typically composed of agglomerates (Fig 7.6)
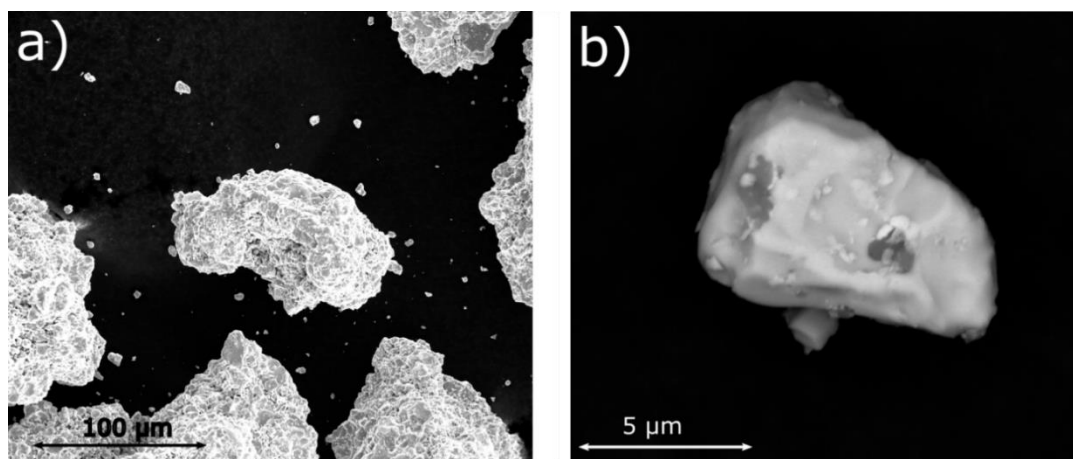
Figure 7.6 *Backscattered images of startingg powder a)low magnification*
b)high mafnificcation

The grains making up each agglomerate were a few µm (< 10 µm) and agglomerates appeared to be composed of phases having different composition, with regions of different brightness in backscattered mode. Small amounts of likely free Sn were also visible as very bright spots in backscatter imaging (Fig 7.6-b), and free Sn was also detected by XRD. Point EDS (Fig 7.7) detected the presence of traces of TiO_2 in certain region of the agglomerates (Tab 7.2 spot 4), confirmed the inhomogeneity of the agglomerates composition and the presence of oxides. The amount of titanium oxide was very small (below the XRD detection limits) and dispersed randomly through the powders, but it might have had some detrimental effect on the sintering of the samples. It was unlikely that the very small amount of titania could have influenced the thermoelectric properties, as the electrical and thermal conductivity or Seebeck. On the other hand, the titania could have influenced the final composition of the sample as it would alter, at least locally the Ti concentration.
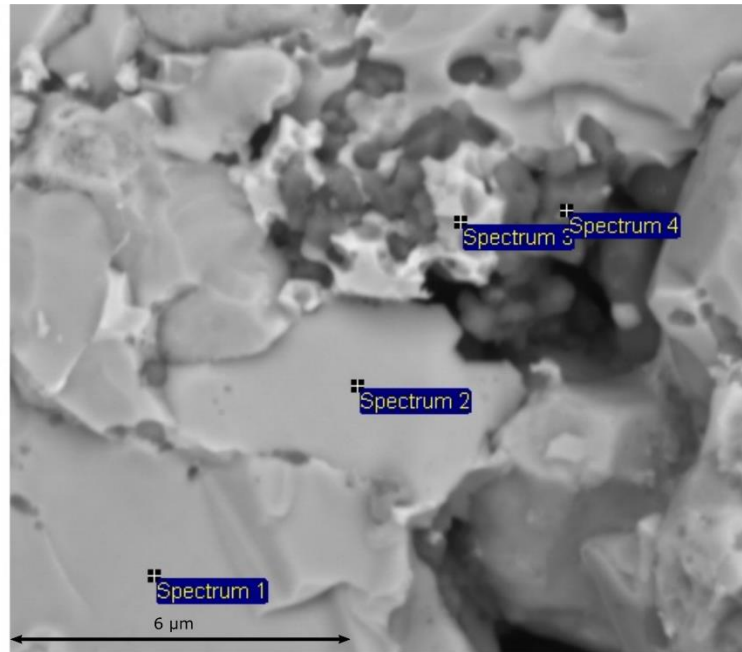
Figure 7.7 *Backscattered image and EDS spot of a powders agglomerate*

Table 7.2 *atomic % of elements from EDS spots in Fig 7.7*

Elements	O	Ti	Ni	Cu	Sn
Spectrum 1	0.19	29.79	36.61	0.68	33.10
Spectrum 2	0.23	29.63	38.03	0.46	32.11
Spectrum 3	19.88	17.15	20.49	5.45	37.03
Spectrum 4	49.08	49.14	0.38	0.41	0.98

The different processing conditions influenced the microstructure and some difference can be spotted in SEM fracture surfaces, at the micron scale. The grains size of the SPS sample (Fig 7.8-a) grew significantly from those seen in the powder, because of the slower heating rate, and ranged from about 10 µm to more than 20 µm. Porosity was visible as the sample was not fully dense. The fracture surface also appeared to be very rough, implying weak intergranular bonding as the fracture path followed the grain boundaries. The weak bonding between grains might have lowered the electrical conductivity, as there was a clear trend with roughness/intergranular failure and electrical resistance as measured in the LSR. From the fracture surface, it was clear that the agglomerates in the powder were not broken up during sintering, as regions with large variations in grain sizes were present. Backscattered images also showed that Sn traces were still present and appear to behave as a sintering aid,

segregating to grain boundaries and triple points, (Fig 7.8-b). Evidence for the presence of the full-Heusler phase could not be found, as their size was probably too small to be clearly identified.
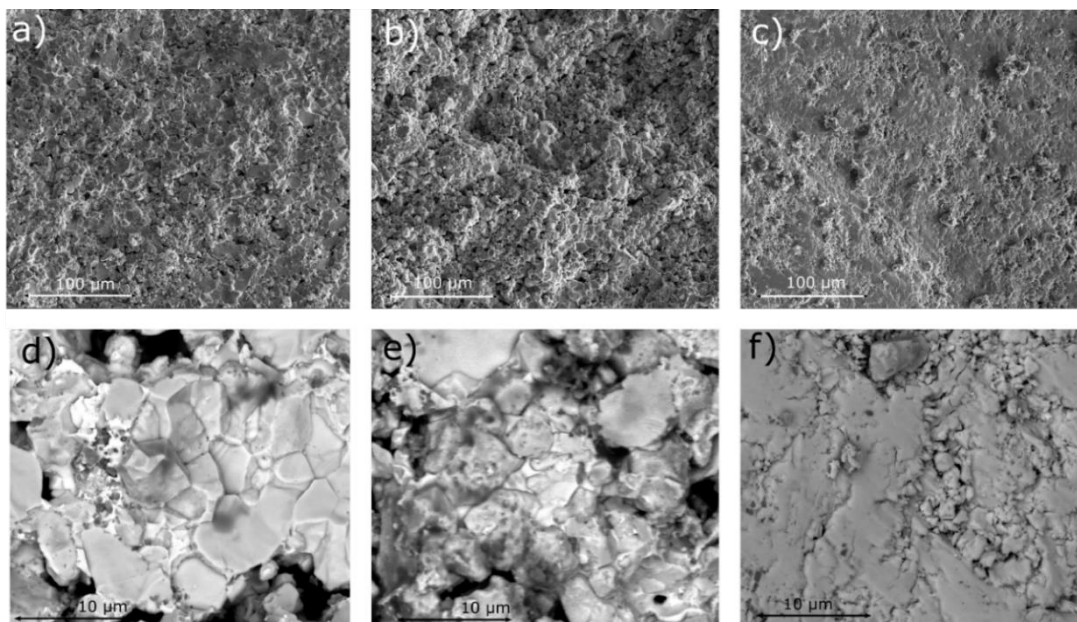
Figure 7.8 Low magnification images of a)SPS b) hFSPS-980 c)hFSPS-1040 and backscattered high magnification images of d) SPS e) hFSPS-980 f) hFSPS-1040

Point EDS was performed on the SPS sample (Fig 7.9), which confirmed the presence of Sn-rich regions (Tab 7.3). The regions near the tin also appeared to be Ni-rich, and some regions (spot 3) also had high oxygen levels, although oxide particles were not visible.
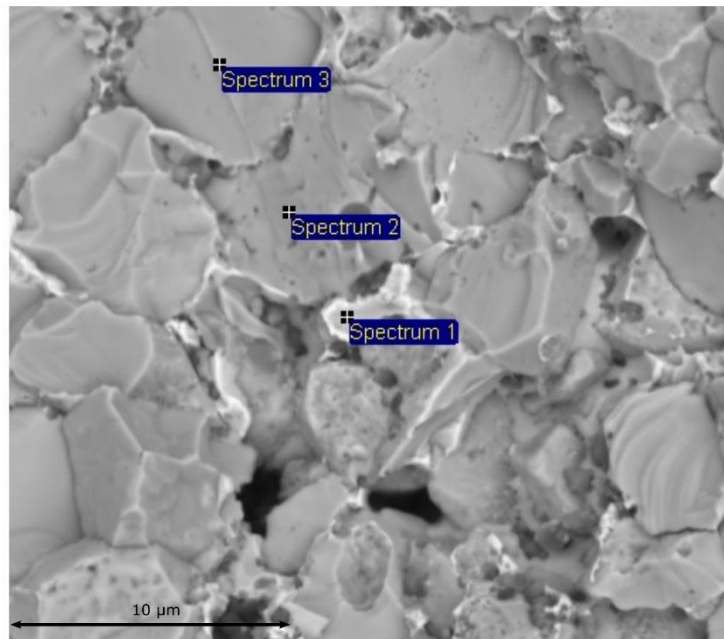
Figure 7.9 Backscattered image and EDS spots of SPS

Table 7.3 atomic % of elements from EDS spots in Fig 7.9

Elements	O	Ti	Ni	Cu	Sn
Spectrum 1	8.97	2.29	3.04	0.84	84.84
Spectrum 2	2.07	28.35	36.96	1.090	31.52
Spectrum 3	0.0	31.11	38.30	1.029	33.30

The hFSPS-980 sample (Fig 7.8-b) showed a rather similar fracture surface; with evidence of limited inter grain bonding and appreciable porosity. Upon closer inspection, a small compositional variation seemed to be present with free Sn behaving as sintering aid (Fig 7.8-e). The grain size appeared to have a larger variation in scale with a mix of larger (> 10 µm) and smaller grains (< 5 µm). Internal grain porosity was visible but not extensive (Fig 7.8-e). The mesoscale structuring of this sample, could have influenced the thermal conductivity as it could scatter phonons of different wavelengths, an effect already reported to improve the properties of other hybrid-flashed samples [8, 175].

EDS point analysis (Fig 7.10) confirmed the presence of Titanium oxide (point 4, Tab 7.4) and small compositional variation among grains. Spectrum 2 in particular

showed that there are regions that had the appearance of a spinodal decomposition. This suggested the core of some grains might be composed of two similar phases deeply mixed, but because of the high volume of interaction of EDS, it was not possible to clearly establish the composition. They appeared to be Ti-deficient probably because of the presence of a nearby region of Titanium oxide.
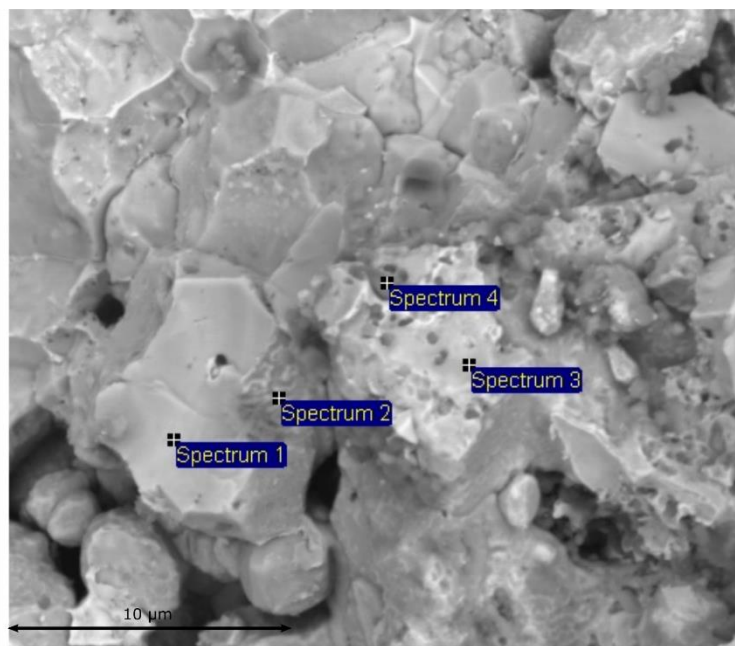
Figure 7.10 *Backscattered image and EDS spots of hFSPS-980*

Table 7.4 *atomic % of elements from EDS spots in Fig 7.10, negative values are due to a very low signal*

Elements	O	Ti	Ni	Cu	Sn
Spectrum 1	2.55	26.32	37.37	3.72	30.02
Spectrum 2	7.65	12.37	46.03	0.0	35.18
Spectrum 3	9.47	27.56	31.75	0.42	30.79
Spectrum 4	72.73	24.81	0.31	0.82	1.321

The hFSPS-1040 sample on the other hand appeared to have a different fracture surface (Fig 7.8-c), despite having practically the same density as the SPS sample (Tab 7.1). The hFSPS-1040 had a smoother surface implying trans granular fracture, this suggested a stronger or more coherent grain boundary, which should improve electrical conductivity [225]. The grain size could only be seen in the regions that had intergranular fracture, in those regions the average size was mixed with some about 5

147

µm and larger grains (> 20 µm, Fig 7.8-f) as well as submicron porosity. This mix of large and small grains with porosity was expected to reduce thermal conductivity because of the multi scale scattering defects. The bright regions assumed to be free Sn were less visible, probably because the higher temperature or current enhanced the sintering aid effect and allowed some Sn incorporation within the crystal structure.
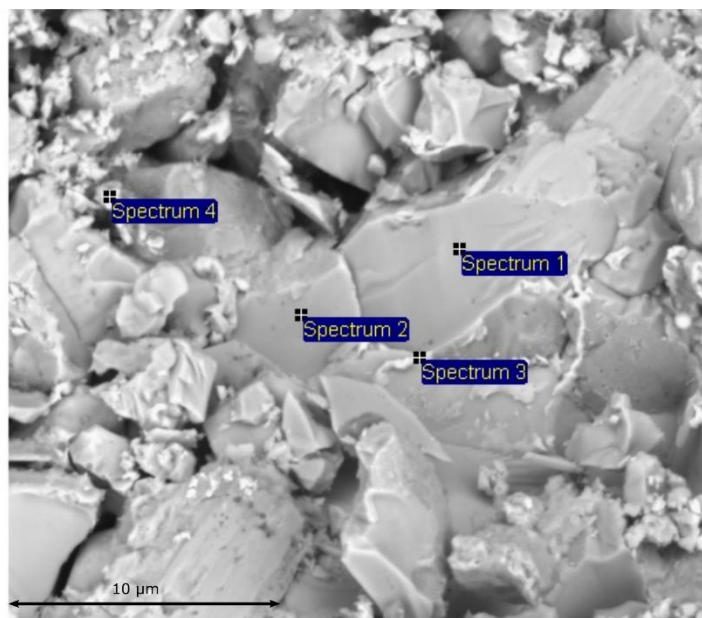
Figure 7.11 *Backscattered image and EDS spots of hFSPS-1040*

Table 7.5 *Atomic % of elements from EDS spot in Fig 7.11*

Elements	O	Ti	Ni	Cu	Sn
Spectrum 1	3.48	20.08	48.65	6.75	21.03
Spectrum 2	7.60	22.43	46.58	0.0	23.59
Spectrum 3	28.08	14.62	27.49	0.0	30.29
Spectrum 4	22.28	17.57	37.92	2.00	20.22

Point EDS analysis on an intergranular fracture region (Fig 7.11) showed the presence of a Ni-richer phase (Tab 7.5). We spotted oxide in the starting powder and high heating rate (7700 °C /min) has been shown to break the oxide surface layer and improve the sinterability [23], however, the oxide still remained within the material but as smaller particles, too small to be seen on a fracture surface. The Ni-rich area , almost in the range of a full-Heusler phase ($TiNi_2Sn$) was not detected by XRD in this sample.

The observed differences in microstructure between the different samples was reflected in the thermo-electrical properties, where the hFSPS-1040 sample showed the strongest inter grain bonding and the best thermoelectric performance.
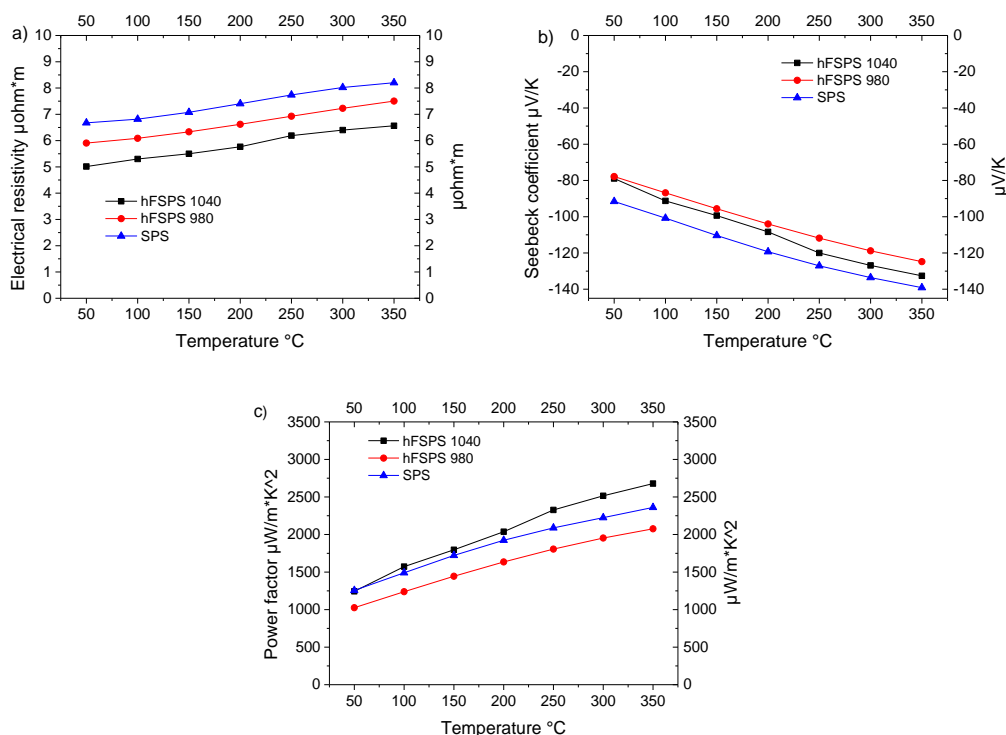
Figure 7.12 *a) Electrical resistivity b) Seebeck coefficient and c) Power factor of the samples*

The electrical resistivity of all of the samples showed low room temperature resistivity, which increased with temperature (Fig 7.12, this was typical of Cu doped HH of this composition [78, 79]). All of the samples had a similar gradient with respect to temperature, typical increasing 1-1.5 µohm*m over the temperature range tested.

The hFSPS-1040 sample showed the lowest resistivity (5 µohm*m at RT), while the SPS had the highest (6.7 µohm*m at RT). The Seebeck coefficient, however, did not follow the expected trend one might have expected from looking at the resistivity data. Typically, when the resistivity decreases, the magnitude of the Seebeck coefficient decreases as well [26]. The SPS sample showed the highest Seebeck value (-92 µV/K at RT) as was expected given its high resistivity, but both the hFSPS samples had similar values despite their different resistivity, (-78 µV/K at RT). The hFSPS-1040 sample had the most interesting properties, as the Seebeck increased with

temperature faster than the other samples, this resulted in the hFSPS-1040 having a higher value than the hFSPS-980 at high temperature (-132 µV/K vs -126 µV/K at 350 °C).

The Seebeck response of the hFSPS-1040 sample was difficult to explain and might have been due to something influencing the band-structure (such as a different distribution of Cu or different degree of dissolution into the lattice). The behaviour of the SPS and hFSPS-980 samples was simpler and likely related to the samples having a slightly different composition. This was due to the presence of the full-Heusler phase in the SPS sample and a different degree of Cu incorporation within the lattice, with the hFSPS-980 appearing to have more (Fig 7.3) [79].

The power factor for all the samples was calculated (Fig 7.12) and the hFSPS-1040 sample had the highest one thanks to its higher conductivity and good Seebeck coefficient. However, the hFSPS-1040 sample was worse than compared to hot pressed material reported in the literature [79] with same compositions (2800 vs 3400 µW/m*K^2 at 350 °C). The lower power factor was mainly because of a lower Seebeck, but the hFSPS-1040 sample still had better properties than solid state reacted pellets [78] (1600-1700 µW/m*K^2).
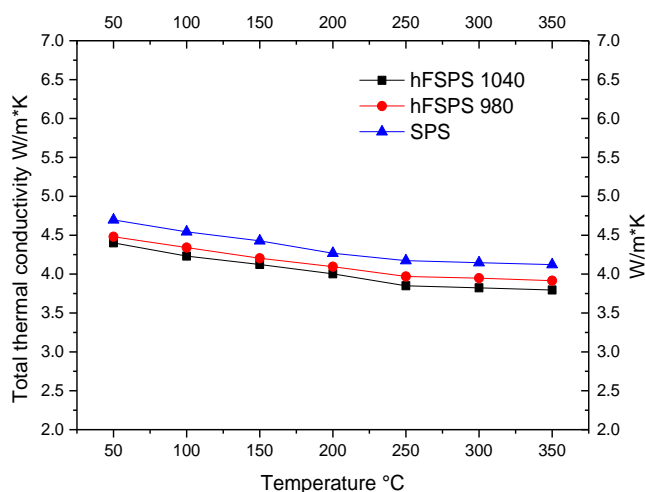
Figure 7.13 *Total thermal conductivity of the samples.*

The total thermal conductivity of all samples (Fig 7.14) decreased with increasing temperature and followed the same trend for all of the samples. The lowest

value of thermal conductivity was for the hFSPS-1040 sample (3.79 W/m*K at 350 °C), while the hFSPS-980 sample had a slightly higher value (3.91 W/m*K at 350 °C) and the SPS sample had the highest value (4.12 W/m*K at 350 °C). These values were lower than those reported in the literature, prepared by hot press (4.5 W/m*K at 350 °C), but probably because of lower density of the sample produced (Tab 7.1 vs 98%).

Electronic thermal conductivity was calculated using the same method introduced in Chapter 4,

$$k_e = \quad L\sigma T \qquad\qquad 5.1$$

Where L is the Lorentz factor, σ is the electrical conductivity and T is the absolute temperature. The Lorentz factor was therefore calculated as suggested by Kim et al.[209] using the relationship

$$L = 1.5 + \exp\left(-\frac{|S|}{116}\right) \qquad\qquad 5.2$$

Where L is in $10^{-8}W\Omega K^{-2}$ and S in µV/K.
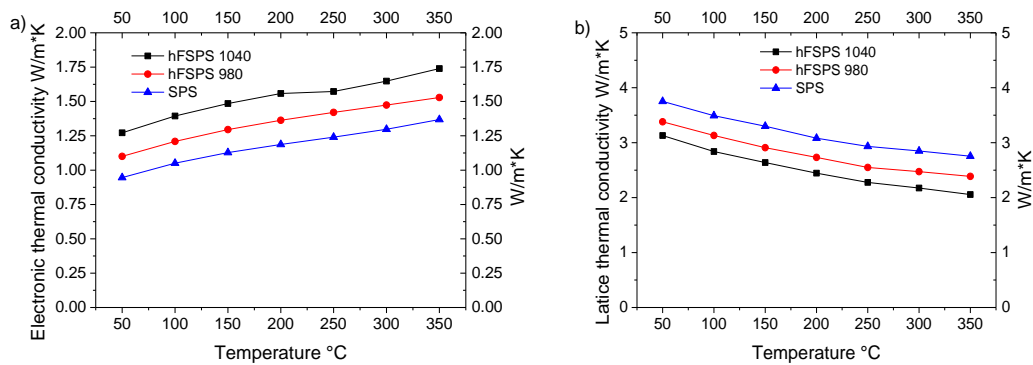
Figure 7.14 a) electronic and b) lattice thermal conductivity of the samples

As expected, the electronic contribution increased with temperature and was higher for the more electrically conductive samples, while the lattice contributions decreased with temperature and had the smallest value in the hFSPS-1040 sample (2.05 W/m*K at 350 °C). Just like the other properties measured, the hFSPS-980 sample had a similar but slightly higher lattice contribution (2.38 W/m*K at 350 °C) and the SPS sample had the highest (2.75 W/m*K). The SPS sample had a similar lattice thermal conductivity compared to the hot pressed samples of a similar

composition reported in the literature [79] (about 2.85 W/m*K at 350 °C), while data for solid state reacted pellet is not available.

The lower value of lattice thermal conductivity of the hFSPS sample suggested the microstructure was the main cause of the lower lattice conductivity, since density was the same for the SPS and hFSPS-1040 samples. The explanation of this behaviour is likely similar to that seen in the Skutterudite samples produced in chapter 4. Specifically the sub-micron porosity and multi-modal/mesoscale grain distribution, which produced scattering of a large range of different wavelength phonons, which reduced the lattice thermal conductivity.

The figure of merit ZT (Fig 7.15) was highest for the hFSPS-1040 sample since it had the highest power factor and lowest thermal conductivity (0.44 at 350 °C), while the SPS and hFSPS-980 samples had similar values for both the peak ZT and the temperature dependence of ZT (0.35 vs 0.33 at 350 °C). The reduction of thermal conductivity in the hFSPS-1040 sample was enough to counterbalance the lower power factor when compared to hot pressed samples reported in the literature, and reached a similar value for peak ZT at 350 °C (0.44 for hFSPS vs 0.47 for hot press).
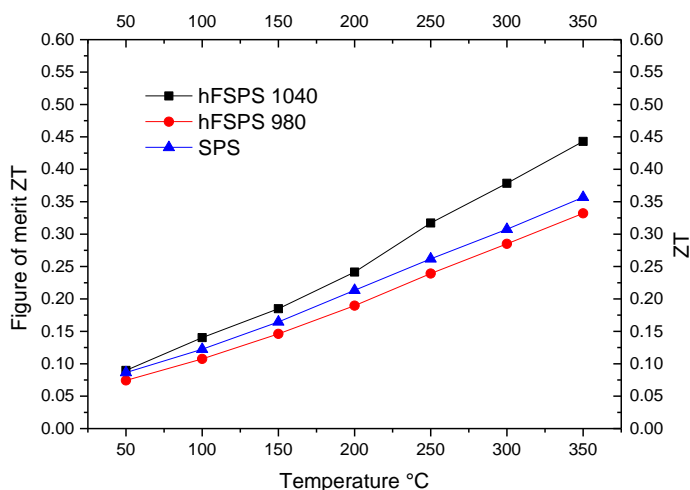
Figure 7.15 *Figure of merit of the samples*

7.4 Conclusion

Polycrystalline samples of TiNiSn-Cu$_{0.05}$ were sintered using SPS and hybrid Flash-SPS. All of the samples produced had similar densities (around 92.5%) and XRD found the main phase of to be TiNiSn with second phases only found in the SPS sample (small amounts of free Sn and TiNi2Sn). The grain size seemed to be smaller in the hFSPS samples as was expected from using a fast heating and cooling process. It also appears that some degree of meso-structuring was obtained, as seen in other hFSPSed materials [216, 226] as well as previous chapters, which are proven to influence the lattice thermal conductivity [8, 9, 159] The variations in microstructure also had some influence on the electrical properties, the hFSPS-1040 sample showed the highest power factor and ZT (0.44 vs 0.35 SPS at 350 °C). The hFSPS-1040 sample's ZT was comparable to the literature (0.44 vs 0.47 hot press at 350 °C), but was obtained with a faster process, leading to less energy consumption.

Chapter 8 Hybrid –coating for thermoelectric materials

8.1 Introduction

In the field of thermoelectric materials, a lot of research has been done to develop new materials or manipulate them to improve their performance. While most research has focused on improving ZT or operating temperature, to make a practical device the material must survive operation in air. As a result, either the chemical properties of the materials must be altered or a coating/sealing needs to be used to protect the material from the atmosphere.

In contrast with the huge amount of information on the properties of thermoelectric materials, there are only a few studies on the oxidation behaviour of uncoated thermoelectric materials. Skutterudites have been shown to oxidize and crack when exposed to oxygen at high temperatures (650 °C >T>500°C) [227] forming oxides on the surface while the interior becomes depleted in antimony which resulted in a quick loss of performance and mechanical strength. For Mg_2Si (above 450 °C) a MgO layer formed on the surface on top of elemental Si [228]. The solid solution of Mg_2Si with Mg_2Sn had a more complex behaviour during oxidation (430-500 °C) and the temperature at which oxidation became catastrophic tended to drop with increasing Sn content [229]. HMS also suffered oxidation issues above 600 °C forming a mixture of SiO_2 and MnSi on the surface [230]. SnSe thermoelectrics formed different oxides depending on the oxidation temperature with SnO, $SnSe_2$ and possibly $Sn(SeO_3)_2$ forming at temperature between 600 and 700°C [231].

Because of the poor performance of the thermoelectric materials discussed above, coatings have been developed to protect against oxidation. In the literature a variety of different coating materials have been investigated: β-FeSi has been proposed as a coating for Mg_2Si but only short time tests were performed [228]. BN has been proposed for coating $Mg_2Si_{0.3}Sn_{0.7}$ [232]. HMS has been successfully

coated with glass-ceramic [230, 233]. Si has been proposed as coating for SnSe [231] and titania rich-borosilicate glasses have been proposed for $CoSb_3$ [234]. For low temperature materials, polymeric coating have been applied to Bismuth telluride [235]. Different thermoelectric materials require different coatings, as a coating must be tailored to the substrate. This is because a coating must fit in the processing window of the thermoelectric, while still being a suitable oxygen barrier at the operating temperature. A coating must also be thermo-mechanically compatible (similar CTE) with the substrate otherwise it would crack off during thermal cycling. A large amount of compositional modification can be done in order to alter the coating to different applications and requirements, such as increased corrosion resistance, improved biocompatibility or modified surface chemistry [236]. One of the more recent popular types of coating used for metal and other material are hybrid coatings, which covers a wide variety of chemistries, but most contain silicone-based resins, which are cured above 150 °C and decompose to form an oxide above 400 °C.

Since several companies produce hybrid coatings that are advertised as operating up to 600 °C and do not require a high temperature firing stage, these coatings could be suitable for intermediate temperature thermoelectrics. HMS and Sb-doped $Mg_2(Si, Sn)$ were chosen as representing typical thermoelectric materials as their ZT reach the highest value is in the middle temperature range (400-600 °C).

8.2 Experimental Details

Before the coatings can be tested, their substrates need to be prepared. The raw powders used to produce the samples were made in collaboration with a commercial company, and as such, limited details are available, however the HMS ($MnSi_{1.74}$) powder may be available upon request. In this work the HMS and $Mg_{2.1}Si_{0.487}Sn_{0.5}Sb_{0.013}$ (Mg-Silicide) samples were sintered by SPS, producing 30 mm diameter samples, but the oxidation behaviour is expected to be very similar to samples produced using other techniques.

Magnesium silicide was sintered as described by Du et al. [23] (composition sintered was the same). The pellets had a density of 2.9 g/cm^3. The pellets were then polished and cut into bars with a square base of 3mm and a height of 10 mm. HMS was sintered as described by Salvo et al. [233], the pellets had a density of 5.2 g/cm^3. Both materials were cut into bars for further testing and all the edges were gently polished to reduce their sharpness and remove any chipping damage.

In this work, two hybrid coating were used, both produced by Aremco and both based on polymer-ceramic emulsion/resin, with oxide inert fillers, one solvent based (cp4040-s1 and labelled Solvent) and one water based. (cp4040 and labelled Water). The composition of the coating material as provided is shown in Table 8.1. Data were taken from the materials MSDS.

Table 8.1 *Composition of cp4040 (Water) and cp4040-s1 (Solvent) as in MSDS*

Ingredient	Percent in Water-based coating	Percent in Solvent-based coating	Purpose
Aluminium Oxide	0%	1-10 %	Inert filler
Magnesium silicate hydrate	1-5 %	1-5 %	Inert filler (CTE)
Mica	5-10 %	1-5 %	Inert filler, with good barrier
Titanium Dioxide	1-5 %	1-5 %	Inert filler
TriZinc-Bis (Orthophosphate)	< 4%	< 4%	Reactive cement binder
Zinc Oxide	< 1 %	< 1 %	Reactive filler
Water	20-30 %	0%	Solvent ecological
Methoxy propyl acetate	0%	30-40 %	Solvent non-ecological
Silicone Emulsion /solution Including	**30-50 %**	**20-30%**	**Converts to silica to fill voids.**
Water	40-50%	0%	Eco solvent
Xylene	5-10%	10-25%	Solvent
Methanol	0.5-1%	(0.5-1%)	Solvent
1-Propanol 2- Methyl	2.5-5 %	2.5-5%	Solvent
Ethyl Benzene	1-2.5%	2.5-5%	Solvent

The operating principle behind these coatings was likely based on two methods, hence the term hybrid, the initial curing of the coating was likely formed from the reaction between reactive cement forming materials (ortho-phosphates) and the reactive oxide fillers (zinc oxide) [237] [238]. This bonds together the inert oxides forming a porous cement. The cement alone would likely be a poor, porous

oxidation barrier; however, the silicone resin would fill the gaps between the particles, and upon heating above 350 °C form silica, effectively blocking the pores in the cement.

The differences between the two coatings was primarily how they dispersed in the silicone within the product. The cp4040-s1 coating used a mixture of solvents to dissolve the silicone resin, and cp4040 used water and surfactants to produce an emulsion. The water emulsion was likely developed to meet strict environmental requirements to limit the use of toxic solvents; however, an emulsion was likely to lead to an inferior distribution of silica in the final coating. The two products also differ in the composition of filler, for example, "Water" has more mica and no alumina. This could affect the CTE of the coating as alumina has a slightly lower CTE ($7*10^{-6}$ [239] vs $9.6*10^{-6}$ K^{-1} [240]). The alumina was typically in spherical form while the mica had a flake-like morphology which should provide a better barrier to oxidation [236]. The composition of the dispersing agent ("Water" contains water in emulsion, while "Solvent" contains methoxy propyl acetate) also affected the viscosity. The viscosity could in turn have affected the thickness and structure of the coating, with "Water" having a higher viscosity due to a lower content of volatile components [241].

As well as testing two different coating materials, the effect of coating thickness was also investigated. Two coating techniques used. In both cases, the coating had to be applied in two steps, as only 5 sides could be coated at a time.

The first technique used produced samples with thick and highly variable coatings, and samples produced using this technique were labelled as "Thick". In the "Thick" technique, a spatula was used to manually spread the coating over the 5 exposed surfaces. Sample were then placed in a graphite boat and cured in Ar flow in a tubular furnace at 250 °C for 45 min, with a heating rate of 1.7 °C /min before cooling. Once the curing was completed the remaining face, (touching the graphite paper boat), was polished and then coated using the same process. This technique produced clearly defective coatings, so the coating manufacturer was contacted to advice on an improved process described below. The results from the thick coatings, tested only on the Mg-Silicide, were included in the results as their performance was surprisingly good considering their visible deficiencies.

The manufacturer recommended changing how the coating was applied (recommending a foam brush) as well as a new curing profile. The samples were heated first to 90°C where they were held for 30 mins to allow any residual solvent or water to be fully removed. The samples were then heated to 230 °C where they were held for 40 mins; as before, a heating rate of 1.7 °C/min was used throughout. These samples were generally thinner, more homogeneous and suffered less cracking, so samples made with this technique were labelled "Thin".

8.2.1 The oxidation

Preliminary testing was done to find an appropriate temperature to oxidize both the HMS and Mg-Silicide, these tests involved finding the minimum temperature at which the properties were significantly degraded. For HMS, 550 °C was chosen as at a lower temperatures the uncoated samples would survive with little degradation, and any higher would require unrealistic performance from the coating. For Mg-Silicide, this temperature was found to be 500 °C.

The oxidation tests were performed in a muffle furnace in air. Samples were placed on an alumina boat inside a graphite paper boat (to avoid the sample fusing to the alumina) and heated up to 500 °C or 550 °C at a heating rate of 1.7 °C /min and held there for 120 h. Samples for each coating type (Water and Solvent) and each coating procedure (Thick and Thin) were subjected to the same long-term oxidation.

Samples were characterized with SEM, XRD and electrical properties were measured. Cross sectional and surface SEM images were taken after the coating and again after the aging to observe coating quality and bulk microstructural changes. The XRD spectra were used to identify the presence of oxides on the surface after the coatings were delaminated from the samples. XRD was also used to look for changes in phase composition in the bulk, which could be caused by preferential oxidation of certain elements. Electrical properties were measured after removing the coating and oxide layer from the samples to measure the properties in the bulk.

8.3 Results and discussion

8.3.1 XRD

XRD of the Magnesium silicide-based samples showed the sintered bars are indeed a single-phase solid solution of Mg2Si-Mg2Sn, (Sb cannot be seen) (Fig 8.1). The samples based on manganese silicide are composed of $MnSi_{1.74}$ with minor presence of a second phase (probably MnSi) (Fig.8.2), which is a common second phase in HMS due to peritectic reaction
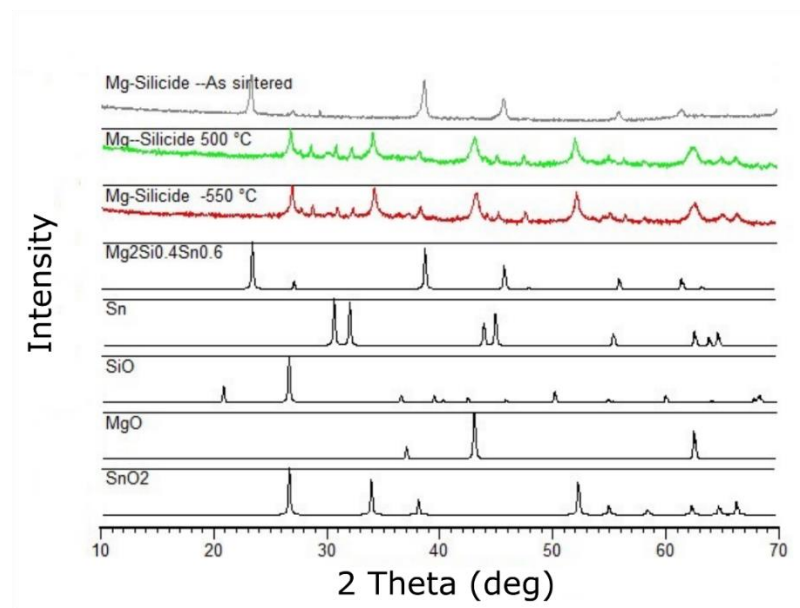
Figure 8.1 *XRD of Mg-Silicide as sintered, aged at 500 °C and 550 °C for 120 h and PDF card of identified phases*
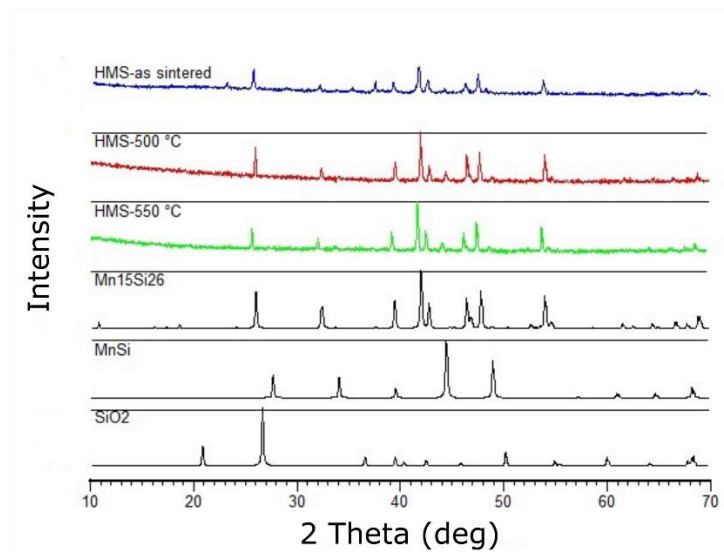
Figure 8.2 *XRD for HMS as sintered, aged at 500 °C and 550 °C for 120 h and PDF card of identified phases.*

The XRD results for the magnesium silicide showed complete oxidation, the strongest silicide peak (24 degrees) was not visible in the oxidized sample, but the silica, magnesia and tin oxide peaks were all visible. This was consistent with the visible results, where the sample burned out (Fig 8.5-a).

The HMS behaved very differently. For the HMS, only the $MnSi_{1.74}$ peaks were visible, with no peaks from any of the oxides or even the MnSi phase. While discoloration was visible (Fig 8.5-b) and a degradation in electrical properties (Fig 8.21), but XRD was not sensitive enough to detect the changes.
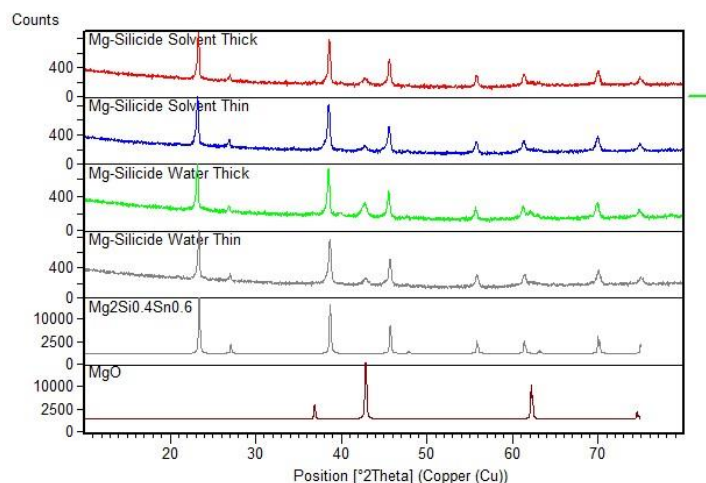
Figure 8.3 *XRD spectra of Mg-Silicide-samples with different coating after 120 h at 500 °C*

The Mg-Silicide samples that were coated showed a significant improvement over the uncoated ones (Fig 8.3). In all the coated samples the Mg_2Si-Mg_2Sn peaks dominated, with the only clear oxide peak being the MgO peak at 43-degree. Their appeared to be only minor differences in the relative peak intensity between the various coated samples, while the MgO peak appeared strongest in the Water-Thick sample, (implying that that was the worst sample). This did not match up with the other analysis done (Fig 8.22 a-b-c) and could have been caused by residual coating remaining attached to the sample.

The HMS samples showed no difference between the coated and uncoated samples, while there was clear difference in thermoelectric performance (Fig 8.21). This was just a further evidence that XRD is not a suitable technique to measure oxidation of the samples.
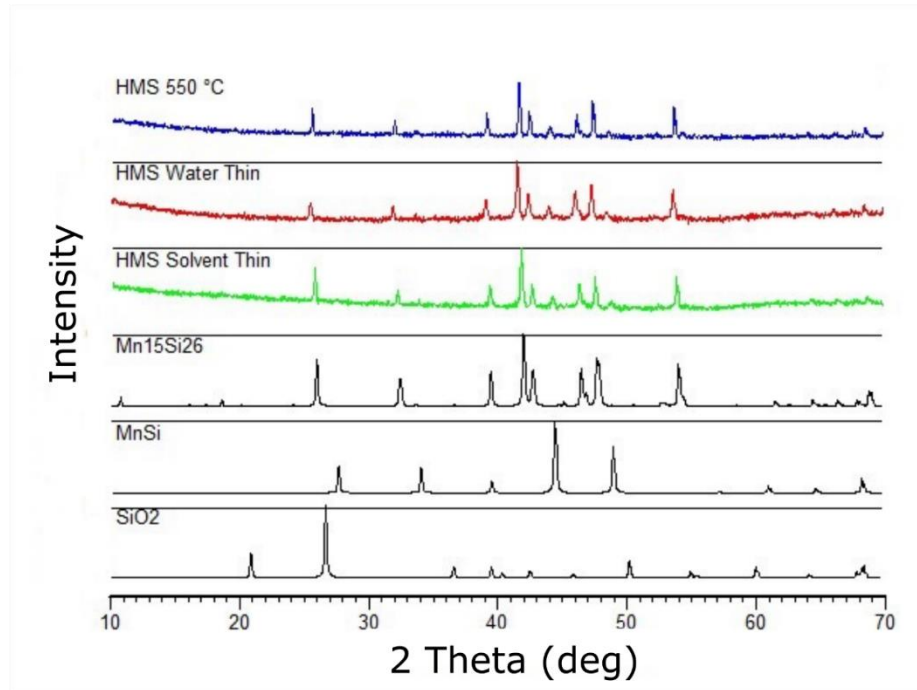
Figure 8.4 XRD spectra for HMS samples uncoated and with different coating after 120 h at 550 °C

8.3.2 Microstructure

After oxidation at 500 °C the uncoated magnesium silicide sample had completely disintegrated, turning into powder (Fig 8.5-a). The uncoated HMS after oxidation at 550 °C was much less affected, with only a dark/coloured layer on the surface (Fig 8.5-b).
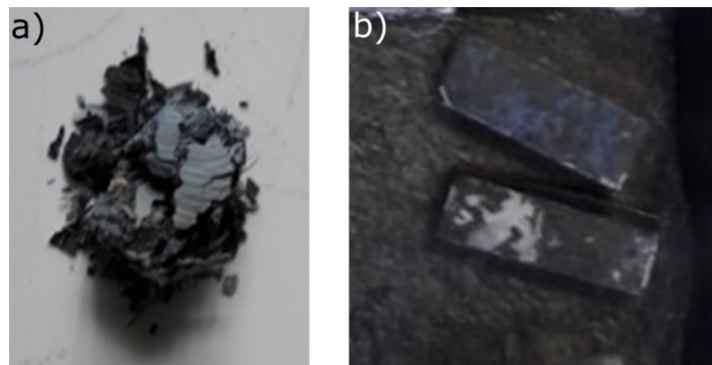
Figure 8.5 left) The Mg-Silicide sample after 120 h at 500 °C, same at 550 °C right) HMS samples oxidized at 550 °C for 120 h

After the curing step the various coatings looked consistent and without visible cracks (Fig 8.6-8.7), the Water samples appeared to have a glossier finish than the Solvent samples. The Thick samples appeared less conforming than the Thin samples (Fig 8.6), with the edges being less visible, but the Thin samples appeared to have a rougher surface (Fig 8.7).
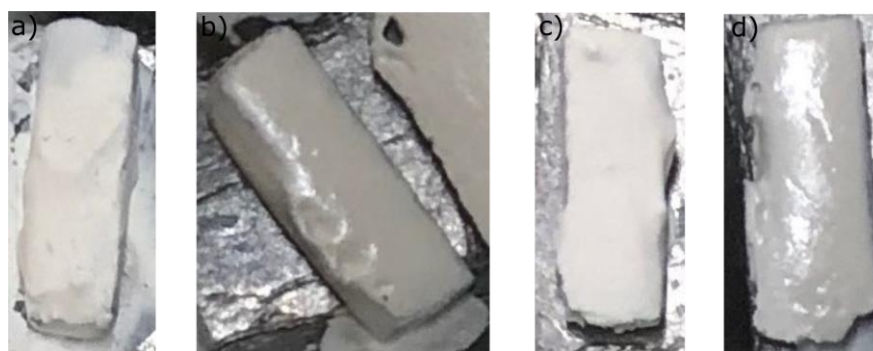
Figure 8.6 Samples after curing for "Thick" layer a) Mg-Silicide Water-Thick b) Mg-Silicide Solvent-Thick c) HMS Water-Thick d) HMS Solvent- Thick
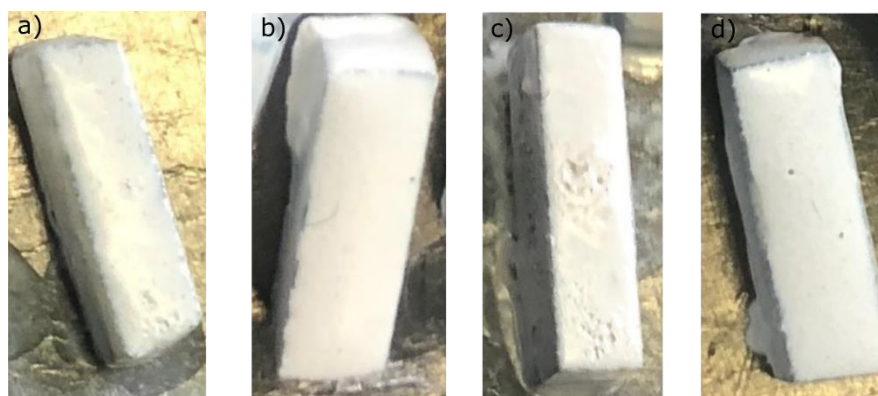
Figure 8.7 Samples after curing for "Thin" layer a) Mg-Silicide Water-Thin b) Mg-Silicide Solvent-Thin c) HMS Water-Thin d) HMS Solvent-Thin
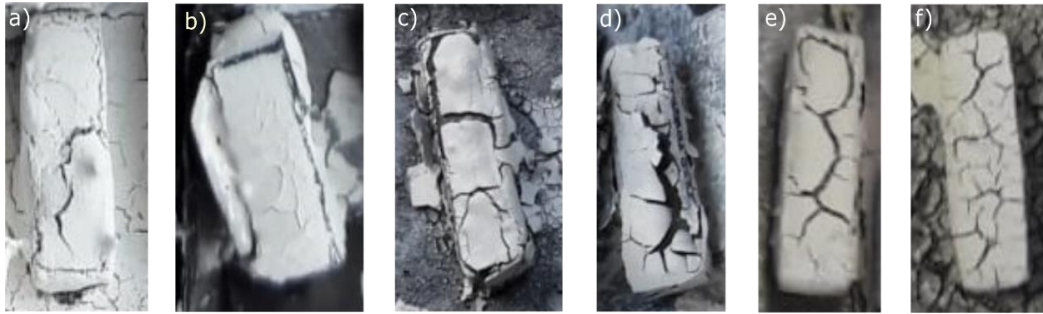
Figure 8.8 Sample after aging at 500 °C a) Mg-Silicide Water-Thick b) Mg-Silicide Solvent-Thick c) Mg-Silicide Water-Thin d) Mg-Silicide Solvent-Thin Sample after aging at 550 °C e) HMS Water-Thin f) HMS Solvent-Thin.

For the Mg-Silicide samples, the Thick coatings seemed to hold together better (Fig 8.8-a-b), with the Thin coatings peeling more (Fig 8.8-c-d). The cracks appeared to start from the edges, which might explain why the thicker samples performed better. However, there was no obvious difference between the Solvent and the Water coatings. HMS aged at 550 °C, (Fig 8.8-e-f), shows smaller cracks on the Solvent than the Water coatings but both did not provide protection. Cross section images were used to observe the quality and adhesion of the two resins after the curing as well as their thickness and coherency. The "Thick" coatings (Fig 8.9-8.10) had a very inhomogeneous thickness, which was up to 100 µm at the thickest point and less than 50 µm at the thinnest. It is worth noting that the corners tended to be the thinnest point, which could explain why the samples cracked at that location (Fig 8.8 a-b).
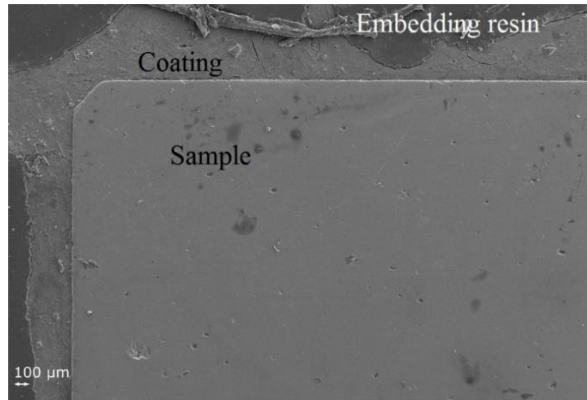
Figure 8.9 *HMS Water-Thick low magnification, the thickness variation is clear. Corner have a smaller thickness but still significant.*
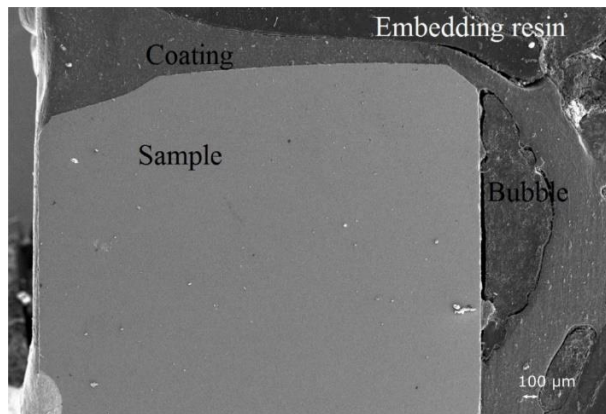
Figure 8.10 *Mg-Silicide Solvent-Thick low magnification. The thickness variation and bubbles are clear. Corner have a smaller thickness but still significant*

From higher magnification images at the sample coating interface (Fig 8.11-8.12-8.13-8.14) it is clear that the coating conformed well to the sample, with no delamination or voids visible at the interface for Solvent samples (Fig 8.12-8.14). However, the coating itself had some obvious flaws, with cracking parallel to the surface. While cracking in the parallel orientation should not be disastrous to the barrier properties, considering the low temperature of the cure (250°C), this was not promising. Apart from interface cracking (Fig 8.13), there was minimal difference between the other coatings.
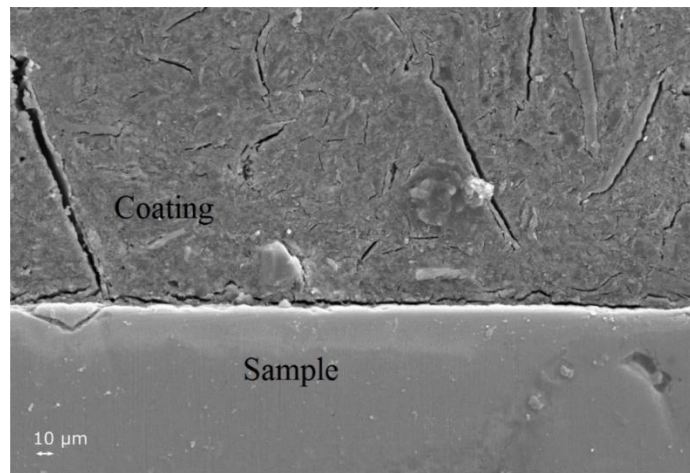
Figure 8.11 *HMS Water-Thick, several cracks are visible in the coating but the adhesion at this point shows some gap*
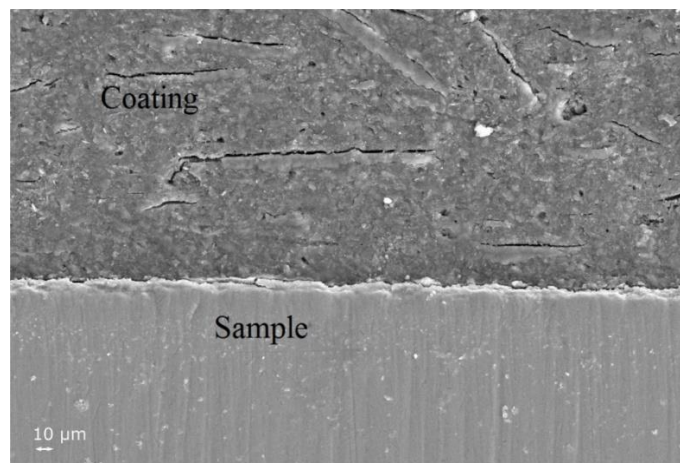
Figure 8.12 *HMS Solvent-Thick, several thin cracks are visible in the coating layer.*
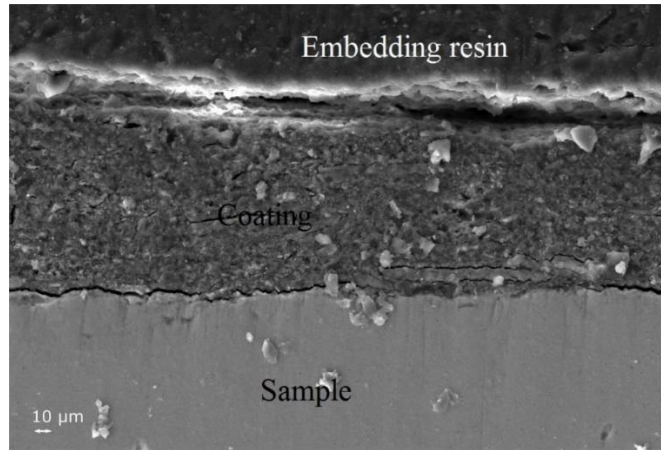
Figure 8.13 Mg-Silicide Water-Thick, several cracks are visible in the coating layer (even in a section with small thickness), adhesion is poor
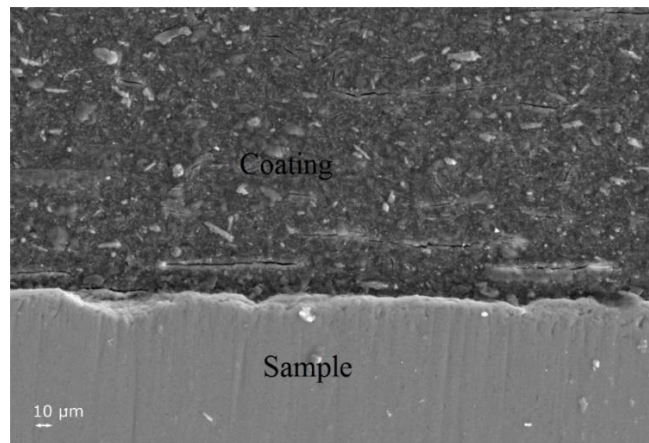
Figure 8.14 Mg-Silicide Solvent-Thick, several thin cracks are visible in the coating layer, adhesion looks good
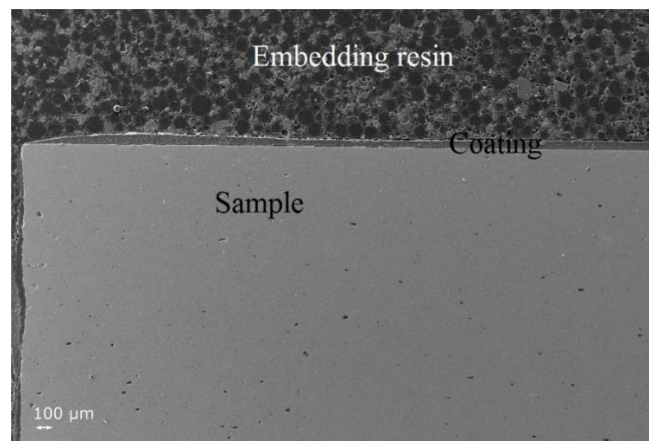
Figure 8.15 HMS Solvent-Thin, the coating is quite homogeneous but very thin at the edges
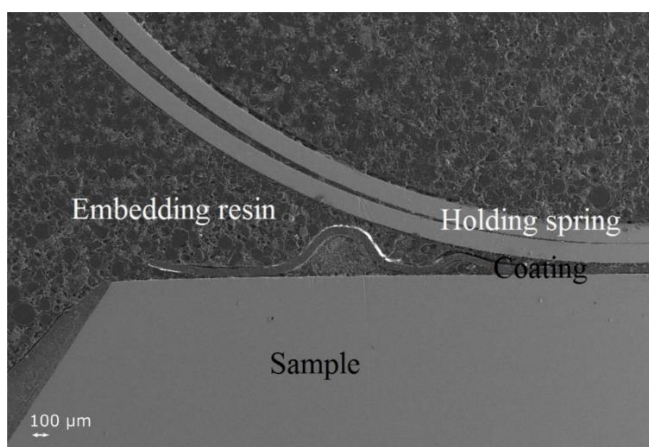
Figure 8.16 *Mg-Silicide Water-Thin, the coating layer has a more homogeneous thickness and is very thin at the edges. The spring was used to hold the sample in place when mounted in resin.*

The coating thickness is different between the samples, due to the application method. This suggested the need of a more standardized procedure to follow or a different approach to ensure homogeneity and repeatability. The corner/edges were particularly weak and surface tension seemed to prevent a good coating at that surface (Fig 8.15).

The purpose of the Thin processing technique was to produce a thinner coating, but also to reduce cracking. From the high magnification images (Fig 8.17-8.18- 8.19- 8.20) this was not completely achieved. HMS Water-Thin (Fig 8.17) showed no obvious cracking so was superior to the Water-Thick coating (Fig 8.11) but porosity was visible between the filler particles. The reduced cracking was likely because the Thin heating profile was designed to allow water to evaporate without boiling, by holding at 90 °C before further heating. But this did not help the solvent samples (Fig 8.18) as methoxy propyl acetate boils at 145 °C so likely did not all evaporate at 90 °C leaving the remaining solvent to boil during further heating, which could have contributed to cracking. The same behaviour is seen in the Mg-Silicide (Fig 8.19-8.20), which is to be expected as they were cured using the same conditions.
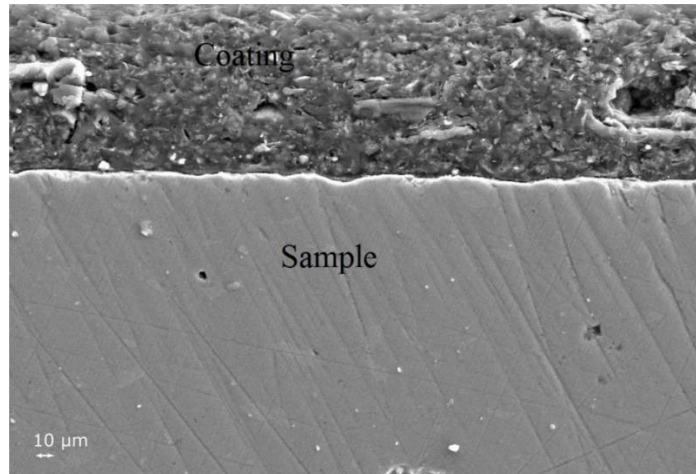
Figure 8.17 HMS Water Thin, several thin cracks are visible, but adhesion looks good
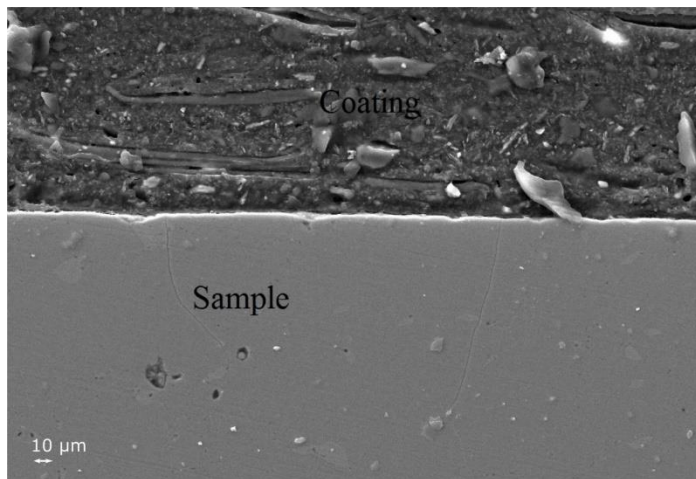
Figure 8.18 HMS-Solvent- thin, several cracks are visible, adhesion looks good
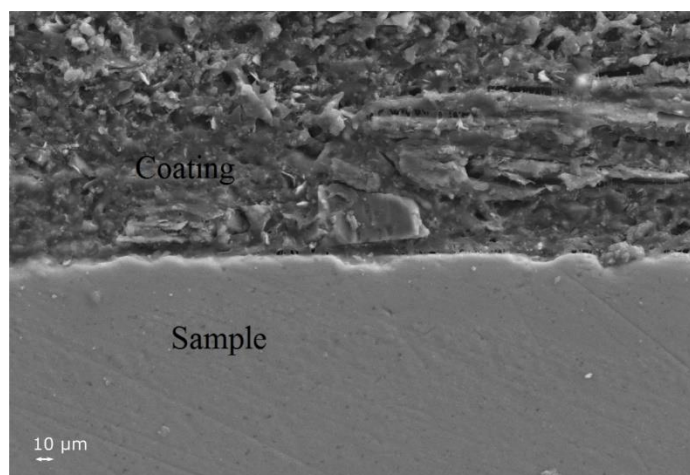
Figure 8.19 Mg-Silicide Water- Thin, several cracks are visible, adhesion looks good
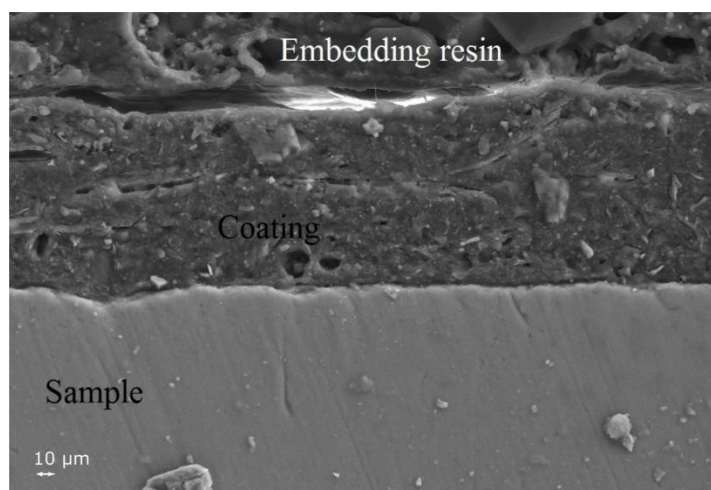
Figure 8.20 Mg-Silicide Solvent- Thin, few cracks are visible, adhesion looks good

From the various SEM images, it was clear that the coating layers, despite appearances after curing, especially the Thin Solvent samples, were not very good oxidation barriers. All of the coatings showed significant cracking on the macro and micro scale, and this cracking appeared to let significant amounts of oxygen through to react with the sample (hence the oxide layers seen in XRD). This surface oxidation only accelerated the oxidation as the oxide was prone to delamination, and when the top oxide later delaminated, it took the coating with it (Fig 8.8). The thickness of the oxide layer under the coatings was a rough estimate for how effective the coatings were. These thickness values, measured on the Mg-Silicide samples (Table 8.2)

suggested the Thick-Solvent coatings were superior, however there was significant variation in the samples as the oxide layer did not grow with uniform thickness.

Table 8.2 *Oxide layer thickness for different sample of Mg-Silicide*

Sample	Measured thickness
Water Thick	2-20 µm
Solvent Thick	6-12 µm
Water Thin	11-20 µm
Solvent Thin	28-36 µm

While the coatings significantly improved the oxidation resistance of Mg-Silicide, (Fig 8.8) the improvement with HMS was much smaller. This suggested the coating may not be suitable for such high temperature operation and would likely perform much better if used at a lower temperature. HMS had no visible oxide (Fig 8.3).

8.3.4 Properties measurements

As mention in the introduction, the aim of this work was to develop a coating that would allow intermediate thermoelectric materials to be operated in air for energy generation applications. For that reason, to be useful not only do the sample have to survive chemically and mechanically but must also retain their thermoelectric properties.

Samples were polished to remove the surface oxide layer and then the electrical properties were evaluated up to 500°C. The thermoelectric performance was then compared to the un-oxidized samples and the uncoated samples. Unfortunately, the uncoated Mg-Silicide sample was destroyed and could not be measured, but that simply meant any sample that could be measured was superior to it.

The coating was not effective at protecting the thermoelectric properties of HMS at 550 °C since the properties of samples with and without coating were very similar, both being significantly worse than the sintered sample (Fig .8.21). Most significant was the substantial increase in resistivity of all of the oxidized samples, typically being double the RT resistivity of the same as sintered sample. The Seebeck increased slightly for the oxidized samples at low temperatures. However, this was a very minor increase and did not compensate for the massive increase in

resistivity, hence why the power factor (Fig 8.21-c) was so much worse. The increase in Seebeck was rather typical, as there is usually a trade-off between resistivity and Seebeck, [242].
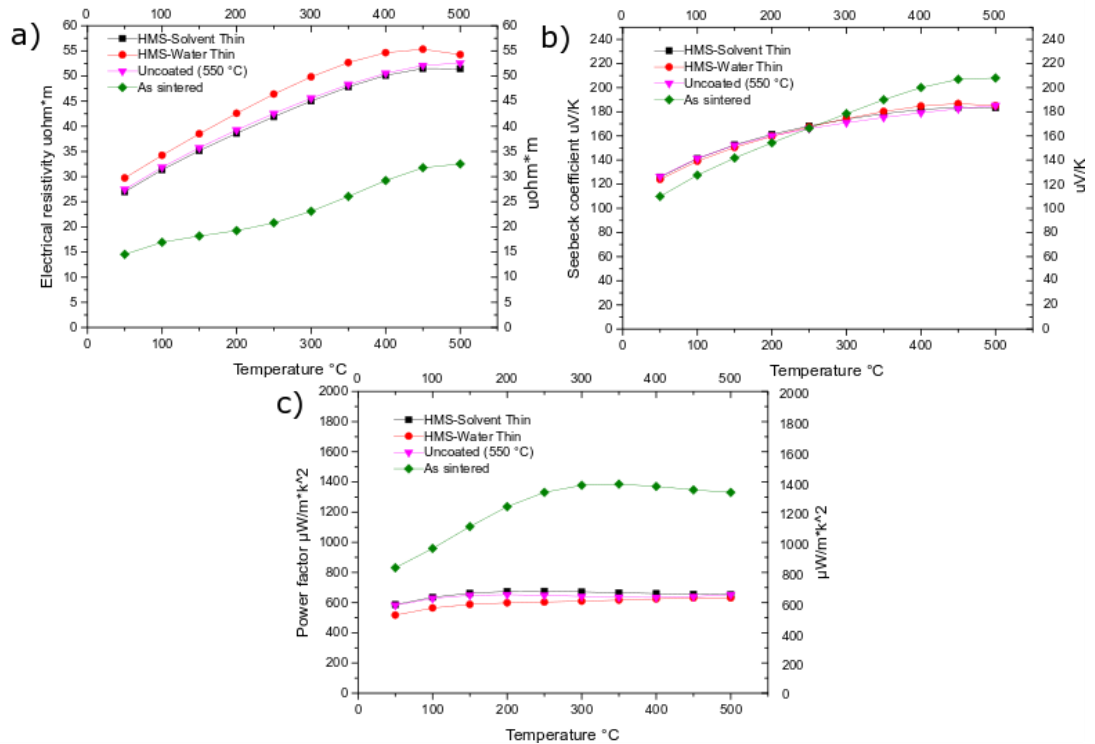
Figure 8.21 *a) Electrical resistivity, b) Seebeck coefficient and c) Power factor of HMS samples.*

The increase in resistivity (Fig 8.21) can be related to a minor compositional shift in the HMS as the silicon was preferentially oxidized. As the silicon was consumed to form silica on the surface this would lead to formation of MnSi in the bulk [243]. MnSi is associated with increased resistivity of HMS [244, 245] so precipitating it inside the HMS would explain the changes seen above. There was some very weak trends visible in the performance of the different coatings, with the Solvent coating performing slightly better than the uncoated sample and significantly better than the Water coating, however, the differences were dwarfed by the change from as sintered to aged. This implied that, either the wrong temperature was chosen for the oxidation testing or the coating was completely unsuitable for the temperature range and material.

The effect of the coating on Mg-Silicide samples was more pronounced since the uncoated samples did not survive, there was also more variation between the different coatings. As with the HMS when oxidized, the electrical resistivity of the Mg-Silicide increased and the absolute value of the Seebeck increased. For the sample with Solvent-Thick coating however the increase in resistance was relatively modest (+ 30% at 500 °C) compared to the other samples and it was counteracted by a modest increase in Seebeck (+18% at 500 °C), resulting in a similar ,or, at higher temperature, higher power factor.
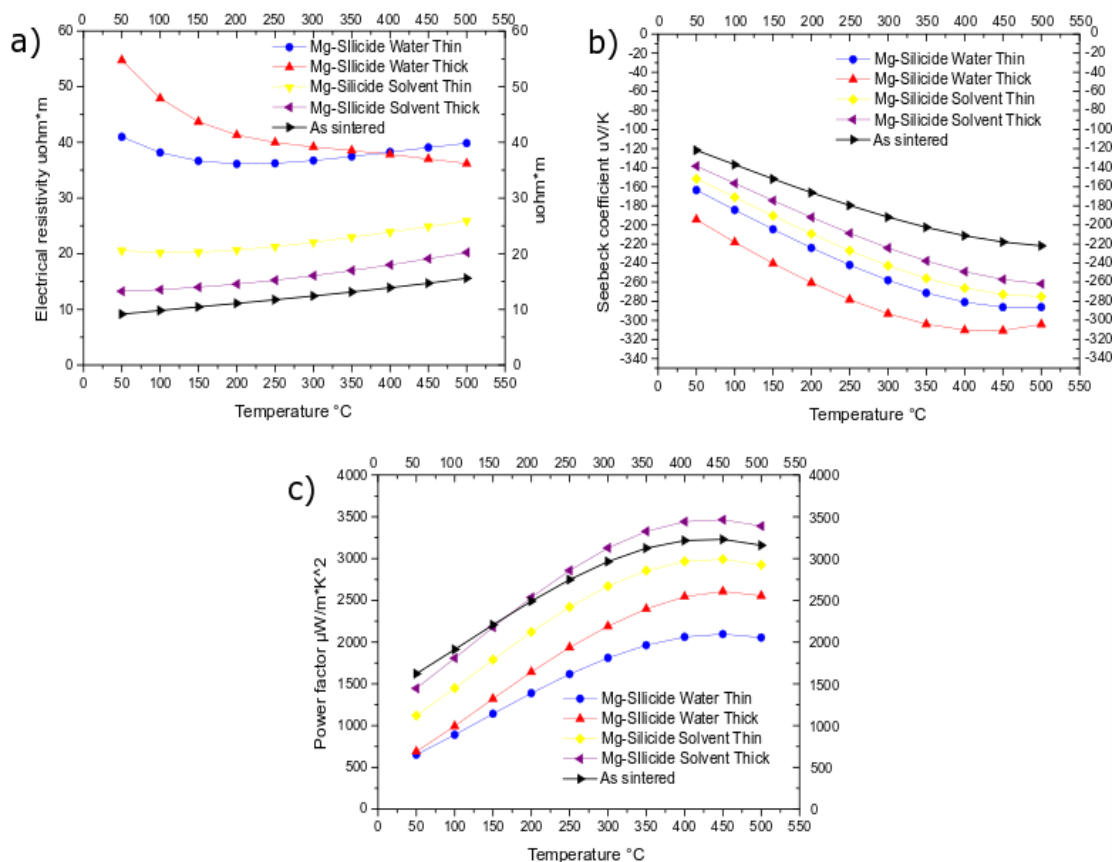
Figure 8.22 a) Electrical resistivity, b) Seebeck Coefficient and c) Power factor of Mg-Silicide samples.

If the increase in resistivity is taken as a proxy for oxidation damage, then the solvent coatings perform better than the water ones, which is consistent with the microstructures (Fig 18-20), where less cracking was visible. The Thick coating performed better than the Thin, even though the Thin coated samples was meant to have superior properties. Thin coatings typically has better adhesion as they suffer

less thermal mismatch and cracking. In this, because both coatings were heavily cracked after oxidation, the thicker coating provided a more torturous path for the oxygen to diffuse through, even when it used the cracks as a short cut. The thicker Water-based coating also performed better than the Thin one, which fits the previous explanation that the improved adhesion did not matter as much as the increased barrier thickness.

The mechanism by which the oxidation lead to a change in the thermoelectric properties was broadly similar to the HMS. During oxidation the magnesium was preferentially oxidized to MgO on the surface (XRD Fig 8.3) and therefore the underneath material was magnesium deficient. Different stoichiometric ratio of Mg_2Si and Mg_2Sn as well as Mg vacancy or interstitial can influence the electronic properties and explain the variation of properties [246-249].

Table 8.3 Summary table

No	Material	Coating	Application	Oxidation Temperature	Label	Layer Thickness μm	Resistivity at RT (μohm*m)	Visible description
1	HMS	None	None	None	HMS-as sintered		14	
2	HMS	None	None	550	HMS 550 °C	Crashed after polishing	28	Darkened
3	HMS	Cp4040	thin	550	HMS Water Thin	Crashed after polishing	30	Coating cracked on edges and faces
4	HMS	Cp4040-s1	thin	550	HMS Solvent Thin	Crashed after polishing	28	Coating cracked on edges and faces
5	Mg-Silicide	None	None	None	Mg-Silicide As-sintered		10	
6	Mg-Silicide	None	None	500 (destroyed)	Mg-Silicide 500 °C			Sample completely burned
7	Mg-Silicide	None	None	550 (destroyed)	Mg-Silicide 550 °C			Sample completely burned
8	Mg-Silicide	Cp4040	thick	500	Mg-Silicide Water Thick	2-20	55	Coating cracked on edges and faces (limited)
9	Mg-Silicide	Cp4040-s1	thick	500	Mg-Silicide Solvent Thick	6-12	14	Coating cracked on edges
10	Mg-Silicide	Cp4040	thin	500	Mg-Silicide Water Thin	11-20	42	Coating cracked on edges and faces
11	Mg-Silicide	Cp4040-s1	thin	500	Mg-Silicide Solvent Thin	28-36	20	Coating cracked on edges and faces

8.4 Conclusion

The hybrid coatings presented in this work were not able to provide protection to HMS at the temperature of 550 °C but proved to be somewhat effective at protecting Mg-Silicide at 500 °C. While the Mg-Silicide survived testing (unlike the uncoated samples), there was some oxidation on the surface, which affected the thermoelectric properties. The reason behind the limited performance of the coating was the significant crack formation, both during curing and more importantly during oxidation. This allowed appreciable amounts of oxygen to diffuse to the surface of the sample to form an oxide (Fig 8.3). Qualitatively it seems that the Solvent based resin had a better capability in reducing the oxidation. The "Thick" procedure seems to be more effective even when cracked as it simply provided a longer diffusion path to the oxygen.

Despite this, hybrid coatings seems to be promising for thermoelectrics, in particular because of their low curing temperature, and the availability of inexpensive commercial products, but further tests will be needed to increase the homogeneity of the layer over the substrate and identify the optimal thickness and curing conditions to prevent cracks. It is highly likely that these coatings would provide excellent protection for lower temperature materials without any further optimization.

Chapter 9 Conclusion and Future work

9.1 Conclusion

In this work a derivative of SPS was developed, allowing the sintering of materials at heating rates of several thousand degrees per minute. The setup was analysed with Finite Element Modelling and the temperature distribution in the setup was calculated using the electrical properties of Ni-doped skutterudite. This was done as it was typical of the type of materials this process was designed to sinter.

The modelling work highlighted the limitations of die-less Flash-SPS, which uses a pre-sintered pellet and is commonly used for high temperature ceramics. The model showed how large the temperature gradients were and the degree of overheating in some regions of the sample. These drawbacks were particularly extreme for thermoelectric materials since they have very low thermal conductivity and the effect of gradients would be more detrimental as they are often not mechanically strong and can suffer unwanted phase changes, melting or evaporation.

Another more practical limitation of traditional FSPS was that it needed cold pressed pellets, and this was a serious limitation for mechanically weak thermoelectric materials, as not only was this another step to processing but often the thermoelectric would be too plastic during sintering and deform excessively.

When attempting to model the SPS the first problem was that the data from the SPS could not be trusted, this was a serious problem and could completely invalidate any modelling done if the model was forced to fit wrong data from the SPS. This might have been a problem with other models developed by researchers using similar equipment. For that reason, everything was verified experimentally, which means the model should be transferable to other models of equipment once that machine is characterized. Once the model was developed it provided many useful insights that explained why FPSP was so difficult to optimize, with large temperature gradients, and why thermoelectric materials were so difficult in particular (the Seebeck effect). Both these problems have been hypothesized by academics working on SPS, but are very hard to actually measure experimentally. Not only does the model allow gradients to be modelled, it was used to develop a new die that reduced the Peltier induced gradient, and future work could include

further die improvements, with optimized metallic punches for even faster heating, and thermal spacers in the die or reducer. These could be optimized to pass current, but transfer limited heat while tolerating the pressing forces. Such spacers could be used to further reduce the energy used and limit axial temperature gradients. The modelling proved reliable, when top and bottom temperature were measured as the value were symmetric, the stainless steel was at a significantly lower temperature (probably sample as well) as it survived a graphite temperature of more than 1000 °C.

The stainless die setup was tested on three different thermoelectric materials belonging to different classes, a skutterudite (mid- temperature material), a sulphide (low temperature material) and a half-Heusler (a high temperature material), the effect on their microstructure and properties was analysed and compared with the literature. This showed that the hybrid setup developed was reasonably versatile, processing different materials with different levels of chemical reactivity (half-Heusler had titanium, Chalcopyrite had sulphur) and at very different temperatures, from 600 °C to 1040 °C, while producing reasonably dense samples (Tab 9.1) for all, even performing reactive sintering. Moreover the energy dissipated was significantly reduced (Tab 9.1)

Table 9.1 Summary of data for best hFSPS sample and reference SPS sample

Material	Process label	Temperature °C	Diameter mm	Density %	Energy dissipation kWh
Skutterudite	SPS	750	20	96	1.27
Skutterudite	hFSPS-cool	750	20	96	0.07
Chalcopyrite	SPS	500	15	99	0.56
Chalcopyrite	hFSPS-2	600	15	97	0.04+0.375
Half-Heusler	SPS	850	15	92.5	0.76
Half-Heusler	hFSPS-1040	1040	15	92.5	0.061

Ni-doped $CoSb_3$ was reactively sintered from elemental powders using three different processes, SPS, hybrid-Flash SPS with rapid cooling and Hybrid Flash SPS with a holding time. The hFSPS-cool sample resulted in high phase purity (92%) and high figure of merit (ZT 0.81 for hFSPS-cool vs 0.46 for SPS at 600 °C). This improvement was related to a reduction of the lattice thermal conductivity, while the electrical propertied remained unchanged. The effective doping is proved by the negative Seebeck of the material, since the un-doped sample is a p-type conductor. The microstructure of the various samples was quite different: the hFSPS-cool sample had an unusual spiral

pattern of grains homogeneously dispersed amongst the sub-micron grains; the hFSPS-hold sample had larger grains and the spiral structure appear to have grown, but lost some of the rotation in the spiral; in the SPS sample the spiral structure was even more devolved, with only regions of large grains instead of spirals. This spiral pattern was believed to be relate to the synthesis, not the flash sintering itself as it was no present in the other samples flashed in this work.

Zn-doped chalcopyrite was produced using SPS (SPS-500 °C) and hybrid-Flash SPS (hFSPS-1 600 °C), with one sample being produced by processing the same powder twice (hFSPS-2). However, the phase structure was difficult to interpret due to the complexity of phase diagram and the similarity of XRD patterns of the various sulphides. The SEM images proved the hFSPS sample to be a mixture of closely related phases, identified as chalcopyrite and talnakhite (a metal-enriched chalcopyrite). The sample processed twice was the only one that showed good temperature stability as the others did not maintain stable properties during a heating and cooling cycle. In all samples there was some change in composition/properties during processing, with annealing typically being used in literature to restore properties after sintering. While flash could not stop this change, it provided the control needed to restore the properties by simply reprocessing the material, which was much quicker than the long annealing times typically used (24 hours). This resulted in the hFSPS-2 having a ZT of 0.2 at 623 K, comparable to other similar compound in literature.

While the previous materials were relatively low temperature, both in their processing temperature and operating region, half-Heusler alloy was chosen to represent high temperature thermoelectric materials. Cu-doped TiNiSn half-Heusler samples were produced using SPS (850 °C) and hFSPS (at 980 °C and 1040 °C). Due to the difficulty of densifying the material, none of the samples were fully dense and the SPS and hFSPS samples had practically the same density (92.5 %). XRD detected small amounts of free Sn in the starting powder, which did not fully react during the sintering, the SPS sample also had XRD peaks of a full-Heusler phase ($TiNi_2Sn$), which was not seen in the flashed samples. The original powder was mostly made of agglomerates of much smaller particles (a few microns or less), while only some of the particles were loose. EDS detected the presence of oxygen in the powder, this was most likely titanium oxide, but no discrete oxide particles were visible (at least in the powder). The fracture surfaces of all samples showed the presence of a second phase at the grain boundaries, this was likely free Sn

acting as sintering aid. This phase was visible as a bright region in backscatter imaging, but could not be detected by EDS, likely due to the small thickness of the region. The SPS sample also showed some oxide particles at the grain boundaries, but no clear evidence of the full-Heusler phase. In the hFSPS-980 sample, EDS also detected oxygen, but no discrete particles could be identified. This suggested that the flash processing was capable of breaking up the oxides into smaller particles below the detection limit. The hFSPS-1040 sample also had a higher degree of grain cohesion since the surface suffered less grain pull out during polishing. Higher cohesion and an apparent meso-structure (grain and porosity) provided higher electrical conductivity and lower thermal conductivity.

With several different thermoelectric materials having been processed with the hybrid FSPS technique, some conclusions can be made about how the process affects materials in general, and advantages and disadvantages of the process evaluated.

- The total processing time was 50% or less (depending on pre-heating) than conventional SPS, and the energy consumption was greatly reduced (Tab 9.1)
- The heat treatment can be controlled (pre-heating, different sintering temperature) unlike traditional flash and FSPS.
- The total thermal conductivity of the samples was reduced for all of the materials tested, and this was not purely due to density or electrical conductivity. The thermal conductivity also became more stable with temperature after hFSPS processing. Fig (9.1)
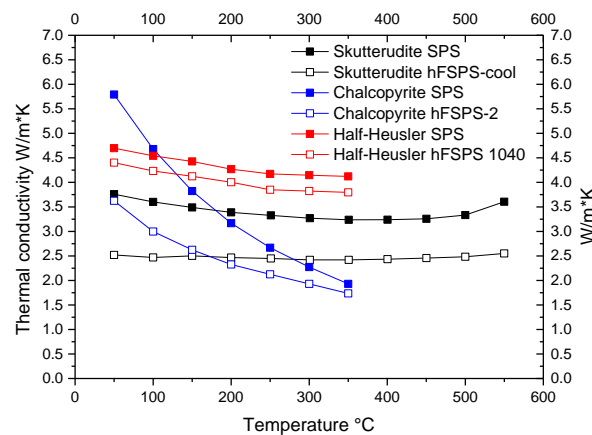
Figure 9.1 Thermal conductivity summary of best hFSPS sample and reference SPS

174

While the development of a new and useful ways to process thermoelectric materials is useful, especially for further academic research, they are of limited commercial use. HFSPS might take many years before it could be exploited industrially and might not ever be scaled up.

In an attempt to produce commercially exploitable improvement in thermoelectric modules, coatings were investigated. The aim was to increase the maximum operating temperature and service life of thermoelectric materials in air. Hybrid coatings were investigated as a way to protect easily oxidizable thermoelectric materials. Hybrid coatings proved to be somewhat effective at protecting Mg-Silicide samples, but left substantial room for improvement. The coating was found to significantly reduce the oxidation rate of the samples when tested at 500 °C, but did not prevent oxidation entirely. The Solvent-based coating material was superior to the water based coating, but not hugely. For HMS no coating was not needed to protect from oxidation at 500 °C and at 550 °C, but HMS was completely destroyed regardless of whether it was coated or not.

9.2. Future work

Flash sintering is a relatively new techniques and few studies have been carried out to understand the effect of fast heating rate on the functional properties of ceramics. As the field of flash sintering of functional materials is so immature, there are many possibilities for future work. Concerning the techniques and materials presented in this thesis, there is some general consideration to make for further work, which applies, to all of them:

- Effect of different doping concentration
- Effect of grain size

This work was a case study were the feasibility of hybrid flash-SPS was demonstrated for different classes of material, at different ranges of sintering temperature. Because of the novelty of the process, our initial work focused more on the effectiveness of the sintering method, simply attempting to achieve dense material as a starting point, more than the compositional optimisation. Since the feasibility has been proven in this work, further studies should focus on composition, since the optimal concentration of dopant will be affected by the hFSPS process.

In this work, the powders were used as provided and no extra processing was used like ball milling or annealing. Just like composition, the hFSPS process can be affected by the condition of the starting powder. Powders with a narrower distribution of particle size and even nano-powder would be of interest for a higher degree of microstructural tuning. In particular, because of the lower grain growth experienced during hFSPS with respect to conventional SPS.

9.2.1 Modelling

The study of the SPS furnace and its electrical output should provide a firm basis for future work. With the use of voltage control, not current, being used in this work, a clear improvement was achieved compared to previous models, as the SPS is fundamentally a voltage-controlled device. However, in any future work it is highly recommended that the particular model of SPS is characterized with respect to the real voltage and current outputs, as well as the fundamental control type (voltage or current).

The modelling work did provide some useful insights into the temperature distribution of FSPS an hFSPS. To further refine the model, the most important parameter to further understand is the vertical contact resistance, as it was shown to significantly influence the temperature distribution. This problem is well known in the literature as it is very difficult to measure directly and it would require significant instrumentation. Alternatively using graphite as a sample and measuring current within the sample and the stainless-steel die could be used to compare modelling and experimental results. The contact resistance could then be adjusted until a good match is found, but this presumes there are no other errors in the model.

9.2.2 Skutterudite

Ni-doped $CoSb_3$ was successfully sintered and synthesized through a single step process obtaining a high figure of merit for the composition used. The same approach could be used for a p-type material to provide a couple of compatible p and n type leg for a thermoelectric devices. A wider range of temperatures could be tested to further optimize the process. Filled skutterudite should be tested, as the effect of fast heating rate and current is unknown on the filling ratio and effectiveness of the rattler element (with filling typically requiring many hours).

9.2.3 Chalcopyrite

The complexity of the phase diagram and the risk of evaporation made this material very challenging to work with, but the potential of this process to stabilize the sample properties is very interesting since sulphides are among the cheapest thermoelectric materials.

A better choice would be to start from an undoped system and perform a careful Rietvald refinement to clearly assess the presence of a single or multiple phases as it can significantly help with the data interpretation. Other sulphides, tetrahedrite as first choice, might represents a better sulphur-based material to work with, as it is a better characterized material.

9.2.4 Half-Heusler

The sintering of the half-Heusler samples was challenging due to the high temperature and pressure required to obtain even a relatively high density (1040°C). The high values needed sometime led to cracking in the graphite and damage to the stainless die. For that reason, further work on hFSPS of half-Heusler would benefit from an improved material for the die, with TZM being a good choice to replace stainless steel. Compositionally a higher content of Cu would be expected to give better properties since the electrical properties of the hFSPS samples were similar to hot press samples with low Cu doping.

9.2.5 Hybrid coatings

The oxidation rate was significantly reduced with a coating for the Mg-silicide but commercial thermoelectric devices are expected to work for several years, equivalent to practically no oxidation during the timescale of the accelerated testing. This meant that the hybrid coating might be more effective in protecting lower temperature thermoelectric materials. The preliminary testing of the two coatings highlighted how important the coating procedure was. The performance of the coating could likely be significantly improved if a new application method could be developed that applied it in a fashion that avoided thinning at the corners. Because the oxidation always seemed to start at the corners, where the coating was thinnest.

In this work a new sintering process was developed, improving on related flash and FSPS techniques. This process was developed with significant input from modelling, and applied to thermometric materials, where it showed noticeable improvements over SPS.

It reduced both the processing time and the energy required to sinter them, allowing the synthesis of complex compounds. There is a large scope for the application of this technique and I can only hope this technique can be built on and applied to new material systems, and the modelling that underpins it develops and grows in accuracy allowing a better planning of experiments.

List of publications

Du, B.; **Gucci, F**.; Porwal, H.; Grasso, S.; Mahajan, A.; and Reece, M. (2017), *Flash Spark Plasma Sintering of Magnesium Silicide Stannide with Improved Thermoelectric Properties*, J Mat Chem C., published online 19 Jan 2017.

Gucci F., Saunders T.G., Reece M. *In situ synthesis of n-type unfilled skutterudite with reduced thermal conductivity by hybrid Flash-Spark Plasma Sintering*, Scripta Materialia, 157, 58-61 (2018)

M.Salvo, F.Smeacetto, F.D`Isanto, G.Viola, P.Demitri, **F.Gucci**, M.J.Reece *Glass Ceramic oxidation protection of higher manganese silicide thermoelectrics* Journal of the European Ceramic Society (2018)

Bhuvanesh Srinivasan , Régis Gautier, **Francesco Gucci**, Bruno Fontaine, Jean-François Halet, François Chevìre, Catherine Boussard-Pledel, Michael J.Reece and Bruno Bureau *Impact of Coinage Metal Insertion on the Thermoelectric Properties of GeTe Solid-State Solution* Journal of Physical Chemistry C, 122(1), 227-235 (2017)

Bhuvanesh Srinivasan, **Francesco Gucci**, Catherine Boussard-Pledel, François Chevìre, Michael J.Reece, Sylvain Tricot, Laurent Calvez, Bruno Bureau *Enhancement in thermoelectric perfomances of n-type Pb-deficit Pb-Sb-Te alloys* Journal of Alloys and Compounds, 729, 198-202 (2017)

M.Yu, T.Saunders, T.C .Su, **F.Gucci**, M.Reece *Effect of heat treatment on the properties of wood-derived biocarbon structures, Materials, (2018)*

Bhuvanesh Srinivasan, Bruno Fontaine, **Francesco Gucci**, Vincent Dorcet, Theo Graves Saunders, Min Yu, François Chevìre, Catherine Boussard-Pledel, Jean-François Halet, Régis Gautier, Mike J. Reece *The effect of Processing Route on the Thermoelectric Performance of Nanostructured CuPb18SbTe20* Inorg.Chem 57 (20) 2018 pp 12976-12986

Bhuvanesh Srinivasan, Alain Gellé, **Francesco Gucci**, Catherine Boussard-Pledel, Bruno Fontaine, Régis Gautier, Jean- François Halet, Mike Reece *Realizing a Stable High Thermoelectric zT of 2 over a Broad Temperature Range in Ge1-x-yGaxSbyTeVia Band Engineering and Hybrid Flash-SPS Processing* Inorg.Chem.Front. 2018

Ruizhi Zhang, **Francesco Gucci**, Hongyu Zhu, Kan Chen, Michael J. Reece *Datadriven Design of Eco-friendly Thermoelectric High Entropy Sulfides* Inorg. Chem. September 2018

Gianmarco Taveri, Salvatore Grasso, **Francesco Gucci**, Jaromir Tousek, Ivo Doulhy, *Bio-Inspired Hydro-Pressure Consolidation of Silica* Adv. Funct. Mater. October 2018

References

1. TATSUO TAKAISH, A.N., RYOUJI NAKANO,KATSUHIKO SAKAGUCHI, *Approach to High Efficiency Diesel and Gas Engines.* Mitsubishi Heavy Industries, Ltd. Technical Review 2008. **1**(1): p. 4.

2. Li, G.Q., et al., *A review of solar photovoltaic-thermoelectric hybrid system for electricity generation.* Energy, 2018. **158**: p. 41-58.

3. Rowe, D.M., *CRC Handbook of Thermoelectrics.* 1995.

4. Hsu, K.F., et al., *Cubic AgPbmSbTe2+m: Bulk thermoelectric materials with high figure of merit.* Science, 2004. **303**(5659): p. 818-821.

5. Cao, Y.Q., et al., *Syntheses and thermoelectric properties of Bi2Te3/Sb2Te3 bulk nanocomposites with laminated nanostructure.* Applied Physics Letters, 2008. **92**(14).

6. Venkatasubramanian, R., et al., *Thin-film thermoelectric devices with high room-temperature figures of merit.* Nature, 2001. **413**(6856): p. 597-602.

7. Rogl, G., et al., *Nanostructuring of p- and n-type skutterudites reaching figures of merit of approximately 1.3 and 1.6, respectively.* Acta Materialia, 2014. **76**: p. 434-448.

8. Zhao, L.D., V.P. Dravid, and M.G. Kanatzidis, *The panoscopic approach to high performance thermoelectrics.* Energy & Environmental Science, 2014. **7**(1): p. 251-268.

9. He, J.Q., M.G. Kanatzidis, and V.P. Dravid, *High performance bulk thermoelectrics via a panoscopic approach.* Materials Today, 2013. **16**(5): p. 166-176.

10. Biswas, K., et al., *High-performance bulk thermoelectrics with all-scale hierarchical architectures (vol 489, pg 414, 2012).* Nature, 2012. **490**(7421).

11. Khan, A.U., et al., *Nano-micro-porous skutterudites with 100% enhancement in ZT for high performance thermoelectricity.* Nano Energy, 2017. **31**: p. 152-159.

12. Liang, T., et al., *Panoscopic approach for high-performance Te-doped skutterudite.* Npg Asia Materials, 2017. **9**.

13. Tian, Z.T., S. Lee, and G. Chen, *Heat Transfer in Thermoelectric Materials and Devices.* Journal of Heat Transfer-Transactions of the Asme, 2013. **135**(6).

14. Sumirat, I., Y. Ando, and S. Shimamura, *Theoretical consideration of the effect of porosity on thermal conductivity of porous materials.* Journal of Porous Materials, 2006. **13**(3-4): p. 439-443.

15. Guillon, O., et al., *Field-Assisted Sintering Technology/Spark Plasma Sintering: Mechanisms, Materials, and Technology Developments.* Advanced Engineering Materials, 2014. **16**(7): p. 830-849.

16. Cologna, M., B. Rashkova, and R. Raj, *Flash Sintering of Nanograin Zirconia in < 5 s at 850 degrees C.* Journal of the American Ceramic Society, 2010. **93**(11): p. 3556-3559.

17. Shomrat, N., et al., *Flash sintering of potassium-niobate.* Journal of the European Ceramic Society, 2015. **35**(7): p. 2209-2213.

18. Zhang, Y.Y., J.Y. Nie, and J. Luo, *Effects of phase and doping on flash sintering of TiO2.* Journal of the Ceramic Society of Japan, 2016. **124**(4): p. 296-300.

19. Zapata-Solvas, E., et al., *Preliminary investigation of flash sintering of SiC.* Journal of the European Ceramic Society, 2013. **33**(13-14): p. 2811-2816.

20. Yu, M., et al., *Review of flash sintering: materials, mechanisms and modelling.* Advances in Applied Ceramics, 2017. **116**(1): p. 24-60.

21. Grasso, S., et al., *Flash Spark Plasma Sintering (FSPS) of Pure ZrB2.* Journal of the American Ceramic Society, 2014. **97**(8): p. 2405-2408.

22. Grasso, S., et al., *Flash Spark Plasma Sintering (FSPS) of and SiC.* Journal of the American Ceramic Society, 2016. **99**(5): p. 1534-1543.

23. Du, B.L., et al., *Flash spark plasma sintering of magnesium silicide stannide with improved thermoelectric properties.* Journal of Materials Chemistry C, 2017. **5**(6): p. 1514-1521.

24. Chen, G., *http://www.sil.si.edu/silpublications/dibner-library-lectures/scientific-discoveries/text-lecture.htm.*

25. Alam, H. and S. Ramakrishna, *A review on the enhancement of figure of merit from bulk to nano-thermoelectric materials.* Nano Energy, 2013. **2**(2): p. 190-212.

26. Shakouri, A., *Recent Developments in Semiconductor Thermoelectric Physics and Materials.* Annual Review of Materials Research, Vol 41, 2011. **41**: p. 399-431.

27. LeBlanc, S., *Thermoelectric generators: Linking material properties and systems engineering for waste heat recovery applications.* Sustainable Materials and Technologies, 2014. **1**: p. 26-35.

28. Zhang, X. and L.-D. Zhao, *Thermoelectric materials: Energy conversion between heat and electricity.* Journal of Materiomics, 2015.

29. He, W., et al., *Recent development and application of thermoelectric generator and cooler.* Applied Energy, 2015. **143**: p. 1-25.

30. Slack, G.A., *The thermal conductivity of nonmetallic crystals.* Solid state physics, 1979. **34**: p. 1-71.

31. Snyder, G.J. and E.S. Toberer, *Complex thermoelectric materials.* Nature Materials, 2008. **7**(2): p. 105-114.

32. Vineis, C.J., et al., *Nanostructured Thermoelectrics: Big Efficiency Gains from Small Features.* Advanced Materials, 2010. **22**(36): p. 3970-3980.

33. Srinivasan, B., et al., *Thermoelectric Properties of Highly-Crystallized Ge-Te-Se Glasses Doped with Cu/Bi.* Materials, 2017. **10**(4).

34. Heremans, J.P., et al., *Enhancement of thermoelectric efficiency in PbTe by distortion of the electronic density of states.* Science, 2008. **321**(5888): p. 554-557.

35. Ko, D.K., Y.J. Kang, and C.B. Murray, *Enhanced Thermopower via Carrier Energy Filtering in Solution-Processable Pt-Sb2Te3 Nanocomposites.* Nano Letters, 2011. **11**(7): p. 2841-2844.

36. Pei, Y.Z., et al., *Convergence of electronic bands for high performance bulk thermoelectrics.* Nature, 2011. **473**(7345): p. 66-69.

37. Sootsman, J.R., D.Y. Chung, and M.G. Kanatzidis, *New and Old Concepts in Thermoelectric Materials.* Angewandte Chemie-International Edition, 2009. **48**(46): p. 8616-8639.

38. Goldsmid, H.J., *Heat Conduction in Bismuth Telluride.* Proc. Phys. Soc., 1958. **71**(4): p. 633.

39. Goldsmid, H.J., *The Electrical Conductivity and Thermoelectric Power of Bismuth Telluride.* Proc. Phys. Soc., 1958. **71**(4).

40. Goldsmid, H.J., *Recent Studies of Bismuth Telluride and Its Alloys.* Journal of Applied Physics, 1961. **32**(10): p. 2198-2202.

41. Goldsmid, H.J., *Bismuth Telluride and Its Alloys as Materials for Thermoelectric Generation.* Materials, 2014. **7**(4): p. 2577-2592.

42. Lim, S.S., et al., *Effect of spark plasma sintering conditions on the thermoelectric properties of (Bi0.25Sb0.75)(2)Te-3 alloys.* Journal of Alloys and Compounds, 2016. **678**: p. 396-402.

43. Jiang, Q.H., et al., *Large ZT enhancement in hot forged nanostructured p-type Bi0.5Sb1.5Te3 bulk alloys.* Journal of Materials Chemistry A, 2014. **2**(16): p. 5785-5790.

44. Shen, J.J., et al., *The texture related anisotropy of thermoelectric properties in bismuth telluride based polycrystalline alloys.* Applied Physics Letters, 2011. **99**(12).

45. Fleurial, J.P., et al., *Thermal-Properties of High-Quality Single-Crystals of Bismuth Telluride .1. Experimental Characterization.* Journal of Physics and Chemistry of Solids, 1988. **49**(10): p. 1237-1247.

46. Ivanova, L.D. and Y.V. Granatkina, *Thermoelectric properties of Bi2Te3-Sb2Te3 single crystals in the range 100-700 K.* Inorganic Materials, 2000. **36**(7): p. 672-677.

47. Jiang, J., et al., *Thermoelectric properties of p-type (Bi2Te3)(x)(Sb2Te3)(1-x) crystals prepared via zone melting.* Journal of Crystal Growth, 2005. **277**(1-4): p. 258-263.

48. Fan, X.A., et al., *Preferential orientation and thermoelectric properties of p-type Bi0.4Sb1.6Te3 system alloys by mechanical alloying and equal channel angular extrusion.* Journal of Alloys and Compounds, 2008. **461**(1-2): p. 9-13.

49. Zhu, T.J., et al., *Hot deformation induced bulk nanostructuring of unidirectionally grown p-type (Bi,Sb)(2)Te-3 thermoelectric materials.* Journal of Materials Chemistry A, 2013. **1**(38): p. 11589-11594.

50. Luo, Y.B., et al., *Melting and solidification of bismuth antimony telluride under a high magnetic field: A new route to high thermoelectric performance.* Nano Energy, 2015. **15**: p. 709-718.

51. Xie, W.J., et al., *High thermoelectric performance BiSbTe alloy with unique low-dimensional structure.* Journal of Applied Physics, 2009. **105**(11).

52. Il Kim, S., et al., *Dense dislocation arrays embedded in grain boundaries for high-performance bulk thermoelectrics.* Science, 2015. **348**(6230): p. 109-114.

53. Morelli, D.T., et al., *Low-Temperature Transport-Properties of P-Type Cosb3.* Physical Review B, 1995. **51**(15): p. 9622-9628.

54. Katsuyama, S., et al., *Effect of NiSb on the thermoelectric properties of skutterudite CoSb3.* Journal of Applied Physics, 2003. **93**(5): p. 2758-2764.

55. Park, K.H., et al., *Thermoelectric properties of Yb-filled CoSb3 skutterudites.* Journal of the Korean Physical Society, 2014. **65**(4): p. 491-495.

56. Kitagawa, H., et al., *Temperature dependence of thermoelectric properties of Ni-doped CoSb3.* Journal of Physics and Chemistry of Solids, 2005. **66**(10): p. 1635-1639.

57. He, Q.Y., et al., *Nanostructured Thermoelectric Skutterudite Co1-xNixSb3 Alloys.* Journal of Nanoscience and Nanotechnology, 2008. **8**(8): p. 4003-4006.

58. Gharleghi, A. and C.J. Liu, *Rapid fabrication and transport properties of n-type Co4-xNixSb12 via modified polyol process synthesis combined with evacuated-and-encapsulated sintering.* Journal of Alloys and Compounds, 2014. **592**: p. 277-282.

59. Tan, G.J., et al., *Rapid preparation of CeFe4Sb12 skutterudite by melt spinning: rich nanostructures and high thermoelectric performance.* Journal of Materials Chemistry A, 2013. **1**(40): p. 12657-12668.

60. Rogl, G., et al., *Effect of HPT processing on the structure, thermoelectric and mechanical properties of Sr0.07Ba0.07Yb0.07Co4Sb12.* Journal of Alloys and Compounds, 2012. **537**: p. 183-189.

61. Rull-Bravo, M., et al., *Skutterudites as thermoelectric materials: revisited.* Rsc Advances, 2015. **5**(52): p. 41653-41667.

62. Kim, M.J., et al., *Electronic transport properties of Ni-doped CoSb3 prepared by encapsulated induction melting.* Ict'06: Xxv International Conference on Thermoelectrics, Proceedings, 2006: p. 439-+.

63. Ur, S.C. and I.H. Kim, *Electronic Transport Properties of Ni-doped CoSb3 Prepared by Hot Pressing.* Journal of the Korean Physical Society, 2009. **55**(3): p. 942-946.

64. Ballikaya, S., et al., *High thermoelectric performance of In, Yb, Ce multiple filled CoSb3 based skutterudite compounds.* Journal of Solid State Chemistry, 2012. **193**: p. 31-35.

65. Khovaylo, V.V., et al., *Rapid preparation of InxCo4Sb12 with a record-breaking ZT=1.5: the role of the In overfilling fraction limit and Sb overstoichiometry.* Journal of Materials Chemistry A, 2017. **5**(7): p. 3541-3546.

66. Zhang, X., et al., *In-situ SPS synthesis and thermoelectric properties of REy(Fe/Ni),Co4-xSb12 compounds.* Rare Metal Materials and Engineering, 2007. **36**(6): p. 968-972.

67. Zhang, X., et al., *In situ synthesis and thermoelectric properties of (Fe/Ni)(x)CO4-xSb12 compounds by SPS.* Journal of Alloys and Compounds, 2008. **457**(1-2): p. 368-371.

68. Zhang, Y.B., et al., *The thermodynamic assessment of the ternary Co-Ni-Sb system.* Calphad-Computer Coupling of Phase Diagrams and Thermochemistry, 2009. **33**(2): p. 405-414.

69. Bertini, L., et al., *Nanostructured Co1-xNixSb3 skutterudites: Synthesis, thermoelectric properties, and theoretical modeling.* Journal of Applied Physics, 2003. **93**(1): p. 438-447.

70. Stiewe, C., et al., *Nanostructured Co1-xNix(Sb1-yTey)(3) skutterudites: Theoretical modeling, synthesis and thermoelectric properties.* Journal of Applied Physics, 2005. **97**(4).

71. Jung, J.Y., K.H. Park, and I.H. Kim, *Transport and Thermoelectric Properties of Sn-filled/Ni-doped CoSb3 Skutterudites.* Physics of Semiconductors: 30th International Conference on the Physics of Semiconductors, 2011. **1399**.

72. Shi, X., et al., *Multiple-Filled Skutterudites: High Thermoelectric Figure of Merit through Separately Optimizing Electrical and Thermal Transports (vol 133, pg 7837, 2011).* Journal of the American Chemical Society, 2012. **134**(5): p. 2842-2842.

73. Rogl, G., et al., *n-Type skutterudites (R,Ba,Yb)(y)Co4Sb12 (R = Sr, La, Mm, DD, SrMm, SrDD) approaching ZT approximate to 2.0.* Acta Materialia, 2014. **63**: p. 30-43.

74. Rogl, G., et al., *New bulk p-type skutterudites DD0.7Fe2.7Co1.3Sb12-xXx (X = Ge, Sn) reaching ZT > 1.3.* Acta Materialia, 2015. **91**: p. 227-238.

75. Huang, L.H., et al., *Recent progress in half-Heusler thermoelectric materials.* Materials Research Bulletin, 2016. **76**: p. 107-112.

76. Sakurada, S. and N. Shutoh, *Effect of Ti substitution on the thermoelectric properties of (Zr,Hf)NiSn half-Heusler compounds.* Applied Physics Letters, 2005. **86**(8).

77. Rogl, G., et al., *(V,Nb)-doped half Heusler alloys based on {Ti,Zr,Hf}NiSn with high ZT.* Acta Materialia, 2017. **131**: p. 336-348.

78. Downie, R.A., et al., *Metal Distributions, Efficient n-Type Doping, and Evidence for in-Gap States in TiNiMySn (M = Co, Ni, Cu) half-Heusler Nanocomposites.* Chemistry of Materials, 2015. **27**(7): p. 2449-2459.

79. Barczak, S.A., et al., *Grain-by-Grain Compositional Variations and Interstitial Metals-A New Route toward Achieving High Performance in Half-Heusler Thermoelectrics.* Acs Applied Materials & Interfaces, 2018. **10**(5): p. 4786-4793.

80. Hea, R., et al., *Achieving high power factor and output power density in p-type half-Heuslers Nb1-xTixFeSb.* Proceedings of the National Academy of Sciences of the United States of America, 2016. **113**(48): p. 13576-13581.

81. Schrade, M., et al., *The role of grain boundary scattering in reducing the thermal conductivity of polycrystalline XNiSn (X = Hf, Zr, Ti) half-Heusler alloys.* Scientific Reports, 2017. **7**.

82. Kim, K.S., et al., *Direct Observation of Inherent Atomic-Scale Defect Disorders responsible for High-Performance Ti1-xHfxNiSn1-ySby Half-Heusler Thermoelectric Alloys.* Advanced Materials, 2017. **29**(36).

83. Lei, Y., et al., *Microwave synthesis, microstructure, and thermoelectric properties of Zr substituted ZrxTi1-xNiSn half-Heusler bulks.* Materials Letters, 2017. **201**: p. 189-193.

84. Kirievsky, K., Y. Gelbstein, and D. Fuks, *Phase separation and antisite defects in the thermoelectric TiNiSn half-Heusler alloys.* Journal of Solid State Chemistry, 2013. **203**: p. 247-254.

85. Romaka, L., et al., *Experimental and DFT study of the V–Co–Sb ternary system.* Journal of Alloys and Compounds, 2018. **739**: p. 771-779.

86. Chen, S. and Z.F. Ren, *Recent progress of half-Heusler for moderate temperature thermoelectric applications.* Materials Today, 2013. **16**(10): p. 387-395.

87. Jager-Waldau, A., *Progress in chalcopyrite compound semiconductor research for photovoltaic applications and transfer of results into actual solar cell production.* Solar Energy Materials and Solar Cells, 2011. **95**(6): p. 1509-1517.

88. Xu, R.C., et al., *Recent Developments of All-Solid-State Lithium Secondary Batteries with Sulfide Inorganic Electrolytes.* Chemistry-a European Journal, 2018. **24**(23): p. 6007-+.

89. Liu, Z.H., et al., *Enhanced thermoelectric performance of Bi2S3 by synergistical action of bromine substitution and copper nanoparticles.* Nano Energy, 2015. **13**: p. 554-562.

90. Yu, Y.Q., et al., *Thermoelectric properties of Ag-doped bismuth sulfide polycrystals prepared by mechanical alloying and spark plasma sintering.* Materials Chemistry and Physics, 2011. **131**(1-2): p. 216-222.

91. Fitriani, F., et al., *Enhancement of Thermoelectric Properties in Cold Pressed Nickel Doped Bismuth Sulfide Compounds.* Electronic Materials Letters, 2018. **14**(6): p. 689-699.

92. Guilmeau, E., Y. Breard, and A. Maignan, *Transport and thermoelectric properties in Copper intercalated TiS2 chalcogenide.* Applied Physics Letters, 2011. **99**(5).

93. Ohta, M., et al., *Thermoelectric properties of Ti1+xS2 prepared by CS2 sulfurization.* Acta Materialia, 2012. **60**(20): p. 7232-7240.

94. Beaumale, M., et al., *Electron doping and phonon scattering in Ti1+xS2 thermoelectric compounds.* Acta Materialia, 2014. **78**: p. 86-92.

95. Zhao, L.D., et al., *High Performance Thermoelectrics from Earth-Abundant Materials: Enhanced Figure of Merit in PbS by Second Phase Nanostructures.* Journal of the American Chemical Society, 2011. **133**(50): p. 20476-20487.

96. Zhao, L.D., et al., *Raising the Thermoelectric Performance of p-Type PbS with Endotaxial Nanostructuring and Valence-Band Offset Engineering Using CdS and ZnS.* Journal of the American Chemical Society, 2012. **134**(39): p. 16327-16336.

97. Johnsen, S., et al., *Nanostructures Boost the Thermoelectric Performance of PbS.* Journal of the American Chemical Society, 2011. **133**(10): p. 3460-3470.

98. Zhou, B.Q., et al., *Thermoelectric Properties of SnS with Na-Doping.* Acs Applied Materials & Interfaces, 2017. **9**(39): p. 34033-34041.

99. Tan, Q., et al., *Thermoelectrics with earth abundant elements: low thermal conductivity and high thermopower in doped SnS.* Journal of Materials Chemistry A, 2014. **2**(41): p. 17302-17306.

100. He, Y., et al., *High Thermoelectric Performance in Non-Toxic Earth-Abundant Copper Sulfide.* Advanced Materials, 2014. **26**(23): p. 3974-3978.

101. Laughlin, D.J.C.D.E., *The Cu-S (Copper-Sulfur) system.* Journal of Phase Equilibria and Diffusion, 1983. **4**(3).

102. Liu, H.L., et al., *Copper ion liquid-like thermoelectrics.* Nature Materials, 2012. **11**(5): p. 422-425.

103. Dennler, G., et al., *Are Binary Copper Sulfides/Selenides Really New and Promising Thermoelectric Materials?* Advanced Energy Materials, 2014. **4**(9).

104. Skoug, E.J. and D.T. Morelli, *Role of Lone-Pair Electrons in Producing Minimum Thermal Conductivity in Nitrogen-Group Chalcogenide Compounds.* Physical Review Letters, 2011. **107**(23).

105. Nielsen, M.D., V. Ozolins, and J.P. Heremans, *Lone pair electrons minimize lattice thermal conductivity.* Energy & Environmental Science, 2013. **6**(2): p. 570-578.

106. Heo, J., et al., *Enhanced Thermoelectric Performance of Synthetic Tetrahedrites.* Chemistry of Materials, 2014. **26**(6): p. 2047-2051.

107. Ang, R., et al., *Thermoelectricity Generation and Electron–Magnon Scattering in a Natural Chalcopyrite Mineral from a Deep-Sea Hydrothermal Vent.* Angewandte Chemie International Edition, 2015. **54**(44): p. 12909-12913.

108. Tsujii, N. and T. Mori, *High Thermoelectric Power Factor in a Carrier-Doped Magnetic Semiconductor CuFeS2.* Applied Physics Express, 2013. **6**(4).

109. Shay, J.L. and J.H. Wernick, *Ternary chalcopyrite semiconductors: growth, electronic properties, and applications: international series of monographs in the science of the solid state.* Vol. 7. 2017: Elsevier.

110. Cabri, L.J., *New data on Phase Relations in the Cu-Fe-S System.* Economic Geology, 1973. **68**(4): p. 443-454.

111. Momma, K. and F. Izumi, *VESTA 3 for three-dimensional visualization of crystal, volumetric and morphology data.* Journal of Applied Crystallography, 2011. **44**: p. 1272-1276.

112. Engin, T.E., A.V. Powell, and S. Hull, *A high temperature diffraction-resistance study of chalcopyrite, CuFeS2.* Journal of Solid State Chemistry, 2011. **184**(8): p. 2272-2277.

113. Li, J.H., Q. Tan, and J.F. Li, *Synthesis and property evaluation of CuFeS2-x as earth-abundant and environmentally-friendly thermoelectric materials.* Journal of Alloys and Compounds, 2013. **551**: p. 143-149.

114. Xie, H.Y., et al., *Thermoelectric performance of CuFeS2+2x composites prepared by rapid thermal explosion.* Npg Asia Materials, 2017. **9**.

115. Li, Y.L., et al., *Thermoelectric transport properties of diamond-like Cu1-xFe1+xS2 tetrahedral compounds.* Journal of Applied Physics, 2014. **116**(20).

116. Tsujii, N., T. Mori, and Y. Isoda, *Phase Stability and Thermoelectric Properties of CuFeS2-Based Magnetic Semiconductor.* Journal of Electronic Materials, 2014. **43**(6): p. 2371-2375.

117. Xie, H.Y., et al., *The Role of Zn in Chalcopyrite CuFeS2: Enhanced Thermoelectric Properties of Cu1-xZnxFeS2 with In Situ Nanoprecipitates.* Advanced Energy Materials, 2017. **7**(3).

118. Kitakaze, A., *Phase relation of some sulfide systems-(4) Especially Cu-Fe-S system.* Vol. 68. 2018.

119. Hall, S.R., *Crystal structures of the chalcopyrite series.* The Canadian Mineralogist, 1975. **13**(2): p. 168-172.

120. Putnis, A. and J.D.C. McConnell, *The transformation behaviour of metal-enriched chalcopyrite.* Contributions to Mineralogy and Petrology, 1976. **58**(2): p. 127-136.

121. Putnis, A., *Talnakhite and mooihoekite; the accessibility of ordered structures in the metal-rich region around chalcopyrite.* The Canadian Mineralogist, 1978. **16**(1): p. 23-30.

122. Svechnikova, T.E., et al., *Thermoelectric properties of (Bi2Te3)(1-x-y)(Sb2Te3)(x)(Sb2Se3)(y) single crystals.* Inorganic Materials, 2005. **41**(10): p. 1043-1049.

123. Saramat, A., et al., *Large thermoelectric figure of merit at high temperature in Czochralski-grown clathrate Ba8Ga16Ge30.* Journal of Applied Physics, 2006. **99**(2): p. 023708.

124. Appel, O., et al., *Effects of Microstructural Evolution on the Thermoelectric Properties of Spark-Plasma-Sintered Ti0.3Zr0.35Hf0.35NiSn Half-Heusler Compound.* Journal of Electronic Materials, 2013. **42**(7): p. 1340-1345.

125. Serrano-Sanchez, F., et al., *Enhanced figure of merit in nanostructured (Bi,Sb)(2)Te-3 with optimized composition, prepared by a straightforward arc-melting procedure.* Scientific Reports, 2017. **7**.

126.   Kuo, C.H., et al., *Thermoelectric transport properties of bismuth telluride bulk materials fabricated by ball milling and spark plasma sintering.* Journal of Alloys and Compounds, 2010. **496**(1-2): p. 687-690.

127.   Peruman, K.V. and M. Mahendran, *Ball milling effect on structural and magnetic properties of Ni-Mn-Ga ferromagnetic nanoparticles.* Pure and Applied Chemistry, 2011. **83**(11): p. 2071-2077.

128.   Schilz, J., et al., *Synthesis of thermoelectric materials by mechanical alloying in planetary ball mills.* Powder Technology, 1999. **105**(1-3): p. 149-154.

129.   Li, J.F., et al., *Processing of advanced thermoelectric materials.* Science China-Technological Sciences, 2017. **60**(9): p. 1347-1364.

130.   Poudel, B., et al., *High-thermoelectric performance of nanostructured bismuth antimony telluride bulk alloys.* Science, 2008. **320**(5876): p. 634-638.

131.   Li, J.H., et al., *BiSbTe-Based Nanocomposites with High ZT : The Effect of SiC Nanodispersion on Thermoelectric Properties.* Advanced Functional Materials, 2013. **23**(35): p. 4317-4323.

132.   Hu, L.P., et al., *Point Defect Engineering of High-Performance Bismuth-Telluride-Based Thermoelectric Materials.* Advanced Functional Materials, 2014. **24**(33): p. 5211-5218.

133.   Liu, W.S., et al., *Enhanced thermoelectric properties in CoSb(3-x)Te(x) alloys prepared by mechanical alloying and spark plasma sintering.* Journal of Applied Physics, 2007. **102**(10).

134.   Yang, J.Y., et al., *Synthesis of CoSb3 skutterudite by mechanical alloying.* Journal of Alloys and Compounds, 2004. **375**(1-2): p. 229-232.

135.   Liu, W.S., et al., *Improvement of Thermoelectric Performance of CoSb3-xTex Skutterudite Compounds by Additional Substitution of IVB-Group Elements for Sb.* Chemistry of Materials, 2008. **20**(24): p. 7526-7531.

136.   Ge, Z.H., et al., *Synthesis and transport property of Cu1.8S as a promising thermoelectric compound.* Chemical Communications, 2011. **47**(47): p. 12697-12699.

137.   Tan, Q. and J.F. Li, *Thermoelectric Properties of Sn-S Bulk Materials Prepared by Mechanical Alloying and Spark Plasma Sintering.* Journal of Electronic Materials, 2014. **43**(6): p. 2435-2439.

138.   Yan, X.A., et al., *Enhanced Thermoelectric Figure of Merit of p-Type Half-Heuslers.* Nano Letters, 2011. **11**(2): p. 556-560.

139.   Zou, M.M., et al., *Synthesis and thermoelectric properties of fine-grained FeVSb system half-Heusler compound polycrystals with high phase purity.* Journal of Physics D-Applied Physics, 2010. **43**(41).

140.   Zou, M.M., et al., *Fabrication and thermoelectric properties of fine-grained TiNiSn compounds.* Journal of Solid State Chemistry, 2009. **182**(11): p. 3138-3142.

141.   Pavuna, D., *Production of Metallic-Glass Ribbons by the Chill-Block Melt-Spinning Technique in Stabilized Laboratory Conditions.* Journal of Materials Science, 1981. **16**(9): p. 2419-2433.

142.   Kumagai, M., et al., *Synthesis and Characterization of Melt-Spun Metastable Al6Ge5.* Journal of Electronic Materials, 2015. **44**(3): p. 948-952.

143.   Shi, W.D., S.Y. Song, and H.J. Zhang, *Hydrothermal synthetic strategies of inorganic semiconducting nanostructures.* Chemical Society Reviews, 2013. **42**(13): p. 5714-5743.

144.   Liu, C.J., et al., *High thermoelectric figure-of-merit in p-type nanostructured (Bi,Sb)(2)Te-3 fabricated via hydrothermal synthesis and evacuated-and-encapsulated sintering.* Journal of Materials Chemistry, 2012. **22**(11): p. 4825-4831.

145.   Nuchter, M., et al., *Microwave assisted synthesis - a critical technology overview.* Green Chemistry, 2004. **6**(3): p. 128-141.

146.   Singh, L.P., et al., *Sol-Gel processing of silica nanoparticles and their applications.* Adv Colloid Interface Sci, 2014. **214C**: p. 17-37.

147. Li, F. and J.F. Li, *Enhanced Thermoelectric Performance of Separately Ni-Doped and Ni/Sr-Codoped LaCoO3 Nanocomposites.* Journal of the American Ceramic Society, 2012. **95**(11): p. 3562-3568.

148. Mehta, R.J., et al., *A new class of doped nanobulk high-figure-of-merit thermoelectrics by scalable bottom-up assembly.* Nature Materials, 2012. **11**(3): p. 233-240.

149. Jin, R.C., J.S. Liu, and G.H. Li, *Facile solvothermal synthesis, growth mechanism and thermoelectric property of flower-like Bi2Te3.* Crystal Research and Technology, 2014. **49**(7): p. 460-466.

150. Tan, Q., et al., *Solvothermally synthesized SnS nanorods with high carrier mobility leading to thermoelectric enhancement.* Rsc Advances, 2016. **6**(50): p. 43985-43988.

151. Ibanez, M., et al., *High-performance thermoelectric nanocomposites from nanocrystal building blocks.* Nature Communications, 2016. **7**.

152. James, D.J., et al., *Solvothermal Synthesis of Tetrahedrite: Speeding Up the Process of Thermoelectric Material Generation.* Acs Applied Materials & Interfaces, 2015. **7**(42): p. 23623-23632.

153. Mi, J.L., et al., *Thermoelectric properties of n-type CoSb3 nanocomposite prepared by in situ solvothermal synthesis and hot pressing.* Journal of Inorganic Materials, 2008. **23**(4): p. 715-718.

154. Zhu, Y.G., H.L. Shen, and H. Guan, *Microwave-assisted synthesis and thermoelelectric properties of CoSb3 compounds.* Journal of Materials Science-Materials in Electronics, 2012. **23**(12): p. 2210-2215.

155. Langer, J., M.J. Hoffmann, and O. Guillon, *Electric Field-Assisted Sintering in Comparison with the Hot Pressing of Yttria-Stabilized Zirconia.* Journal of the American Ceramic Society, 2011. **94**(1): p. 131-138.

156. Dong, Y. and G.S. Nolas, *Crystal Growth through Field-Assisted Electrochemical Redox and Ion-Exchange Reactions: A Case Study of K4.2Na3.8Si46 Clathrate-I.* Crystal Growth & Design, 2015. **15**(10): p. 4731-4734.

157. Delaizir, G., et al., *A comparative study of Spark Plasma Sintering (SPS), Hot Isostatic Pressing (HIP) and microwaves sintering techniques on p-type Bi2Te3 thermoelectric properties.* Materials Research Bulletin, 2012. **47**(8): p. 1954-1960.

158. Mi, J.L., et al., *Nanostructuring and thermoelectric properties of bulk skutterudite compound CoSb3.* Journal of Applied Physics, 2007. **101**(5).

159. Wu, H.J., et al., *Broad temperature plateau for thermoelectric figure of merit ZT > 2 in phase-separated PbTe0.7S0.3.* Nature Communications, 2014. **5**.

160. Vivekanandhan, P., R. Murugasami, and S. Kumaran, *Rapid in-situ synthesis of nanocrystalline magnesium silicide thermo-electric compound by spark plasma sintering.* Materials Letters, 2017. **197**: p. 106-110.

161. Omerasevic, M., et al., *Safe trapping of cesium into pollucite structure by hot-pressing method.* Journal of Nuclear Materials, 2016. **474**: p. 35-44.

162. Yang, F., et al., *Lattice Thermal Conductivity Reduction Due to In Situ-Generated Nano-Phase in Bi0.4Sb1.6Te3 Alloys by Microwave-Activated Hot Pressing.* Journal of Electronic Materials, 2014. **43**(11): p. 4327-4334.

163. LaLonde, A.D., T. Ikeda, and G.J. Snyder, *Rapid consolidation of powdered materials by induction hot pressing.* Review of Scientific Instruments, 2011. **82**(2).

164. Zhou, M., J.F. Li, and T. Kita, *Nanostructured AgPbmSbTem+2 system bulk materials with enhanced thermoelectric performance.* Journal of the American Chemical Society, 2008. **130**(13): p. 4527-4532.

165. Zhao, L.D., et al., *SnSe: a remarkable new thermoelectric material.* Energy & Environmental Science, 2016. **9**(10): p. 3044-3060.

166. Shen, J.J., et al., *Recrystallization induced in situ nanostructures in bulk bismuth antimony tellurides: a simple top down route and improved thermoelectric properties.* Energy & Environmental Science, 2010. **3**(10): p. 1519-1523.

167. Pan, Y. and J.F. Li, *Thermoelectric performance enhancement in n-type Bi-2(TeSe)(3) alloys owing to nanoscale inhomogeneity combined with a spark plasma-textured microstructure.* Npg Asia Materials, 2016. **8**.

168. Raj, R., et al., *Methods of flash sintering*. 2013, Google Patents.

169. Yoshida, H., et al., *Densification behaviour and microstructural development in undoped yttria prepared by flash-sintering.* Journal of the European Ceramic Society, 2014. **34**(4): p. 991-1000.

170. Karakuscu, A., et al., *Defect Structure of Flash-Sintered Strontium Titanate.* Journal of the American Ceramic Society, 2012. **95**(8): p. 2531-2536.

171. Zhang, Y.Y., J.I. Jung, and J. Luo, *Thermal runaway, flash sintering and asymmetrical microstructural development of ZnO and ZnO-Bi2O3 under direct currents.* Acta Materialia, 2015. **94**: p. 87-100.

172. Yoshida, H., et al., *Formation of grain boundary second phase in BaTiO3 polycrystal under a high DC electric field at elevated temperatures.* Journal of the Ceramic Society of Japan, 2016. **124**(4): p. 388-392.

173. Castle, E., et al., *Rapid sintering of anisotropic, nanograined Nd-Fe-B by flash-spark plasma sintering.* Journal of Magnetism and Magnetic Materials, 2016. **417**: p. 279-283.

174. Yu, M., et al., *Magnéli phase titanium suboxides by Flash Spark Plasma Sintering.* Scripta Materialia, 2018. **146**: p. 241-245.

175. Srinivasan, B., et al., *Effect of the Processing Route on the Thermoelectric Performance of Nanostructured CuPb(18S)bTe(20).* Inorganic Chemistry, 2018. **57**(20): p. 12976-12986.

176. Srinivasan, B., et al., *Realizing a stable high thermoelectric zT ~ 2 over a broad temperature range in Ge1−x−yGaxSbyTe via band engineering and hybrid flash-SPS processing.* Inorganic Chemistry Frontiers, 2018.

177. Mikami, M., et al., *Flash-sintering of antimony telluride and its thermoelectric properties.* Journal of Applied Physics, 2018. **124**(10).

178. Tsujii, N., et al., *Effect of Nanostructuring and High-Pressure Torsion Process on Thermal Conductivity of Carrier-Doped Chalcopyrite.* Journal of Electronic Materials, 2016. **45**(3): p. 1642-1647.

179. *LSR-3 Instrument manual* 2016.

180. *Principle of the LFA method.* https://www.netzsch-thermal-analysis.com/en/landing-pages/principle-of-the-lfa-method/.

181. Feng, B., et al., *Enhanced thermoelectric properties of p-type CoSb3/graphene nanocomposite.* Journal of Materials Chemistry A, 2013. **1**(42): p. 13111-13119.

182. Lefevre, R., et al., *Thermoelectric properties of the chalcopyrite Cu1-xMxFeS2-y series (M = Mn, Co, Ni).* Rsc Advances, 2016. **6**(60): p. 55117-55124.

183. Birkel, C.S., et al., *Improving the thermoelectric properties of half-Heusler TiNiSn through inclusion of a second full-Heusler phase: microwave preparation and spark plasma sintering of TiNi1+xSn.* Physical Chemistry Chemical Physics, 2013. **15**(18): p. 6990-6997.

184. *https://www.linseis.com/en/products/thermoelectrics/lsr-3/*.

185. *https://www.netzsch-thermal-analysis.com/en/products-solutions/thermal-diffusivity-conductivity/lfa-457-microflash/*.

186. Maizza, G., et al., *Peltier effect during spark plasma sintering (SPS) of thermoelectric materials.* Journal of Materials Science, 2017. **52**(17): p. 10341-10352.

187. McWilliams, B., J. Yu, and A. Zavaliangos, *Fully coupled thermal-electric-sintering simulation of electric field assisted sintering of net-shape compacts.* Journal of Materials Science, 2015. **50**(2): p. 519-530.

188. Wei, X.L., et al., *Experimental Investigation of Electric Contact Resistance in Spark Plasma Sintering Tooling Setup.* Journal of the American Ceramic Society, 2015. **98**(11): p. 3553-3560.

189. Vanmeensel, K., et al., *Modelling of the temperature distribution during field assisted sintering.* Acta Materialia, 2005. **53**(16): p. 4379-4388.

190. Maniere, C., et al., *Contact resistances in spark plasma sintering: From in-situ and ex-situ determinations to an extended model for the scale up of the process.* Journal of the European Ceramic Society, 2017. **37**(4): p. 1593-1605.

191. Gucci, F., T.G. Saunders, and M.J. Reece, *In-situ synthesis of n-type unfilled skutterudite with reduced thermal conductivity by hybrid flash-spark plasma sintering.* Scripta Materialia, 2018. **157**: p. 58-61.

192. Moore, J.P., R.S. Graves, and D.L. McElroy, *Thermal and Electrical Conductivities and Seebeck Coefficients of Unirradiated and Irradiated Graphites from 300 to 1000°K.* Nuclear Technology, 1974. **22**(1): p. 88-93.

193. Kinchin, G.H., *The Electrical Properties of Graphite.* Proceedings of the Royal Society of London. Series A, Mathematical and Physical Sciences, 1953. **217**(1128): p. 9-26.

194. Gutierrez, R., et al., *Material selection for Latent heat based high temperature solar thermal energy storage.* International Conference on Technologies and Materials for Renewable Energy, Environment and Sustainability -Tmrees15, 2015. **74**: p. 1525-1532.

195. *https://www.upmet.com/sites/default/files/datasheets/302.pdf*.

196. *https://www.sglgroup.com/cms/_common/downloads/products/product-groups/gs/tds/expanded/SIGRAFLEX_TDS-TH_NH_THP_S_HP_UHP_Foil.02.pdf*.

197. Graftech, *Grafoil Engineering Design Manual.* https://neograf.com/wp-content/uploads/NGS_GrafoilEngineeringDesignManual.pdf.

198. *https://www.sglgroup.com/cms/_common/downloads/products/product-groups/gs/tds/expanded/SIGRAFLEX_TDS-TH_NH_THP_S_HP_UHP_Foil.02.pdf*, Sigraflex, Editor.

199. Maniere, C., et al., *Finite-element modeling of the electro-thermal contacts in the spark plasma sintering process.* Journal of the European Ceramic Society, 2016. **36**(3): p. 741-748.

200. Maniere, C., et al., *Pulse analysis and electric contact measurements in spark plasma sintering.* Electric Power Systems Research, 2015. **127**: p. 307-313.

201. Maizza, G., S. Grasso, and Y. Sakka, *Moving finite-element mesh model for aiding spark plasma sintering in current control mode of pure ultrafine WC powder.* Journal of Materials Science, 2009. **44**(5): p. 1219-1236.

202. Giuntini, D., et al., *Localized Overheating Phenomena and Optimization of Spark-Plasma Sintering Tooling Design.* Materials, 2013. **6**(7): p. 2612-2632.

203. Matsugi, K., et al., *Temperature distribution at steady state under constant current discharge in spark sintering process of Ti and A1203 powders (vol 134, pg 225, 2003).* Journal of Materials Processing Technology, 2004. **146**(2): p. 273-281.

204. Zavaliangos, A., et al., *Temperature evolution during field activated sintering.* Materials Science and Engineering a-Structural Materials Properties Microstructure and Processing, 2004. **379**(1-2): p. 218-228.

205. Munoz, S. and U. Anselmi-Tamburini, *Temperature and stress fields evolution during spark plasma sintering processes.* Journal of Materials Science, 2010. **45**(23): p. 6528-6539.

206. Shanbogh, P.P. and S.C. Peter, *Low cost nano materials crystallize in the NiAs structure type as an alternative to the noble metals in the hydrogenation process.* RSC Advances, 2013. **3**(45): p. 22887-22890.

207. Caillat, T., A. Borshchevsky, and J.P. Fleurial, *Properties of single crystalline semiconducting CoSb3.* Journal of Applied Physics, 1996. **80**(8): p. 4442-4449.

208. May, A.F., J.P. Fleurial, and G.J. Snyder, *Thermoelectric performance of lanthanum telluride produced via mechanical alloying.* Physical Review B, 2008. **78**(12).

209. Kim, H.S., et al., *Characterization of Lorenz number with Seebeck coefficient measurement.* Apl Materials, 2015. **3**(4).

210. al., P.e., *The Transformation Behaviour of Metal-Enriched Chalcopyrite.* Contrib. Mineral. Petrol, 1976. **58**.

211. a., P., *Talnakhite and Mooiohekite:The Accessibility of Ordered Structure in teh Metal-Rich Region Around Chalcopyrite.* Canadian Mineralogist, 1978. **16**.

212. Mos, Y.M., et al., *X-Ray Diffraction of Iron Containing Samples: The Importance of a Suitable Configuration.* Geomicrobiology Journal, 2018. **35**(6): p. 511-517.

213. Li, J., Q. Tan, and J.-F. Li, *Synthesis and property evaluation of CuFeS2−x as earth-abundant and environmentally-friendly thermoelectric materials.* Journal of Alloys and Compounds, 2013. **551**: p. 143-149.

214. Kim, S.W., Y. Kimura, and Y. Mishima, *High temperature thermoelectric properties of TiNiSn-based half-Heusler compounds.* Intermetallics, 2007. **15**(3): p. 349-356.

215. Muta, H., et al., *High-temperature thermoelectric properties of Nb-doped MNiSn (M = Ti, Zr) half-Heusler compound.* Journal of Alloys and Compounds, 2009. **469**(1-2): p. 50-55.

216. Srinivasan, B., et al., *Realizing a Stable High Thermoelectric zT ~ 2 over a Broad Temperature Range in Ge1-x-yGaxSbyTe via Band Engineering and Hybrid Flash-SPS Processing.* Inorganic Chemistry Frontiers, 2018.

217. Downie, R.A., et al., *Effect of Spark Plasma Sintering on the Structure and Properties of Ti1-xZrxNiSn Half-Heusler Alloys.* Materials, 2014. **7**(10): p. 7093-7104.

218. Douglas, J.E., et al., *Phase stability and property evolution of biphasic Ti-Ni-Sn alloys for use in thermoelectric applications.* Journal of Applied Physics, 2014. **115**(4).

219. R.Connolly, J. *Diffraction Basics, Part 2*.

220. Chen, J.L., et al., *Improved Thermoelectric Performance Achieved by Regulating Heterogeneous Phase in Half-Heusler TiNiSn-Based Materials.* Journal of Electronic Materials, 2018. **47**(6): p. 3248-3253.

221. Gelbstein, Y., et al., *Thermoelectric properties of spark plasma sintered composites based on TiNiSn half-Heusler alloys.* Journal of Materials Research, 2011. **26**(15): p. 1919-1924.

222. Bos, J.W.G. and R.A. Downie, *Half-Heusler thermoelectrics: a complex class of materials.* Journal of Physics-Condensed Matter, 2014. **26**(43).

223. Hazama, H., et al., *Study of Electronic Structure and Defect Formation in Ti1-x Ni1+x Sn Half-Heusler Alloys.* Journal of Electronic Materials, 2010. **39**(9): p. 1549-1553.

224. Downie, R.A., et al., *Enhanced thermoelectric performance in TiNiSn-based half-Heuslers.* Chemical Communications, 2013. **49**(39): p. 4184-4186.

225. Lu, K., L. Lu, and S. Suresh, *Strengthening Materials by Engineering Coherent Internal Boundaries at the Nanoscale.* Science, 2009. **324**(5925): p. 349-352.

226. Srinivasan, B., et al., *Effect of the Processing Route on the Thermoelectric Performance of Nanostructured CuPb18SbTe20.* Inorganic Chemistry, 2018. **57**(20): p. 12976-12986.

227. Zhao, D.G., et al., *High temperature oxidation behavior of cobalt triantimonide thermoelectric material.* Journal of Alloys and Compounds, 2010. **504**(2): p. 552-558.

228. Tani, J., M. Takahashi, and H. Kido, *Thermoelectric properties and oxidation behaviour of Magnesium Silicide.* IOP Conference Series: Materials Science and Engineering, 2011. **18**(14): p. 142013.

229. al, S.e., *High temperature oxidation of Mg(Si-Sn.* Journal of corrosion Science, 2016. **111**: p. 8.

230. Ning, H.P., et al., *Oxidation protective glass-ceramic coating for higher manganese silicide thermoelectrics.* Journal of Materials Science, 2016. **51**(20): p. 9484-9489.

231. Li, Y., et al., *High-temperature oxidation behavior of thermoelectric SnSe.* Journal of Alloys and Compounds, 2016. **669**: p. 224-231.

232. Yin, K., et al., *Thermal stability of Mg2Si0.3Sn0.7 under different heat treatment conditions.* Journal of Materials Chemistry C, 2015. **3**(40): p. 10381-10387.

233. Salvo, M., et al., *Glass-ceramic oxidation protection of higher manganese silicide thermoelectrics.* Journal of the European Ceramic Society, 2018.

234. Zawadzka, K., et al., *Enhancement of oxidation resistance of CoSb3 thermoelectric material by glass coating.* Materials & Design, 2017. **119**: p. 65-75.

235. Brostow, W., I.K. Chen, and J.B. White, *Effects of polymeric coatings on the service life of bismuth telluride-based thermoelectric materials.* Sustainable Energy & Fuels, 2017. **1**(6): p. 1376-1380.

236. Joseph, A.M.a.R., *Nanotechnology-A New Prospective in Organic Coating -*

Review. International Journal of Chemical Engineering and Applications, 2011. **2**(4): p. 12.

237. Ballard, R.L., et al., *Inorganic-organic hybrid coatings with mixed metal oxides.* European Polymer Journal, 2001. **37**(2): p. 381-398.

238. Oilo, G., *Luting cements: a review and comparison.* Int Dent J, 1991. **41**(2): p. 81-8.

239. Chou, Y.S. and J.W. Stevenson, *Phlogopite mica-based compressive seals for solid oxide fuel cells: effect of mica thickness.* Journal of Power Sources, 2003. **124**(2): p. 473-478.

240. Cao, X.Q., R. Vassen, and D. Stoever, *Ceramic materials for thermal barrier coatings.* Journal of the European Ceramic Society, 2004. **24**(1): p. 1-10.

241. *https://www.aremco.com/wp-content/uploads/2016/07/A0_Catalog_16.pdf*, AREMCO, Editor.

242. Kanatzidis, M.G., *Nanostructured Thermoelectrics: The New Paradigm?* Chemistry of Materials, 2010. **22**(3): p. 648-659.

243. Okamoto, H., *Mn-Si (Manganese-Silicon).* Journal of Phase Equilibria, 1991. **12**(4): p. 505-507.

244. Sadia, Y., L. Dinnerman, and Y. Gelbstein, *Mechanical Alloying and Spark Plasma Sintering of Higher Manganese Silicides for Thermoelectric Applications.* Journal of Electronic Materials, 2013. **42**(7): p. 1926-1931.

245. Famengo, A., et al., *Phase Content Influence on Thermoelectric Properties of Manganese Silicide-Based Materials for Middle-High Temperatures.* Journal of Electronic Materials, 2013. **42**(7): p. 2020-2024.

246. Zaitsev, V.K., et al., *Highly effective Mg2Si1-xSnx thermoelectrics.* Physical Review B, 2006. **74**(4).

247. Liu, W., et al., *Optimized Thermoelectric Properties of Sb-Doped Mg2(1+z)Si0.5-ySn0.5Sby through Adjustment of the Mg Content.* Chemistry of Materials, 2011. **23**(23): p. 5256-5263.

248. Du, Z.L., et al., *Roles of interstitial Mg in improving thermoelectric properties of Sb-doped Mg2Si0.4Sn0.6 solid solutions.* Journal of Materials Chemistry, 2012. **22**(14): p. 6838-6844.

249. Fedorov, M.I. and G.N. Isachenko, *Silicides: Materials for thermoelectric energy conversion.* Japanese Journal of Applied Physics, 2015. **54**(7).